# Rayleigh-Plateau-type Instabilities in Thin Liquid Films

Dissertation
zur Erlangung des Grades
des Doktors der Naturwissenschaften
der Naturwissenschaftlich-Technischen Fakultät II
- Physik und Mechatronik -
der Universität des Saarlandes

von

Sabrina Haefner

Saarbrücken

2015

Tag des Kolloquiums: 17.05.2016

Dekan: Univ.-Prof. Dr.-Ing. Georg Frey

Mitglieder des Prüfungsausschusses:

| | |
|---|---|
| Vorsitzender: | Univ.-Prof. Dr.-Ing. Michael Vielhaber |
| Gutachter: | Univ.-Prof. Dr. rer. nat. Karin Jacobs |
| | Univ.-Prof. Dr. rer. nat. Ludger Santen |
| Akademischer Mitarbeiter: | Dr. rer. nat. Elke Neu |

# Kurzzusammenfassung

Fließprozesse von Flüssigkeiten auf kleinen Längenskalen gewinnen aktuell durch den zunehmenden Trend der Miniaturisierung, wie z. B. in Lab-on-a-Chip Anwendungen, an Bedeutung. Infolgedessen stellen die Wechselwirkungen an der Grenzfläche zwischen Substrat und Flüssigkeit sowie deren Einflüsse auf die Stabilität und die Fließdynamik dünner Flüssigkeitsfilme zentrale Fragestellungen dar.

Diese Arbeit beschäftigt sich mit der Charakterisierung der Auswirkungen der hydrodynamischen Randbedingung an der fest/flüssig Grenzfläche auf die Rayleigh-Plateau Instabilität (RPI). Im ersten Teil wird die RPI eines Flüssigkeitsfilms auf einer zylinderförmigen Faser untersucht. Die Variation der Randbedingung zeigte einen signifikanten Einfluss auf die Dynamik der RPI. Der Vergleich zwischen den experimentell bestimmten Wachstumsraten und einem Dünnfilmmodell liefert ein Maß für die Schlupflänge. Des Weiteren wurde gezeigt, dass das späte Stadium der RPI auf einer hydrophoben Faser die Bildung von sich bewegenden Tropfen ermöglicht. Dies gestattet die quantitative Untersuchung des, durch Kapillarität getriebenen, Flüssigkeitstransports entlang einer Faser. Für eine entnetzende gerade Front in einem dünnen Film auf einem flachen Substrat wurde schließlich gezeigt, dass nicht nur die Dynamik der RPI durch die Randbedingung beeinflusst wird, sondern auch die Morphologie. Die sich zurückziehende Front weist charakteristische Merkmale auf, die in numerischen Berechnungen unter Berücksichtigung von hydrodynamischem Rutschen modelliert werden. Die Ergebnisse dieser Studie heben die Bedeutung der hydrodynamischen Randbedingung auf Fließprozesse auf kleinen Längenskalen hervor.

# Abstract

To date, flow processes of liquids on small scales have gained soaring attention due to the increased miniaturization trend, e. g. in lab-on-a-chip applications. As a result, the interactions at the interface between a solid and a liquid and their effects on the stability and the flow dynamics of thin liquid films denote essential questions.

This study focusses on characterizing the impact of the hydrodynamic boundary condition at the solid/liquid interface on the Rayleigh-Plateau instability (RPI). In the first part, the RPI of a liquid film on a cylindrical fibre is studied. The variation of the boundary condition revealed a significant influence on the dynamics of the RPI. The comparison between the growth rates in the experiments and a thin film model provides a measure for the slip length. It is also found that the late stage of the RPI on a hydrophobic fibre provides moving droplets. That enabled the quantitative examination of the capillary-driven liquid transport along a fibre. For a dewetting straight front in a thin film on a planar substrate it is finally shown that not only the dynamics of the RPI is affected by the boundary condition, but also the morphology. The receding front shows characteristic fingerprints, that are reproduced in numerical calculations comprising hydrodynamic slip. The findings of this study highlight the importance of the hydrodynamic boundary condition for flows on small scales.

# Contents

# 1 Introduction

Understanding the flow processes of liquids represents a fundamental subject which is attracting the attention of scientists since more than 300 years. Already in the 1680s, Edme Mariotte, a french physicist, addressed the phenomenon of a decaying water stream, flowing from a hole of the bottom of a water reservoir, into droplets. Nowadays, the investigation of the mechanisms which govern the flow of liquids has become even more important with respect to many technological applications. As an illustrative example, researchers recently developed a promising and low-cost method to harvest drinking water from fog in remote regions. Inspired by efficient examples known from nature, as e. g. the water collection ability of the cactus family, artificial fog nets collect water droplets by the condensation of atmospheric water vapor at their web filaments. While small droplets may be pinned to the web, the impact of gravity causes big droplets to flow down, coalesce with others and finally drip into a reservoir.

In contrast to the gravity-driven motion of liquids, on small scales, fluids may be forced to flow by capillarity. For example, several species of birds rely on a capillary-driven collection of water and nectar using their tongues acting as a capillary tube. Understanding the fundamental mechanisms of the dynamics of fluids in various geometries, e. g. liquid films and filaments as well as small droplets, on small length scales is of great interest. In light of the ongoing miniaturization of fluid systems towards micro- and nanofluidic devices, understanding the influence of interfacial effects on flow processes becomes more and more important. In this context, in particular, the hydrodynamic boundary condition at the interface between a liquid and a solid plays an important role. While macroscopic flows assume a no-slip boundary condition at the solid/liquid interface, the flow behavior of fluids on small scales may, however, reveal a deviation from the no-slip case: the fluids may show a non-zero velocity of the first liquid molecules at the interface, i. e. the liquids may slip along the substrate.

While industrial applications, as e. g. the technology of optical fibre coating, require the fabrication of a homogeneous film, the fog harvesting technique benefits from the spontaneous formation of droplets on the web filaments. In analogy to the everyday life phenomenon of the breakup of a water jet flowing out of a faucet, the formation of surface undulations and the final decay into a regular droplet pattern of a liquid film on a fibre is caused by the Rayleigh-Plateau instability (RPI). The instability is named after Joseph Plateau and Lord Rayleigh, who experimentally (Plateau, 1873) and theoretically (Rayleigh, 1878) investigated this fundamental instability for the first time. Patterning and printing processes represent important technological applications that take advantage of the Rayleigh-Plateau instability. A liquid film on a substrate does, in general, strive towards its energy minimum. This can be achieved by either minimizing the surface area via the formation of droplets, as in case of the RPI, or by the reduction of the contact area to the substrate. In the latter case, the film exposes the substrate of a lower surface energy, resulting in a receding liquid rim, which grows over time due to the accumulation of the residual film. This process is called dewetting. Besides liquid

films on fibres, dewetting straight fronts in thin films on planar substrates may also be subject to an instability of the Rayleigh-Plateau type. The classical case of a decaying liquid cylinder can be described by considering the free surface only. The characterization of the RPI of a liquid film on a substrate may, however, require the consideration of the additional solid/liquid interface.

The major goal of this work is to precisely characterize the influence of the hydrodynamic boundary condition at the solid/liquid interface on the RPI of a viscous liquid film on small scales. Two different geometries will be considered: a) a viscous liquid film on a microfibre and b) a moving straight front in a viscous film on a planar substrate. The second aspect refers to the transport of liquid droplets along a fibre driven by capillary forces. Here, the question arises whether the hydrodynamic boundary condition influences the droplet dynamics.

All experiments are performed using polymeric liquids, as they represent ideal model fluids to address the questions elaborated above: polymers can be obtained as nearly monodisperse liquids while exhibiting precisely tunable chemical properties. As the viscosity reveals a unique dependence on temperature, the time scale of the liquid flow can easily be adjusted over several orders of magnitude. In addition, polymeric liquids may exhibit a significant amount of slip. In this work, polystyrene of different molecular weights is used, which for the applied shear rates displays a Newtonian liquid.

The current state of the art and open questions, addressed in this thesis, are summarized in **chapter 2**. The description of the basic properties of polymeric liquids is followed by the fundamental concepts of hydrodynamics in thin films. The Navier-Stokes equation, the hydrodynamic boundary conditions and the thin film equation are revisited. In addition, the stability conditions of thin liquid films as well as their mechanisms and dynamics are illustrated. The explanation of the classical Rayleigh-Plateau instability of a free liquid cylinder is followed by an overview of the current state of the art with respect to the RPI evolving in different geometries. The chapter closes with a summary of recent studies on droplet propulsion processes while putting an emphasis on the motion of droplets on fibres.

The experimental techniques, which have been applied in this thesis, are outlined in **chapter 3**. The sample preparation section includes the coating of the substrates with a hydrophobic layer, the application of homogeneous polymer films as well as the generation of moving droplets. The description of the measurement methods is followed by a detailed overview of the data analysis techniques.

**Chapter 4** contains the results concerning the Rayleigh-Plateau instability of a viscous liquid film on a fibre. The focus of the first section lies on the influence of the hydrodynamic boundary condition at the solid/liquid interface on the spatial and temporal evolution of the RPI. The variation of the boundary condition at the interface from no slip to slip revealed a significant influence on the dynamics of the RPI. The comparison of the experimental data to the developed fibre thin film theory provides a measure for the slip length. In the second section, the slip length is varied by using a different molecular weight and by changing the surface treatment of the fibre.

The late stage of the RPI on a hydrophobic fibre is accompanied by the spontaneous formation of moving droplets. **Chapter 5** provides results on the capillary-driven propulsion of droplets

on hydrophobic fibres. First, the study concentrates on the propulsion dynamics, purely governed by viscous flow. The experimental results are compared to a force balance model based on purely viscous dissipation. The second part of the chapter presents first results on the influence of slippage at the solid/liquid interface on the droplet propulsion dynamics. The comparison of the droplet velocity data with the force balance model, which additively superposes the dissipation due to friction of the liquid molecules at the interface and the viscous dissipation, enables the estimation of the slip length.

As outlined above, the comparison of experimentally obtained data with the respective theoretical models provides a measure for the slip length. **Chapter 6** contains a comparison of the slip length obtained from the different studies and puts the values in perspective to the existing literature.

In previous works it has been shown that the dynamics of the RPI of a receding straight front in a thin film on a planar substrate is affected by slip. Beyond the impact on the dewetting dynamics, also its morphology displays certain fingerprints, which are characteristic for the hydrodynamic slip boundary condition. **Chapter 7** revisits the main features of the RPI in a dewetting straight front observed in experiments and establishes a direct comparison to numerical calculations of the full instability evolution: from the onset up to the final stage of the RPI.

In **chapter 8** the presented results of this work are summarized and discussed, followed by an outlook of possible future works.

# 2 State of the art

The work at hand, in general, concentrates on the investigation of liquid flows on small scales, where a polymeric liquid is used as a model system. The influence of the hydrodynamic boundary condition (no-slip or slip) at the solid/liquid interface between the polymer melt and a solid substrate is of particular interest. In the following, the short term 'boundary condition' is used, which always refers to the boundary condition at the solid/liquid interface. The examined questions are on the one hand: how does slippage at the solid/liquid interface influence the evolution of the Rayleigh-Plateau instability of a viscous liquid film on a fibre (Sec. 4) as well as on a planar substrate (Sec. 7). On the other hand, we present results on moving droplets on fibres with a varying boundary condition, propelled by capillary forces (Sec. 5). In the following, we focus on the properties of polymers (Sec. 2.1) and the hydrodynamics of thin liquid films with varying boundary conditions (Sec. 2.2 and 2.3). The description of the dynamics of dewetting (Sec. 2.4) is followed by the current state of research concerning the RPI in various geometries (Sec. 2.5) and droplets on fibres (Sec. 2.6).

## 2.1 Basic properties of atactic polystyrene

In 1920, polymer research came into focus with the description of polymers as molecules made of covalently bonded elementary units, called monomers, by Staudinger, a german chemist, who was awarded the Nobel Prize in 1953 [1]. At the same time, Ziegler and Natta established a way to perform low-pressure polymerization at room temperature by using specific catalysts (receiving the Nobel prize in 1963) [2, 3]. This pioneering invention fostered the industrial production of modern plastics, as e. g. packing materials. Several textbooks describe the properties of polymers, as e. g. the behavior of polymers in solutions or their viscoelasticity [4, 5, 6, 7]. In the following, only the most relevant characteristics are described. For further details, the reader is referred to the above mentioned textbooks.

In this work, a polymer melt is used as a model system to study the physics of fluids in confined geometries. In general, polymers are very suitable because of their abundant availability, their purity and monodispersity as well as the simplicity of controlling the material properties, as e. g. the viscosity.

Polymers are synthesized by polymerization of monomers with molar mass $M_{\mathrm{mono}}$. In our study, we used Polystyrene (PS), which is a linear homopolymer with a molar mass of $M_{\mathrm{mono}} = 104\,\mathrm{g/mol}$ [8]. The distribution of the lengths of the polymer chains depends on the polymerization process and is characterized by a statistical distribution of lengths, the measure of which is given as polydispersity index $M_{\mathrm{w}}/M_{\mathrm{n}}$ (with the weight average, $M_{\mathrm{w}}$, and the number average, $M_{\mathrm{n}}$, molecular weight). Depending on the production process different tacticities can

be generated: isotactic (all phenyl rings are located at the same side of the chain), syndiotactic (alternating on both sides) or atactic (random distribution of phenyl rings). The overall polymer architecture may vary between linear, branched, star-shaped or ringlike. A measure for the spatial dimension of polymers in equilibrium is given by the radius of gyration $R_G$, the mean square displacement between monomers and the center of mass. In this work, we exclusively use monodisperse, atactic polystyrene with molecular weights ranging from 4 kg/mol up to 390 kg/mol. All chains exhibit a linear architecture with a gyration radius of $R_G = b^2 N_k/6$, where $b = 1.8\,\text{nm}$ displays the length and $N_k = M_N/720\,\text{g/mol}$ the number of Kuhn-monomers for PS [8]. In the following, we focus on the properties of the used atactic polystyrene.

Depending on the temperature, the PS melts are either in a glassy or a liquid state. By heating them above their characteristic glass transition temperature $T_g$, the PS melts undergo a second-order phase transition from glassy to liquid. Because of its random distribution of side groups, the used atactic polystyrene does not form crystals below $T_g$, it is completely amorphous. Undergoing a glass transition is a purely kinematic effect and is not caused by a restructuring of the polymer chains. Hence, the phase transition occurs over a certain temperature range rather than at one particular temperature. Furthermore, by considering short chains, we see that $T_g$ is significantly decreased due to their high mobility [8]. A reduction in the glass transition temperature has also been observed in case of confined geometries, such as thin films [9, 10, 11, 12, 13, 14].

### 2.1.1 Viscosity

Temperature has an influence on the polymer viscosity $\eta$, which is a measure of the resulting friction forces inside a sheared fluid. As the mobility of polymer chains increases with increasing temperature, the viscosity $\eta$ decreases. The Williams-Landel-Ferry (WLF) equation describes this temperature dependence of $\eta$ [8, 15]:

$$\eta = \eta_0 \exp\left(\frac{B}{f_0}\frac{T_g - T}{T - T_\infty}\right), \tag{2.1}$$

where, for PS, $\eta_0 = 6.3 \cdot 10^8\,\text{Pa s}$ represents the viscosity at the glass transition temperature $T_g = T_g(\infty) - C/M_w$ for the respective $M_w$, with $T_g(\infty) = 372\,\text{K}$ and $C = 70\,\text{K kg/mol}$. The Vogel temperature is given by $T_\infty = T_g - 48\,\text{K}$ and the ratio $B/f_0 = 30.3$ [8].

Despite the dependence on $T$, the molecular weight $M_w$ itself has a significant influence on the melt viscosity: an increase in $M_w$ results in a decreasing chain mobility, which in turn causes the relaxation of stress inside the polymer melt to be decelerated. Hence, the viscosity increases. If $M_w$ is smaller than a so-called critical molecular weight $M_c$, a linear dependence $\eta \propto M_w$ is predicted by the so-called Rouse model [8]. For $M_w > M_c$, an algebraic increase $\eta \propto M_w^3$ is expected from the reptation model by de Gennes [16], which experimentally was found to equal $\eta \propto M_w^{3.4}$ [8]. $M_c$ displays the critical chain length, above which polymer chains start to form entanglements with a mean filament length of $M_e$. For PS, Rubinstein *et al.* report $M_c = 35\,\text{kg/mol}$ and $M_e = 18\,\text{kg/mol}$ [8].

Shearing a liquid, in general, leads to a strain $\gamma$. If strain rate $\dot{\gamma}$ and shear stress $\sigma$ are proportional, the liquid is called Newtonian:

$$\sigma = \eta\dot{\gamma}, \tag{2.2}$$

where the constant of proportionality is equal to the viscosity $\eta$. In case of Newtonian liquids, the viscosity is independent of the strain rate $\dot{\gamma}$. Polymers with a high molecular weight may, however, exhibit viscoelastic effects, where the viscosity depends on the shear rate, i. e. $\eta(\dot{\gamma})$ (see Sec. 2.1.2).

To determine the viscosity $\eta$ of a liquid, several independent methods have been developed: one can measure $\eta$ by using a viscosimeter [17], where the viscosity can be extracted from measuring the drag of a fluid which is sheared by means of external driving forces. Studying the leveling process of stepped viscous films also allows for a direct extraction of the viscosity $\eta$ [18]. By measuring the glass transition temperature $T_\mathrm{g}$ via e. g. the determination of the thermal expansion coefficient of a liquid film using ellipsometry [19], the course of viscosity as a function of molecular weight and temperature can be extrapolated by projecting the data according to the WLF equation (Eq. 2.1). In the **publications in ADDENDUM I and II**, we show further independent and rapid methods to quantify the viscosity of a fluid.

### 2.1.2 Viscoelasticity

If the viscosity decreases while shearing the liquid, the behavior is referred to as shear-thinning, whereas a viscosity increase is called shear-thickening. These liquids are called viscoelastic, as on short timescales ($t < \tau$) they react like an elastic fluid, where deformations recover slowly. On long timescales ($t > \tau$), however, the liquid features purely viscous properties. The so-called relaxation time $\tau$ is a specific timescale, on which deformations of a viscoelastic liquid relax. Thereby shear strain $\gamma$ and shear stress $\sigma$ are proportional via the elastic modulus $G$:

$$\sigma = G\gamma. \tag{2.3}$$

The dynamics of the stress relaxation can be described by several models. The simplest example is the so-called Maxwell model (linear viscoelasticity), in which the fluid is described by a serial connection of a perfectly elastic element, which is represented by a Hookean spring, and a perfectly viscous element, given by a dashpot (see Fig. 2.1a). Hence, the shear strain corresponds to the sum of those two contributions:

$$\gamma = \gamma_\mathrm{e} + \gamma_\mathrm{v}. \tag{2.4}$$

Given a constant shear stress $\sigma$, where

$$\sigma = G\gamma_\mathrm{e} = \eta\dot{\gamma}_\mathrm{v}, \tag{2.5}$$

with the specific relaxation time $\tau$ given by the ratio of the viscosity $\eta$ of the viscous element and the elastic modulus $G$ of the elastic element:

$$\tau = \eta/G, \tag{2.6}$$

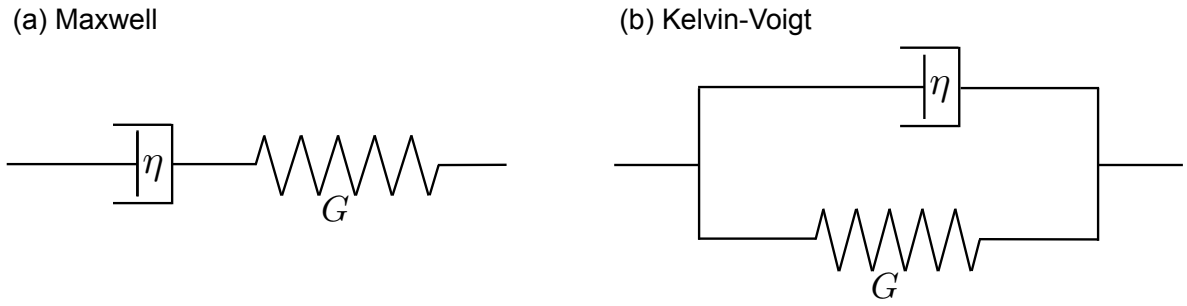


**Figure 2.1:** The simplest method to model the dynamics of stress relaxation is to describe the fluid by a connection of a spring (elastic element) and a dashpot (viscous element) when either (a) connecting them in series (Maxwell model) or (b) in parallel (Kelvin-Voigt model).

Eq. 2.4 reads:

$$\frac{\eta}{G}\dot{\gamma}_\mathrm{v} + \gamma_\mathrm{v} = \gamma \quad \Leftrightarrow \quad \tau\dot{\gamma}_\mathrm{v} = \gamma - \gamma_\mathrm{v}. \tag{2.7}$$

Hence, we see that the shear stress $\sigma$ of a viscoelastic fluid is time dependent. By assuming the initial condition $\gamma_\mathrm{v}(t=0) = 0$, the solution is given by an exponential decay of $\sigma(t)$:

$$\begin{aligned} \gamma_\mathrm{e}(t) &= \gamma \exp(-t/\tau), \\ \sigma(t) &= G\gamma_\mathrm{e}(t) = G\gamma \exp(-t/\tau). \end{aligned} \tag{2.8}$$

For small shear strains $\gamma$, the elastic modulus $G$ and the shear strain $\gamma$ are independent of each other and the liquid shows a linear behavior (linear response region). Here, a constant shear flow of a viscoelastic liquid can be regarded as a linear superposition of an infinite number of small strains. For larger shear rates $\dot{\gamma}$, however, the response is no longer linear and, hence, the linear superposition is not valid any more.

The Kelvin-Voigt model is represented by a parallel arrangement of spring and dashpot (see Fig. 2.1b). Consequently, all shear strains are identical and the total shear stress reads:

$$\sigma = \sigma_\mathrm{e} + \sigma_\mathrm{v} = G\gamma + \eta\dot{\gamma}. \tag{2.9}$$

Assuming $\gamma(t=0) = 0$ finally leads to:

$$\gamma(t) = \frac{\sigma}{G}\left(1 - e^{-\frac{G}{\eta}t}\right). \tag{2.10}$$

## 2.2 Hydrodynamics in thin films

The presented work examines the influence of the hydrodynamic boundary condition on the morphology and dynamics of thin film flows (c. f. Sec. 4 - 7). The purpose of this chapter is to give a brief overview of the theoretical background. The starting point is given by the introduction of several dimensionless numbers, which characterize the rheology of liquids and the relative importance of viscous forces, inertia, capillary forces and viscoelastic effects. The illustration of the Navier-Stokes equation is followed by the different boundary conditions at the solid/liquid interface. The current state of research on the slip length $b$ is described. Finally, the equation of motion for thin Newtonian liquid films is derived.

### 2.2.1 Dimensionless numbers

The Weissenberg number $Wi$ is a measure whether a liquid behaves viscoelastic or whether the flow dynamics is purely viscous:

$$Wi = \tau\dot{\gamma}. \tag{2.11}$$

$\tau$ displays the specific relaxation time and $\dot{\gamma}$ stands for the strain rate. Hence, we see that viscoelastic effects do not play a role, if $Wi \ll 1$.

The Reynolds number $Re$, defined as

$$Re = \frac{\rho u h}{\eta}, \tag{2.12}$$

gives the ratio of inertia to viscous forces, where $\rho$ displays the fluid density, $u$ being the mean flow velocity, a characteristic length $h$ (here: thickness of the liquid film) and viscosity $\eta$ [20]. For low Reynolds numbers, $Re \ll 1$, viscous forces are predominant, which results in a laminar liquid flow. Turbulence and vortices occur in the inertia dominated high $Re$ regime. In this work, $Re \ll 1$ and, thus, all experiments are exclusively performed in the laminar liquid flow regime.

The Weber number $We$ gives a measure of the ratio between deforming inertia and stabilizing surface forces for liquids flowing through another fluid phase (liquid or gas):

$$We = \frac{\rho u^2 h}{\gamma}. \tag{2.13}$$

Hence, $We$ characterizes e. g. the atomization process of sprays or the deformation of droplets. In the presented work, $We \ll 1$ for all experiments, which implies that the stabilizing interfacial tension dominates inertia.

The influence of viscosity $\eta$ compared to inertia and surface tension forces on the flow process can be expressed by the Ohnesorge number:

$$Oh = \frac{\eta}{\sqrt{\rho h \gamma}} = \frac{\sqrt{We}}{Re}. \tag{2.14}$$

Here, we worked in the $Oh \gg 1$ regime, indicating that the flow dynamics is influenced by viscosity.

### 2.2.2 Navier-Stokes equations

In case of liquid flows, we derive the equation of continuity, as a consequence of mass conservation:

$$\partial_t \rho + \vec{\nabla} \cdot (\rho \vec{u}) = 0, \tag{2.15}$$

with the liquid density $\rho$ and the velocity field $\vec{u} = (u_x, u_y, u_z)$. Given an incompressible liquid with a spatially and temporally constant density $\rho$ simplifies Eq. (2.15) to

$$\vec{\nabla} \vec{u} = 0. \tag{2.16}$$

Based on momentum conservation, the equation of motion for an incompressible Newtonian liquid is given by (Navier-Stokes equation) [21]:

$$\rho(\partial_t + \vec{u} \cdot \vec{\nabla})\vec{u} = \vec{f} - \vec{\nabla} p + \eta \vec{\nabla}^2 \vec{u}, \tag{2.17}$$

which is a force balance of the acting inertial forces (left side) and body forces $\vec{f}$, pressure gradients $\vec{\nabla} p$ as well as viscous dissipation. In the present work, experiments were performed in the low Reynolds number regime, $Re \ll 1$. As a result the Navier-Stokes equation, Eq. (2.17), simplifies to the so-called Stokes equation:

$$0 = \vec{f} - \vec{\nabla} p + \eta \vec{\nabla}^2 \vec{u}, \tag{2.18}$$

as inertia terms can be neglected.

In case of liquid flows in confined geometries, such as thin films, we assume the velocity component parallel to the surface $\vec{u}_{||}$ to be much bigger than the perpendicular velocity component $\vec{u}_{\perp}$. In addition, we state that the length scale of film thickness variations is much larger in the lateral ($\mathbb{L}$) than in the vertical ($\mathbb{H}$) direction, which is called lubrication approximation:

$$\epsilon = \mathbb{H}/\mathbb{L} \ll 1. \tag{2.19}$$

In the following $\epsilon$ denotes the lubrication parameter. For film thicknesses much smaller than the capillary length $l_c = \sqrt{\gamma_{lv}/\rho g}$, where $\gamma_{lv}$ displays the surface tension between the liquid (l) and the vapor (v) phase with $l_c \sim \mathcal{O}(10^{-3}\mathrm{m})$ for PS and in the absence of any external forces $\vec{f}$, Eq. (2.18) reads [22]:

$$0 = -\vec{\nabla}(p + \phi'(h)) + \eta \vec{\nabla}^2 \vec{u}, \tag{2.20}$$

where gravitational effects can be neglected, but interactions of the fluid molecules with the substrate need be considered. This leads to an additional term, $\phi'(h)$, representing the disjoining pressure. $\phi'(h)$ is the first derivative of the effective interface potential $\phi(h)$ with regard to the film thickness $h$ (see Sec. 2.3).

In this work, a surface tension value of $\gamma_{lv} = 30.8\,\mathrm{mN/m^{-1}}$ is used for PS. We note that the surface tension of a polymer melt depends on temperature and molecular weight [23]. For the used molecular weights and temperatures, the variation in the surface tension values is, however, small ($< 10\,\%$) [23, 24, 25]. Furthermore, the dynamics of polymer films is governed by the capillary velocity $\gamma/\eta$. The viscosity $\eta$ is extremely sensitive to temperature variations (see Eq. 2.1). As the error caused by the uncertainty of the viscosity (at least a factor of 2) is much larger compared to the variation in surface tension, we used the mean value of $\gamma_{lv} = 30.8\,\mathrm{mN/m}$ for PS in all calculations (see the **publication in ADDENDUM III**).

### 2.2.3 Hydrodynamic boundary conditions

When considering the dynamics of liquid thin film flows, the hydrodynamic boundary conditions at both interfaces (solid/liquid and liquid/vapor) play an important role. As the viscosity of the gas phase, which in most cases is air, is negligible, no shear forces are present at the liquid/air interface. The tangent $\mathbf{t}$ to the free surface of the liquid is given by:

$$(\mathcal{T} \cdot \mathbf{n}) \cdot \mathbf{t} = 0, \tag{2.21}$$

with the surface normal $\mathbf{n}$. Thereby, $\mathcal{T}_{\mathrm{ij}}$ represents the stress tensor, which is equal to $\mathcal{T}_{\mathrm{ij}} = \sigma_{\mathrm{ij}} + p\delta_{\mathrm{ij}} = \eta(\partial_{\mathrm{i}} u_{\mathrm{j}} + \partial_{\mathrm{j}} u_{\mathrm{i}}) + p\delta_{\mathrm{ij}}$ with shear stress $\sigma_{\mathrm{ij}} = \eta\dot{\gamma}_{\mathrm{ij}}$ and pressure $p$. Given a homogeneous surface tension at the liquid/air interface $\gamma_{\mathrm{lv}}$, the normal component can be written as:

$$(\mathcal{T} \cdot \mathbf{n}) \cdot \mathbf{n} = \gamma_{\mathrm{lv}}\kappa, \tag{2.22}$$

with the average curvature of the surface $\kappa$. If we consider the stationary state, with $\vec{u} = 0$, Eq. (2.22) simplifies to

$$p_{\mathrm{L}} = \gamma_{\mathrm{lv}}\kappa = \gamma_{\mathrm{lv}} \left( \frac{1}{R_1} + \frac{1}{R_2} \right), \tag{2.23}$$

which is the so-called Laplace equation. It describes the pressure difference between both sides of the curved liquid surface. $R_1$ and $R_2$ are the radii of the free surface curvature. The sign for $p$ varies and the sign convention gives positive curvature if convex and negative for concave boundaries. In the following, we discuss the different boundary conditions at the solid/liquid interface, which are strongly influenced by the specific substrate composition.

The classical case of macroscopic fluid flow (e. g. oil flow in a pipeline) allows for assuming the tangential velocity $\vec{u}_{||}$ at the solid/liquid interface ($z = 0$) to be equal to zero, which we refer to as no-slip boundary condition (see Fig. 2.2). On microscopic length scales, however, slippage of the fluid at the solid/liquid interface becomes relevant. In 1823, Navier already introduced the linear boundary condition, which up to now is used to characterize slippage of fluids at interfaces [26]: the tangential velocity $\vec{u}_{||}$ is proportional to the shear rate perpendicular to the substrate:

$$\vec{u}_{||} = b\vec{n} \cdot \dot{\gamma}, \tag{2.24}$$

where the constant of proportionality is given by the so-called slip length $b$. Assuming simple shear flow in the $x$-direction while the $xy$-plane is representing the solid/liquid interface, the slip length $b$ is defined as:

$$b = \left. \frac{u_x}{\partial_z u_x} \right|_{z=0} = \frac{u_x \eta}{\sigma} = \frac{\eta}{\mu}, \tag{2.25}$$

with the shear stress $\sigma = \eta\dot{\gamma}$ normal to the surface and the friction coefficient at the solid/liquid interface $\mu = \sigma/u_x$. As an illustrative model the slip length can be described as the extrapolation length of the velocity profile into the substrate until the velocity is zero (see Fig. 2.2). The slip length gives a quantitative measure of the amount of slip at the solid/liquid interface. Even the limit cases can be understood by this model: $b = 0$ gives the no-slip case and $b = \infty$ represents the so-called full-slip case (see Fig. 2.2), which corresponds to e. g. a solid sliding on top of another solid. In general, all cases are superpositions of the two limiting cases. Beyond

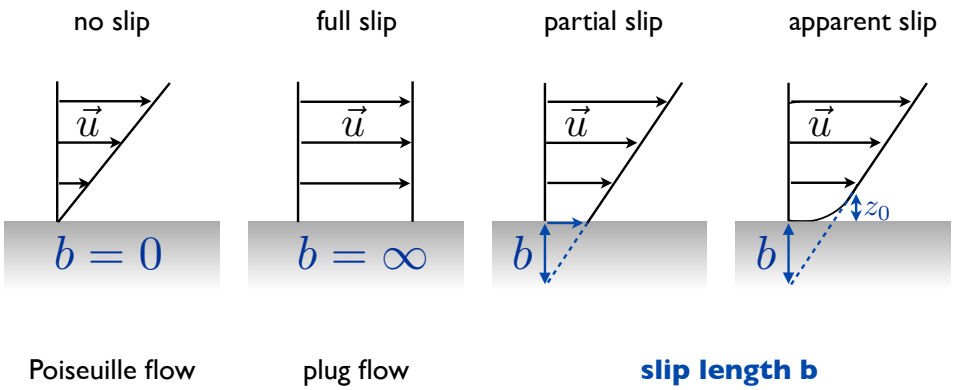


**Figure 2.2:** Fluid flow profiles close to the solid/liquid interface representing the interpretation of the slip length $b$ by Navier [26]. In case of apparent slip a non-zero slip length can be measured, but the velocity of the liquid molecules at the interface is zero, which is caused by a thin layer of thickness $z_0$ exhibiting a reduced viscosity.

that, apparent slip may occur, where a non-zero slip length can be measured, but where the velocity of the molecules at the interface is zero, which is caused by a thin layer of reduced viscosity (see Fig. 2.2).

The slip length at the boundary can be measured by various techniques: drainage experiments, where the force to drag a liquid, which is squeezed between e. g. a flat substrate and an atomic force microscope (AFM) colloidal probe, is measured [27, 28] or by probing the interfacial fluid velocity using tracer particles [29, 30]. From force/distance measurements between two oscillating cylinders which are arranged perpendicular to each other, the slip length can be measured via fitting a theoretical progression [31]. A very robust way to determine $b$ of a dewetting thin film is given by analyzing the profile of a rim surrounding a hole which forms in the course of the dewetting process (see Sec. 2.2.5) [20, 32, 33]. Measuring the dynamics of the growing hole also gives information about the amount of slip at the solid/liquid interface (cf. the **publication in ADDENDUM I**) [34, 35]. In this work, we also show a new and robust way to determine the slip length $b$ of viscous films on the micro-scale by analyzing the Rayleigh-Plateau instability of these films on fibres (cf. the **publication in ADDENDUM II**). In addition, the dynamics of receding droplets on hydrophobized fibres enables the estimation of the slip length $b$ (see Sec. 5.2).

Several parameters can influence the slip length, as for example molecular interactions between the liquid molecules and the substrate. In case of a substrate which is completely wettable, i. e. interactions are attractive, friction is expected to increase which in turn causes the slip length to decrease compared to values obtained for partial or non-wettable substrates. Consequently, the slip length increases with increasing contact angle, which has been shown in several studies [36, 37, 38, 39]. The roughness or the structure of the underlying surface plays also an important role, as for different roughness length scales, the friction at the solid/liquid interface can either increase or decrease with increasing roughness [39, 40]. Hence, a rough substrate, which is expected to show an increased friction between the liquid and the substrate, may actually

exhibit a large slip length $b$. A potential explanation for this counterintuitive increase in the slip length $b$ might be a thin layer of gas cavities located at the interface [41, 42, 43]. In addition, the shape of the liquid molecules itself can also influence the condition at the boundary. In this regard, it has been shown that elongated linear molecules compared to branched molecules exhibit a higher slip length. This might be understood by the ordering of liquid molecules and alignment effects close to an interface [44, 45, 46]. Besides this, the slip length can also be affected by properties as the fluid flow itself, temperature, viscosity or shear rate. In case of a slow flowing polymer melt, the measured slip lengths were found to be lower than expected [47]. This can be understood by adsorbed polymer chains at the substrate, which in further course of fluid motion form entanglements with chains in the melt. This in turn increases the friction at the interface and lowers slippage. By increasing the shear rate above a critical value, which strongly depends on the molecular weight, that is the length of the polymer chains, the entangled chains become disentangled and slippage is enhanced [48, 49, 50, 51].

In case of long-chained polymer melts on a non-adsorbing substrate, de Gennes revealed a significant increase of $b$ with increasing the polymer chain length [52]:

$$b = a\frac{N^3}{N_\mathrm{e}^2}, \tag{2.26}$$

with the size of a monomer $a$, the number of monomers $N$ and the entanglement length $N_\mathrm{e}$. For polystyrene, the literature values are $a = 3\,\text{Å}$ and $N_\mathrm{e} = 163$ [8, 53].

This particular dependence of the slip length $b$ on $M_\mathrm{w}$ has been reproduced experimentally by studying rim profiles of holes in dewetting thin polystyrene films with varying molecular weights on hydrophobized (amorphous AF1600 layer on top of a Si wafer) substrates [35], see Fig. 2.3. Additionally, Bäumchen *et al.* found the slip length to be independent of temperature or rather viscosity. In contrast, Fetzer *et al.* revealed a strong correlation between the measured slip length and the used annealing temperature, when again studying holes in dewetting thin films, but using hydrophobic self-assembled monolayers as substrates [32]. Hence, the specific substrate/liquid combination of AF1600 and polystyrene provides an optimal technique to vary the dynamics of a fluid without changing the slip length. Slippage, however, can easily be varied by a change in the chain length $b \sim M_\mathrm{w}^3$. Note that for $M_\mathrm{w} < M_\mathrm{c}$, the slip length is constant in the range of $10 - 100\,\text{nm}$ (see Fig. 2.3). Considering typical film heights of $100 - 200\,\text{nm}$, this means that the contribution of slip vanishes, equivalent to a weak- or roughly a no-slip situation. However, the study revealed a significantly larger entanglement length of $N_\mathrm{e} = 517$ [35], indicating that close to the substrate the effective inter-chain entanglement density is reduced by a factor of roughly 3. The reduction in $N_\mathrm{e}$ is corroborated by other experimental works [54, 55]. In addition, Brown and Russell showed that the entanglement length of a polymer close to an interface is enlarged by a factor of $\sim 4$. This specific interface effect is a result of the reduced volume, which is infused with a chain at the interface and ranges maximum over one gyration radius away from the surface [56].

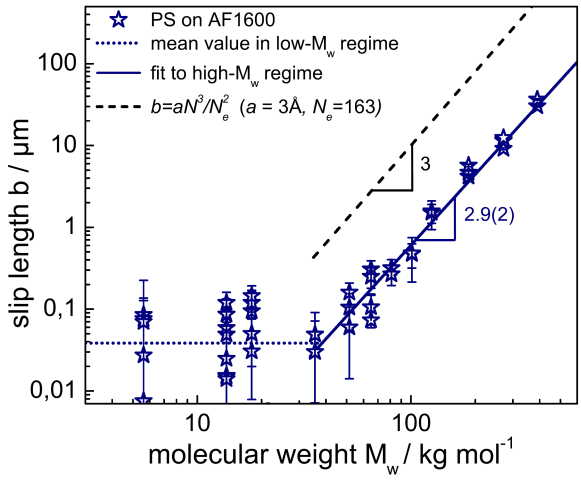


**Figure 2.3:** Double-logarithmic representation of the slip length $b$ as a function of molecular weight $M_\mathrm{w}$ for PS films on AF1600 substrates. The slip length $b$ has been determined by analyzing the profile of a rim surrounding a hole in a dewetting PS film. The black dashed line represents the model by de Gennes using the bulk entanglement length $N_\mathrm{e} = 163$ [52]. A best fit to the experimental data from PS(35.6k) to PS(390k) is given by the blue solid line, while the average of slip lengths for PS(5.6k) to PS(18k) is shown by the blue dotted line. Adopted from [35].

### 2.2.4 Thin film equation for Newtonian liquids

To finally derive the equation of motion for thin Newtonian liquid films, we start with the kinematic condition:

$$\partial_t h = -\vec{\nabla}_{||} \int_0^h \vec{u}_{||} dz, \tag{2.27}$$

which displays the relation between the temporal evolution of the film height $h(x, y, t)$ and the flow field of the liquid parallel to the substrate ($\vec{\nabla}_{||} = (\partial_x, \partial_y)$ and $\vec{u}_{||} = (u_x, u_y)$). The solid/liquid interface is represented by the $xy$-plane and the film height is aligned in positive $z$-direction. In order to obtain dimensionless variables only, in the following all variables are rescaled based on the lubrication approximation (see Eq. 2.19). As the system is translationally invariant, we consider the one-dimensional case, which simplifies Eqs. 2.16 and 2.20 to:

$$\partial_x(p + \phi') = \partial_x^2 u_x, \quad \partial_z(p + \phi') = 0, \quad \partial_x u_x + \partial_z u_z = 0, \tag{2.28}$$

where terms of $\mathcal{O}(\epsilon^2)$ have been ignored (with the lubrication parameter $\epsilon \ll 1$ for thin films). Thereby, the interfacial boundary conditions are described by:

$$\partial_z u_x \mid_{z=0} = \frac{u_x \mid_{z=0}}{b}, \tag{2.29}$$

and

$$u_z \mid_{z=0} = 0. \tag{2.30}$$

Eq. 2.29 implies that friction at the solid/liquid interface ($z = 0$) causes a velocity gradient in $z$-direction and Eq. 2.30 accounts for the impermeability of the substrate. As inertia terms can be neglected, the tangential and normal boundary conditions at the free liquid interface ($z = h(x)$) can be written as:

$$\partial_z u_x = 0 \quad , \quad p + \partial_x^2 h = 0. \tag{2.31}$$

Integration of the first and second part of Eq. 2.28 with respect to $z$ including the boundary conditions given by Eqs. 2.29 and the first part of 2.31 provides the velocity profile

$$u_x = \left( \frac{z^2}{2} - h(z+b) \right) \partial_x (p + \phi'(h)). \tag{2.32}$$

Eqs. 2.27, 2.32 and the second condition of 2.31 lead to the three-dimensional equation of motion for thin liquid films:

$$\partial_t h = -\vec{\nabla}(m(h)\vec{\nabla}[\gamma \vec{\nabla}^2 h - \phi'(h)]), \tag{2.33}$$

which here is given in dimensional variables and where $m(h)$ represents the mobility of the liquid film. In the no-slip regime ($B = b/h_0 = 0$) the mobility is given by $m(h) = h^3/3\eta$. For systems in the weak-slip regime (with $B \ll 1$), the mobility is represented by $m(h) = (3\eta)^{-1}(h^3 + 3bh^2)$, whereas for the intermediate-slip regime ($B \simeq 1$) the mobility is equal to $m(h) = bh^2/\eta$ [22].

As a result of applying the lubrication approximation to derive the thin film equation (Eq. 2.33), the model is only valid for weak- or intermediate slip situations. Therefore, Münch *et al.* and Kargupta *et al.* independently developed a model including strong-slip, where the slip length is represented by $b \sim 1/\epsilon^2$. The equation of motion and the kinematic condition in one dimension are given by [20, 57]:

$$u = \frac{2b}{\eta} \partial_x (2\eta h \partial_x u) + \frac{bh}{\eta} \partial_x (\gamma \partial_x^2 h - \phi'(h)), \tag{2.34}$$

$$\partial_t h = -\partial_x (hu). \tag{2.35}$$

### 2.2.5 Rim shapes

In order to gain information about the rim shape of a hole in a dewetting thin film, a linear stability analysis is needed. Münch *et al.* introduced a small perturbation $\delta h \ll h_0$, which is traveling in the reference frame of the moving rim:

$$h(x,t) = h_0 + \delta h \exp(k\zeta), \tag{2.36}$$

where

$$\zeta = x - x_c(t), \tag{2.37}$$

with $x_c(t)$ the position of the three-phase contact line. Hence, the respective dewetting velocity is represented by $\dot{x}_c(t)$. As a consequence this results in the characteristic third-order polynomial for $k$:

$$(h_0 k)^3 + 4Ca(h_0 k)^2 - Ca\frac{h_0}{b} = 0, \tag{2.38}$$

with the capillary number $Ca = (\dot{x}_c \eta)/\gamma_{lv}$. As this model, however, is only valid for very large slip length $b$ compared to the initial film height $h_0$, Fetzer *et al.* developed a universal model, the so-called Stokes model [32]. Here, the evolution of a rim profile is derived from a third-order Taylor expansion of the characteristic equation, which originates from the linear stability analysis of a flat film while using the full Stokes equations:

$$\left(1 + \frac{h_0}{3b}\right)(h_0 k)^3 + 4Ca\left(1 + \frac{h_0}{2b}\right)(h_0 k)^2 - Ca\frac{h_0}{b} = 0. \tag{2.39}$$

Respectively three solutions exist for $k$ (see Eq. 2.38 and 2.39), where one solution is real and positive. As the rim profiles decay, in the following we do not account for this solution. The remaining solutions $k_1$ and $k_2$ are either two real numbers $< 0$ or a pair of two complex conjugated numbers with a negative real part:

$$k_{1,2} = k_r \pm i k_i. \tag{2.40}$$

In general, we distinguish between two different morphologies of the moving rim: (i) a monotonic decay of the rim profile into the residual film or (ii) an oscillatory rim shape. Hence, the two sets of solutions symbolize these two rim shapes, where an oscillatory shape on the 'wet side' of the rim is given by:

$$\delta h(\zeta)_{osc} = \delta h_0 \cos(k_i \zeta + \psi)\exp(k_r \zeta), \tag{2.41}$$

with the real part $k_r$ and the imaginary part $k_i$ of $k_1$ and $k_2$, the amplitude $\delta h_0$ and $\psi$ representing the fitting parameters.

In case of monotonically decaying rim profiles we derive:

$$\delta h(\zeta)_{mon} = \delta h_1 \exp(k_1 \zeta) + \delta h_2 \exp(k_2 \zeta), \tag{2.42}$$

with the fitting parameters $\delta h_1$ and $\delta h_2$ illustrating the amplitudes and $k_1$ and $k_2$ representing the decay lengths. From solving Eq. 2.39 and fitting the respective function for a monotonic or an oscillatory decay to the rim profiles, the slip length $b$ and the capillary number $Ca$ can be determined separately:

$$b_{Taylor} = \frac{1}{4h_0}\frac{k_1^2 + k_1 k_2 + k_2^2}{k_1^2 k_2^2} - \frac{h_0}{2}, \tag{2.43}$$

$$Ca_{Taylor} = -\frac{h_0}{4}\frac{k_1^2 + k_1 k_2 + k_2^2}{k_1^2 + k_2^2} + \frac{h_0^3}{6}\frac{k_1^2 k_2^2}{k_1 + k_2}. \tag{2.44}$$

## 2.3 Stability of thin liquid films

Usually the studied systems are composed of multiple layers, as e. g. a PS film on a hydrophobized Si wafer which has a native $SiO_2$ layer. The stability of the thin liquid films on such substrates is determined by the effective interface potential $\phi$, which comprises the relevant

short-range (repulsive) and long-range (attractive) interactions as a function of the film thickness $h$ [58]. The potential describes the excess free energy (per unit area) to bring two interfaces (here: the solid/liquid and the liquid/air interface) from infinity to a certain distance $h$ [59]. Whether a thin liquid layer on top of a substrate is stable or whether it decays into droplets, is determined by the specific combination of the substrate properties and the liquid: for dielectric systems (no charges and electrostatic interactions) $\phi(h)$ is composed of steric repulsive and chemical interactions, which are relevant only within a few Å of film thickness $h$ (short-ranging) [60], and the attractive long-range van der Waals forces between molecules. The superposition of these interactions determines the shape of the effective interface potential:

$$\phi(h) = \phi_{\text{short}}(h) + \phi_{\text{vdW}}(h) = \frac{C}{h^8} - \frac{A_1}{12\pi h^2} - \frac{A_2 - A_1}{12\pi(h+d_1)^2} - \frac{A_3 - A_2}{12\pi(h+d_1+d_2)^2} - ..., \quad (2.45)$$

with $C$ representing a characteristic repulsion constant and $A_{\text{i}}$ being the Hamaker constants [61] of the liquid film interacting with the $i$-th substrate component. $h$ describes the thickness of the liquid film and $d_i$ stands for the thickness of layer $i$.

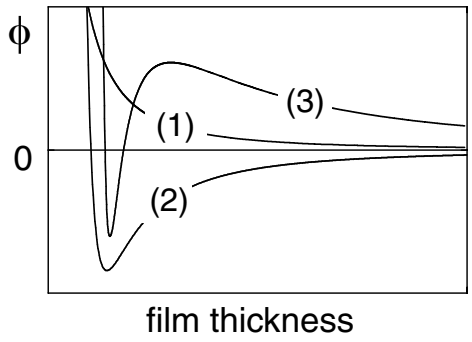


**Figure 2.4:** Schematic representation of the effective interface potential $\phi$ as a function of film thickness $h$. Curve (1) corresponds to the case of a stable liquid film, (2) displays the unstable and (3) the metastable situation. Adopted from [58].

Figure 2.4 represents the effective interface potential $\phi(h)$ for three important scenarios. In curve (1), $\phi(h) > 0$ and the global minimum is reached at infinite film thickness, which causes the liquid film to be stable. Scenario (2) exhibits a global minimum at $h = h^*$. By changing the thickness of the liquid film from $h$ to $h^*$, the system is able to gain energy. Therefore, films thicker than $h^*$ become unstable and dewet from the substrate [62]: holes in the film are nucleated, which grow during the dewetting process. Thereby, the three-phase contact line recedes and the rim, which is surrounding the hole, accumulates the residual material. In a later stage, hole coalescence occurs, which leads to the formation of liquid ridges. These roughly semi-cylindrical ridges again become unstable due to the Rayleigh-Plateau instability (see Sec. 2.5) [60, 63, 64] and subsequently decay into a characteristic droplet pattern [64, 65]. The dewetting process can be initiated by either any chemical or topographical heterogeneity, referred to as nucleation, or the amplification of capillary waves (spinodal dewetting) [58, 62]. Curve (3) in Fig. 2.4 shows the typical shape of $\phi(h)$ for metastable films. Here, thin films with $\phi''(h) < 0$ are unstable and start to dewet, whereas for thicker films dewetting can be initiated by nucleation only.

## 2.4 Flow dynamics of dewetting thin films

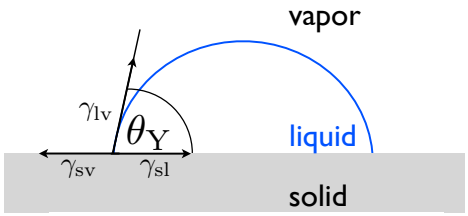


**Figure 2.5:** The balance of the interfacial tensions accounts for the equilibrium contact angle $\theta_Y$.

The dewetting process of a thin liquid film on a substrate, in general, ends in a specific droplet pattern, where all droplets are in equilibrium. In this configuration, the droplets exhibit the so-called Young's contact angle $\theta_Y$, which results from the balance of all participating interfacial tensions (see Fig. 2.5):

$$\cos\theta_Y = \frac{\gamma_{sv} - \gamma_{sl}}{\gamma_{lv}}, \tag{2.46}$$

with the interfacial tension $\gamma_{ij}$ between two phases i and j, where v represents the vapor, l the liquid and s the solid phase. To characterize the wettability of a substrate, we introduce the spreading parameter $S$, which is defined as:

$$S = \gamma_{sv} - (\gamma_{sl} + \gamma_{lv}) = \gamma_{lv}(\cos\theta_Y - 1). \tag{2.47}$$

It denotes the energy difference per unit area between a dry substrate and a liquid covered surface. If $S > 0$, the substrate will be completely wetted by the liquid, whereas for $S < 0$ the system is able to gain energy by lowering the contact area between the liquid and the underlying substrate, partial wetting occurs. Thereby, a wedge-shaped liquid front with contact angle $\theta_{rec}$ at the three-phase contact line is receding while collecting the residual material (mass conservation), see Fig. 2.6.

The dewetting process is driven by capillary forces acting on the contact line. The driving force, here given as force per unit length, results from balancing the interfacial tensions acting on the contact line:

$$\frac{F_c}{l} = \gamma_{sv} - (\gamma_{sl} + \gamma_{lv}\cos\theta_{rec}) = \gamma_{lv}(\cos\theta_Y - \cos\theta_{rec}). \tag{2.48}$$

On the side of the rim where the three-phase contact line is located, the so-called 'dry' side, a negative capillary force is pulling the contact line:

$$\frac{F_c}{l} = S + \gamma_{lv}(1 - \cos\theta_{rec}). \tag{2.49}$$

The 'wet' side, where the front merges into the residual film, however, reveals a positive capillary force per unit length:

$$\frac{F_c}{l} = \gamma_{lv}(\cos\theta_Y - \cos\theta_{rec}) = \gamma_{lv}(1 - \cos\theta_{rec}), \tag{2.50}$$

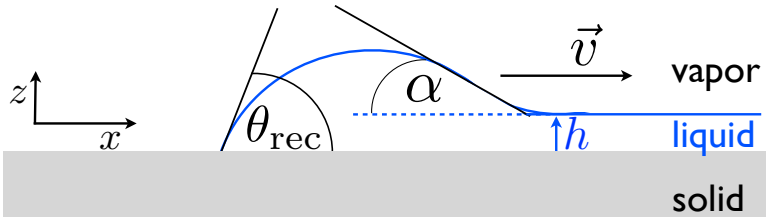


**Figure 2.6:** A dewetting wedge-shaped liquid front accumulates the residual material and exhibits a contact angle $\theta_{\mathrm{rec}}$ at the three-phase contact line.

with $\theta_{\mathrm{Y}} = 0$. Summing up the two forces yields the effective driving force per unit length for a receding wedge in thin liquid films:

$$\frac{F_{\mathrm{c}}}{l} = |S| = |\gamma_{\mathrm{lv}}(\cos\theta_{\mathrm{Y}} - 1)|. \tag{2.51}$$

The dewetting process is mediated by energy dissipation due to friction forces. In general, the power balance is given by [66]:

$$|S|v = \sum_{\mathrm{i}} F_i v_i, \tag{2.52}$$

with the dewetting velocity of the wedge $v$, the acting friction forces $F_{\mathrm{i}}$ and their respective velocity contributions $v_{\mathrm{i}}$. Considering dewetting thin films, two different dissipation mechanisms may be present: viscous friction within the liquid itself and friction of the liquid molecules at the solid/liquid interface.

First we concentrate on the viscous dissipation term only. It has been shown that a no-slip boundary condition at the solid/liquid interface causes the dissipation mechanism to be dominated by viscous friction only [67]. Following de Gennes' model [68, 69], which is based on the findings by Huh and Scriven [70], we see that the inverse dewetting velocity is given by:

$$\frac{1}{v_{\mathrm{v}}} = \frac{3l}{|S|\tan\theta_{\mathrm{rec}}}\eta, \tag{2.53}$$

where $l$ is a logarithmic factor, which incorporates the divergence of the dissipation at the contact line. Here, de Gennes considered exclusively the energy, which is dissipated at the three-phase contact line. Studies by Merabia *et al.*, however, have shown that although energy is predominantly dissipated at the contact line, there is an additional weak contribution to the dissipated energy term originating from the position, where the front merges into the residual film [71]. In order to derive Eq. 2.53, both, the capillary driving force as well as the viscous friction are weighted per unit length of the contact line. Thus, the model is invariant with regard to the length of the contact line. Therefore, if viscous dissipation is dominant, the 2D model can be applied to dewetting holes and straight fronts in thin films or even to receding droplets on axisymmetric fibres, which we investigate in this work (cf. the **publication in ADDENDUM III**). Experimental studies by Bäumchen *et al.* have shown that dewetting holes in unentangled PS films on hydrophobized substrates (exhibiting a no-slip boundary condition) show a linear dependence between the dewetting velocity and the inverse melt

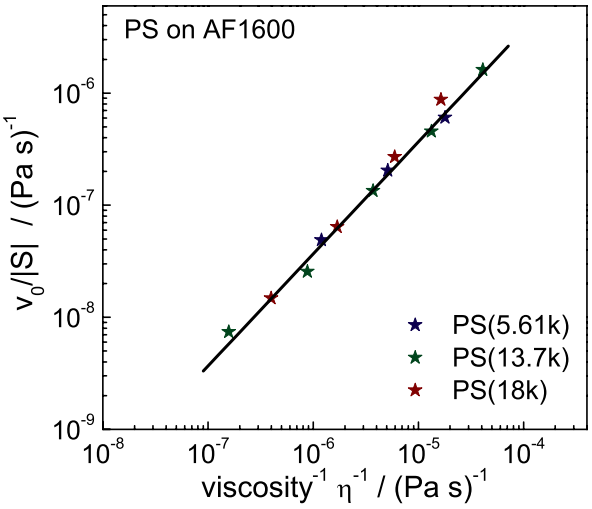


**Figure 2.7:** Double-logarithmic representation of the linear scaling between $v_0$ normalized by the spreading parameter $|S|$ as a function of the inverse melt viscosity $1/\eta$. $v_0$ has been obtained from the y-axis intercept of representing the dewetting velocity $v$ (measured from hole growth experiments in unentangled PS films with varying molecular weights) as a function of $1/\sqrt{R}$ (for $1/\sqrt{R} \to \infty$). Adapted from [17].

viscosity. They obtained a universal proportionality constant when using different molecular weights (unentangled) of the same polymer (see Fig. 2.7) [17]. Entangled polymers, however, imply slippage at the interface (see Eq. 2.26) which causes a significant change of the flow field close to the three-phase contact line. Therefore, the constant of proportionality may vary by orders of magnitude. By adjusting the theory and including the slip length $b$, a similar model is capable to describe the dewetting process when slippage dominates viscous friction [34, 53, 66, 67, 68]. The inverse dewetting velocity was found to equal:

$$\frac{1}{v_\mathrm{s}} = \frac{3w}{|S|b}\eta. \tag{2.54}$$

As dissipation is due to the friction of the liquid molecules at the solid/liquid interface, here, the relevant distance concerning energy dissipation is given by the width $w$ of the moving front. In order to depict scenarios where both mechanisms, pure viscous flow and slippage, are responsible for the energy dissipation, Jacobs *et al.* presented a combination of the two models by additively superposing their velocities: $v = v_\mathrm{v} + v_\mathrm{s}$ [66].

## 2.5 Rayleigh-Plateau instability

### 2.5.1 Rayleigh-Plateau instability of a free liquid cylinder

The Rayleigh-Plateau instability (RPI) is one of the most frequently observable instabilities in our everyday life. The classical case describes the decay of a free cylindrical liquid jet into a regular droplet pattern, e. g. the breakup of a water jet flowing out of a water tab (see Fig. 2.8). First experimental studies have been done by Savart and mostly Plateau [72, 73]. In 1878, Rayleigh developed a theoretical model to describe the classical breakup mechanism [63], which is in good agreement with these experimental findings. In general, the instability evolves, because small surface perturbations, i. e. modulations of the radius $R$ of the liquid jet, are amplified as a result of fluid moving from thinner to thicker regions due to the difference in Laplace pressure [63, 75]:

$$p_{\mathrm{L}} = \gamma_{\mathrm{lv}}\kappa = \gamma_{\mathrm{lv}}\left(\frac{1}{R(1+R'^2)^{1/2}} - \frac{R''}{(1+R'^2)^{3/2}}\right), \tag{2.55}$$

where $R$ is the local radius of the jet. The prime denotes the partial derivative with respect to $z$, representing the direction of the central axis of the liquid jet. The perturbed radius can be written as:

$$R = R_0 + \varepsilon e^{\omega t + ikz}, \tag{2.56}$$

where $R_0$ displays the initial radius of the jet, $\varepsilon$ stands for the perturbation amplitude and $k$ represents the wavenumber in $z$-direction. The wavelength is given by $\lambda = 2\pi/k$. In comparison to the initial shape, the formation of a sinusoidal perturbation leads to a change in the surface area of the liquid and, hence, to a change in surface energy at a given time $t$ [63, 75]:

$$\Delta E = E_{\mathrm{pert}} - E_0 = 2\pi\gamma\left(\int_0^{\lambda} R(1+R'^2)^{1/2}dz - \int_0^{\lambda} R_0 dz\right), \tag{2.57}$$

with the initial and intermediate surface energies, $E_0$ and $E_{\mathrm{pert}}$, surface tension $\gamma$ and wavelength $\lambda$. By considering small surface perturbations with $\varepsilon \ll R_0$, and thus $R' \ll 1$, Eq. 2.57 reads:

$$\Delta E = \frac{E_0\varepsilon^2}{4R_0^2}[(kR_0)^2 - 1]. \tag{2.58}$$

We see that all modes with a wavelength $\lambda = 2\pi/k$ greater than the perimeter of the initial cylinder exhibit a reduced energy and, hence, are unstable [63, 75].

Following the work by Rayleigh and Plateau [63, 73], we assume the liquid jet to be an infinitely long, steady and inviscid fluid cylinder with the initial radius $R_0$, density $\rho$ and surface tension $\gamma$. Further we state that gravity is neglected and the external pressure is zero. The pressure $p_0$ inside the column is set to be constant and equals:

$$p_0 = \gamma\vec{\nabla}\cdot\vec{n} \Rightarrow p_0 = \frac{\gamma}{R_0}, \tag{2.59}$$

with the surface normal $\vec{n}$. Assuming infinitesimal perturbations at the interface allows for linearizing the leading equations as follows:

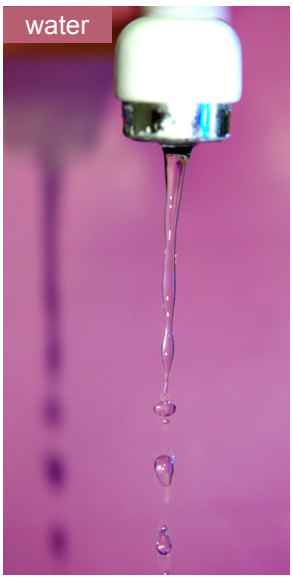


**Figure 2.8:** A water jet flowing out of a faucet decays into droplets due to the Rayleigh-Plateau instability. The droplets display a regular wavelength which is connected to the radius of the water jet, see Eq. 2.79. Adopted from [74].

$\tilde{u}_\mathrm{r}$ stands for the radial and $\tilde{u}_\mathrm{z}$ for the axial components of the perturbation velocity, $p$ is the perturbation pressure. Invoking the Navier-Stokes equation (Eq. 2.17) and considering terms to lowest order in $\varepsilon$ gives:

$$\frac{\partial \tilde{u}_\mathrm{r}}{\partial t} = -\frac{1}{\rho}\frac{\partial \tilde{p}}{\partial r}, \tag{2.60}$$

$$\frac{\partial \tilde{u}_\mathrm{z}}{\partial t} = -\frac{1}{\rho}\frac{\partial \tilde{p}}{\partial z}. \tag{2.61}$$

The equation of continuity (Eq. 2.15) yields:

$$\frac{\partial \tilde{u}_\mathrm{r}}{\partial r} + \frac{\tilde{u}_\mathrm{r}}{r} + \frac{\partial \tilde{u}_\mathrm{z}}{\partial z} = 0. \tag{2.62}$$

Furthermore, we state that the disturbances in velocity and pressure are of the same form as the surface disturbances:

$$\tilde{u}_\mathrm{r} = U(r)e^{\omega t + ikz} \quad , \quad \tilde{u}_\mathrm{z} = Z(r)e^{\omega t + ikz} \quad , \quad \tilde{p} = P(r)e^{\omega t + ikz}, \tag{2.63}$$

while the respective amplitudes $U(r)$, $Z(r)$ and $P(r)$ are independent with respect to the $z$-direction. Inserting Eq. 2.63 in Eqs. 2.60, 2.61 and 2.62 implies:

$$\omega U(r) = -\frac{1}{\rho}\frac{dP(r)}{dr}, \tag{2.64}$$

$$\omega Z(r) = -\frac{ik}{\rho}P(r), \tag{2.65}$$

$$\frac{dU(r)}{dr} + \frac{U(r)}{r} + ikZ(r) = 0. \tag{2.66}$$

Combining the last three equations and deriving the last one once, produces a differential equation for $U(r)$:

$$r^2 \frac{d^2U(r)}{dr^2} + r\frac{dU(r)}{dr} - (1 + (kr)^2)U(r) = 0. \tag{2.67}$$

As Eq. 2.67 is a modified Bessel equation, the solution of the differential equation can be written in form of the modified Bessel functions of the first $I_1(kr)$ and second $K_1(kr)$ kinds. Note that $K_1(kr) \to \infty$ for $r \to 0$. Hence, we state:

$$U(r) = CI_1(kr), \tag{2.68}$$

with $C$ being a constant, which will be determined when applying the respective boundary conditions. Via using the Bessel function identity $I_0'(x) = I_1(x)$, we can obtain the pressure from Eqs. 2.64 and 2.68:

$$P(r) = -\frac{\omega\rho C}{k} I_0(kr). \tag{2.69}$$

The boundary conditions are given by (i) the kinematic condition at the free surface, which reads:

$$\frac{\partial R}{\partial t} = \vec{\tilde{u}} \cdot \vec{n} \simeq \tilde{u}_{\mathrm{r}}(R), \tag{2.70}$$

where with Eqs. 2.56 and 2.68 it follows:

$$C = \frac{\varepsilon\omega}{I_1(kR)}; \tag{2.71}$$

and (ii) the normal-stress balance at the free interface, which reads:

$$p_0 + \tilde{p} = \gamma\vec{\nabla} \cdot \vec{n}, \tag{2.72}$$

where the curvature can be expressed by:

$$\vec{\nabla} \cdot \vec{n} = \frac{1}{R_1} + \frac{1}{R_2}, \tag{2.73}$$

with $R_1$ and $R_2$ the radii of curvature of the free surface, here given by:

$$\frac{1}{R_1} = \frac{1}{R_0 + \varepsilon e^{\omega t + ikz}} \simeq \frac{1}{R_0} - \frac{\varepsilon}{R_0^2} e^{\omega t + ikz}, \tag{2.74}$$

$$\frac{1}{R_2} = \varepsilon k^2 e^{\omega t + ikz}. \tag{2.75}$$

Inserting Eqs. 2.74 and 2.75 into Eq. 2.72 leads to:

$$p_0 + \tilde{p} = \frac{\gamma}{R_0} - \frac{\varepsilon\gamma}{R_0^2}(1 - k^2R_0^2)e^{\omega t + ikz}, \tag{2.76}$$

which by using Eq. 2.59 ends in:

$$\tilde{p} = -\frac{\varepsilon\gamma}{R_0^2}(1 - k^2 R_0^2)e^{\omega t + ikz}. \tag{2.77}$$

The dispersion relation $\omega(k)$ finally follows from combining Eqs. 2.63, 2.69, 2.71 and 2.77:

$$\omega(k)^2 = \frac{\gamma}{\rho R_0^3}(kR_0)[1 - k^2 R_0^2]\frac{I_1(kR_0)}{I_0(kR_0)}. \tag{2.78}$$

Hence, the liquid cylinder becomes unstable for $kR_0 < 1$ only, corresponding to a wavelength which is larger than the perimeter of the unperturbed column. The fastest amplified wavenumber, i e. maximizing $\omega(k)$, is $k^* R_0 \approx 1/\sqrt{2}$ and hence, the wavelength of the fastest growing mode is given by:

$$\lambda^* \approx 2\sqrt{2}\pi R_0, \tag{2.79}$$

corresponding to a rise time of $\tau \approx 3\sqrt{\frac{\rho R_0^3}{\gamma}}$. Hence, the finale stage of the liquid column breakup features a regular pattern of large droplets with wavelength $\lambda^*$. In between these droplets smaller droplets, so-called satellite droplets, may occur due to the recurrent breakup of the thinning liquid filament.

Note that the viscosity $\eta$ does not affect the wavelength $\lambda^*$ of the fastest growing mode, but has a huge impact on the dynamics of the instability [63, 75]: a large viscosity (with $Re \gg 1$) results in the 'viscous slowing' of the instability growth.

### 2.5.2 Rayleigh-Plateau instability in other geometries

The breakup of free cylindrical liquid filaments is an intensively studied problem: experimentally as well as theoretically, much has been learned about the instability evolution of e. g. soft threads [76, 77], cylinders suspended in a fluid [78] and polymer filaments [79, 80, 81].

Many other geometries underly the Rayleigh-Plateau instability, such as e. g. straight fronts in dewetting thin liquid films on planar substrates [48, 82, 83, 84, 85], the ridge which forms as a result of coalescing holes during dewetting (cf. the **publication in ADDENDUM I**) [60, 64], liquid filaments in wedge-shaped grooves [86], viscous toroids [87, 88] (see Fig. 2.9a), viscous liquids deposited on a cylindrical solid fibre (cf. the **publication in ADDENDUM II**) or in capillary tubes [69, 89] or even the wavelength selection in a crown splash (see Fig. 2.10) [90]. In addition to the liquid/air interface, these geometries require the consideration of the solid/liquid interface, which adds additional complexity to the system.

The evolution of the gravitationally influenced RPI of a film coating or flowing down a vertical fibre is well-understood (see Fig. 2.9b) [91, 92, 93, 94, 95]. There are also several studies

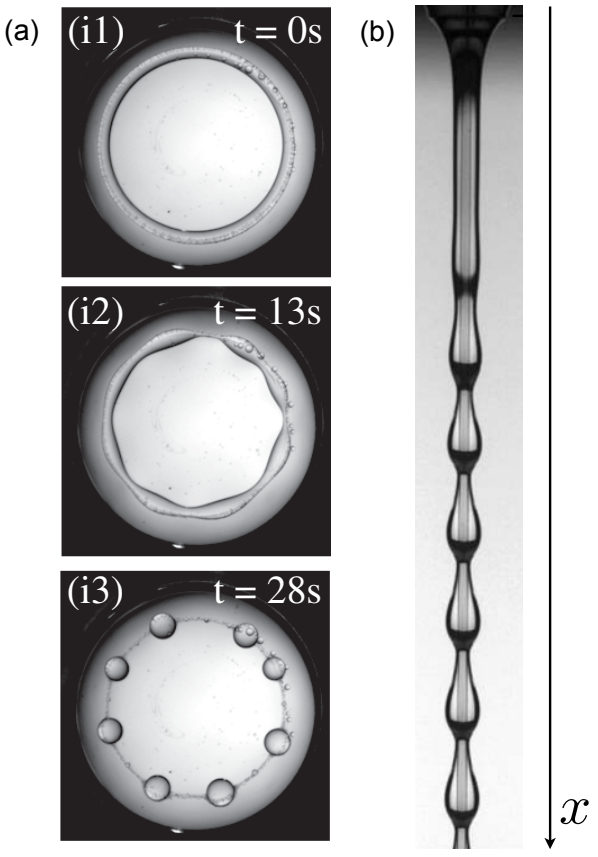


**Figure 2.9:** Collection of instabilities of Rayleigh-Plateau type occurring in various geometries as (a) a glycerin torus injected in silicone oil [87] and (b) silicone oil flowing down a Nylon fishing thread [95].

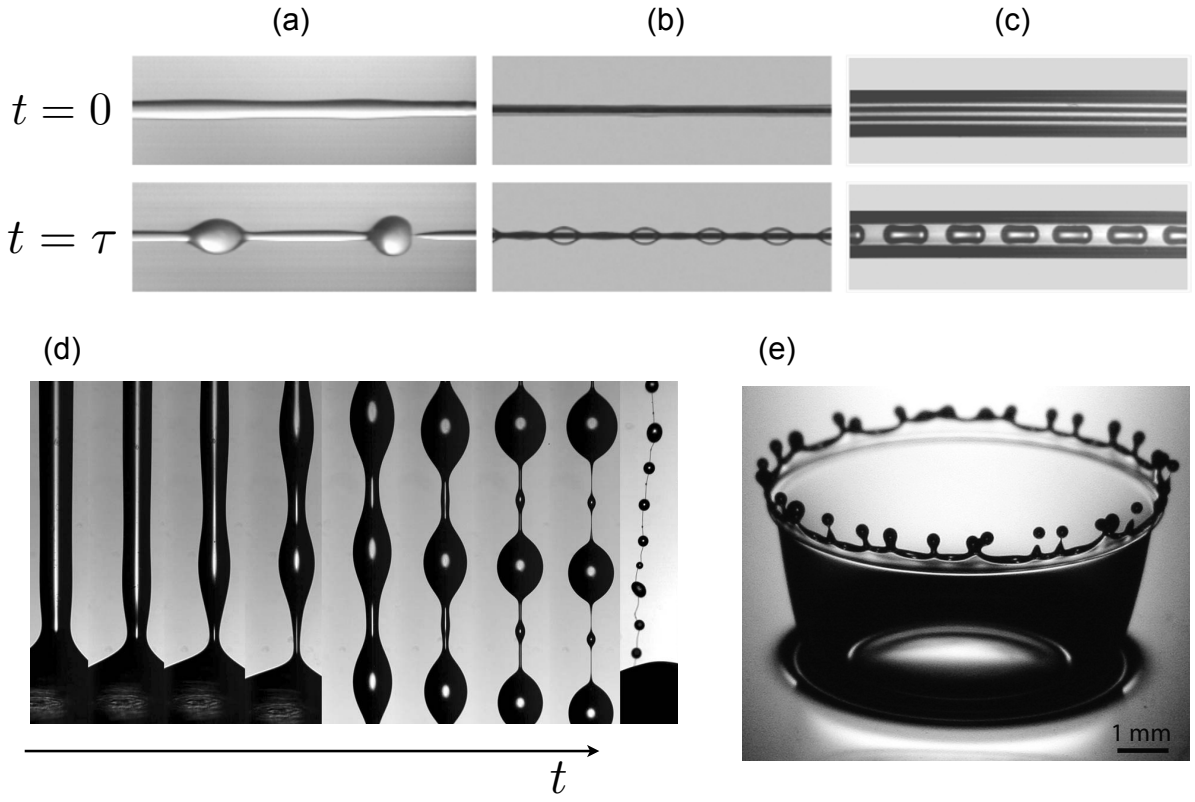


**Figure 2.10:** (a) A liquid jet [89], (b) a liquid film on a fibre [89], (c) a liquid film in a tube [89], (d) a thread of human saliva [81] and (e) the generation of secondary droplets in the crown splash [90] are also subject to an instability of Rayleigh-Plateau type.

investigating the morphology and dynamics of viscous liquid films coating axisymmetric fibres, where gravitational effects do not play a role (see Fig. 2.10b) [91, 96, 97]. An experimental study by Goren verified the exponential rise of surface undulations, first stated by Rayleigh in 1878 (see Sec. 2.5). Furthermore, he found that the wavelength $\lambda^*$ of the fastest growing disturbance of a honey film applied onto a metal wire is unaffected by material properties [96]. The theoretical examination of the same geometry by Roe in 1975, corroborates this finding: $\lambda^*$ does exclusively depend on the film thickness to fibre radius ratio $e_0/r$ [97]. Figure 2.11a, however, shows that the growth rate of the fastest growing mode, here named $q_{\max}$, is controlled by both, the geometry of the system $s = e_0/r - 1$ and the specific material properties, represented by the viscosity $\eta$ [97]. For a given value of $\eta$, it is shown that if the thickness of the liquid film is either much smaller or much larger than the fibre radius, the maximal growth rate becomes small (see Fig. 2.11a) [97]. This can be understood by the fact that as $s$ converges to $-1$, which means a huge decrease in film thickness, the mobility of the flowing liquid film is reduced and thus the growth of the instability is slowed down. If, however, the film thickness $e_0$ is much larger than the fibre radius $r$, corresponding to a large value for $s$, the curvature is reduced and so is the driving force of the RPI. The relationship between maximal growth rate $q_{\max}$ and

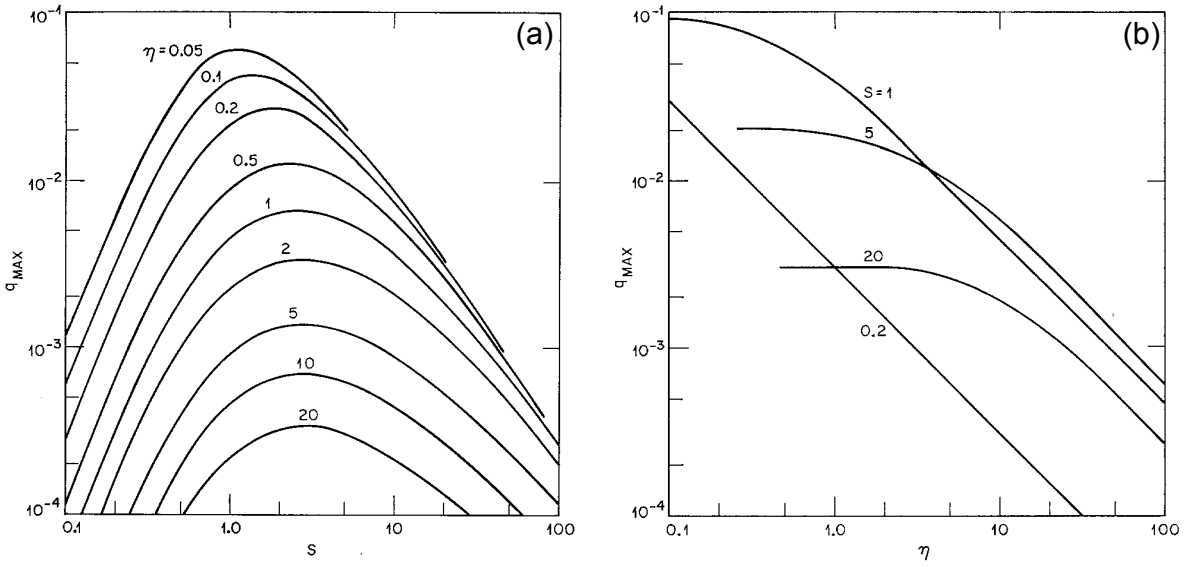


**Figure 2.11:** Maximal instability growth rate $q_{\max}$ (a) plotted as a function of the film thickness $e_0$ to fibre radius $r$ ratio, represented by $s = e_0/r - 1$, for different viscosity values $\eta$ and (b) presented as a function of viscosity $\eta$ for different system geometries $s$. Both graphs are taken from [97].

viscosity $\eta$, for given values of the film thickness to fibre radius ratio $s$, is shown in figure 2.11b. From this plot, we learn that in case of a low viscosity $\eta$ and very thin films (corresponding to a small value of $s$) the maximal growth rate is inversely proportional to viscosity. Whereas, for thick films (large $s$) and low viscosities $\eta$, there is no direct dependence of $q_{\max}$ on $\eta$. This indicates that for thin films the growth of the instability is controlled by viscosity, whereas in case of thick films inertia is the leading force [97], see Eq. 2.12.

These results have been obtained implementing a no-slip boundary condition at the solid/liquid interface. Nevertheless, we already know that the hydrodynamic boundary condition, indeed, has a significant impact on the morphology and the dynamics of a dewetting liquid rim, which is subject to an instability of Rayleigh-Plateau type [82, 83, 84, 85]. Compared to the classical RPI, the system of a dewetting liquid rim displays three fundamental differences: (i) the rim shape is semicylindrical, (ii) the dewetting rim is continuously growing due to the accumulation of the residual film (see Fig. 2.12) and (iii) the receding rim displays a three-phase contact line. Analyzing the morphology of the instability showed that the fastest growing wavelength $\lambda^*$ depends on the rim width $w$ only [83, 85]. This is consistent with the classical case of a free-flowing liquid cylinder (see Eq. 2.79) and the film on a fibre case [63, 69, 96]. In other words, $\lambda^*$ is entirely independent of the hydrodynamic boundary condition.

The dynamics and the rim morphology, however, are considerably affected by the boundary condition at the solid/liquid interface: on the one hand, slippage, which facilitates a higher mobility of the molecules at the solid/liquid interface [34, 98], accelerates the growth of the instability (see Fig. 2.12b) [85]. On the other hand, it has been shown experimentally as well

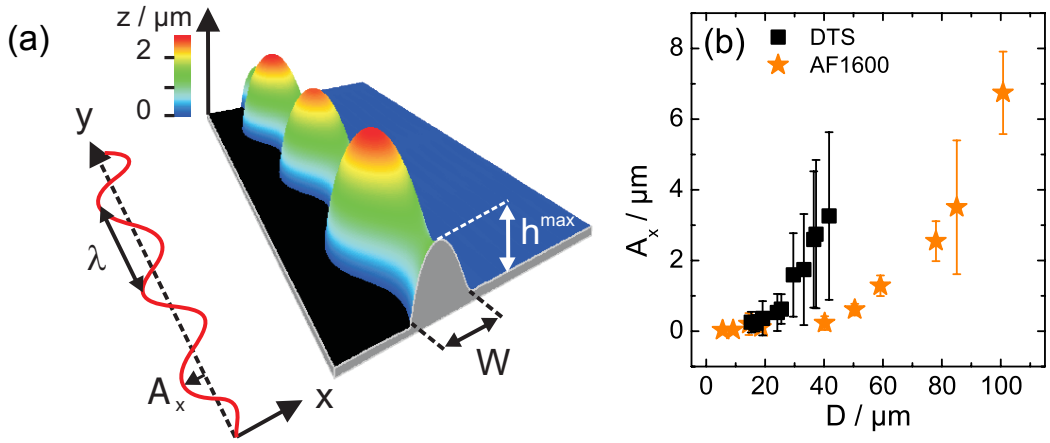


**Figure 2.12:** (a) Atomic force microscope image of an unstable straight front in a dewetting thin film illustrating the characteristic instability parameters like rim width $w$, maximal rim height $h_{\max}$, lateral amplitude $A_x$ and wavelength $\lambda$. (b) The lateral amplitude $A_x$ of the rim instability as a function of dewetted distance $D$ for unentangled PS films ($h_0 = 115 \pm 5\,\mathrm{nm}$, $M_w = 10.3\,\mathrm{kg/mol}$ and $T = 120\,^\circ\mathrm{C}$) on DTS (squares), which corresponds to a slip boundary condition, and on AF1600 (stars), equal to the no-slip case, clearly shows that slippage accelerates the growth of the RPI. Both graphs were taken from [85].

as theoretically that the shape of the rim profiles is also controlled by the boundary condition. While in the no-slip case, the undulations and bulges feature a symmetric shape with respect to the front and the rear of the ridge (see Fig. 2.13b,d,f), slippage at the solid/liquid interface leads to an asymmetric instability formation (see Fig. 2.13a,c,e). This is due to the fact that for a slip boundary condition the dewetting velocity depends on the width $w$ of the receding rim: broader regions dewet more slowly than thinner ones [82, 85]. In the further course of the dewetting process, the difference in velocity causes the formation of fingers and finally results in the pinch-off of droplets, see Fig. 2.13a. The remaining liquid fingers are in turn subject to this effect, i. e. in consequence there is a periodic repetition of finger formation and droplet detachment. Hence, in the final stage, the entire sample is covered with droplets, which exhibit a characteristic pattern, from which one can judge if slippage was present or not. A detailed description concerning the pattern formation is given in the **publication in ADDENDUM I**. In their study, Bäumchen *et al.* derived a single thin film model, which is capable to quantitatively capture the characteristics of the rim evolution [85]. The aim of the presented work was to achieve a universal quantitative agreement between experimentally determined and theoretically predicted growth dynamics of the RPI including slippage, as this, however, was still lacking. Therefore, we studied the influence of slip on the evolution of the RPI of viscous liquid films on fibres while varying the boundary condition at the solid/liquid interface between no-slip and slip (cf. the **publication in ADDENDUM II**).

In technological applications it might be desired to design stable and homogeneous coatings. Thus, it is important to find systems for which the Rayleigh-Plateau instability can be sup-

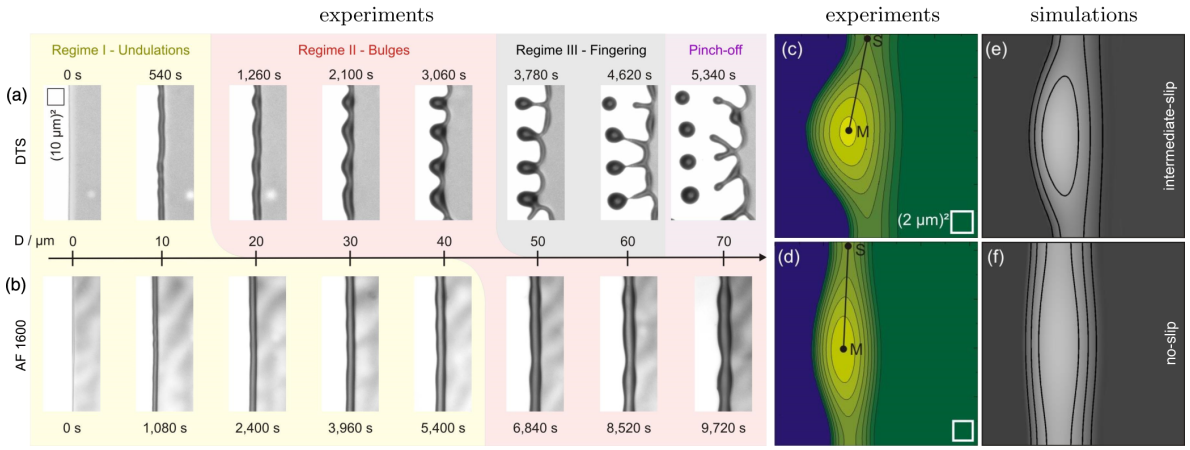


**Figure 2.13:** Optical micrographs showing the morphology of unstable straight fronts in dewetting unentangled PS films on (a) DTS (slip) and (b) AF1600 (no slip). During dewetting, both fronts pass through different regimes: the semicylinder becomes unstable (I) and the resulting undulations grow and form bulges (II). A no-slip boundary condition features a symmetric instability with respect to the front and the rear of the rim, whereas in case of slip, the resulting asymmetry causes the formation of fingers (III) with a final droplet detachment event (IV). The experimental AFM images (c, d) as well as the 3D numerical simulations (e, f) emphasize the distinct difference in the morphological evolution of the rim instability for varying boundary conditions. Images adopted from [85].

pressed. Possible ways to do so are e. g. applying a radially decaying azimuthal magnetic field caused by a current in a wire, which is in turn coated with a magnetic fluid [99]. Mora *et al.* exhibited that the capillary instability of a thin elastic filament is counterbalanced by elastic forces [76]. When $r < \gamma/(6G)$, with the filament radius $r$ and $\gamma/G$ the ratio of surface tension to elastic modulus, the RPI is completely depressed. This is also valid for an elastic fluid coating a fibre. In case of placing the elastic fluid inside a cylindrical tube, Henann *et al.* found a threshold of $r_\mathrm{i} = \gamma/(2G)$, where $r_\mathrm{i}$ is the inner tube radius [77]. Another way to suppress the growth of surface perturbations when applying a coating might be achieved if the phase transition from the liquid to the solid state is accompanied by a cooling of the coating [100]. The regular formation of liquid beads is nevertheless very useful for various applications as we will learn in Sec. 2.6.

## 2.6 Droplets on a fibre

Droplets located on a fibre are an everyday life phenomenon: the most familiar example are dew drops on a spider's web [101]. While the small droplets stick to the web filament, big droplets may flow down due to gravitation. As explained in the previous section and in the **publication in ADDENDUM II**, even initially homogeneous films supported by a fibre can become unstable and breakup into a regular droplet pattern due to the Rayleigh-Plateau instability (see Sec. 2.5.2). Many technological applications require the application of stable and homogeneous films to fibres. Quéré *et al.* studied e. g. the coating of fibres, when pulling them out of a liquid bath [102, 103], and the flow of annular films on vertical fibres driven by gravity [104]. Nevertheless, there is a large number of applications on microscopic length scales, which take advantage of the regular droplet pattern formed by the RPI. These are water collection techniques [105, 106, 107], patterning [108] and printing [109] methods or chemical reactions [110, 111] to name just a few.

Using microfluidic devices is a common and well-established way to generate and transport equally sized drops on the micro scale [112]. As described above, the breakup mechanisms of liquid films on cylindrical fibres have also been studied intensively in the past and much has been learned about gravity-driven droplet motion along a filament [93, 104, 113, 114, 115, 116, 117]. Quéré investigated the flow of annular films on vertical fibres, where the downward flow is induced by gravity [104]. Studying films that are thin compared to the fibre radius $r$ showed that films with a thickness of $e < e_c$ flowing down a vertical fibre do not exhibit surface undulations. The growth of the RPI is suppressed by the vertical liquid flow, where the film is stabilized by van der Waals intermolecular forces [104]. Rotating a vertical fibre with a stable film of thickness $e \approx e_c$ by $90\,^\circ$, resulting in a horizontally oriented fibre, shows that, after a short time, the instability sets in, as the stabilizing vertical flow is missing. Placing the fibre vertically again, consequently, causes the undulations to disappear [104]. The critical film thickness $e_c$ was found to scale as $r^3$ [104]. For thick films compared to the fibre radius $r$, the flowing film does, however, develop a regular droplet pattern due to the RPI. As a consequence of gravity being present, the droplets likewise flow down the fibre [104]. Studies by Quéré and Gilet *et al.* revealed that the droplet velocity is determined by the balance of viscous friction and gravity [104, 115]. The bigger the droplet, the faster its dynamics. Hence, big droplets eventually coalesce with others. In addition, it has been shown that big, rapidly flowing droplets leave behind a residual film, which likewise breaks up into droplets (for $e > e_c$) [104, 115]. The related loss of material, however, causes the gravity-driven flow of the droplet to slow down [115].

Up to date, the mechanisms inducing the movement of drops along filaments, where gravitation is absent, is less investigated: here, droplet motion is achieved by e. g. a temperature gradient [118] or a pressure difference [119, 120]. A study by Style *et al.* using planar substrates showed that even a gradient in stiffness of the underlying material can lead to droplet propulsion [121]. The behavior of droplets at fibre intersections or rather in networks, however, gains more and more attention, as it plays an important role when e. g. performing chemical reactions on small scales [110, 111, 114] or designing highly efficient water collection webs [107].

The shape of droplets on a fibre, in general, has been investigated by many studies [122, 123,

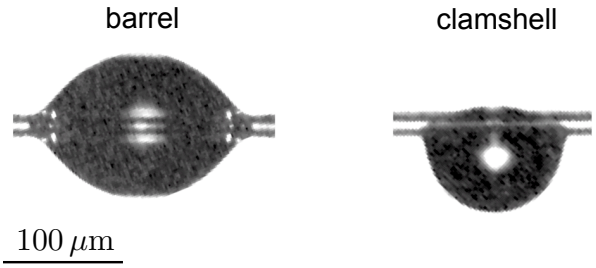


**Figure 2.14:** Droplets (polystyrene with $M_w = 186\,\mathrm{kg/mol}$ at $T = 200\,^\circ\mathrm{C}$) on fibres exist in two competing morphologies: barrel or clamshell shape.

124, 125]. Caroll showed that, for droplets which are smaller than the capillary length $l_c$ (see Sec. 2.2), the Laplace pressure of a droplet in equilibrium located on a fibre, is constant and is given by [122]:

$$p_L = \frac{2\gamma}{R + r}, \tag{2.80}$$

with the maximal droplet radius $R$ and fibre radius $r$. Furthermore, the mechanisms to form different droplet conformations, barrel or clamshell shape (see Fig. 2.14), have been studied in detail [125, 126, 127].

Several studies investigated the velocity of droplets climbing up conical fibres [119, 120]. Here, the droplets were forced to move by the gradient in the fibre radius $r$, corresponding to a gradient in Laplace pressure, see Eq. 2.80. All fibres exhibited a no-slip boundary condition at the solid/liquid interface. In order to avoid material loss during droplet motion, the fibres were pre-wetted with the respective liquids. After releasing the droplets at the hollow tip of the fibre (see inset of Fig. 2.15b), the velocity of the moving droplet was measured for different liquids exhibiting different viscosities. In general, the velocity was found to be nonuniform: Li *et al.* showed that for very low viscosities (consequently high Reynolds numbers), large droplets accelerate at first, reach a maximum velocity $v_{max}$ at a certain cone radius $r$ and subsequently decelerate (illustrated in Fig. 2.15a using the example of water) [120]. The decrease in velocity, when moving towards the region with lower curvature, can be understood by the decrease of the driving force, which is proportional to $1/r^2$. In addition, the velocity is decreasing due to the fact that as the fibre becomes thicker, the viscous friction force, which mostly acts within the liquid wedge (see Sec. 2.4), increases [119]. A study by Lorenceau *et al.* corroborates this by showing that, when using liquids with high viscosities, the droplet speed decreases right from the beginning of the movement [119]. The initial acceleration regime (see Fig. 2.15a), when using low viscosity liquids, can be understood by considering inertia: whereas, Lorenceau *et al.* used liquids with a high viscosity, Li *et al.* mostly studied low viscosity liquids, which leads to an enhanced influence of inertia effects. Furthermore, Li *et al.* found that with increasing the volume of the droplet, the velocity maximum is shifted to a larger cone radius (Fig. 2.15a) [120]. The influence of both parameters, viscosity $\eta$ and droplet volume, on the speed of a climbing droplet is summarized in the characteristic capillary-inertial time scale, which here can be estimated as: $\tau \sim \sqrt{\rho R_0 (r + R_0)^2/(2\gamma\alpha)}$, with maximal droplet radius $R_0$, cone radius $r$, surface tension $\gamma$ and semi cone angle $\alpha$. Hence, large droplets provide large values for

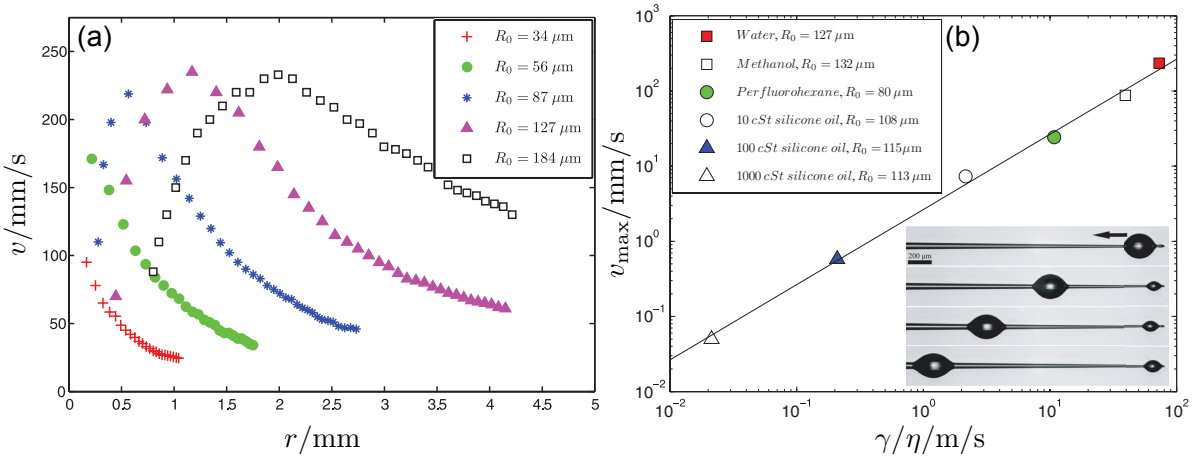


**Figure 2.15:** (a) Velocity $v$ of water droplets climbing up a conical fibre with radius $r$ for different droplet radii $R_0$. (b) Maximum droplet velocity $v_{\max}$ as a function of capillary velocity $\gamma/\eta$ using different liquids. Modified from [120].

$\tau$ and, thus, the initial motion needs to be considered within the acceleration phase until a balance between capillary driving force and viscous friction is reached [120]. For $t > \tau$, the droplet motion process is dominated by viscous forces. In general, both studies revealed that an increase in viscosity and consequently an increase in viscous dissipation causes the droplet speed to decrease (see Fig. 2.15b and Eq. 2.53) [119, 120].

Even though these studies provide insight into droplet motion processes on filaments, all measurements are accompanied by a variation of the experimental parameters during the course of the experiments. Inducing droplet motion by e. g. a temperature gradient, is accompanied by significant variations in viscosity (see Eq. 2.1) [15]. Studies on droplet motion on conical fibres, in contrast, have the advantage of using liquids with a constant viscosity, but do exhibit an inhomogeneous fibre geometry (see inset of Fig. 2.15b) [119, 120]. Inducing droplet motion by stiffness gradients of the underlying material again implies a drastic change of the surface properties [121]. For this reason, a very interesting and open-ended question is the propulsion of liquid droplets with a constant viscosity on fibres, where both, the radius as well as the surface properties, are kept constant during the entire motion process. In the presented work, we studied droplet propulsion of viscous polystyrene droplets on hydrophobized fibres, with a constant viscosity $\eta$, radius $r$ and surface properties. Experimental details and results are explained in the **publication in ADDENDUM III**. In addition, we present first results on the influence of slippage on the droplet dynamics (see Sec. 5.2).

# 3 Experimental techniques

Experiments to study the evolution of the Rayleigh-Plateau instability and the flow dynamics of thin films were performed on substrates with varying boundary conditions and of different geometries. This chapter comprises the employed sample preparation and sample characterization techniques as well as the experimental methods, followed by a detailed explanation of the data analysis.

## 3.1 Sample preparation

### 3.1.1 Planar AF1600 substrates

In order to study the RPI of a receding straight front in a thin PS film, hydrophobized silicon (Si) wafers were used as substrates. Prior to the application of a hydrophobic layer, the Si wafers (Si-Mat, Landsberg) with a native $SiO_2$ layer were cleaned: adhering particles were mechanically removed by using a focussed jet of $CO_2$ crystals (Snow Jet, Tectra, Frankfurt). To get rid of organic residues, the samples were subject to the well-established 'piranha'-cleaning procedure: here, the Si wafers are exposed to a 1:1 mixture of unstabilized hydrogen-peroxide $H_2O_2$ (Merck, Darmstadt) and concentrated sulfuric acid $H_2SO_4$ (BASF, Ludwigshafen) for 30 minutes. To remove residues of the 'piranha'-solution, the samples were rinsed in hot MilliQ$^{TM}$ water (Millipore, USA) for 15 minutes. These steps were repeated two times for 15 minutes each. By using a jet of ultra clean nitrogen (Praxair) the samples were dried. As e. g. any dust particle may act as a nucleus for the dewetting process, prior to any further use, the cleanliness of all samples was checked by dark field microscopy using a magnification of 500x.

In order to hydrophobize the Si wafers, the samples were coated with a thin amorphous fluoropolymer layer via dip-coating. Using a 0.5 w/v% solution of AF1600 (Poly[4,5-difluoro-2,2-bis(trifluoromethyl)-1,3-dioxole-co-tetrafluoroethylene]) (Aldrich) dissolved in a perfluorocompound solvent (FC75$^{TM}$, Arcos Organics) and a dip-coating speed of 1 mm $s^{-1}$ leads to a $14 \pm 1$ nm thick Teflon® layer, which exhibits a RMS roughness of $0.5 \pm 0.03$ nm. The thickness of the AF1600 layer was measured by using ellipsometry and the roughness was obtained from atomic force microscope (AFM) measurements (see Secs. 3.2.3 and 3.2.4). Following the product handling informations by DuPont$^{TM}$, the AF1600 samples were annealed at 112 °C for 10 minutes in ambient conditions, in order to remove the excess solvent. To improve the adhesion of the coating, the substrates were heated for additional 10 minutes at a temperature of 165 °C, which is well above the glass transition temperature of the fluoropolymer ($T_g = 160$ °C).

### 3.1.2 Fibres

To generate fibres with diameters on the micro-scale, heated glass capillary tubes (World Precision Inst.) were pulled to a final radius varying between $10 < r < 25\,\mu$m (see Fig. 3.1b). The capillary tubes are made of borosilicate glass with an outer diameter of 1 mm, an inner diameter of 0.58 mm and a length of 152 mm. We used a pipette puller (Narishige, PN30), consisting of two clamps (one is static and one can be moved), where the capillary tube is mounted on. In order to heat the glass, the capillary is put through a semicylindrical platinum plate. By heating it up to $\sim 900$°C, the glass locally melts and by quickly pulling the movable clamp, the capillary is stretched and thins out. At the end of the pulling procedure, the capillary breaks into two parts: one very long fibre (length $\sim 5-7$ cm), which we use for the experiments and a short one (length $\sim 1-2$ cm). We made sure to prepare homogeneous fibres. Although the pulled fibres exhibit a very small diameter gradient at both ends (at the very tip and where the pulled fibre merges into the initial glass capillary), the fibre does not show any measurable thickness variation in between the two ends. In each case, the fibre radius $r$ is determined from optical micrographs by using two independent techniques: by an image analysis software (Image Pro Plus, Media Cybernetics) and by a custom-made edge detection software written in MATLAB (see Sec. 3.3.1). Hereby, the radius can be determined with an accuracy of $\pm 1\,\mu$m. Given this precision and the fact that, in the experiments, we record fibres with a length of $\sim 2200\,\mu$m, the cone half angle is always safely smaller than $0.05\,^\circ$. In all experiments presented in this work, we ensured to use parts of the fibres with a homogeneous radius. Thus, the influence of a fibre radius gradient on the presented results can safely be excluded. In addition, Li *et al.* showed that the surface roughness of glass fibres remains very low after heating and pulling, with an upper bound of 50 nm obtained from a scanning electron microscope (SEM) image [120].

In order to vary the boundary condition at the solid/liquid interface, the glass fibres were hydrophobized by dip coating in a 0.5 wt% solution of AF2400 (Poly[4,5-difluoro-2,2-bis(trifluoromethyl)-1,3-dioxole-co-tetrafluoroethylene]) (Aldrich) in a perfluorocompound solvent (FC72$^{\mathrm{TM}}$, Fisher Scientific). A dip coating velocity of 1 mm s$^{-1}$ leads to a nanometric thin amorphous fluoropolymer (AF2400) layer, which has a glass transition temperature of $T_{\mathrm{g}} = 240\,^\circ$C. The thickness of the AF2400 layer can be estimated from ellipsometry measurements of planar substrates which were prepared by using AF1600 in FC75$^{\mathrm{TM}}$ as well as in FC72$^{\mathrm{TM}}$ solutions with a concentration of 0.5 wt% and a dip-coating speed of 1 mm s$^{-1}$ (see Sec. 3.1.1) [129]. To remove the excess solvent, the AF2400 fibres have been annealed in ambient conditions at $T = 80\,^\circ$C for 90 minutes. Note that, in order to study the RPI on fibres, AF2400 instead of AF1600 was used as annealing temperatures well above $T_{\mathrm{g}} = 160\,^\circ$C of AF1600 were needed.

In addition, the boundary condition at the fibre/liquid interface was varied by silanizing the glass fibres with dodecyl-trichlorsilane (DTS, Sigma Aldrich) forming a hydrophobic self-assembled monolayer (SAM) [34]. The samples were prepared following the detailed preparation instructions given in [130]. For details concerning the surface properties and the preparation process the reader is referred to [130].

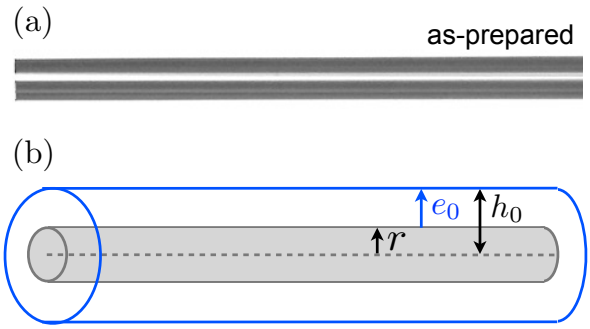


**Figure 3.1:** (a) Optical micrograph and (b) schematic illustration of the initial stage of the PS-coated fibre. The width of the optical image is 560 $\mu$m. Modified from [128].

### 3.1.3 Films on planar substrates

To prepare thin polymer films on planar substrates, Polystyrene (PSS, Mainz) with a molecular weight of $M_w = 5.6$ kg/mol and 101 kg/mol (with a polydispersity index of $M_w/M_n \approx 1$) was dissolved in toluene (Merck, Darmstadt).

Homogeneous PS films generated via spin-coating can be achieved e. g. by using hydrophilic substrates as Si wafers. The AF1600 surfaces are, however, hydrophobic. Therefore, the PS films can not directly be applied to these substrates. As a substrate, freshly-cleaved mica sheets (Plano, Wetzlar) with a size of 25 x 25 mm$^2$ were used, which are hydrophilic and exhibit a roughness on the atomic scale. Hence, the PS films were applied to the mica sheets by spin-coating (WS-200-4NPP, Laurell, USA). Here, a droplet of the PS solution is positioned on a sample, which is located on a rotation plate. Immediately after the droplet deposition, the sample starts to rotate with a speed of $\omega$. As a result of the rotation, the solution is spread over the entire sample, the solvent evaporates and a thin homogeneous PS film forms. The thickness $h_0$ of the remaining film is controlled by the concentration $c$ of the solution, the rotation speed $\omega$, the acceleration of the rotation as well as the molecular weight $M_w$ of the polymer. A given $M_w$ and using the maximal acceleration leads to $h_0 \propto \sqrt{c^3/\omega}$. The parameters used in this work are summarized in Tab. 3.1.

| $M_w$ / kg/mol | $c$ / w/v% | $\omega$ / rpm | $h_0$ / nm |
|---|---|---|---|
| 5.6 | 33.8 | 3500 | $125 \pm 5$ |
| 101 | 25.5 | 3300 | $106 \pm 4$ |

**Table 3.1:** The thickness $h_0$ of a polymer film with a certain molecular weight, which results from spin-coating the polymer solution with concentration $c$ while using a spin-coating speed of $\omega$ (at maximum acceleration), scales with $\sqrt{c^3/\omega}$.

In order to transfer a PS film from a mica sheet to a hydrophobized wafer, the so-called floating technique was used: by slowly dipping the mica sheet into a bath of MilliQ water (where the angle between the mica sheet and the water surface is $\sim 45°$), the PS film peels off and

starts to float on top of the water surface. The film can easily be picked up with a hydrophobic substrate. Therefore, the wafer is dipped into the water while touching the PS film from above. By pulling the sample out of the water, where the surface of the wafer is parallel to the water surface, the PS film sticks to the AF1600 and forms a flat layer. When using a short-chained PS melt, the film on the water surface often is disrupted into several pieces. Using a highly entangled PS melt results, however, in a homogeneous layer without any gap. Hence, studying the RPI of a receding front in a film made of a long-chained PS melt requires, first of all, the preparation of a straight front. Following the procedure described in [131], a straight front was generated by scratching a heated PS film with a heated AFM tip (with a radius of 2 nm). The temperature of both, sample and tip, was $T = 97\,^{\circ}\mathrm{C}$. As the phase transition from the glassy to the liquid state of a polymer film occurs over a certain temperature range, the PS film is nearly liquid, although $T = 97\,^{\circ}\mathrm{C} < T_g$. This strongly facilitates the scratching process, but keeps the flow dynamics slow enough to prevent the film from a sudden dewetting after the preparation of the contact line.

### 3.1.4 Films on fibres

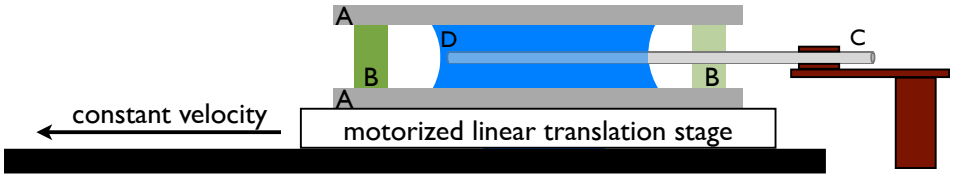


**Figure 3.2:** Schematic of the horizontal PS film preparation setup, where a droplet of the PS solution (D) is placed on a fibre (C), which is positioned close to a glass plate (A). Separated by two Si spacers (B), the system is covered with a second glass slide. The PS solution is dragged along the fibre with a constant speed by using a motorized linear translation stage. As a result, a homogeneous axisymmetric PS film with a thickness of $e_0$ is formed. Adopted from [132].

In order to apply homogeneous PS films on fibres (see Fig. 3.1), we prepared concentrated solutions ($c \sim 35\,\mathrm{wt\%}$) of atactic PS (Polymer Source Inc.). The molecular weights varied between 4 and 390 kg/mol ($M_w/M_n = 1.05$). The evolution of variations in the height of the PS film caused by evaporation [133] is avoided by dissolving PS in chloroform (Fisher scientific), instead of the commonly used toluene, as the vapor pressure of chloroform ($p_v = 213\,\mathrm{mbar}$ at $T = 20\,^{\circ}\mathrm{C}$) is much higher than the one of toluene ($p_v = 29\,\mathrm{mbar}$ at $T = 20\,^{\circ}\mathrm{C}$) [134]. Note that the chloroform does not dissolve the hydrophobic AF2400 layer. Considering the evaporation effects on the formation of the PS film, we changed from the typical vertical dip coating arrangement to a horizontal setup, shown in Fig. 3.2. Here, a fibre is positioned close to a glass plate and a PS droplet is placed on the fibre. Separated by two Si spacers, the system is covered with a second glass slide. By using this 'sandwich' technique (glass slide - fibre in PS droplet - glass slide while using spacers), it can be guaranteed that the fibre is located in the center of the PS droplet without being in direct contact with one of the two glass slides. The PS droplet forms a perfect meniscus at the ends. Via a motorized linear travel

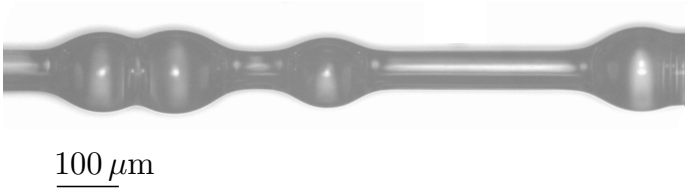


**Figure 3.3:** As a result of preparing a film on a fibre, where the PS solution has been used right after the shaking step, entrapped air bubbles in the film may occur randomly upon annealing the sample ($M_w = 78\,\mathrm{kg/mol}$ at $T = 180\,^\circ\mathrm{C}$).

stage (Newport), the entire setup, yet without the fibre is moved with a constant velocity. Hence, the fibre is solely pulled out of the PS solution, which causes the formation of an axisymmetric homogeneous PS film surrounding the fibre (see Fig. 3.1). By changing either the concentration $c$ of the PS solution or the pulling speed of the stage, the thickness $e_0$ of the PS film can be varied. Here, we obtained thicknesses ranging from $e_0 = 5$ to $93\,\mu\mathrm{m}$ (see Fig. 3.1), when varying the speed between $80 - 150\,\mathrm{mm\ s^{-1}}$. All samples have been prepared at room temperature, well below $T_g$ for all molecular weights.

To reproducibly prepare homogeneous polymer films on fibres, a few experimental tricks should be considered:

- Usually, the last step of preparing a polymer solution is to fully dissolve the polymer powder by shaking the solution for several hours. If a freshly prepared solution is used to apply a film on a fibre, the film may form a homogeneous layer surrounding the fibre. The subsequent annealing of the sample above $T_g$, however, might cause large air bubbles and bumps to occur randomly all over the sample (see Fig. 3.3). In the course of further annealing these samples, the air bubbles may extend until they burst. As the concentration of the used PS solutions is quite high ($c \sim 35\,\mathrm{wt\%}$), the solutions are very viscous. As a consequence, it takes some time for the entrapped air, caused by the shaking procedure, to vanish. The answer to this problem is to leave the fully dissolved solution at rest for at least 3 hours.
- Even air bubbles caused by the pipetting procedure of the PS solution may cause this effect. Therefore one has to be careful to avoid the formation of air bubbles, already, when bringing the PS solution into the pipette.
- An inhomogeneous film on the fibre can also be caused by a fibre which is not positioned right in the center of the PS solution or even a fibre which is in direct contact with one of the glass slides. Hence, moving the PS solution along the fibre might cause a homogeneous film, which is not axisymmetric. Therefore, it is very important to make sure that the fibre is placed in an appropriate position before moving the stage.
- When applying the PS solution to the fibre and covering the system with the second glass slide, one has to be very careful to be fast enough, as the chloroform evaporates very quickly. If the time interval between applying the PS droplet to the fibre and moving the stage is too long, a significant gradient in the solvent concentration occurs, which causes an inhomogeneous film thickness.

- Furthermore, it has to be ensured that the amount of polymer solution applied to the fibre is large enough in order to make a good contact with the second glass slide. If the amount of liquid is too low, there is no meniscus at the end and the formation of an axisymmetric homogeneous film is also rather unlikely.

### 3.1.5 Moving droplets on fibres

**Figure 3.4:** The final stage of the RPI of a viscous liquid film (PS with $M_w = 78\,\mathrm{kg/mol}$ at $T = 180\,^\circ\mathrm{C}$) on a fibre consists of a regular droplet pattern, where the large droplets exhibit a wavelength of $\lambda^* = 2\sqrt{2}\pi h_0$ (see Eq. 2.79). The film in between the large droplets is again undergoing a RPI, which leads to the formation of satellite droplets. The width of the optical image equals $1500\,\mu\mathrm{m}$.

In order to study the motion of polymer droplets on fibres (cf. the **publication in ADDENDUM III**), moving droplets were generated by taking advantage of the Rayleigh-Plateau instability. In the final stage of the liquid column breakup, the fibres are decorated with a regular droplet pattern, shown in Fig. 3.4. Since the mass of the individual droplet is too small for gravitational forces to be significant, interfacial forces dominate the form and all droplets are in an axisymmetric barrel-shaped conformation (see Fig. 2.14). Furthermore, we discovered that in case of using hydrophobized fibres a three-phase contact line at one side of a droplet can be formed spontaneously in the course of further annealing of the sample above $T_g$. The thinning film in between the droplets is metastable and, hence, any chemical or topographical heterogeneity can lead to a random rupture of the thinning film (see Sec. 2.3). Thus, a three-phase contact line at one side of a droplet is formed. The distance $\lambda^*$ between the biggest droplets is determined by the initial radius $h_0$ via $\lambda^* = 2\sqrt{2}\pi h_0$ (see Sec. 2.5 and the **publication in ADDENDUM II**). Consequently, the width $w$ and the maximal height $h_{max}$ of the big droplets are both related to the initial film thickness $e_0$ and the fibre radius $r$. The same argument holds for the satellite droplets (see Fig. 3.4). Here, the used system geometries, $e_0$ and $r$, led to an initial droplet width varying between $w(t_0) = 100 - 320\,\mu\mathrm{m}$ and a maximal height in the range of $h_{max}(t_0) = 40 - 200\,\mu\mathrm{m}$ (see Fig. 3.5b). The formation of a three-phase contact line at one side of a droplet is accompanied by the adjustment of the contact angle to the receding contact angle $\theta_{rec}$ (see Fig. 3.5). The other side, however, where the droplet merges into the residual PS film with a typical thickness of $e_{res} = 0.5 - 1\,\mu\mathrm{m}$, exhibits the apparent contact angle $\alpha$. As a consequence of the difference in the contact angles at the two sides of the droplet, a capillary imbalance is induced, which in turn causes the droplet to dewet on the fibre (see Sec. 2.4). Hence, by further annealing the sample above $T_g$, the droplet keeps moving along the fibre while accumulating the residual PS film and thereby growing in size (see Fig. 3.5a).

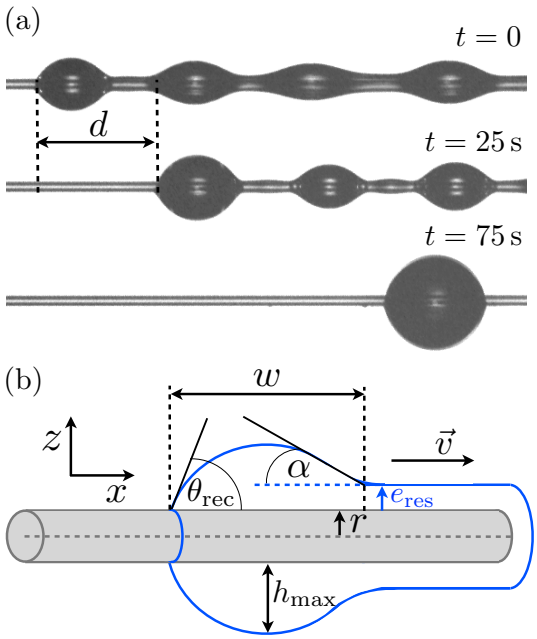


**Figure 3.5:** (a) Optical micrographs (image width: 1120 $\mu$m) representing the dewetting process of a PS droplet ($M_{\mathrm{w}} = 8.1\,\mathrm{kg/mol}$ at $T = 150\,^{\circ}\mathrm{C}$) on a hydrophobized fibre. (b) Schematic of a receding droplet on a fibre, illustrating the relevant parameters. Adopted from [132].

## 3.2 Measurement techniques

### 3.2.1 Experimental setup to study thin films on fibres

The as-prepared samples (PS film on a fibre, shown in Fig. 3.1a) were placed across two teflon spacers ($\sim 0.5\,\mathrm{mm}$ thick). To guarantee a good image contrast, these spacers were located on top of a reflective Si wafer. The entire setup was placed on a hot stage (Linkam). To ensure temperature control within $1\,^{\circ}\mathrm{C}$, the freely suspended fibre is surrounded by a metal ring (in direct contact with the hot stage) which is covered by a glass slide (see Fig 3.6). In addition, the heating plate is surrounded by a metallic housing which can be sealed by the means of a metallic lid. The fibres were annealed in ambient conditions at temperatures ranging from $T = 140 - 220\,^{\circ}\mathrm{C}$, which is well above $T_{\mathrm{g}}$. Optical micrographs were *in situ* recorded in certain time intervals. All images were taken with a very high image contrast between the background and the actual sample (see Fig. 3.1a and Fig. 3.5a).

### 3.2.2 Optical microscopy

The RPI of a film on a fibre has been recorded with an optical microscope (Olympus BX51) using a long distance objective with 5x magnification. The camera had a resolution of 1392 x 1040 pixels (QImaging, QIClick). The pixel resolution yields $1\,\mathrm{pixel}/1.28\,\mu\mathrm{m}$. Experiments

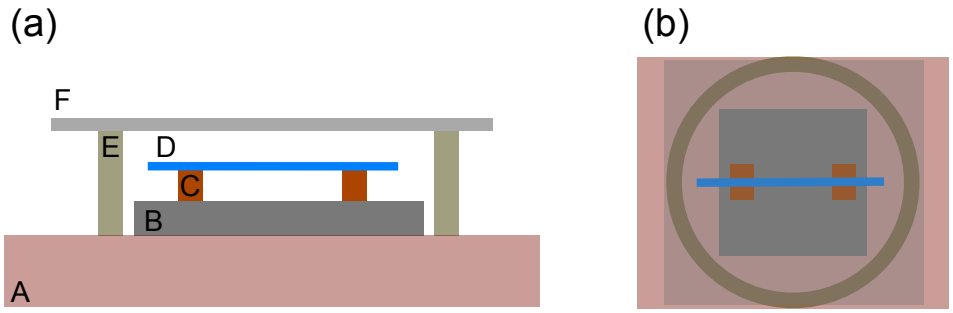


**Figure 3.6:** Schematic representation of (a) the side view and (b) the top view of the experimental setup. On top of a hot stage (A), a Si wafer (B) with two teflon spacers (C) is placed. To generate free standing fibres (D), they are positioned across the spacers. Temperature control is ensured by surrounding the fibres with a metal ring (E) covered by a glass slide (F). Adopted from [128].

concerning the motion of droplets on fibres have been recorded with an Leica DM 2700 M optical microscope using a 5x and 10x magnification long distance objective. The resolution of the camera (Leica MC 170 HD) was 1024 x 768 pixels, which results in a pixel resolution of 1 pixel/2.1 $\mu$m for the 5x objective and 1 pixel/1.05 $\mu$m in case of the 10x objective. The RPI of straight fronts in dewetting thin films on planar substrates was measured using a reflected-light microscope (Leitz Laborlux, Leitz Wetzlar) with 50x and 100x magnification objectives. An additional magnification by a factor of 10 is achieved by placing an objective into the light path. In order to record images, a CCD camera (Coolsnap Pro) with a resolution of 1392 x 1040 pixels was used. Thereby, the pixel resolution equals 1 pixel/0.14 $\mu$m using the 50x and 1 pixel/0.07 $\mu$m using the 100x objective. The cleanliness of the planar sample surfaces was checked using dark field microscopy and a magnification of 500x.

### 3.2.3 Atomic force microscopy

Using an atomic force microscope (AFM) provides the opportunity to measure the topography and the surface properties, as e. g. the elasticity, of a sample. The information is gained from moving a probe along a surface and measuring the interactions between the probe and the sample. The probe of an AFM consists of a tip (made of silicon), which is mounted on a cantilever. Typically, the radius of the tip is in the order of several nanometers. While the tip is moved along the surface forces between the tip and the sample cause the cantilever to deflect. A laser beam is pointing on the back side of the cantilever and the reflected light is detected by a segmented photodiode.

In general, an AFM provides different modes of operation. In the presented work, only tapping mode$^{TM}$ was used (Multimode®, Dimension Icon® and DimensionFastScan Bio®, Bruker). Here, the cantilever is forced to oscillate close to its resonance frequency. In consequence, approaching the surface leads to a damping of the oscillation, caused by e. g. van der Waals interactions between the tip and the surface. Hence, the frequency is decreased. The frequency difference contains, however, information about differences in the height of the surface. The

raw images were analyzed by using the AFM image analysis software (Nanoscope Analysis, Bruker). With the help of several image processing steps, the raw data was flattened with respect to different scan lines and by a first-order plane fit, a potential tilt of the whole image was eliminated. As a result, the desired quantities can directly be measured from the processed images, as e. g. the rim profile of a straight front in a film or the height of the initial film close to a float gap. In order to determine the roughness of a substrate, several images at different spots all over the sample with a size of 1 $\mu$m x 1 $\mu$m each were recorded. The roughness of the surface was determined from the root mean square of the height data. For further details on the basic principles and the different work modes the reader is referred to [135, 136].

### 3.2.4 Ellipsometry

The layer thicknesses as well as the optical properties, as e. g. the index of refraction, of a sample can be obtained from analyzing the reflection and interference of polarized light using an ellipsometer. To determine the thickness of the hydrophobic AF1600 layer on a Si wafer, an $EP^3$ (Accurion, Göttingen) ellipsometer was used. The wavelength of the laser beam was 532 nm and the angle of incidence AOI could be varied between 54° and 80°. With a varying AOI, laser light was emitted through a polarizer (causing linearly polarized light) and a compensator (elliptically polarized light) to the sample. Given a parallel arrangement of the different layers of a sample, the reflected light is again linearly polarized. The intensity of the reflected light is measured as a function of the position of an analyzer. The relative positions of the polarizer and the analyzer, measured for the intensity being minimal, provide a measure for the ellipsometric angles $\Psi$ and $\Delta$, where $\tan(\Psi)$ represents the ratio of the amplitudes and $\Delta$ is the phase shift. By theoretically modeling $\Psi$ and $\Delta$ as a function of AOI [137], which incorporates the dielectric properties and the thicknesses of the underlaying material, the refractive index and the thickness of the AF1600 layer can be measured.

## 3.3 Data analysis

### 3.3.1 Rayleigh-Plateau instability of a PS film on a fibre

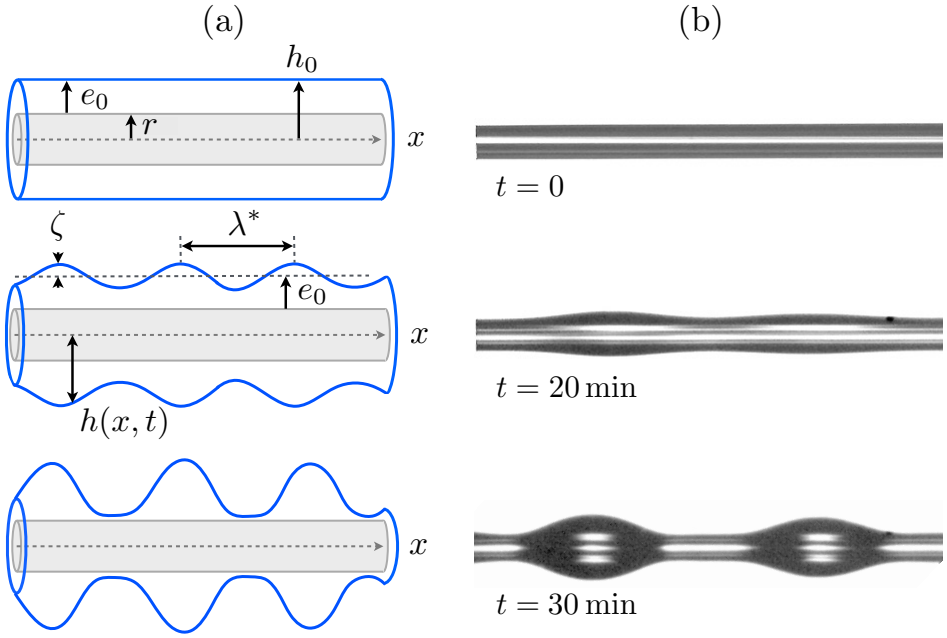


**Figure 3.7:** (a) Schematic representation and (b) optical micrographs displaying the RPI of a PS film with a thickness of $e_0 = 13.2 \pm 1\,\mu\mathrm{m}$ on a glass fibre with a radius equal to $r = 9.6 \pm 1\,\mu\mathrm{m}$ ($M_\mathrm{w} = 78\,\mathrm{kg/mol}$ at $T = 180\,^\circ\mathrm{C}$). In course of heating the sample above $T_\mathrm{g}$, the PS film becomes liquid and decays into droplets. Modified from [128].

In order to study the evolution of the Rayleigh-Plateau instability of PS films on fibres, the optical micrographs were analyzed by using a custom-made edge detection software written in MATLAB: after rotating the image from a random to a horizontal orientation of the fibre, the area of interest was picked by hand. With choosing a certain intensity threshold, the software starts to detect the upper and lower edges of the fibre while exporting the respective height profiles $h_1(x,t)$ and $h_2(x,t)$ for every image (see Fig. 3.8). Hence, it is important to record images with a sufficiently high contrast. From $h_1(x,t)$ and $h_2(x,t)$ information about e. g. volume, surface area, diameter and amplitude as a function of time can be gained.

The initial total radius $h_0$ of the system can be calculated from the absolute difference in the height profiles for $t = 0$:

$$h_0 = \frac{1}{2}|h_2(x,t_0) - h_1(x,t_0)|. \tag{3.1}$$

Similarly, the radius $r$ of the fibre can be determined from the minimum in the absolute difference of the profiles regarding the final equilibrium stage at $t = t_\mathrm{f}$. Here, only parts of the

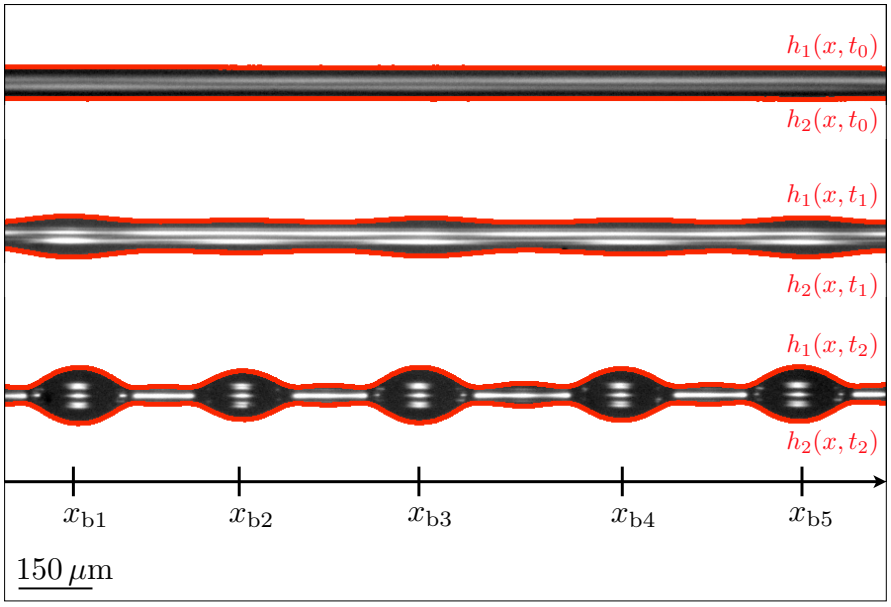


**Figure 3.8:** The temporal evolution of the RPI can be measured by using an edge detection software: for all times $t$ the height profiles $h_1(x,t)$ and $h_2(x,t)$ along the fibre axis $x$ are extracted from detecting the change in the position of the intensity threshold at the edge of the fibre.[1]

fibre in between the droplets are considered:

$$r = \min\left(\frac{1}{2}|h_2(x,t_f) - h_1(x,t_f)|\right). \tag{3.2}$$

Note that, in the final stage of the RPI, the fibre is still covered with a very thin residual PS film in between the droplets (cf. Fig. 3.4). For hydrophobized fibres, however, a complete dewetting of the PS film on the fibre can occur (see Sec. 3.1.5 and the **publication in ADDENDUM III**). Measuring $r$ from the late stage of the RPI and from a fully dewetted fibre showed that the error in $r$, caused by the residual film, is within the error bar. In consequence, the thickness $e_0$ of the PS film results from:

$$e_0 = h_0 - r. \tag{3.3}$$

By independently using the edge detection process and additionally the image analysis software Image Pro Plus (Media Cybernetics), the geometry of the system can be measured with an accuracy of $\pm 1\,\mu$m.

To gain information about the temporal evolution of the RPI, the change in the amplitudes $\zeta$ of all evolving bulges was measured (see Fig. 3.7a). As the instability evolves symmetrically around the fibre, the bulges exhibit the maximal amplitude. The position of the $n$ bulges is given by $x = x_{\mathbf{b}j}$ (cf. Fig. 3.8), where $j = [1;\mathrm{n}]$ is the number of the respective bulge. Hence,

[1] Note that for the purpose of clarity, the red lines are exaggerated, which causes the reduction of the image quality.

the evolution of the amplitudes $\zeta(x_{\mathrm{b}j}, t)$ equals:

$$\zeta(x_{\mathrm{b}j}, t) = \frac{1}{2}|h_2(x_{\mathrm{b}j}, t) - h_1(x_{\mathrm{b}j}, t)| - h_0. \tag{3.4}$$

In order to measure the pure capillary-driven RPI, drainage effects must be absent. Hence, volume conservation of the liquid films within the area of interest has been checked for all experiments. As known from theory (see Sec. 2.5 and the **publication in ADDENDUM II**), the growth of the surface undulations is exponential for early times. Hence, from plotting the logarithm of the amplitudes $\zeta(x_{\mathrm{b}j}, t)$ as a function of time $t$ (with $t$ small enough), the respective growth rate $1/\tau_{\mathrm{b}j}$ of every bulge growing on one fibre can be extracted separately from the slopes. In the **publication in ADDENDUM II**, we developed a theory for the growth rates $1/\tau^*$ of the fastest growing modes with respect to the system geometry $h_0$. We respectively consider only the largest growth rate values when measuring $1/\tau_{\mathrm{b}j}$ for several bulges on the same fibre. Note that all experiments concerning the RPI, presented in the **publication in ADDENDUM II**, were performed by using the same molecular weight ($M_w = 78\,\mathrm{kg/mol}$) and the same temperature ($T = 180\,^\circ\mathrm{C}$). The resulting constant material properties of the liquid combined with a given no-slip boundary condition (glass fibre) enable us to determine the capillary velocity $\gamma/\eta$: when comparing the measured no-slip growth rates $1/\tau^*$ for different system geometries $h_0$ with the respective theoretically predicted growth rate values, the capillary velocity $\gamma/\eta$ is the only free parameter. The value for $\gamma/\eta$ was applied to the measured growth rate data of the slip fibres. Here, the comparison of the experimentally obtained growth rate values $1/\tau^*$ with the predicted theory leaves the slip length $b$ as a fitting parameter (see the **publication in ADDENDUM II**).

Besides the growth of the instability amplitude, also the wavelength formation provides a characteristic fingerprint of the RPI. Therefore, the fastest growing wavelength $\lambda^*$ (see Fig. 3.7a) of the surface undulations was measured. As the linear stability analysis is only valid for the initial stage of the instability, the wavelength was analyzed at early stages of the RPI (see Fig. 3.7a and b with $t = 20\,\mathrm{min}$). Typically, within one experiment, the wavelength was averaged over $4 - 5$ wavelengths.

### 3.3.2 Dewetting process of a PS droplet on a hydrophobic fibre

In order to study the motion of droplets on fibres, an extended version of the edge detection program (see Sec. 3.3.1) was used. Again, all geometric parameters ($h_o, r$ and $e_0$) were determined as stated above. The position $x_{\mathrm{c}}$ of the three-phase contact line on the fibre was detected via measuring the height profiles $h_1(x, t)$ and $h_2(x, t)$ close to the contact line. The fibre was always positioned in an orientation where droplets moved from left to right, which corresponds to a contact line that moves along the fibre starting at a small value for $x$. From

$$h(x_{\mathrm{c}} + 1.28\,\mu\mathrm{m}, t) > h(x_{\mathrm{c}}, t) + 3\,\mu\mathrm{m}, \tag{3.5}$$

with $h = \{h_1, h_2\}$ the position $x_{\mathrm{c}}$ of the contact line on the fibre was determined as a function of time. The difference in $x$ of $1.28\,\mu\mathrm{m}$ equals the size of one pixel. By choosing a height profile difference of $3\,\mu\mathrm{m}$, we ensured to eliminate any noise. From plotting the travelled distance

$$d(t) = |x_{\mathrm{c}}(t) - x_{\mathrm{c}}(t = 0)| \tag{3.6}$$

of the three-phase contact line as a function of time $t$, the mean global dewetting velocity $\overline{v}$ was measured from the slope of the curve. Following a model by de Gennes [68, 69], which is based on the findings by Huh and Scriven [70], we developed a theory, which is explicitly explained in the **publication in ADDENDUM III**. In order to compare the measured data with theory, only those sections were considered, where the moving droplet accumulates the residual thin film. Coalescence steps with static droplets sitting on the fibre were ignored. By applying the Savitzky-Golay algorithm with a frame size of $n = 3$ and a second order polynomial ($p = 2$) to these portions of the data sets, we determined the local dewetting velocity $v$.

The receding and the equilibrium contact angle, $\theta_{\mathrm{rec}}$ and $\theta_{\mathrm{e}}$, of the droplets were determined by using again both techniques, the MATLAB software as well as the image analysis software. In MATLAB, the droplet profile near the contact line is used to determine the contact line position $x_{\mathrm{c}}$, which is given by the minimum of the best fitting second order polynomial:

$$p = p_2 x^2 + p_2 x + p_3. \tag{3.7}$$

The slope of of the droplet profile at $x = x_{\mathrm{c}}$, which is equal to

$$p'(x_{\mathrm{c}}) = 2p_2 x_{\mathrm{c}} + p_2 \tag{3.8}$$

yields the respective contact angle. In the image analysis software, the angle measurement tool is used, where one line is drawn parallel to the substrate and a second line which is tangential to the droplet profile $h(x, t)$ close to the contact line. Hence, the contact angle is enclosed between the two lines. Both measurement techniques provide consistent results (cf. the **publication in ADDENDUM III**).

The width $w(t)$ as well as the maximum droplet height $h_{\max}(t)$ were measured by using the image analysis software. The definition of both quantities is illustrated in Fig. 3.5: the maximal droplet height $h_{\max}(t)$ at a specific time $t$ is given by the difference of the droplet radius $R(t)$ and the fibre radius: $h_{\max}(t) = R(t) - r$. The width $w(t)$ of the droplet is usually obtained as the horizontal distance between the three-phase contact line and the position where the rim merges into the residual film.

### 3.3.3 Rayleigh-Plateau instability of a dewetting straight front in a thin PS film

For the purpose of investigating the evolution of the RPI of a receding straight front in a thin PS film on a planar substrate, the recorded optical micrographs were analyzed by using the image analysis software. The instability of a receding rim is not axisymmetric and, consequently, the edge-detection software could not be applied. As the dewetting dynamics is, in general, significantly influenced by the viscosity of the polymer melt (see Sec. 2.4), only the comparison of different films with the identical thickness $h_0$ at the same dewetted distance $D(t)$ provides the same volume of the receding front. Following the method described in [131], the dewetted distance $D(t)$ was determined as follows: for every image, we measured the distance $d(t)$ between the receding straight front and a reference line parallel to the front. In order to account for a potential drift of the optical image during the experiment, the reference line

is usually placed across e. g. a dust particle. Hence, via $D(t) = |d(t) - d(t_0)|$ the dewetted distance $D(t)$ of the receding straight front can be calculated for all times $t$. In addition, the height profiles $h(x, t)$ of the front were measured using AFM (see Sec. 3.2.3).

# 4 The Rayleigh-Plateau instability on a fibre

## 4.1 The influence of the hydrodynamic boundary condition

As discussed in Section 2.5.2, instabilities of Rayleigh-Plateau type are present in many different systems. In addition, we already know that for the complex system of a straight front in a dewetting thin film, the dynamics as well as the morphology of the RPI are strongly influenced by the hydrodynamic boundary condition at the interface between the liquid and the solid substrate [85]. So far, a quantitative agreement between experiments and theory for the growth of the instability with a varying boundary condition was still missing. Here, the simplest setup is chosen to study the influence of slip on the RPI: a polymer film with a thickness of $e_0$ is prepared on a cylindrical fibre of radius $r$, which displays the classical case of a fluid cylinder, but involves the contact with a solid/liquid interface. The initial total radius of the system is equal to $h_0 = e_0 + r$, which is non-dimensionalized via $H_0 = h_0/r$. A no-slip system was generated by covering a pure glass fibre with a polystyrene film (with a molecular weight of $M_w = 78\,\mathrm{kg/mol}$) [18]. The same PS melt can be forced into a slip boundary condition if prepared on a non-adsorbing substrate, e. g. in our case a teflon® surface [52]. From an earlier study, we know that polystyrene with a molecular weight of $M_w > M_c$, with $M_c = 35\,\mathrm{kg/mol}$, on a teflon® surface represents a system where slippage is present [35]. Thus, in order to study the influence of a variation of the boundary condition, the PS films were applied to glass fibres with or without a thin amorphous fluoropolymer layer (similar to teflon®, called AF2400), for the preparation see Sec. 3.1.2.

The influence of the boundary condition on the spatial as well as the temporal evolution of the RPI was investigated by recording the evolution of the instability on both types of substrates: bare glass fibres ('no-slip fibres') and hydrophobized fibres ('slip fibres'). All experiments were performed using a constant temperature of $T = 180\,^{\circ}\mathrm{C}$. As shown in the **publication in ADDENDUM II**, the wavelength $\lambda^*$ of the fastest growing mode is not affected by slippage at the fibre/liquid interface. In agreement with earlier findings [85], $\lambda^*$ does exclusively depend on the initial total radius $h_0 = e_0 + r$ of the fibre system. In addition, we found that at short times the surface undulations grow exponentially on both, slip and no-slip fibres, which again is consistent with former studies [63, 91].

The analysis of the growth rates $1/\tau^*$ of the fastest growing modes shows a significant difference when varying the boundary condition: slippage at the solid/liquid interface induces a considerable increase of the growth rates. In the **publication in ADDENDUM II** a thin-film model including slippage is developed, which is in perfect agreement with the experimental data (wavelength as well as growth rates). The comparison of the measured growth rates with the theoretically predicted values for the no-slip case enables the determination of the respective capillary velocity $\gamma/\eta$. The obtained value of $\gamma/\eta = 294 \pm 43\,\mu\mathrm{m/min}$ was found to be

in excellent agreement with former studies, based on the extrapolation of available data using the WLF equation (Eq. 2.1) [17, 18]. Applying the measured $\gamma/\eta$ value in order to compare the experimental and theoretical values of $1/\tau^*$ in the presence of a slip boundary condition provides a robust way to obtain the corresponding slip length $b$. Thereby, the studied PS(78k) films on AF2400 fibres reveal a slip length of $b = 4.0 \pm 0.4\,\mu$m.

Aside from the slip-induced amplification of the instability, the growth rates $1/\tau^*$ show a similar geometry dependence for both boundary conditions: in agreement with the results of Roe [97], we found a decrease in the fastest growth rates $1/\tau^*$ for either very thin films compared to the fibre radius or for very large ratios of $e_0/r$. This can be understood by the fact that as the film thickness $e_0$ decreases, the mobility of the liquid is reduced. Large ratios of $e_0/r$, however, display a lowered curvature, which results in a decrease of the driving force. In accordance with the developed theory, $1/\tau^*$ shows a maximum for $e_0/r \sim 4$ with a given no-slip boundary condition. Using slip fibres, however, causes an enhanced mobility of the PS melt at the interface and as a consequence, the maximum in the growth rate $1/\tau^*$ is shifted to a smaller $e_0/r$ value. As thinner films are much more sensitive to the non-zero mobility at the interface, the slip-induced amplification of the instability is more pronounced as the film thickness to fibre radius ratio $e_0/r$ decreases. For the smallest value of $e_0/r \sim 0.4$, the growth of the RPI is enhanced by a factor of $\sim 4$.

A detailed description of the experiments, the theoretical model and a discussion of the results is given in the **publication in ADDENDUM II**.

## 4.2 The influence of increasing slippage

Motivated by these results, first measurements on the effect of a further increased slip length $b$ at the solid/liquid interface on the RPI have been performed. For $M_\mathrm{w} > M_\mathrm{c}$, the slip length $b$ is known to scale with $b \sim M_\mathrm{w}^3$ [35, 52]. Thus, PS with a molecular weight of $M_\mathrm{w} = 186\,\mathrm{kg/mol}$ was used. Since entangled polymers may show viscoelastic effects, the upper limit of the Weissenberg number $Wi$ (see Sec. 2.2.1) regarding the presented experiments for PS(186k) will be calculated in the following. Concerning the RPI, the strain rate $\dot\gamma$ along the fibre axis can be estimated by $\dot\gamma = v/\Delta x$, where the velocity is defined by the growth of the amplitude $\zeta$ during the initial regime $\Delta t$ and the typical distance is given by $\Delta x = \lambda^*/2$. Consequently, with the largest measured velocity of $v = 2.6\,\mathrm{nm/s}$ and $\Delta x = 221\,\mu$m, the largest strain rate is found to equal $\dot\gamma = 1.2 \cdot 10^{-5}\,1/\mathrm{s}$. Using the respective relaxation time[2] of $\tau = 0.13\,\mathrm{s}$ for PS(186k) at $T = 200\,^\circ$C, the Weissenberg number is given by $Wi = 1.5 \cdot 10^{-6}$. Considering the strain rate component in $z$-direction, the typical distance is equal to $\Delta z = e_\mathrm{res} + b$. As will be shown in the following, the slip length for PS(186k) can be estimated by $b = 10 \pm 3\,\mu$m. With a typical residual film height of $e_\mathrm{res} = 1\,\mu$m, the Weissenberg number, which corresponds to the dominating $z$-component of the shear rate ($\dot\gamma = 2.4 \cdot 10^{-4} 1/\mathrm{s}$), reads $Wi = 3.1 \cdot 10^{-5}$. Hence, as $Wi \ll 1$, the influence of viscoelastic effects on the evolution of the RPI can safely be neglected.

[2] For PS(390k) at $T = 130\,^\circ$C, Bach *et al.* measured a relaxation time of $\tau = 11300\,\mathrm{s}$ [139]. Projecting this value according to the WLF equation (Eq. 2.1) yields the desired relaxation time $\tau$ for PS(186k) at $T = 200\,^\circ$C.

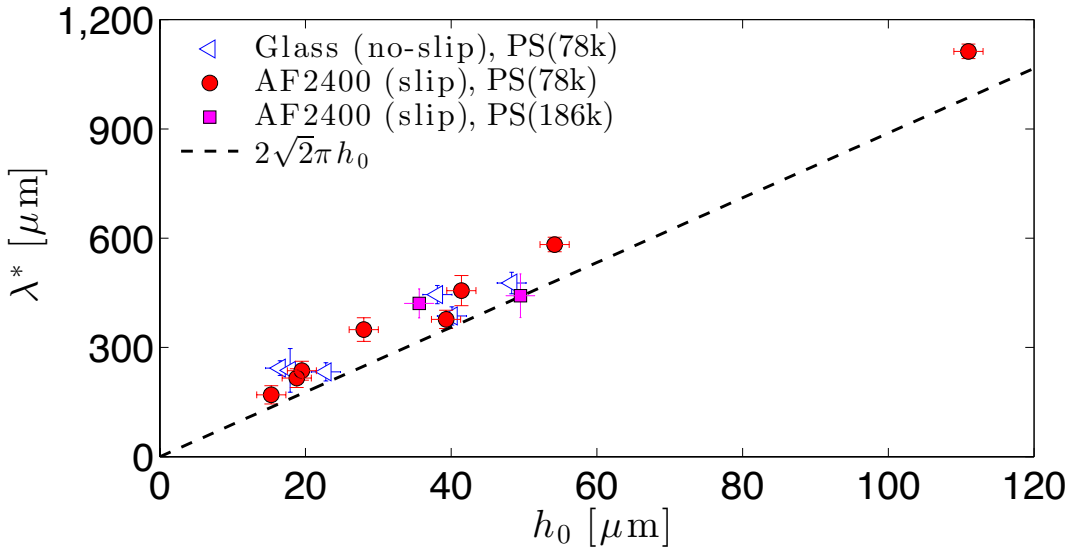


**Figure 4.1:** Wavelength $\lambda^*$ of the fastest growing mode as a function of the initial total radius $h_0$ for PS(78k) on glass and AF2400 fibres as well as PS(186k) on AF2400 fibres. The black dashed line represents the theoretical prediction (Eq. 4.1). The error bars are determined from the error in the geometry and the inaccuracy in the measurement of the wavelength. Modified from [128].

Figure 4.1 illustrates the measured wavelength $\lambda^*$ of the fastest growing modes as a function of the initial total radius $h_0$ for PS(186k) on slip fibres (squares) in comparison to the wavelength data for PS(78k) on no-slip (triangles) and slip (circles) fibres. The dashed line displays the theoretically predicted dependence between $\lambda^*$ and $h_0$, given by (cf. the **publication in ADDENDUM II**):

$$\lambda^* = 2\sqrt{2}\pi h_0. \tag{4.1}$$

As expected from the results for PS(78k) and Eq. 4.1, the fastest growing wavelength $\lambda^*$ of PS(186k) is not affected by slippage and grows linearly with the initial total system radius $h_0$.

Hence, the respective growth rates $1/\tau^*$ need to be considered, in order to resolve an influence of an increased slip length on the evolution of the RPI. According to the developed thin film theory, the dimensionless growth rate $1/\tau^*$ of the fastest growing mode is given by (see the **publication in ADDENDUM II**):

$$\frac{1}{\tau^*} = \alpha B + \beta, \tag{4.2}$$

where $B = b/r$ is the dimensionless slip length and

$$\alpha = \alpha(H_0) = \frac{1}{16H_0^3}\left(H_0 - \frac{1}{H_0}\right)^2, \tag{4.3}$$

$$\beta = \beta(H_0) = \frac{1}{64H_0^3}\left(4H_0^2 \log H_0 - 3H_0^2 - \frac{1}{H_0^2} + 4\right) \tag{4.4}$$

are dimensionless parameters which depend on the geometry only. Thus, the no-slip case is represented by $B = 0$, corresponding to $1/\tau^* = \beta$. According to Eqs. 4.2 - 4.4, the fastest growth rate $1/\tau^*$ is expected to increase with increasing the slip length $b$, for a given system geometry $H_0$. Similar to the results shown in the **publication in ADDENDUM II**, we measured the growth rates $1/\tau^*$ of the fastest growing modes of PS(186k) films on slip fibres for different geometries $H_0$. In order to determine $1/\tau^*$ using slip fibres, the respective capillary velocity $\gamma/\eta$ is needed. For PS(78k), $\gamma/\eta$ has directly been determined from the comparison of the experimentally measured and theoretically predicted values of $1/\tau^*(H_0)$ (see Sec. 3.3.1 and the **publication in ADDENDUM II**). The measured $\gamma/\eta$ value turned out to be in good agreement with earlier works [17, 18]. Hence, in order to determine $1/\tau^*$ of PS(186k) at $T = 200\,^\circ\mathrm{C}$, the corresponding capillary velocity $\gamma/\eta$ was determined as follows: the viscosity $\eta$ was calculated from independent viscosimeter and ellipsometric measurements [17] by extrapolating the data according to the WLF equation (Eq. 2.1). The surface tension $\gamma$ was taken as $\gamma = 30.8 \cdot 10^{-3}\,\mathrm{N/m}$ [23] (see Sec. 2.2).

Figure 4.2 displays the measured growth rate data $1/\tau^*$ for PS(186k) on slip fibres (squares) in comparison to the measured data for PS(78k) on no-slip (triangles) and slip (circles) fibres. In order to determine the slip length $b$, the inset of Fig. 4.2 shows $1/\tau^*$ normalized by the no-slip case $\beta$ as a function of $\alpha/(\beta a)$, representing the geometry of the system (see Eq. 4.2). Note that a large value of $\alpha/(\beta a)$ corresponds to a small value of $H_0 = e_0/r + 1$, i. e. a very thin film $e_0$ as compared to the fibre radius $r$. The ratio $1/(\tau^*\beta)$ shows that increasing the molecular weight indeed causes an increase in the growth rate of the RPI. From a best linear fit to the PS(186k) data shown in the inset, the slip length is found to equal $b = 10 \pm 3\,\mu\mathrm{m}$ (see Eq. 4.2). Note that only two data points were provided to the fitting procedure. Hence, the slip length for PS(186k) displays a rough estimate and more data points are needed to confirm this trend. A detailed discussion about the slip length obtained from analyzing the growth rates of the RPI is presented in chapter 6.

By knowing the slip length $b$ as well as the fibre radii $r$, the respective values of the dimensionless slip length $B = b/r$ can be calculated. Here, we obtain $B = 0.40$ for $r = 25.2\,\mu\mathrm{m}$ and $B = 0.89$ with $r = 11.2\,\mu\mathrm{m}$. The main plot of Fig. 4.2 shows the measured dimensionless growth rates $1/\tau^*$ as a function of the dimensionless initial total radius $H_0$ (filled symbols), which are in excellent agreement with the respective theoretically predicted values (open symbols), see Eq. 4.2. As presented in the **publication in ADDENDUM II**, the values of the fibre radius regarding the experiments using PS(78k) on slip fibres are in the range of $r = 11 - 16\,\mu\mathrm{m}$ and the slip length was found to equal $b = 4.0 \pm 0.4\,\mu\mathrm{m}$. Consequently, the values for $B$ vary between 0.25 and 0.37. Therefore, in Fig. 4.2 a typical curve for PS(78k) is introduced as a guide to the eye, where $B = 0.3$ with $r = 13.5\,\mu\mathrm{m}$ (red thin dashed line). In order to compare the course of $1/\tau^*(H_0)$ with respect to the used molecular weights, the theoretically predicted curve using the slip length $b = 10 \pm 3\,\mu\mathrm{m}$ of PS(186k) and a fibre radius of $r = 13.5\,\mu\mathrm{m}$ (equal to the fibre radius used to obtain the PS(78k) curve) is added to Fig. 4.2 (Eq. 4.2 with $B = 0.74$, magenta thick dashed line). The identical fibre curvature ($r$ =const.) enables the direct comparison of the two curves with regard to the influence of slippage. We see that, in general, the amplification of the growth of the instability is more pronounced as the molecular weight and, hence, the slip length increases. This can be understood by the fact that the mobility of the PS melt at the solid/liquid interface increases with the slip length $b$

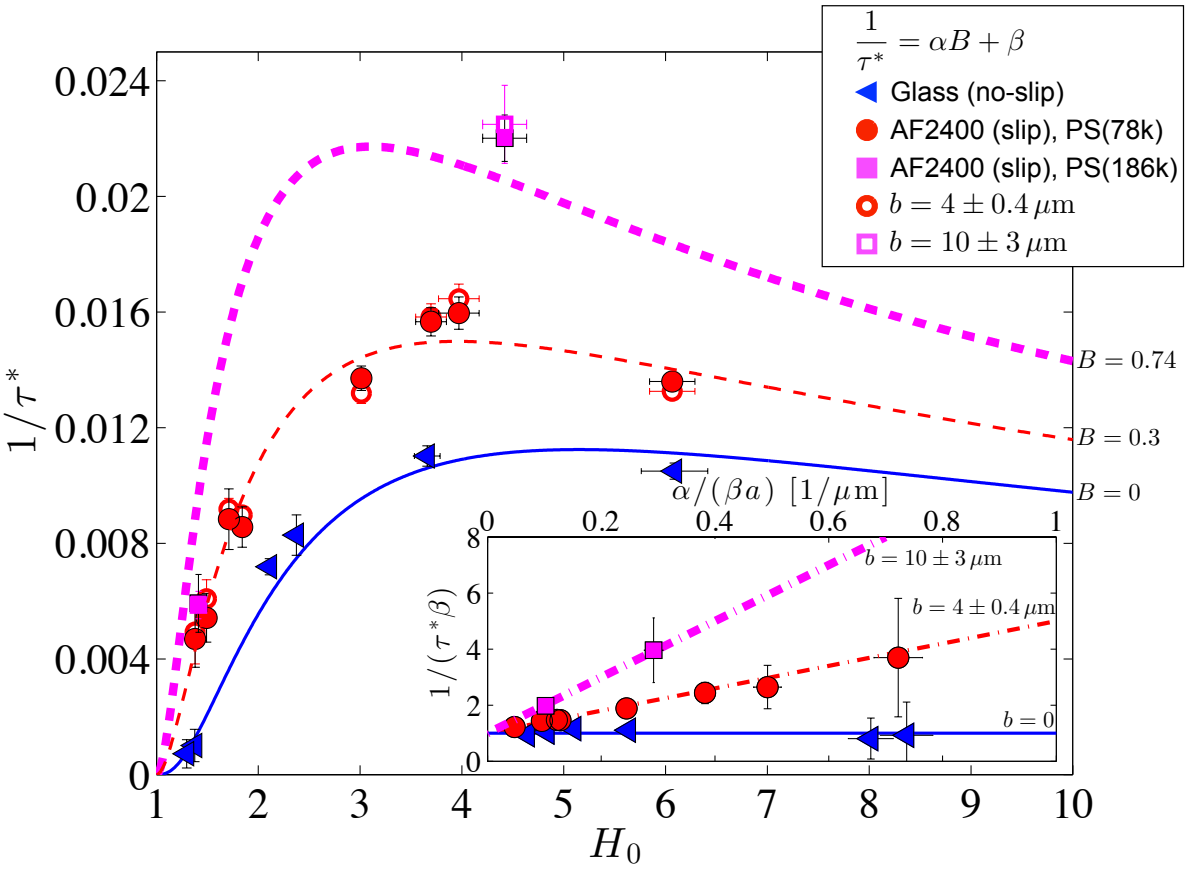


**Figure 4.2:** The influence of slip on the growth rate. The inset displays the dimensionless growth rate $1/\tau^*$ rescaled by the no-slip case $\beta$ for PS(78k) on glass and AF2400 fibres as well as PS(186k) on AF2400 fibres as a function of $\alpha/(\beta a)$, representing the geometry of the system (see Eq. 4.2). From a best linear fit to the respective data (dash-dotted lines) the slip length $b$ of PS(78k) and PS(186k) can be determined. The main plot displays the dimensionless growth rates $1/\tau^*$ of the fastest growing modes as a function of the dimensionless initial total radius $H_0 = e_0/r+1$ of the system (filled symbols). The theoretically predicted growth rates $1/\tau^*$ for the respective slip length values are calculated according to Eq. 4.2 by using the corresponding experimental geometry (open symbols). The solid line represents the theoretical curve for $B = 0$. In order to compare the course of the curves with respect to the used molecular weights, the theoretical curves are shown by the dashed lines using the respective slip length of $b = 4\,\mu$m for PS(78k) and $b = 10\,\mu$m for PS(186k), while the fibre curvature is kept constant ($r = 13.5\,\mu$m). The error bars are calculated from the error in the geometry and the inaccuracy of the growth rate measurements. Modified from [128].

[34, 98]. In addition, Fig. 4.2 shows that the maximum of $1/\tau^*$ for PS(186k) in comparison to PS(78k) is shifted to an even smaller value of $H_0$. As the fibre curvature of the presented

curves for $B = 0.3$ and $B = 0.74$ is constant, the enhancement of the mass transport at the interface for PS(186k) compared to PS(78k) is also responsible for the horizontal shift.

**Short Summary**

- The wavelength $\lambda^*$ of the fastest growing mode is unaffected by an increase in the slip length $b$, induced by a long-chained molecular weight. In excellent agreement with former experimental and theoretical results, presented in the **publication in ADDENDUM II**, the wavelength $\lambda^*$ grows linearly with the initial radius $h_0$ of the system.
- An influence of the increased slip length is, however, observed for the growth rates $1/\tau^*$ of the fastest growing modes. The comparison of $1/\tau^*$ for PS(78k) on glass (no-slip) and AF2400 fibres (slip) showed a slip-induced amplification of the growth of the instability. The results for PS(186k) on slip fibres reveal an additional enhancement of the RPI for a given geometry.

## 4.3 The influence of changing the origin of slippage

Based on the results concerning the RPI on AF2400 fibres, the question arises whether the origin of slip has an influence on the evolution of the RPI. So far, the presented results were obtained from measurements, where slippage is induced by the molecular weight [35]. From earlier works, we know that slippage can also be generated by the choice of the substrate, e. g. by silanizing the substrate with a hydrophobic self-assembled monolayer, here DTS (see Sec. 3.1.2) [34]. In order to study the influence of the origin of slip, the PS(78k) films were applied on glass fibres coated with DTS. Hence, slippage is now induced by both, the substrate as well as the entanglements [34, 35]. Using the same annealing temperature of $T = 180\,^{\circ}\mathrm{C}$ enables the direct comparison to the results for PS(78k) on glass and AF-coated fibres. Note that, in contrast to AF-coated fibres, the slip length $b$ on DTS substrates was found to exhibit a significant temperature dependence: for a given molecular weight, the slip length decreases with increasing the temperature [34].

Figure 4.3 displays the measured wavelength $\lambda^*$ of the fastest growing modes as a function of the initial total system radius $h_0$ for PS(78k) on DTS fibres (diamonds). In comparison, the results obtained for PS(78k) on glass (triangles) and AF2400 fibres (squares) as well as for PS(186k) on AF-coated fibres (circles), are shown. The dashed line represents again the theoretically predicted relation between the wavelength $\lambda^*$ and the system radius $h_0$, given by (see the **publication in ADDENDUM II**): $\lambda^* = 2\sqrt{2}\pi h_0$. From Fig. 4.3, we see that the wavelength $\lambda^*$ of the fastest growing modes is not affected by the origin of slip and increases linearly with the initial total radius $h_0$ of the fibre system. Hence, the spatial evolution of the RPI is invariant with respect to the mechanism, chosen to generate slippage.

The presented results concerning the growth rate $1/\tau^*$ of the fastest growing mode revealed an increase with increasing the slip length $b$, for a given system geometry $H_0$ (see Sec. 4.2). In analogy, Fig. 4.4 illustrates the measured growth rate data for PS(78k) on DTS fibres in comparison to PS(78k) on glass and AF2400 fibres as well as PS(186k) on AF-coated fibres. Equivalent to the results presented earlier in this chapter as well as in the **publication in**

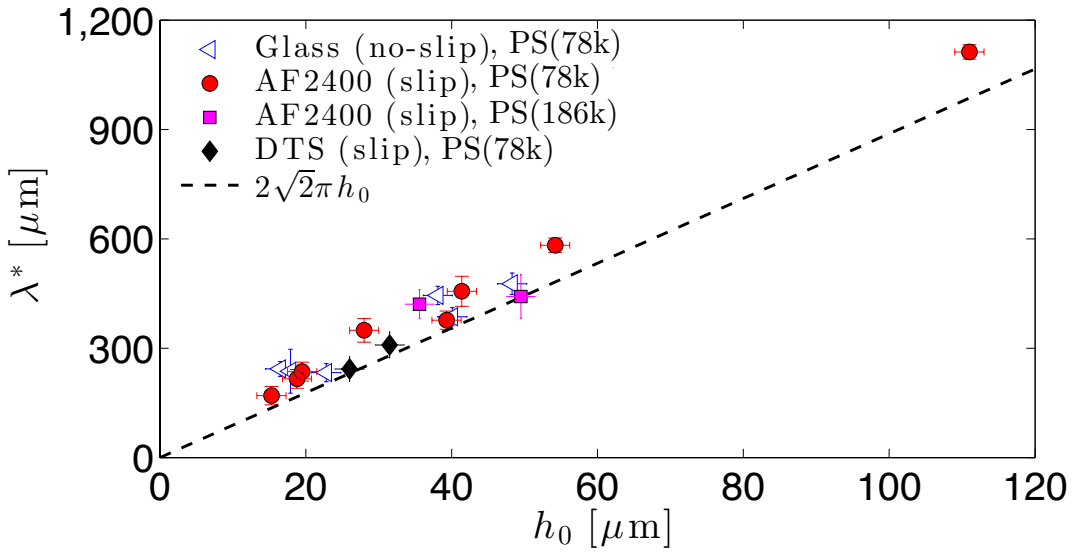


**Figure 4.3:** Wavelength $\lambda^*$ of the fastest growing mode as a function of the initial total radius $h_0$ for PS(78k) on glass, AF2400 and DTS fibres as well as PS(186k) on AF2400 fibres. The black dashed line represents the theoretical prediction (Eq. 4.1). The error bars are determined from the error in the geometry and the inaccuracy in the measurement of the wavelength. Modified from [128].

**ADDENDUM II**, the illustration of $1/\tau^*$ normalized by $\beta$ as a function of $\alpha/(\beta a)$ enables the determination of the slip length $b$ (see the inset of Fig. 4.4). From the best linear fit to the data for PS(78k) on DTS fibres, we determined a slip length of $b = 1.4 \pm 0.8\,\mu$m (see Eq. 4.2). For a detailed discussion of the slip length values we refer to chapter 6.

The main plot of Fig. 4.4 illustrates the measured dimensionless growth rates $1/\tau^*$ for PS(78k) on DTS fibres as a function of the dimensionless initial total radius $H_0$ (filled black diamonds), showing excellent agreement with the respective theoretically predicted values (open black diamonds), see Eq. 4.2. The experimental and theoretical results for PS(78k) on glass (triangles) and AF2400 fibres (circles) as well as for PS(186k) on AF-coated fibres (squares) are shown in comparison (see Fig. 4.4). In analogy to Fig. 4.2, the course of the $1/\tau^*(H_0)$ curves, with respect to the used molecular weights and substrates, is illustrated by typical theoretical curves (dashed lines), using the measured slip lengths, but for a constant fibre curvature of $r = 13.5\,\mu$m. Hence, the dimensionless slip length for PS(78k) on DTS fibres results in $B = 0.1$. The measured growth rates as well as the theoretically predicted curve for PS(78k) on DTS-coated fibres do additionally corroborate the influence of slip, in particular the influence of the amount of slip, on the temporal evolution of the RPI (see Fig. 4.4). As the mobility of the liquid molecules at the interface is lowered by the lowered slip length for PS(78k) on DTS in comparison to AF2400 fibres [34, 98], the RPI evolves more slowly on DTS fibres, for a given system geometry. In addition, the maximum of $1/\tau^*$ is shifted to a larger value of $H_0$. Although it is clear from the inset of Fig. 4.4 that the origin of slip is varied by using DTS-coated fibres, the characteristics of the spatial as well as the temporal evolution of the

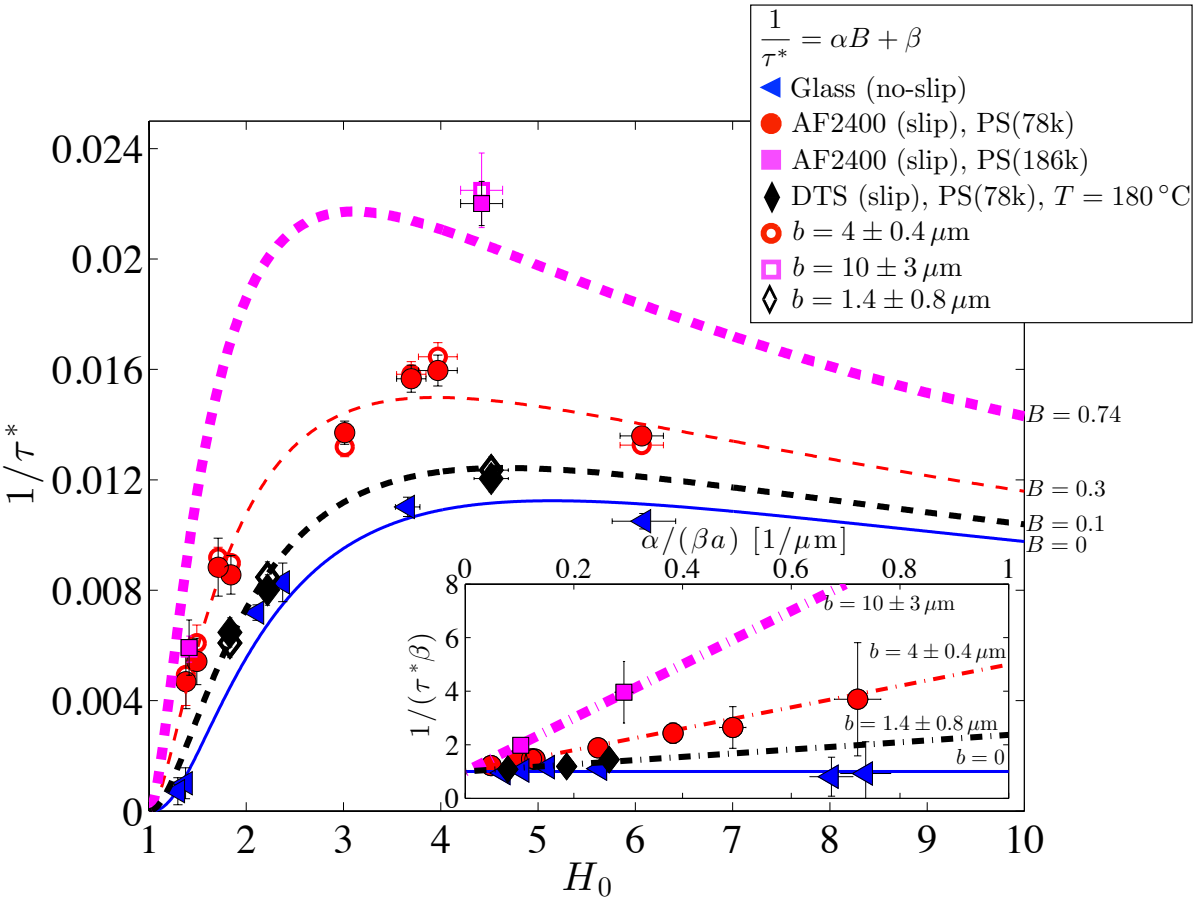


**Figure 4.4:** The influence of slip on the growth rate. The inset displays the dimensionless growth rate $1/\tau^*$ rescaled by the no-slip case $\beta$ for PS(78k) on glass, AF2400 and DTS fibres as well as PS(186k) on AF2400 fibres as a function of $\alpha/(\beta a)$, representing the geometry of the system (see Eq. 4.2). From a best linear fit to the respective data (dash-dotted lines) the slip length $b$ can be determined. The main plot displays the dimensionless growth rates $1/\tau^*$ of the fastest growing modes as a function of the dimensionless initial total radius $H_0 = e_0/r + 1$ of the system (filled symbols). The theoretically predicted growth rates $1/\tau^*$ for the respective slip length values are calculated according to Eq. 4.2 by using the corresponding experimental geometry (open symbols). The solid line represents the theoretical curve for $B = 0$. In order to compare the course of the curves with respect to the used molecular weights and substrates, the theoretical curves are shown by the dashed lines using the respective slip length of $b = 4\,\mu m$ for PS(78k) on AF2400 and $b = 1.4\,\mu m$ on DTS fibres as well as $b = 10\,\mu m$ for PS(186k) on AF2400 fibres, while the fibre curvature is kept constant ($r = 13.5\,\mu m$). The error bars are calculated from the error in the geometry and the inaccuracy of the growth rate measurements. Modified from [128].

RPI are not affected (see Figs. 4.3 and 4.4).

However, since both slip-inducing possibilities were combined (silane substrate and entanglements), it remains open whether slippage, purely induced by the choice of the substrate, in comparison to slippage generated by the molecular weight shows a difference in the evolution of the RPI. Results on the RPI of receding straight fronts in thin PS films on planar substrates provide evidence that the characteristic fingerprints of the RPI are identical for both slip mechanisms. For details the reader is referred to chapter 7.

**Short Summary**

- The aim of these series of experiments was to probe the effects of the origin of slip on the results described in the previous sections of chapter 4, where the slip was solely achieved by increasing the molecular weight. Here, a combination of both slip-inducing mechanisms - a silane substrate and entanglements - was used in order to vary the origin of slip.
- All results of Secs. 4.1 and 4.2 were corroborated: (i) the wavelength $\lambda^*$ of the fastest growing mode is not affected by the origin of slip. $\lambda^*$ grows linearly with the initial total system radius $h_0$ and (ii) the temporal evolution, i. e. the growth rate $1/\tau^*$, of the RPI is also unaffected by the mechanism chosen to induce slippage. Simply the lowered value of the slip length $b$ causes the instability to evolve more slowly, for a given system geometry.

# 5 Capillary droplet propulsion on a fibre

The present chapter depicts results on the dynamics of moving droplets on hydrophobized fibres, which are generated by taking advantage of the Rayleigh-Plateau instability (see Sec. 4 and the **publication in ADDENDUM II**). The first part covers the capillary-driven droplet motion which is exclusively governed by viscous dissipation. Section 5.2 deals with the influence of slippage at the fibre/liquid interface on the droplet motion. Here, a global analysis of the droplet dynamics is followed by a detailed examination of the local droplet speed. The local analysis of the dewetting speed is divided into two regimes: (i) the initial droplet motion regime, which is defined as the period between the onset of motion right after the formation of a contact line and the first coalescence event with a static droplet and (ii) the later stages of droplet motion. The resulting findings concerning the dewetting speed of the initial droplet motion regime enable the estimation of the respective slip lengths.

## 5.1 Droplet motion governed by viscous flow

The propulsion of liquid droplets, in general, is an intensively studied topic (see Sec. 2.6). Up to now, the motion of liquid droplets on fibres, where gravity is absent, has been studied by varying at least one parameter during the course of the experiments: either the liquid properties [118], the substrate composition [121] or the system geometry [119, 120]. In the **publication in ADDENDUM III**, we examine the motion of viscous liquid droplets on hydrophobized fibres while keeping those parameters constant in the different experiments. In the system studied, the droplets move due to an imbalance of contact angles: in order to generate droplets on a fibre, we utilized the fact that a homogeneous liquid film decays into a regular droplet pattern due to the Rayleigh-Plateau instability (cf. the **publication in ADDENDUM II**). As explained in Sec. 3.1.5, a moving droplet originates from the spontaneous formation of a three-phase contact line at one side of a droplet on a hydrophobic fibre. This process is accompanied by the adjustment of the contact angle to the receding contact angle $\theta_{\mathrm{rec}}$. At the other side of the droplet, however, the apparent contact angle remains constant and is equal to $\alpha$, with $\alpha < \theta_{\mathrm{rec}}$ (cf. Fig. 3.5). The resulting capillary imbalance at the two sides of the droplet provides the driving force, which causes the droplet to move along the fibre. Hence, the movement and the accumulation of the residual material by the moving droplet lasts as long as $\theta_{\mathrm{rec}} < \theta_{\mathrm{e}}$, with $\theta_{\mathrm{e}}$ being the contact angle of a droplet in equilibrium. We obtained $\theta_{\mathrm{rec}} = 60 \pm 5\,^{\circ}$ and $\theta_{\mathrm{e}} = 83 \pm 5\,^{\circ}$ (see Sec. 3.3.2), which is in excellent agreement with former studies on polymer films on planar hydrophobized surfaces, where $\theta_{\mathrm{e}}/\theta_{\mathrm{rec}} \approx \sqrt{2}$ has been shown as a fixed ratio between equilibrium and receding contact angle [17, 34, 138].

The dewetting process of the droplets was studied as a function of molecular weight $M_{\mathrm{w}}$ and temperature $T$. Therefore, the travelled distance $d(t) = |x_{\mathrm{c}}(t) - x_{\mathrm{c}}(t = 0)|$ of a droplet was

measured as a function of time $t$. A detailed description of the determination of the three-phase contact line position $x_c(t)$ is given in Sec. 3.3.2. Here, the molecular weight was varied from $M_w = 4.2\,\mathrm{kg/mol}$ to $78\,\mathrm{kg/mol}$. Plotting the temporal evolution of the dewetted distance $d(t)$ showed that the droplet motion is linear for all times $t$ and geometry invariant within the range of tested droplet sizes. Hence, from the slope of these curves, the mean value of the dewetting velocity $\overline{v}$ could be obtained for every experiment. The analysis of the entire motion process, however, revealed the alternation of the droplet speed around the mean value $\overline{v}$. In detail, during the accumulation of the residual thin film a constant dewetting speed was obtained. A coalescence event with a residual static droplet on the fibre, however, caused the contact angle at the three-phase contact line to decrease and, hence, the dewetting speed to increase. At the end of the coalescence process, the receding contact angle $\theta_{rec}$ readjusted and the speed decreased. For the reason of simplicity, the coalescence steps have been neglected. The evaluation of the local velocity $v$ considered only portions of the motion process, where the droplet consumed the residual thin film.

For the used molecular weights and temperatures, the inverse local dewetting velocity $1/v$ was found to scale linearly with viscosity $\eta$, which is consistent with the findings by Lorenceau *et al.* and Li *et al.* [119, 120] as well as the classical force balance model of a dewetting liquid wedge based on purely viscous dissipation by de Gennes [68, 69]. A single proportionality constant was determined to describe the data, consistent with an earlier work on the dynamics of holes in dewetting thin films (unentangled PS) on hydrophobized planar substrates, exhibiting a no-slip boundary condition at the solid/liquid interface [17]. For $M_w > M_c$ on AF-coated surfaces, however, we know that slippage is present and from the study on the RPI of viscous liquid films on AF2400 fibres a slip length of $b = 4 \pm 0.4\,\mu\mathrm{m}$ has been measured for PS(78k) (cf. the **publication in ADDENDUM II**). Hence, the fact that a universal constant of proportionality is capable to describe the measured droplet motion data suggests that viscous dissipation at the three-phase contact line dominates slippage at the solid/liquid interface. This can be understood by considering the range of measured droplet sizes: in all experiments, the maximal height $h_{max}(t)$ of the droplets is at least ten times larger than the respective slip length: $b/h_{max}(t) < 0.1$. Consequently, the effect of the enhanced mobility at the interface on the dewetting dynamics is negligible. The experimental details, an explicit description of the force balance model as well as a discussion of the results is given in the **publication in Addendum III**.

## 5.2 The influence of slippage at the solid/liquid interface on the droplet dynamics

In the light of technological applications, as e. g. the collection of water by using fibre networks and performing chemical reactions on small scales, an enhancement of the droplet dynamics on a fibre would be beneficial. As known from [35], the mobility of a PS melt at the solid/liquid interface can be enhanced by using high molecular weights on AF-coated surfaces. The results, presented in the **publication in ADDENDUM III**, showed that the droplet dynamics of PS(78k) on AF2400 fibres is governed by viscous dissipation, although PS(78k) exhibits a slip length of $b = 4.0 \pm 0.4\,\mu$m. Within the range of tested droplet sizes, the effect of the enhanced mobility for PS(78k) is negligible. Therefore, we studied the dewetting process of polystyrene droplets with a molecular weight of $M_w = 186\,$kg/mol and 390 kg/mol on AF2400 fibres. In the following, the molecular weights ranging from $M_w = 4.2\,$kg/mol$-78\,$kg/mol are referred to as 'short-chained PS' or 'short entangled PS chains'. $M_w = 186\,$kg/mol and 390 kg/mol are respectively named 'long-chained PS' or rather 'long entangled PS chains'.

In analogy to the experiments outlined in the **publication in ADDENDUM III**, Fig. 5.1 shows typical data for the travelled distance $d(t)$ of the three-phase contact line as a function of recording time $t$ for PS(186k) at $T = 200\,^\circ$C and $210\,^\circ$C as well as PS(390k) using $T = 210\,^\circ$C. The solid black lines indicate the respective linear best fit to the data with a fixed intercept at $d(t = 0) = 0$. Thus, the slopes represent the mean droplet speed $\overline{v}$ (see Tab. 5.1), including both processes: the accumulation of residual thin film and the coalescence steps with static droplets.

### 5.2.1 Global droplet dynamics

First, we focus on the motion of droplets with a molecular weight of $M_w = 186\,$kg/mol (see Fig. 5.1a). Note that the presented data has been obtained right after the formation of the three-phase contact line. The comparison of the global mean velocity $\overline{v}$ for two separate measurements using PS(186k) at $T = 200\,^\circ$C reveals a difference by a factor of $\sim 2$ (see Fig. 5.1a, symbols: $\Diamond$ and $\triangleleft$ and Tab. 5.1). Hence, in contrast to the results on dewetting droplets using PS with low molecular weights (see the **publication in ADDENDUM III**), this result indicates that the motion is not exclusively controlled by the viscosity $\eta$. From earlier studies on the dewetting process of liquid fronts on planar substrates exhibiting a slip boundary condition, it is known that the dewetting velocity is influenced by the material properties (as e. g. the viscosity $\eta$), the slip length $b$ and the width $w$ of the moving front (see Eq. 2.54) [34, 53, 66, 67, 68]. In particular, the inverse of the dewetting velocity $1/v$ is expected to scale with $w$ in the presence of hydrodynamic slip, for the same molecular weight and temperature. The analysis of the global dewetting process of PS(186k) droplets at $T = 200\,^\circ$C exhibits a velocity ratio of $\overline{v}_\Diamond/\overline{v}_\triangleleft = 2.4 \pm 0.6$. Measuring the initial widths $w(t = 0)$ of the respective droplets yields a ratio of $w_\triangleleft(t_0)/w_\Diamond(t_0) = 2.4 \pm 0.1$, suggesting a first agreement with earlier works (see Tab. 5.1).

In addition, Fig. 5.1a (symbols: $*$) shows the temporal displacement of a PS(186k) droplet at a temperature of $T = 210\,^\circ$C, corresponding to a change in the melt viscosity $\eta$. From

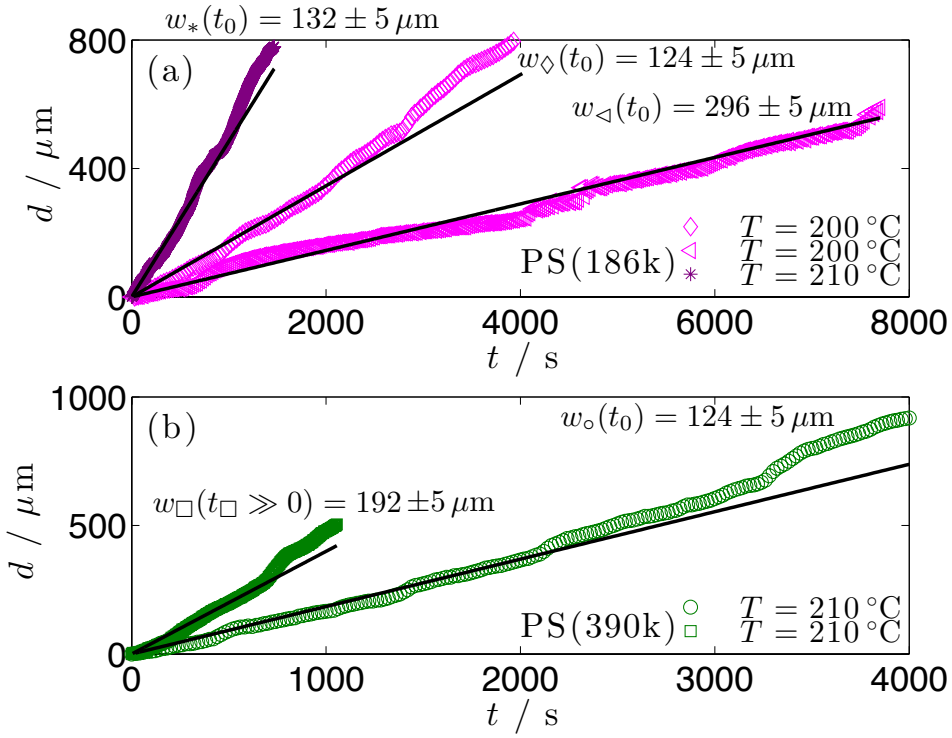


**Figure 5.1:** Travelled distance $d$ of the three-phase contact line on the fibre as a function of recording time $t$ for dewetting droplets using (a) PS(186k) at $T = 200\,^\circ$C and $210\,^\circ$C and (b) PS(390k) at $T = 210\,^\circ$C. The solid black lines indicate the respective linear best fit with a fixed intercept at $d(t = 0) = 0$. The slopes provide a measure for the global mean velocity $\overline{v}$ of the droplet. The four curves marked with the initial width $w(t_0)$ of the droplet represent data, which has been recorded right after the formation of the three-phase contact line (symbols: $\diamond, \triangleleft, *$ and $\circ$). The remaining data set (symbol: $\square$) was taken after the droplet has already accumulated a certain number of static droplets.

earlier works, it is know that the slip length of PS films on AF-coated substrates is not affected by temperature [35]. Thus, the difference in the curves shown in Fig. 5.1a are not due to a difference in slip. The initial width of the droplet at $T = 210\,^\circ$C equals $w_*(t_0) = 132 \pm 5\,\mu$m. By extrapolating the mean global droplet velocity $\overline{v}_* = 0.49\,\mu$m/s, which is obtained for a width of $w_*(t_0) = 132\,\mu$m, by using the inverse scaling of the velocity $1/v$ with the droplet width $w$, we obtain a velocity of $\overline{v}'_* = 0.52\,\mu$m/s, corresponding to a width of $w(t_0) = 124\,\mu$m. This accounts for the difference in the velocity caused by different droplet widths and enables the direct comparison to $\overline{v}_\diamond$ at $T = 200\,^\circ$C (with $w_\diamond(t_0) = 124 \pm 5\,\mu$m). The velocity ratio exhibits a value of $\overline{v}'_*/\overline{v}_\diamond = 2.98 \pm 0.60$. The respective viscosities $\eta_*$ and $\eta_\diamond$ were determined from independent viscosimeter and ellipsometric measurements [17] by projecting the data according to the WLF equation (Eq. 2.1) (similar to the **publication in ADDENDUM III**). The ratio accounts for $\eta_\diamond/\eta_* = 1.8$ (see Tab. 5.1). Considering the error originating from the uncertainty of the viscosity (at least a factor of 2), this finding corroborates the well-established velocity

| Symbol | $M_w$ / kg mol$^{-1}$ | $T$ / °C | $w(t_0)$ / $\mu$m | $\overline{v}$ / $\mu$m/s | $\eta$ / Pa s |
|---|---|---|---|---|---|
| $\Diamond$ | 186 | 200 | $124 \pm 5$ | $0.17 \pm 0.02$ | $7.6 \cdot 10^3$ |
| $\triangleleft$ | 186 | 200 | $296 \pm 5$ | $0.07 \pm 0.01$ | $7.6 \cdot 10^3$ |
| $*$ | 186 | 210 | $132 \pm 5$ | $0.49 \pm 0.05$ | $4.2 \cdot 10^3$ |
| $\circ$ | 390 | 210 | $124 \pm 5$ | $0.18 \pm 0.03$ | $5.1 \cdot 10^4$ |
| $\square$ | 390 | 210 | $(192 \pm 5)$ | $(0.40 \pm 0.04)$ | $5.1 \cdot 10^4$ |

**Table 5.1:** Mean global velocity $\overline{v}$, obtained from the slope of the linear best fit to the droplet displacement data with a fixed intercept at $d(t = 0) = 0$ (see Fig. 5.1). The initial width $w(t_0)$ of the droplets was measured right after the formation of a three-phase contact line. The values marked in brackets for PS(390k) at $T = 210\,°C$ (symbol: $\square$) were determined from a data set, which was taken after the droplet has already accumulated a certain number of droplets. The viscosity was determined from independent viscosimeter and ellipsometric measurements [17] by projecting the data according to the WLF equation (Eq. 2.1).

dependence on viscosity: $1/v \sim \eta$ for identical $b$ and $w$ (cf. the **publication in ADDENDUM III**) [119, 120].

Fig. 5.1b illustrates two typical data sets for dewetting droplets with a molecular weight of $M_w = 390\,\text{kg/mol}$, both at a temperature of $T = 210\,°C$. Note that the two curves differ in the point of time where the image recording was started. Here, $\overline{v}_\circ$ displays the mean droplet velocity obtained from displacement data recorded right after the formation of the contact line up to the final stage. For $\overline{v}_\square$, however, the data collection started after the droplet has already accumulated a certain number of static droplets. First, we want to focus on $\overline{v}_\circ$. The initial width of the droplet equals $w_\circ(t_0) = 124 \pm 5\,\mu\text{m}$. Hence, by taking advantage of the correlation between velocity and viscosity, the comparison between the velocity $\overline{v}_\circ$ of a PS(390k) and $\overline{v}_\Diamond$ corresponding to a PS(186k) droplet with the same initial droplet width of $124 \pm 5\,\mu\text{m}$, provides a direct measure for the influence of the increased chain length. The viscosity ratio is given by $\eta_\circ/\eta_\Diamond = 6.71$, whereas the ratio of the global mean velocities equals $\overline{v}_\Diamond/\overline{v}_\circ = 0.94 \pm 0.27$ (see Tab. 5.1). In consideration of $1/v \sim \eta$ (see the **publication in ADDENDUM III**) and the error originating from the uncertainty of the viscosity values, the matching velocity values indicate an enhancement of the dewetting dynamics for PS(390k) as compared to PS(186k) droplets, for a given initial droplet width $w(t_0)$. This finding yields a first evidence for the influence of the chain length, i. e. the presence and the influence of slip. For the detailed determination and discussion of the slip length values we refer to Secs. 5.2.2 and 6.

Regarding the dynamics of the entire dewetting process (symbols) with respect to the corresponding mean velocities $\overline{v}$ (solid lines), in general, shows that the motion is not linear over the entire range of recorded data. From earlier works, however, we know that with a given slip boundary condition the velocity slows down during the dewetting process. This can be understood by the growing width $w$ of the moving front due to material accumulation and the energy dissipation due to friction over $w$ (see Eq. 2.54) [34, 53, 66, 67, 68]. Fig. 5.1, however, does not reveal a decrease in the velocity although the droplet widths typically grow by a factor of 1.2 to 2 over the entire motion process. On contrary, for late times $t$, the data

shows even an enhancement of the local dewetting speed. For a detailed analysis of this effect we refer to Sec. 5.2.2.

The comparison of the data sets for PS(390k) at $T = 210\,^{\circ}\mathrm{C}$ (Fig. 5.1b) corroborates this trend: the displacement data of the droplet with $w_{\circ}(t_0) = 124 \pm 5\mu\mathrm{m}$ reveals a mean global velocity of $\overline{v}_{\circ} = 0.18 \pm 0.03\,\mu\mathrm{m/s}$. Note that the displacement data has been obtained from optical images which have been recorded right after the formation of the three-phase contact line. Analyzing the motion process of a droplet with the same molecular weight and temperature, which, however, has not been recorded right from the beginning, exhibits a mean global speed of $\overline{v}_{\square} = 0.40 \pm 0.04\,\mu\mathrm{m/s}$. The respective droplet width of $w_{\square}(t_{\square}) = 192 \pm 5\,\mu\mathrm{m}$ was measured from the first image of the time series, with $t_{\square} \gg 0$. Contradictory to what is known so far, the comparison of these results reveals a larger global mean dewetting velocity $\overline{v}$ for the droplet which exhibits a larger width $w$.

**Short Summary**

- Given the fact that the image recording of the droplet dewetting process starts right after the formation of the contact line, the inverse global mean velocity $1/\overline{v}$ scales with: (i) viscosity $\eta$, (ii) the initial droplet with $w(t = 0)$ and (iii) the inverse of the polymer chain length.
- Locally the motion dynamics may differ and droplets may even dewet faster although the width increases during the motion process.

The dynamics of droplets using a low molecular weight revealed a constant droplet velocity over the entire dewetting process (see the **publication in ADDENDUM III**). In order to understand the deviating behavior for droplets with a high molecular weight, the dewetting process of the PS(186k) and PS(390k) droplets will be investigated locally. In the following, the different regimes of the droplet motion (accumulation of the thin residual film and coalescence events) will be analyzed in detail.

### 5.2.2 Local droplet velocity

#### Initial droplet motion regime

We now focus on the initial local velocity $v_0$ of a dewetting droplet and compare the findings to the results presented in the **publication in ADDENDUM III**. $v_0$ is defined as the droplet speed during the first regime of the droplet motion process, which is the period between the onset of motion right after the formation of the three-phase contact line and the first coalescence event with a static droplet. In this regime, the moving droplet accumulates only the thin residual film with a typical thickness of $e_{\mathrm{res}} \sim 1\,\mu$m. As the moving droplet typically exhibits an initial width in the range of $w(t_0) = 100 - 320\,\mu$m, the increase in volume is negligible. Furthermore, Fig. 5.2 shows that the droplet motion is linear in time during this regime. Thus, the respective initial local velocity $v_0$ can be obtained from the slope.

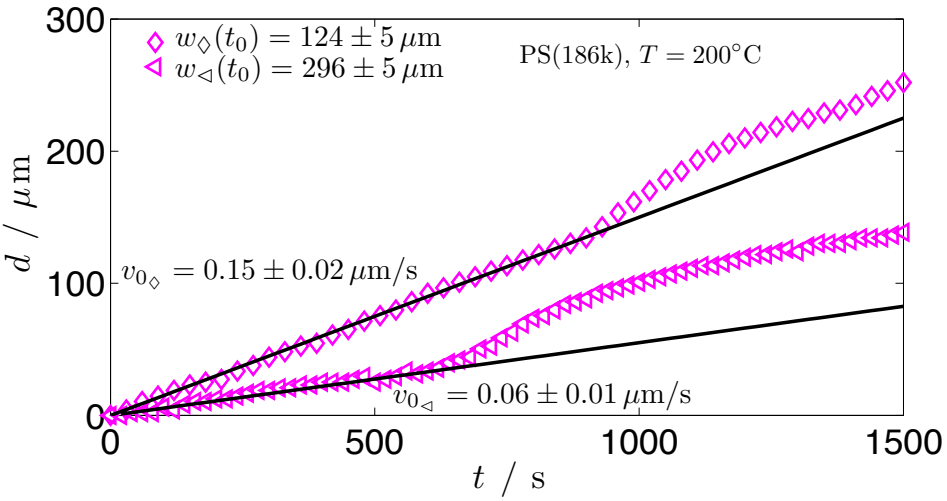


**Figure 5.2:** Travelled distance $d$ of the three-phase contact line as a function of time $t$ for PS(186k) droplets on AF2400 fibres with an initial width of $w_\diamond(t_0) = 124 \pm 5\,\mu$m and $w_\triangleleft(t_0) = 296 \pm 5\,\mu$m at a temperature of $T = 200\,°$C. Both data sets are obtained from optical micrographs, which were recorded right from the beginning of the motion process. The initial droplet motion is linear in time until the first coalescence event with a static droplet occurs. The slope of the best linear fit to the corresponding data provides the initial local droplet velocity $v_0$.

While the results presented in the **publication in ADDENDUM III** showed that the dewetting process of droplets with molecular weights ranging from 4.2 kg/mol to 78 kg/mol is dominated by viscous dissipation, the analysis of the global mean dewetting speed $\overline{v}$ for long entangled polymer chains indicates that the process might be influenced by slippage. As a consequence, both mechanisms are expected to be present, dissipation due to friction of the liquid molecules at the solid/liquid interface as well as viscous dissipation. Jacobs *et al.* derived a model to describe the growth of holes in thin films, which accounts for viscous flow and

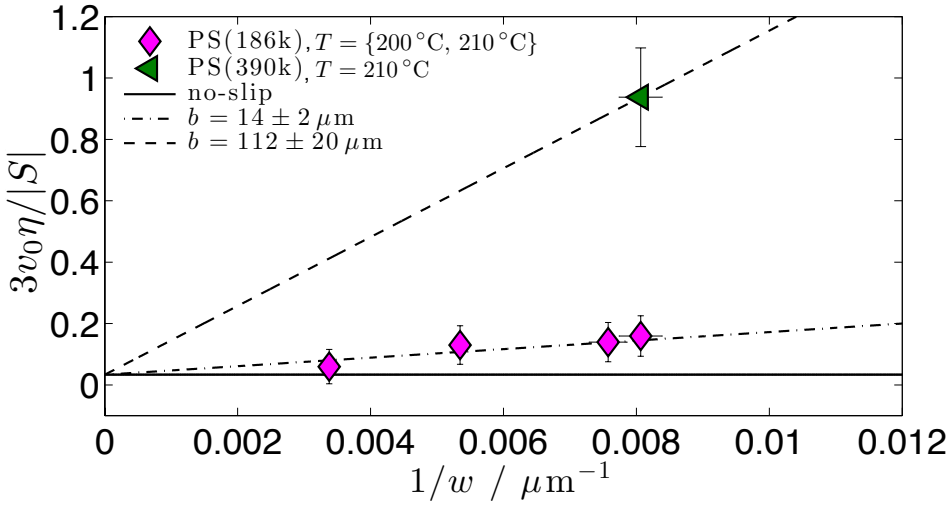


**Figure 5.3:** Representation of the measured initial dewetting velocity $v_0$ normalized by $(3\eta)/|S|$ as a function of $1/w$. According to Eq. 5.2, the slope of the best linear fit to the data enables the direct estimation of the respective slip length $b$. Hence, the no-slip case ($b = 0$) yields a constant value, which is equal to $(3v_0\eta)/|S| = 0.033$. In order to fit the data, the $y$-axis intercept is fixed at 0.033, accounting for the viscous-dominated regime for initially large droplets ($w \to \infty$). The slip length of PS(186k) can be estimated to equal $b = 14 \pm 2\,\mu$m and the approximation for PS(390k) yields $b = 112 \pm 20\,\mu$m.

slippage by additively superposing the velocities [66] (see Sec. 2.4):

$$v = v_\mathrm{v} + v_\mathrm{s} = \frac{|S|\theta_\mathrm{rec}}{3l}\frac{1}{\eta} + \frac{|S|b}{3w}\frac{1}{\eta}. \tag{5.1}$$

As the model is derived by a power balance, where the acting forces are weighted per unit length, Eq. 5.1 is invariant with regard to the length of the contact line (here the fibre radius $r$). Hence, the model (Eq. 5.1) can directly be applied in order to analyze the dewetting dynamics of droplets on fibres.

From the results on dewetting droplets using short polystyrene chains, which revealed purely viscous flow only, the corresponding constant pre factor $1/A = (|S|\theta_\mathrm{rec})/(3l)$ is already known (see the **publication in ADDENDUM III**). The spreading parameter $|S| = |\gamma_\mathrm{lv}(\cos\theta_\mathrm{e} - 1)|$ or rather the equilibrium contact angle $\theta_\mathrm{e}$ as well as the width $w$ of a droplet display experimental quantities which can be determined right from the optical micrographs. In analogy to the **publication in ADDENDUM III**, the viscosities (see Tab. 5.1) are obtained from independent viscosimeter and ellipsometric measurements by projecting the data according to the WLF equation (Eq. 2.1) [17]. Hence, the slip length $b$ is the only free parameter in Eq. 5.1.

A dewetting scenario which is exclusively governed by viscous dissipation represents a no-slip situation, $b = 0$. The dewetting velocity is entirely independent of the droplet width

$w$ and can be written as: $v = (|S|\theta_{\mathrm{rec}})/(3l\eta)$. The results presented in the **publication in ADDENDUM III** revealed a linear dependence between $v$ and $1/\eta$ with the universal prefactor of $(|S|\theta_{\mathrm{rec}})/(3l) = 1/A = 1/(3900 \pm 300)\mathrm{N/m}$. Equation. 5.1 can be converted as follows:

$$\frac{3v\eta}{|S|} = \frac{\theta_{\mathrm{rec}}}{l} + \frac{b}{w}. \tag{5.2}$$

As a consequence, the illustration of $(3v_0\eta)/|S|$, with the initial droplet velocity $v_0$, as a function of $1/w$ for PS(186k) and PS(390k) in Fig. 5.3 enables us to gain information about the influence of slip on the dewetting process. The slope of the best linear fit to the data provides an estimate of the respective slip length (see Eq. 5.2 and Fig. 5.3) [34]. Applying the proportionality constant $A = 3900 \pm 300$ m/N for the no-slip case ($b = 0$), where only viscous dissipation is present, yields a constant value of $(3v_0\eta)/|S| = \theta_{\mathrm{rec}}/l = 3/(A|S|) = 0.033$ (solid black line in Fig. 5.3). As the extrapolation for infinitely large droplet widths $w$ results in a diminished influence of slippage, the finite value of $(3v_0\eta)/|S|$ is equal to the one obtained for the no-slip case [34]. Therefore, the $y$-axis intercept, where $w \to \infty$, is fixed at $(3v_0\eta)/|S| = 0.033$ during the fitting procedure. Thereby, we obtain a slip length of $b = 14 \pm 2\,\mu$m for PS(186k) and PS(390k) accounts for $b = 112 \pm 20\,\mu$m. A detailed discussion of the slip length values in comparison to former results is presented in chapter 6.

**Entire motion process**

In the following paragraphs, the entire droplet motion process will be analyzed in detail. As discussed earlier in the text, the droplet dynamics is not linear over the entire range of recorded data and the droplet speed does even show an increase for late times $t$ (see Fig. 5.1). By having a closer look at one exemplary data set showing the local velocity $v$ as a function of time $t$, several distinct regimes can be identified. Fig. 5.4 displays a typical data set of a PS(186k) droplet with an initial width of $w(t_0) = 85 \pm 5\,\mu$m at $T = 200\,^{\circ}$C, obtained from images which were recorded right after the formation of the contact line. Similar to what we already discussed for the first regime, the droplet motion is linear in time and the initial local speed $v_0$ can be determined from the slope of the curve (see Fig. 5.1a). Whenever the moving droplet (M) coalesces with one of the static droplets (A, B, C, D), a steep increase in the dewetting speed can be observed (see the marked regions A, B, C and D in Fig 5.4a). In analogy to the measurements of moving droplets with a low molecular weight, this effect can be understood by the sudden decrease in the receding contact angle $\theta_{\mathrm{rec}}$ as two droplets come into direct contact (cf. the **publication in ADDENDUM III**). The results, presented in the **publication in ADDENDUM III**, showed that the recuperation of the receding contact angle at the end of the droplet merging process is accompanied by a decrease in the coalescence velocity. On the contrary, the droplet motion process, using long entangled PS chains, does not reveal a deceleration of the coalescence speed, although $\theta_{\mathrm{rec}}$ readjusts. The coalescence dynamics is linear in time (see Fig. 5.4c).

Each coalescence step is followed by a region where the droplet moves along the fibre while accumulating residual thin film only. Fig. 5.4a shows that the motion of the droplet in these regions is linear in time and the black solid lines indicate the respective local velocity $v_{\mathrm{i}}$. The

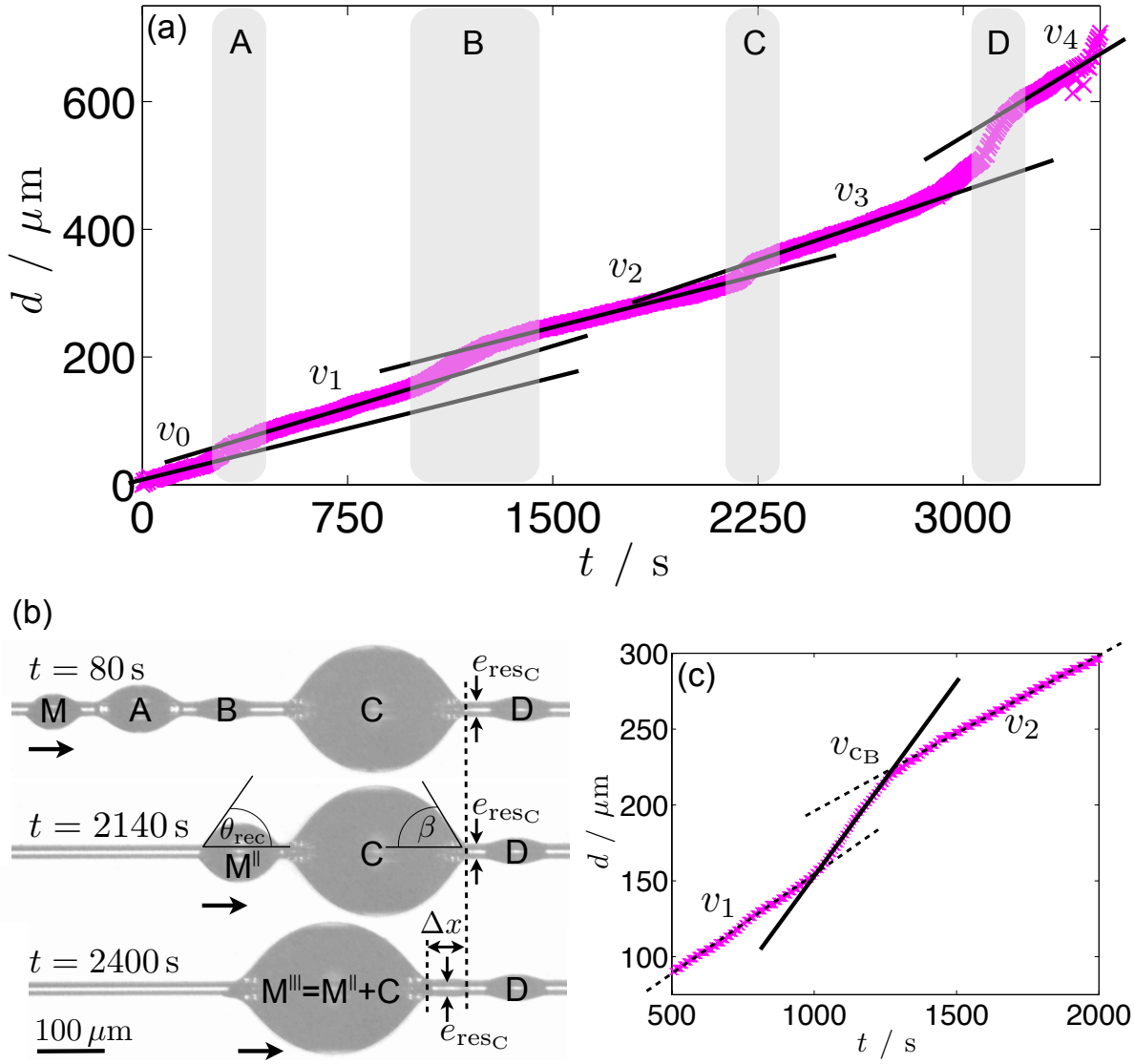


**Figure 5.4:** Typical data set of a receding PS(186k) droplet on a hydrophobized fibre at a temperature of $T = 200\,^{\circ}\mathrm{C}$. The initial droplet width equals $w(t_0) = 85 \pm 5\,\mu$m. (a) Dewetted distance $d(t)$ of the contact line as a function of time. The solid black lines indicate the best linear fit to the regions, where the moving droplet accumulates only the residual film. The regions named A, B, C and D mark the coalescence events with static droplets. (b) Illustration of the corresponding optical micrographs at various times $t$, indicating parameters which are relevant for the coalescence events. (c) Droplet displacement data $d(t)$ during the coalescence of the moving droplet with the static droplet named B. The solid black line represents the best linear fit to the data of the coalescence regime. The slope provides a measure for the coalescence velocity $v_{\mathrm{c}}$.

comparison of the local speed before and after the coalescence with a static droplet, however, does not reveal a monotonic trend. Fig. 5.4a shows that the local velocity, measured before and after coalescence, may increase ($v_2$ and $v_3$) or decrease ($v_1$ and $v_2$).

A fundamental difference regarding the dewetting process of long- and short-chained PS droplets is given by the dynamics of the droplet coalescence events themselves. Droplets with short chains showed the exact same coalescence behavior for all experiments with a constant viscosity $\eta$. The use of long PS chains, however, reveals variations in the coalescence event. These variations become noticeable by comparing the time intervals $\Delta t$ as well as the evolution of $d(t)$ for the single coalescence steps (see marked regions in Fig. 5.4a). Hence, the coalescence speed $v_c$ of two droplets differs significantly. Furthermore, we obseverd the displacement of an actual static droplet towards the moving droplet in case of small moving droplets coalescing with bigger static ones. This can be understood by considering the respective contact angles of the merging droplets. Whereas a moving droplet exhibits a constant receding contact angle of $\theta_{rec}$, the apparent contact angle $\beta$ of the static droplets varies (see Fig. 5.4b). Note that the droplets were generated by taking advantage of the RPI, i. e. the droplets grew over time as a result of the decaying liquid cylinder. As a consequence, the apparent contact angle $\beta$ of these droplets increases during the growth of the instability (see Sec. 5.1). Hence, big droplets may exhibit a contact angle $\beta$ which is larger than $\theta_{rec}$.

The direct contact between the receding and the static droplet with a significant difference in the droplet radii $R$ (see Fig. 5.4b) is accompanied by a large pressure difference (see Eq. 2.80). This, in turn, causes a sudden increase in the driving force. As a consequence, the bridge in between the two droplets levels rapidly while probably benefitting from a significant amount of hydrodynamic slippage at the solid/liquid interface (see Fig. 5.3). Nevertheless, the receding droplet has to overcome the remaining viscous dissipation, located at the three-phase contact line. The static droplet, however, decays into the thin residual film with the apparent contact angle $\beta$. The combination of a smooth decay into $e_{res}$ and $\theta_{rec} \leq \beta$ (see Fig. 5.4b, here: $\theta_{rec} = 58 \pm 3\,^\circ$ and $\beta = 60 \pm 3\,^\circ$) makes it energetically more favorable for the static droplet to move towards the receding droplet at the beginning of the coalescence process, as a response to the large driving force (see Fig. 5.4b) [67, 68, 69]. This effect might be enabled by the presence of a slip boundary condition.

As a result of the sudden displacement, the 'static' droplet leaves behind a residual film, which is thicker than the typical residual film height of $e_{res} \sim 1\,\mu$m. As an example, Figure 5.4b displays optical images, showing the positions of moving (M, M$^{||}$ and M$^{|||}$) and static droplets (A, B, C and D) on a fibre recorded after $t = 80\,$s, 2140 s and 2400 s. For $t = 80\,$s and $t = 2140\,$s, the residual film height, located to the right-hand side of the big static droplet (C), equals $e_{res_C} = 1\,\mu$m (see Fig.5.4b). The situation at $t = 2400\,$s shows that the static droplet (C) has been shifted towards the moving droplet by a distance $\Delta x$ in consequence of the coalescence of the droplets M$^{||}$ and C. In addition, the residual film height $e_{res_C}$ increased by a factor of $\sim 2$ due to material left behind by the 'static' droplet.

The comparison between the dewetting process of droplets with short and long entangled PS chains reveals significant differences with respect to the local droplet velocity $v_i$, the coalescence dynamics as well as the influence of the coalescence event on the residual film height $e_{res}$. Table 5.2 summarizes the results on calculating the upper limit estimation of the Weissenberg

| $M_w$ / kg mol$^{-1}$ | $T$ / °C | $\dot{\gamma}_{max}$ / s$^{-1}$ | $\tau$ / s | $Wi$ |
|---|---|---|---|---|
| 186 | 200 | 0.29 | 0.13 | 0.0387 |
| 186 | 210 | 0.61 | 0.072 | 0.0441 |
| 390 | 210 | 0.23 | 0.92 | 0.2116 |

**Table 5.2:** Upper limit estimation of the Weissenberg number $Wi$ for the studied molecular weights and temperatures. The maximum strain rate is given by $\dot{\gamma}_{max} = v_{max}/e_{res}$, where $v_{max}$ displays the fastest velocity and $e_{res}$ represents the corresponding residual film height. For PS(390k) at $T = 130\,°C$, Bach *et al.* measured a relaxation time of $\tau = 11300\,s$ [139]. Projecting this value according to the WLF equation (Eq. 2.1) yields the estimated relaxation times $\tau$.

number $Wi$ for the different molecular weights and temperatures, in order to determine the actual influence of viscoelastic effects, which might be induced by the use of long entangled PS chains. As for all experiments $Wi \ll 1$, viscoelastic effects can safely be excluded.

Figures 5.1 - 5.4 indicate that the initial motion of the droplets is controlled by slippage and $v_0$ is in good agreement with Eq. 5.1. The first deviation from this behavior of the local speed $v$ occurs right after the coalescence of two droplets. In addition, the local velocity $v$ changes subsequent to every coalescence event (see Fig. 5.4a). The resulting dewetting speeds $v_i$, however, do not follow the trends suggested by the slip model, i. e. Eq. 5.1. Hence, with respect to Fig. 5.4a, the local velocity $v$ might be linked to the preceding coalescence scenario.

In order to gain information about the coalescence events, the velocity $v_c$ of two merging droplets is analyzed. In analogy to the measurement of the local dewetting velocity $v$, the coalescence speed is obtained from the three-phase contact line displacement data $d(t)$ during the regime of coalescence (see Fig. 5.4c).

Figure 5.5 illustrates the local velocity $v$ as a function of the speed $v_c$ of the preceding coalescence event for PS(186k) at $T = 200\,°C$ and $T = 210\,°C$ as well as PS(390k) at $T = 210\,°C$ (obtained from the data shown in Fig. 5.1). Note that the local velocity $v$ which corresponds to the limiting case of $v_c = 0$ is equal to the initial droplet velocity $v_0$, which can directly be measured from the first regime of the droplet motion (see earlier in this paragraph). The presented velocity data indicates a linear scaling between both quantities: the faster the coalescence speed $v_c$, the faster the subsequent dewetting velocity $v$. In addition, the slopes of the linear best fit to the curves yield roughly the same proportionality constant of $0.17 \pm 0.02$ for all data sets, which suggests a universal relation between $v$ and $v_c$.

According to the presented slip model (Eq. 5.1), three potential reasons may be responsible for a variation in the dewetting dynamics: (i) the dependence of the local dewetting velocity $v$ on the width $w(t)$ of the receding droplet, (ii) a shear rate dependent viscosity $\eta(\dot{\gamma})$ and (iii) a shear rate dependent apparent slip effect. The influence of the droplet width $w(t)$ on the local dewetting velocity $v$ can safely be excluded for all presented measurements: in contrast to earlier studies [34, 66], the droplet displacement data $d(t)$ shows an increase of the local speed $v$ over the entire dewetting process (see Figs. 5.1, 5.2 and 5.4). According to Eq. 5.1, however, one would expect the droplet velocity to consistently decrease as a result of the uptake of liquid volume and increase of the width $w(t)$, rather than increase. In addition,

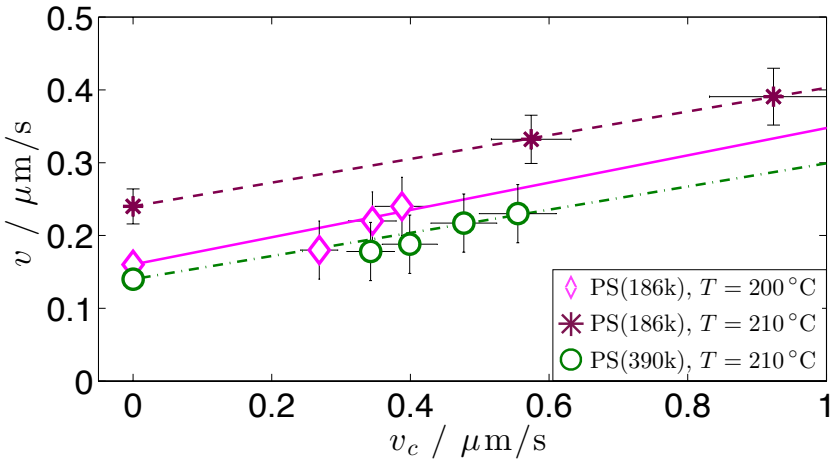


**Figure 5.5:** Local velocity $v$ of dewetting droplets plotted versus the speed $v_c$ of the preceding coalescence event for PS(186k) at $T = 200\,^{\circ}\mathrm{C}$ and $T = 210\,^{\circ}\mathrm{C}$ and PS(390k) at $T = 210\,^{\circ}\mathrm{C}$. The lines illustrate the linear best fits to the data. The representation suggests a linear scaling between $v$ and $v_c$ with a universal constant of proportionality.

the upper limit estimation of the Weissenberg numbers, which relate the time scale of stress relaxation $\tau$ with the time scale of the applied shear, clearly reveal $Wi \ll 1$ for all experiments (see Tab. 5.2). Hence, viscoelastic effects, that is the dependence of the viscosity on the coalescence-induced shear rate, can also be excluded. Consequently, based on our current knowledge, the presented variation of the dewetting speed $v$ as a function of the preceding coalescence velocity $v_c$ suggests a first indication of a shear-dependent apparent slip effect (see Sec. 2.2.3). In case of apparent slip the velocity of the molecules at the interface is zero, but a considerable slip length is measured. The presented experiments do, however, not allow to access the absolute value of the velocity at the interface. Hence, the detailed understanding of the mechanisms, which govern the droplet propulsion dynamics using long entangled PS, requires more experiments: a systematic variation of the shear rate $\dot{\gamma}$ via a variation of the viscosity $\eta$, for a constant molecular weight and a constant initial droplet width $w(t_0)$ may help to gain information about the interactions at the interface.

**Short Summary**

- The local dewetting process of droplets with long entangled PS chains reveals three significant characteristics: (i) The local droplet velocity $v$, measured during the accumulation of the residual film $e_{res}$, exhibits variations over the entire experiment. (ii) The travelled distance $d(t)$ is linear in time during the entire coalescence regime. The coalescence speed $v_c$ varies for the different coalescence events. (iii) A displacement towards the receding droplet is observed for static droplets with a contact angle $\beta$, which is larger than the receding contact angle $\theta_{rec}$.
- By applying the universal constant of proportionality, obtained for low molecular weights (see Sec. 5.1 and the **publication in ADDENDUM III**), the analysis of the initial

local dewetting velocity $v_0$ (during the motion regime beginning with the formation of the contact line until the first coalescence event) enables the direct estimation of the slip length $b$ from the slip model (Eq. 5.1).

- The local dewetting velocity $v$ subsequent to any coalescence event does not follow the trend suggested by Eq. 5.1. On the contrary, the data indicates a linear relation between the local dewetting velocity $v$ and the preceding coalescence speed $v_c$.

# 6 Comparison of slip lengths obtained from different studies

The results presented in the **publication in ADDENDUM II** and Sec. 4.2 show that studying the RPI of viscous liquid PS films with varying molecular weights on hydrophobized fibres provides a possibility to determine the slip length $b$. In addition, the investigation of the capillary droplet propulsion process on AF2400 fibres using long-chained PS melts enables us to estimate $b$ from a simple model based on a power balance (see Sec. 5.2). Figure 6.1 summarizes the measured values of the slip length $b$ as a function of the molecular weight in comparison to results obtained from analyzing both, the hole growth dynamics and the rim profiles of holes in dewetting thin PS films on planar AF1600 substrates. For $M_w < M_c$, the analysis of hole growth and rim profile measurements provide constant slip lengths in the range of 10 to 100 nm. In case of large $M_w$, the slip length $b$ was, however, found to increase with a power of 3 with respect to $M_w$ (stars and diamonds in Fig. 6.1), which is in excellent agreement with the theoretical prediction by de Gennes (black solid line in Fig. 6.1) [52]. Keeping the value for $a = 3\,\text{Å}$ from the literature [52], the entanglement length $N_e$ was, however, found to be increased by roughly a factor of $\sim 2$ for the hole growth data and a factor of $\sim 3$ analyzing the rim profiles compared to the bulk ($N_e = 163$) [140]. For further details concerning the reduction of the entanglement length in the vicinity of an interface the reader is referred to [35, 56, 140].

In general, Figure 6.1 shows that the slip lengths obtained from four different measurements are consistent and reveal the same trend with respect to the molecular weight: $b \sim M_w^3$. However, the slip length values obtained from measurements on the growth of holes in thin films, the propulsion of droplets and the RPI on fibres show larger values in comparison to slip lengths measured by studying rim profiles of dewetting holes. The conceptional differences between the different experimental techniques and their potential implications on the quantification of the slip length will be discussed in the following.

In Fig. 6.1, we see that the slip length, obtained from studying the motion of droplets on fibres depends on the molecular weight exact the way de Gennes predicts (Eq. 2.25) [52]. The best linear fit to the data yields an entanglement length of $N_e = 353$, while keeping $a$ from the literature [52]. The slip lengths as well as the length of the inter-chain entanglements $N_e$ are in excellent agreement with the values obtained from the analysis of the hole growth data (see Fig. 6.1). This can be understood by the fact that the same model was applied to analyze the data (see Eq. 5.1). Thereby, the moving droplet as well as the dewetting rim surrounding the hole are characterized by a receding wedge-shaped liquid front. The model assumes that the friction of the liquid molecules at the solid/liquid interface is homogeneous and that the entire contact area between the receding front and the substrate contributes to the dissipation. In addition, both dewetting scenarios exhibit the same capillary driving force. As the driving force

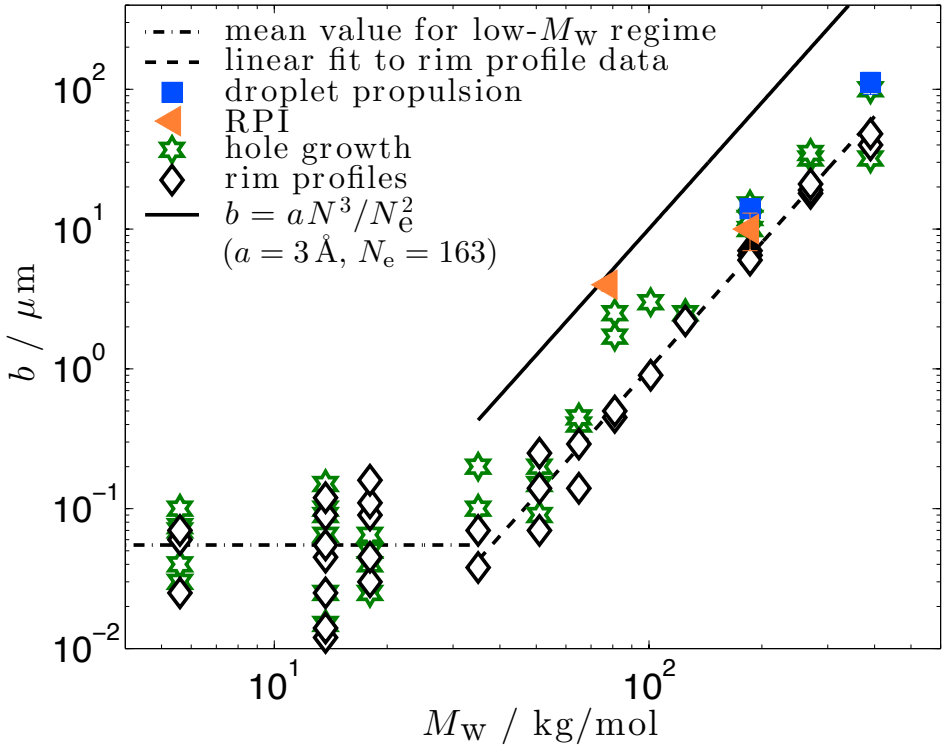


**Figure 6.1:** Double-logarithmic representation of the slip length $b$ obtained from different measurement techniques as a function of the molecular weight $M_w$: mean values for $b$ obtained from the capillary droplet propulsion and the RPI on AF2400 fibres as well as separate slip length values measured from the hole growth and the rim profile analysis of holes in dewetting thin films on planar AF1600 substrates. The solid black line represents the model by de Gennes using the bulk entanglement length of $N_e = 163$ for PS [52]. The mean value for the low molecular weight regime, combining the results of the hole growth and rim profile analysis, is illustrated by the dash-dotted line. The dashed line shows the best linear fit to the rim profile data, exhibiting an increased entanglement length of $N_e = 517$. Data obtained from the hole growth and the rim profile analysis is adapted from [140].

as well as the dissipated energy are weighted per unit length, the applied model is invariant with respect to the length of the three-phase contact line. Hence, the 2D model is valid for both geometries.

Slip lengths obtained from analyzing the motion of droplets on fibres and the growth of holes in thin films typically reveal larger values in comparison to slip lengths measured by studying rim profiles (see Fig. 6.1). In the following, we outline a potential hypothesis to explain the systematic shift to larger values, when determining the slip length $b$ from experiments concerning moving droplets and the growth of holes: both geometries, a moving droplet on

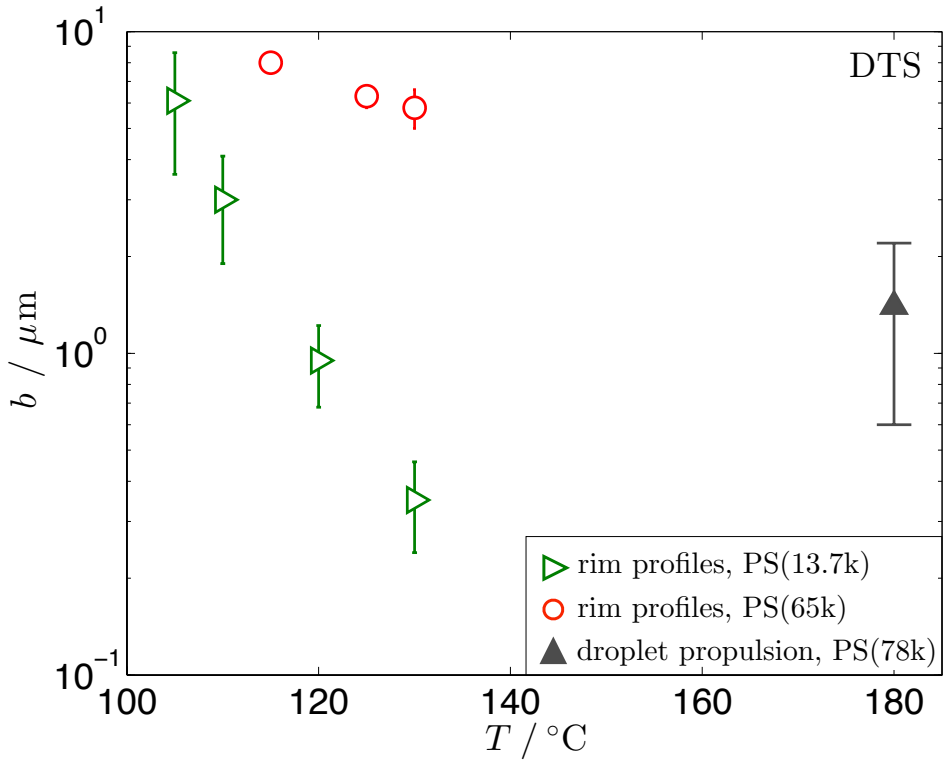


**Figure 6.2:** Slip length $b$ as a function of temperature $T$ for different molecular weights on DTS substrates. The values for PS(13.7k) and PS(65k) were obtained from analyzing the rim profiles of dewetting holes in thin films on planar DTS substrates [19]. The value for PS(78k) is measured from the RPI on a fibre (see Sec. 4.3). The data for PS(13.7k) and PS(65k) is adapted from [19].

a fibre as well as a dewetting hole in a film, can be described by the same theoretical model (Eq. 5.1), which is derived by assuming a superposition of viscous flow and slippage [66]. The lateral scale of slippage is estimated by the width $w$ of the droplet or rather the rim. Note that, in analogy to the definition of the width $w$ of a receding rim (the width equals the horizontal distance between the three-phase contact line and the position at the wet side where the rim height equals $1.1h_0$), the width $w$ of a moving droplet is given by the horizontal distance between the contact line and the position where the droplet merges into the residual film (see Sec. 3.3.2). Hence, the determination of the slip length by applying this model is significantly influenced by the entire extent of the liquid wedge $w$. On contrary, the analysis of rim profiles is only sensitive to the side of the liquid wedge, where the front merges into the residual film [140]. Furthermore, we note that assuming the lateral extent of slip being equal to the rim width $w$ displays only a rough estimate. If the lateral extent of slippage is actually systematically larger than the width $w$, the slip length values calculated from Eq. 5.1 would be too large.

With regard to the experiments on the evolution of the RPI, the fundamental difference in comparison to the other studies, presented in Fig. 6.1, is given by the underlying model to

determine the slip length. As discussed, slip length values from hole growth, droplet propulsion as well as rim profile data are determined from analyzing the dynamics and respectively the decaying rim shape of a dewetting front. In case of the RPI of a viscous film on a fibre, the slip length is, however, measured from the growth of the amplitude during the initial regime of the RPI. As stated above, the model applied to analyze the droplet propulsion and the hole growth data, is sensitive to the rim width $w$, with respect to the lateral extent of slippage. The analysis of the rim shapes is sensitive to the side, where the front decays into the residual film. The model which is applied to investigate the RPI is not restricted in terms of the lateral extent of slippage. Hence, scatter in the slip length data can be understood by the outlined fundamental differences between the different experimental techniques and applied models (see Fg. 6.1).

The results concerning the RPI on a fibre revealed a significant change of the slip length $b$ for changing the substrate (see Sec. 4.3). Whereas for PS(78k) at $T = 180\,^{\circ}\mathrm{C}$ on AF2400 fibres, the slip length was found to equal $b = 4.0 \pm 0.4\,\mu\mathrm{m}$, the same PS films using the identical temperature exhibit a slip length of $b = 1.4 \pm 0.8\,\mu\mathrm{m}$, if applied to DTS-coated fibres. Note that by using PS with a molecular weight of $M_\mathrm{w} = 78\,\mathrm{kg/mol}$ on DTS substrates, slippage is induced by both, the substrate as well as the entanglements [34, 35]. As discussed in Sec. 4.3 and chapter 7, the evolution of the RPI is not affected by the variation of the origin of slippage. Additionally, we stress the fact that in contrast to AF-coated substrates, the slip length $b$ on DTS substrates has shown a significant temperature dependence: for a given molecular weight, $b$ decreases with increasing temperature (see Fig. 6.2) [34]. From Fig. 6.2 we see that, with respect to the temperature dependence, the obtained slip length value of $b = 1.4 \pm 0.8\,\mu\mathrm{m}$ for PS(78k) at $T = 180\,^{\circ}\mathrm{C}$ is in excellent agreement with former works on the dewetting of holes in thin PS(65k) films [19].

**Short Summary**

- Both physical phenomena, the Rayleigh-Plateau instability of a viscous liquid film on a fibre as well as the motion of droplets on a fibre, induced by capillary forces, provide a robust and reliable method to determine the slip length.
- In case of AF-coated substrates, the measured slip lengths are consistent with former results obtained from analyzing the growth of holes and the shape of a rim profile surrounding a hole in thin films. Within the experimental error, the slip lengths reveal the same trend with respect to the molecular weight: $b \sim M_\mathrm{w}^3$ for $M_\mathrm{w} > M_\mathrm{c}$.
- With respect to the temperature dependence of the slip length on DTS substrates, the slip length measured from the RPI on a fibre shows excellent agreement with former results on dewetting holes in thin films.

# 7 The Rayleigh-Plateau instability of a receding straight front

After having studied the influence of slip on the Rayleigh-Plateau instability of a viscous film on a fibre (see the **publication in ADDENDUM II** and Sec. 4), we focus in the following on the evolution of the RPI of a receding straight front in a thin film on a planar substrate. A recent study by Bäumchen *et al.* investigated the influence of slip on the evolution of the Rayleigh-Plateau instability of a receding straight front in a thin ($h_0 = 125 \pm 5\,\mathrm{nm}$) PS(13.7k) film on two different types of planar substrates [85]. Experiments on both substrates were performed at the same temperature of $T = 120\,^{\circ}\mathrm{C}$ and slippage was induced by the choice of the substrate: a weak-slip situation (see Sec. 2.2.3) with a slip length in the range of $b \approx 0.04\,\mu\mathrm{m}$ was generated by using the combination of a short-chained PS melt and AF1600 surfaces [35, 85]. However, applying the same PS film on DTS-covered Si wafers yields a strong-slip boundary condition (see Sec. 2.2.3), with $b \approx 1\,\mu\mathrm{m}$ for $T = 120\,^{\circ}\mathrm{C}$ [34, 85]. In analogy to the results presented in the **publication in ADDENDUM II** and Sec. 4, the obtained results show that slippage amplifies the growth of the instability. The wavelength $\lambda^*$ of the fastest growing mode is, however, unaffected by changing the boundary condition. The effect of a slip-induced amplification of the growth of the undulations is corroborated by results on the RPI of a receding straight front in thin PS films [131]: here, in contrast to Ref. [85], the slip length was continuously varied between the experiments, induced by using large molecular weights ($M_\mathrm{w} > M_\mathrm{c}$) on AF1600 substrates [35, 131].

In the following paragraphs, we will focus on the comparison of the experimental findings to numerical results concerning the morphological characteristics of a receding straight front exhibiting intermediate-slip (see Sec. 2.2.3). The numerical simulations were performed by D. Peschka *et al.* [141]. In contrast to Ref. [85], the presented numerical simulations do even provide the possibility to predict the late stages of the RPI.

## 7.1 Numerical simulations of straight receding fronts

In order to numerically simulate the evolution of the RPI of a receding straight front in a thin film, the fourth-order differential equation of motion for thin Newtonian liquid films must be solved (see Eq. 2.33):

$$\partial_t h - \vec{\nabla} \cdot (m(h)\vec{\nabla}\Pi) = 0, \tag{7.1}$$

where

$$\Pi = -\vec{\nabla}^2 h + \phi'(h) \tag{7.2}$$

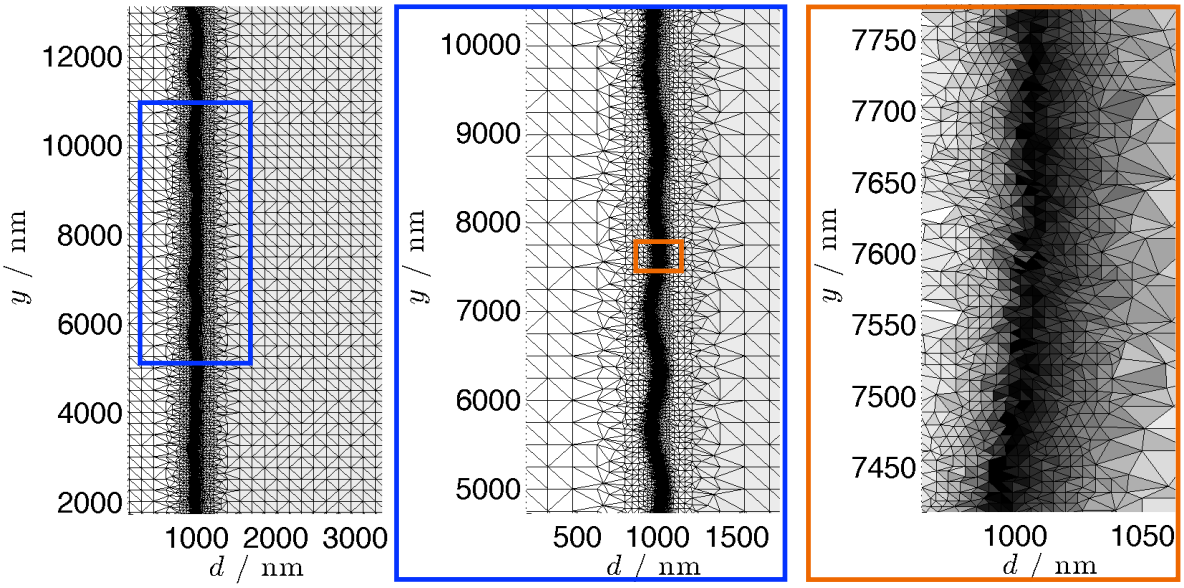


**Figure 7.1:** Illustration of the polygonal domain, consisting of a receding (to the right of the rim, which is shown in black) and a precursor film (to the left of the rim), approximated by a mesh of triangles, at a dewetted distance of $D = 1\,\mu$m [141].

represents a generalized pressure. Formally, the pressure $\Pi$ can be written as the first variation

$$\Pi = \frac{\delta F}{\delta h} \tag{7.3}$$

of an energy functional:

$$F(h) = \int_\Omega \frac{1}{2}||\nabla h||^2 + V(h)dx, \tag{7.4}$$

representing the driving force of the system, which counteracts the friction mechanisms. The intermolecular potential $V(h)$ is chosen as follows:

$$V(h) = \hat{V}\left(\frac{h}{h_\mathrm{p}}\right) \quad , \quad \hat{V}\left(\frac{h}{h_\mathrm{p}}\right) = \frac{\Sigma}{m-n}\left(n\left(\frac{h}{h_\mathrm{p}}\right)^{-m} - m\left(\frac{h}{h_\mathrm{p}}\right)^{-n}\right), \tag{7.5}$$

with $m = 2$ and $n = 8$ being the exponents of the potential, so that $V'(h_\mathrm{p}) = 0$ and $V(h_\mathrm{p}) = -\Sigma = S/\gamma_{\mathrm{l}v}$. $h_\mathrm{p}$ stands for the dimensionless thickness of the precursor film, which is implemented into the model in order to account for the receding contact angle $\theta_\mathrm{rec}$ located at the sharp three-phase contact line. Here, the mobility $m(h)$ of the film is equal to the intermediate-slip case with $m(h) = h^2$. Note that, in contrast, the thin film model in the **publication in ADDENDUM II** and Sec. 4 comprises $m(h) = h^3 + 3bh^2$ (weak-slip).

The model (Eq. 7.1) is solved using a finite element method (FEM) [142]. Thereby, the polygonal domain, consisting of the receding and the precursor film, is approximated by a mesh of triangles. For the purpose of precision, the mesh is locally refined close to the contact line (see Fig. 7.1). For further details concerning the FEM the reader is referred to [142, 143].

## 7.2 Comparison between experimental and numerical results

In the following, we concentrate on the comparison of the evolution of the RPI of a straight front in a thin film obtained from experiments using PS(5.6k) and PS(101k) with the theoretical predictions obtained for intermediate slip. Here, a linear geometry has been chosen in order to eliminate geometrical restrictions on the wavelength of the instability along the rim. Note that the system of a receding straight front displays three major differences, in contrast to what has been discussed so far concerning the classical case of the RPI (see Secs. 2.5.1 and 4 as well as the **publication in ADDENDUM II**): (i) the rim shape is approximated as a half-cylinder, which (ii) continuously grows during the dewetting process and (iii) features a three-phase contact line. As the comparison of different films with equal film thickness $h_0$ at the same dewetted distances $D$ ensures the identical volume in the rim, we compare the results taken at certain dewetted distances.

### 7.2.1 PS(101k): intermediate-slip experiments

In order to study the evolution of the RPI of a receding straight front in a thin viscous film in the presence of an intermediate-slip boundary condition, we performed dewetting experiments using PS films with a molecular weight of $M_\mathrm{w} = 101\,\mathrm{kg/mol}$ and an initial film thickness of $h_0 = 106 \pm 4\,\mathrm{nm}$ on AF1600 substrates ($T = 140\,^\circ\mathrm{C}$) [35]. The employment of the experimental parameters, as e. g. the initial film thickness $h_0$ and the receding contact angle $\theta_\mathrm{rec}$, to the model for intermediate slip (see Sec. 7.1) enables the direct comparison between the experimental and numerical results.

Figure 7.2 summarizes the experimental and numerical results: Figure 7.2a and b show typical optical micrographs of a receding straight front in a $h_0 = 106 \pm 4\,\mathrm{nm}$ thick PS(101k) film on AF1600 ($T = 140\,^\circ\mathrm{C}$), taken at different dewetted distances $D$. In comparison, Fig. 7.2c illustrates the numerical results obtained from the intermediate-slip model (see Sec. 7.1). In order to solve Eq. 7.1, the respective initial film height $h_0 = 106 \pm 4\,\mathrm{nm}$ as well as the receding contact angle, which for PS on AF6100 substrates was found to equal $\theta_\mathrm{rec} = 68 \pm 2\,^\circ$ [140], have been applied. From Figure 7.2 we see that the numerical solution of Eq. 7.1 is capable to mimic the characteristic morphological features of the RPI: at first, the front dewets from the substrate and maintains its straight shape. However, at a certain dewetted distance $D$ undulations occur - the so-called peaks and valleys are formed. In the further course of dewetting, the undulations grow due to the constant accumulation of the residual material. Driven by Laplace pressure, the valleys start to empty into the peaks. As a consequence of the intermediate-slip boundary condition at the solid/liquid interface and the associated dependence of the dewetting velocity on the rim width [53], i. e. $v = v(w)$, the peaks dewet slower than the valleys, which causes the formation of so-called bulges [85]. The combination of the difference in the dewetting speed between the peaks and the valleys and the fact that material transport from the valleys into the peaks is present, leads in turn to the formation of so-called fingers [85]. In the further course of dewetting, the fingers thin out, starting at the tip, where the finger is connected to the droplet, which finally results in the detachment of the droplets. The droplets adopt a spherical shape while exhibiting the equilibrium contact angle of $\theta_\mathrm{e} = 88 \pm 2\,^\circ$ [140]. The

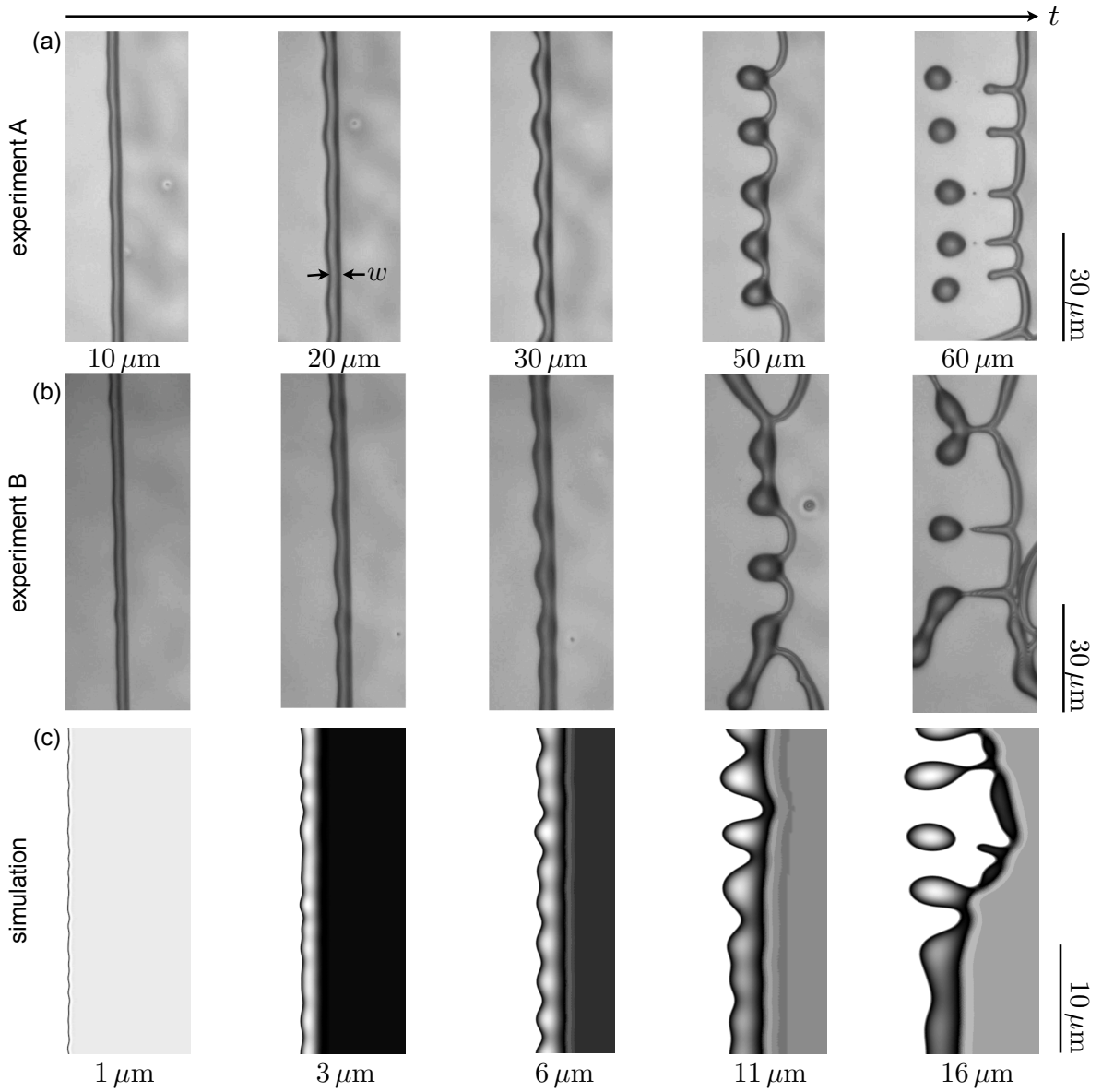


**Figure 7.2:** Snapshots of a receding straight front in a viscous liquid film taken at different travelled distances $D$. (a), (b) Optical micrographs of a PS film with a molecular weight of $M_\mathrm{w} = 101\,\mathrm{kg/mol}$ on AF1600 at a temperature of $T = 140\,^\circ\mathrm{C}$. The initial film thickness equals $h_0 = 106 \pm 4\,\mathrm{nm}$ and a slip length of $b = 478 \pm 7\,\mathrm{nm}$ was obtained from the rim profile analysis of dewetting holes in thin PS(101k) films on AF1600 [35]. Hence, the dewetting takes place in the intermediate-slip regime. The optical images are obtained from [131]. (c) Numerical simulation for intermediate slip employing the precise parameters of the experiments in (a) and (b) [141].

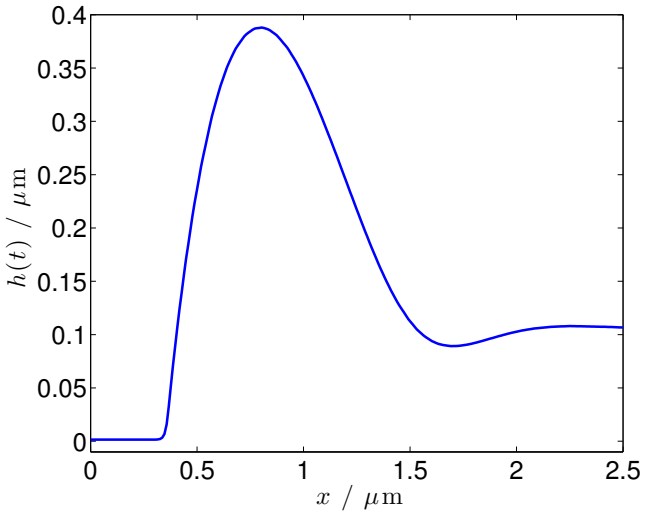


**Figure 7.3:** Rim profile $h(x,t)$ obtained from the numerical simulation of a $h_0 = 106\,\mathrm{nm}$ thick viscous liquid film dewetting on a substrate with an intermediate-slip boundary condition, extracted at a dewetted distance of $D = 3\,\mu\mathrm{m}$ (see Fig. 7.2). The rim width is equal to $w = 1.17\,\mu\mathrm{m}$ and the maximal height was measured with $h_{\max} = 0.39\,\mu\mathrm{m}$ [141].

fingers continue to retract and potentially leave behind secondary droplets. As the undulations are due to the Rayleigh-Plateau-type instability, the resulting bulges are equally distributed with wavelength $\lambda^*$ (see Sec. 2.5) and do exhibit the same size (see Fig. 7.2a at $D = 50\,\mu\mathrm{m}$). Hence, the final droplet pinch-off occurs at the same dewetted distance $D$ and the remaining droplets are located on a vertical line (see Fig. 7.2a at $D = 60\,\mu\mathrm{m}$). Often, the coalescence of two neighboring bulges is observed in the experiments (see Fig. 7.2b at $D = 50\,\mu\mathrm{m}$), which is even captured by the numerical simulations (see Fig. 7.2c at $D = 11\,\mu\mathrm{m}$).

The comparison of the absolute values of the dewetted distance $D$, which the front has moved until a certain morphological change of the rim becomes visible, shows that the experimental values exceed the theoretical values by a factor of $4-6$. Measuring the length $l_\mathrm{d}$ of a finger, right before the droplet pinch-off occurs, yields an experimental value of $l_\mathrm{d} = 12.8 \pm 0.4\,\mu\mathrm{m}$, whereas the simulations reveal a finger length of $l_\mathrm{d} = 2.6\,\mu\mathrm{m}$. Hence, the experimental value exceeds the simulation again by a factor of $\sim 5$. In addition to these lateral characteristics, also the maximal height $h_{\max}$ of the rim profile represents a morphological feature of the RPI. From former works it is know that the maximal height $h_{\max}$ and the rim width $w$ are directly correlated as a result of the conservation of volume: $w = (3.7 \pm 0.3)h_{\max} + (0.35 \pm 0.03)\,\mu\mathrm{m}$ [140, 144]. In general, the width $w$ of a rim is defined as the distance between the three-phase contact line and the position where the rim height is dropped to $1.1h_0$. Typically, the width $w$ is measured from the analysis of the rim profiles (see Sec. 3.2.3). Here, the rim width $w$ of the experimental data sets is measured from the optical micrographs, as illustrated in Fig. 7.2a. With respect to the onset of the instability, we find $w(D = 20\,\mu\mathrm{m}) = 3.9 \pm 0.3\,\mu\mathrm{m}$, corresponding to a calculated maximal rim height of $h_{\max} = (w - (0.35 \pm 0.03)\,\mu\mathrm{m})/(3.7 \pm 0.3) = 0.96 \pm 0.16\,\mu\mathrm{m}$. Note

that the determination of the rim width from optical micrographs is significantly influenced by the illumination of the sample (see Fig. 7.2a). Depending on the contrast, the moving front (the dark colored part in the middle of the images shown in Fig. 7.2) might appear broader. Hence, the value of the rim width, obtained from optical micrographs, denotes a rough estimate compared to values obtained from the analysis of rim profiles, which provide a precision in the nanometer range. Regarding the theoretical results, the corresponding morphological state is obtained for $D = 3\,\mu$m (see Fig. 7.2c). As the numerical simulation allows to extract the rim profile, the maximal height is found to equal $h_{\max} = 0.39\,\mu$m (see Fig. 7.3) with a rim width of $w = 1.17\,\mu$m. We find roughly a factor of $\sim 3$ between the experimentally and the theoretically determined characteristic parameters.

The potential source for the systematic and consistent deviation in the absolute values might be a difference in the mobility $m(h)$. The presented experiments were performed using $h_0 = 106 \pm 4$ nm thick PS(101k) films on AF1600 substrates, exhibiting a slip length of $b = 478 \pm 7$ nm [35]. Hence, the dimensionless slip length is equal to $B = b/h_0 \approx 5$. As a consequence, the mobility $m(h)$, acting on the first liquid molecules close to the solid/liquid interface, might actually be weaker than the mobility used in the simulation [141]. The mobility does, however, determine the onset of the instability. For weak- and intermediate slip, we found: the higher the mobility $m(h)$, the smaller the dewetted distance at which the undulations occur [131].

**Short Summary**

- Dewetting experiments of straight fronts in thin PS films show that the semicylindrical rim undergoes a Rayleigh-Plateau-type instability.
- The presence of interfacial slip causes the perturbed front to pass through several characteristic regimes (undulations, bulges, fingers and droplet pinch-off).
- Using a finite element method to solve the equation of motion for thin films featuring an intermediate-slip boundary condition, one gains results that qualitatively agree with the experimental findings. All characteristic features of the instability evolution are captured by the numerical simulation. In contrast to former studies, the numerical simulations do even provide the late stages of the RPI - the fingering and the pinch-off regime.
- The quantitative comparison between the experimental and numerical results, as e. g. the dewetted distance and the finger length, shows that the evolution of the RPI is 'faster' for the simulation: the characteristic morphological changes set in at a smaller dewetted distance $D$.
- A potential reason for the discrepancy in the absolute values might be a difference in the mobility $m(h)$ of the liquid molecules at the interface.

### 7.2.2 PS(5.6k): weak-slip experiments

In order to compare the experimental and theoretical results concerning the height profiles of a receding rim, the dewetting process of a straight front in a PS film on AF1600 was recorded using an atomic force microscope (AFM). PS with a molecular weight of $M_w = 5.6\,\mathrm{kg/mol}$ was used. Note that the film preparation for short-chained PS is accompanied by the formation of 'float gaps' (see Sec. 3.1.3). Hence, the prepared samples offer straight fronts. The initial film thickness of the PS films equals $h_0 = 125 \pm 5\,\mathrm{nm}$ and the dewetting experiments were performed at a temperature of $T = 110\,^\circ\mathrm{C}$. Images were taken *in-situ* every minute. As the slip length of thin dewetting PS(5.6k) films on AF1600 has been measured to equal $b = 53 \pm 34\mathrm{nm}$ [35], these experiments provide a weak-slip scenario with $B = b/h_0 = 0.4$ (see Sec. 2.2.3). In former studies, experiments with a dimensionless slip length $B$ on the same order were even referred to as no-slip systems in comparison to strong-slip systems with $B = 10$ [85]. Strictly speaking, even low molecular weight PS films on AF1600 substrates do typically exhibit a very small amount of slip at the solid/liquid interface [35]. As a consequence, a receding straight front in such a PS film does also become unstable and form fingers, but at a much later stage compared to the intermediate-slip case [131]. In other words, a dewetting straight front in a film of thickness $h_0$, where a very small slip length $b_1$ is present, undergoes the RPI not until the front has moved the distance $D_1$. The undulations of a dewetting rim in a film of the same thickness $h_0$ with a slip length of $b_2 > b_1$ do, however, occur at $D_2 < D_1$. Hence, the slip length $b$ determines the onset of the instability, but the characteristic morphological evolution of the RPI (undulations, bulges, fingers and droplet detachment, see Sec. 7.2.1) is the same for both scenarios [131]. Only for a given ideal no-slip substrate, the receding rim would indeed become unstable, but would not form bulges and fingers. Hence, the formation of fingers displays a fingerprint for the presence of slippage at the interface and even from the final stage of the dewetting process, one can judge if slippage was present (see the **publication in ADDENUM I**) [85].

Solving Eq. 7.1 while applying the weak-slip mobility term does, in contrast to the described experimental findings, result in a stable situation [141]. A potential reason might be given by the selected window size in the simulation: as the weak-slip experiments showed that the onset of the instability occurs not until the front has travelled a distance $D$, which is much larger than for intermediate slip [85], the tested window sizes in the simulations might be too small to reach the regime of undulations [141]. Within the tested window sizes, only the implementation of a big perturbation of the front or increasing the slip length up to $b = 5h_0$ caused the receding front to become unstable [141]. The morphological evolution was, however, found to be qualitatively identical for weak and intermediate slip [131]. In addition, Münch *et al.* showed that the rim profiles - obtained for both boundary conditions - exhibit an oscillatory decaying tail [84]. Hence, the experimental (for weak slip) and theoretical (for intermediate slip) results are comparable with respect to morphological fingerprints. The absolute values are, however, not comparable, as the mobility $m(h)$ of the liquid molecules at the solid/liquid interface is different.

In the following, we present results from dewetting experiments of PS(5.6k) on AF1600, where weak slip is present, in qualitative comparison to numerical results, derived by applying an intermediate-slip boundary condition. All experimental parameters, as e. g. the initial film

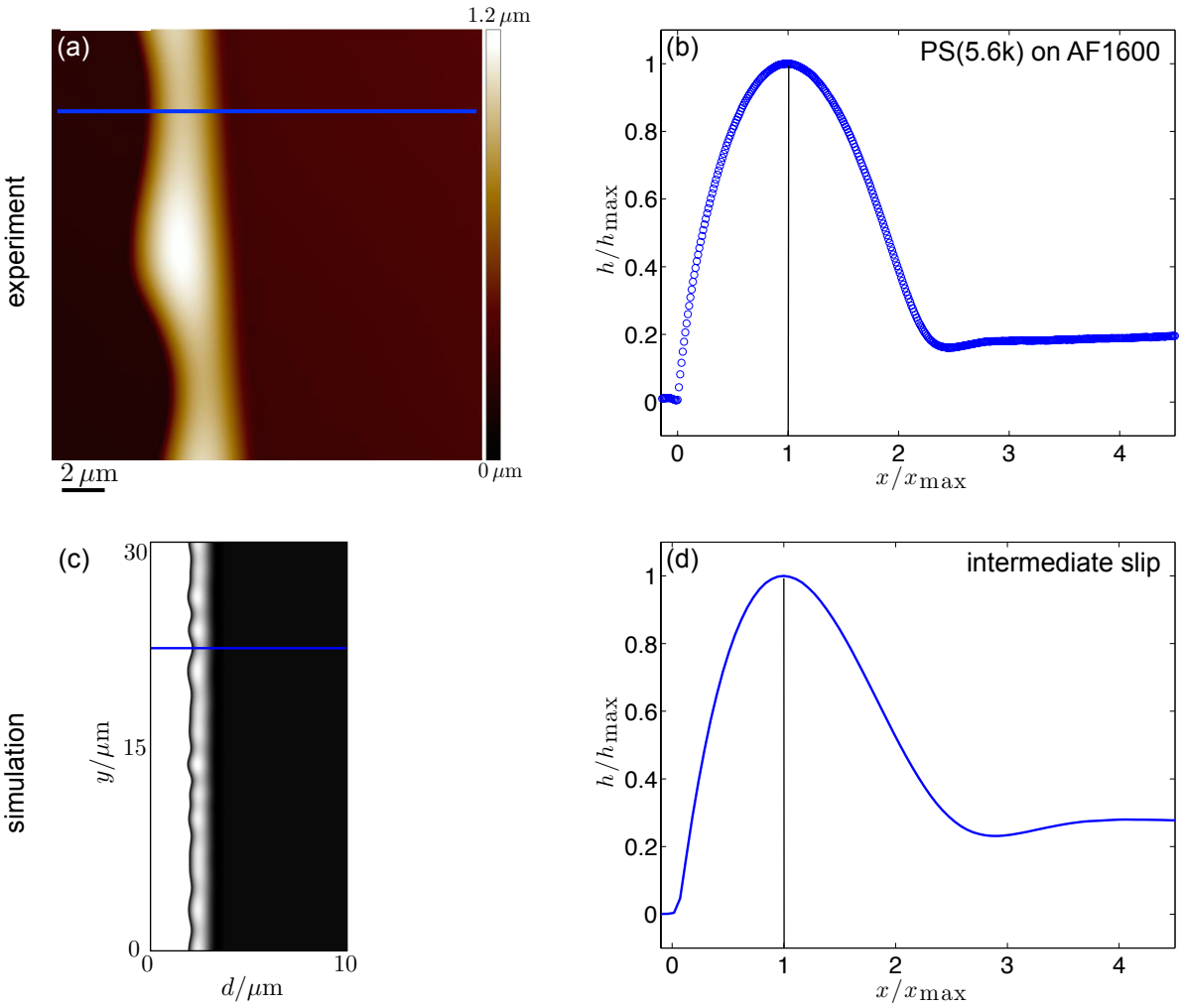


**Figure 7.4:** Comparison of experiment and simulation for the early stage of the RPI: (a) AFM image showing a perturbed front in a dewetting PS(5.6k) film on AF1600 at $T = 110\,^{\circ}\mathrm{C}$ after $t = 84\,\mathrm{min}$ ($h_0 = 125 \pm 5\,\mathrm{nm}$). The slip length equals $b = 53 \pm 34\,\mathrm{nm}$ [35]. Hence, the system exhibits a weak-slip scenario, where $B = b/h_0 = 0.4$. (b) Rim profile $h(x,t)$, extracted from the AFM scan shown in (a) for $t = 84\,\mathrm{min}$ at the position of a valley. The height $h$ and the distance $x$ from the three-phase contact line are normalized by the coordinates at maximum $h_{\mathrm{max}}$ and $x_{\mathrm{max}}$. (c) Numerical simulation of a dewetting straight liquid front for intermediate slip, illustrating the early stage of the instability. (d) Normalized height profile taken from image (c) at a valley, shown by the blue line [141].

thickness $h_0$, are the same. Figure 7.4 illustrates results obtained from AFM measurements as well as numerical simulations with respect to the onset of the RPI. As discussed in the previous section, comparing the top view of the receding rims shows the exact same characteristic morphological state (see Fig. 7.4a, c): at a certain dewetted distance $D$ the front becomes

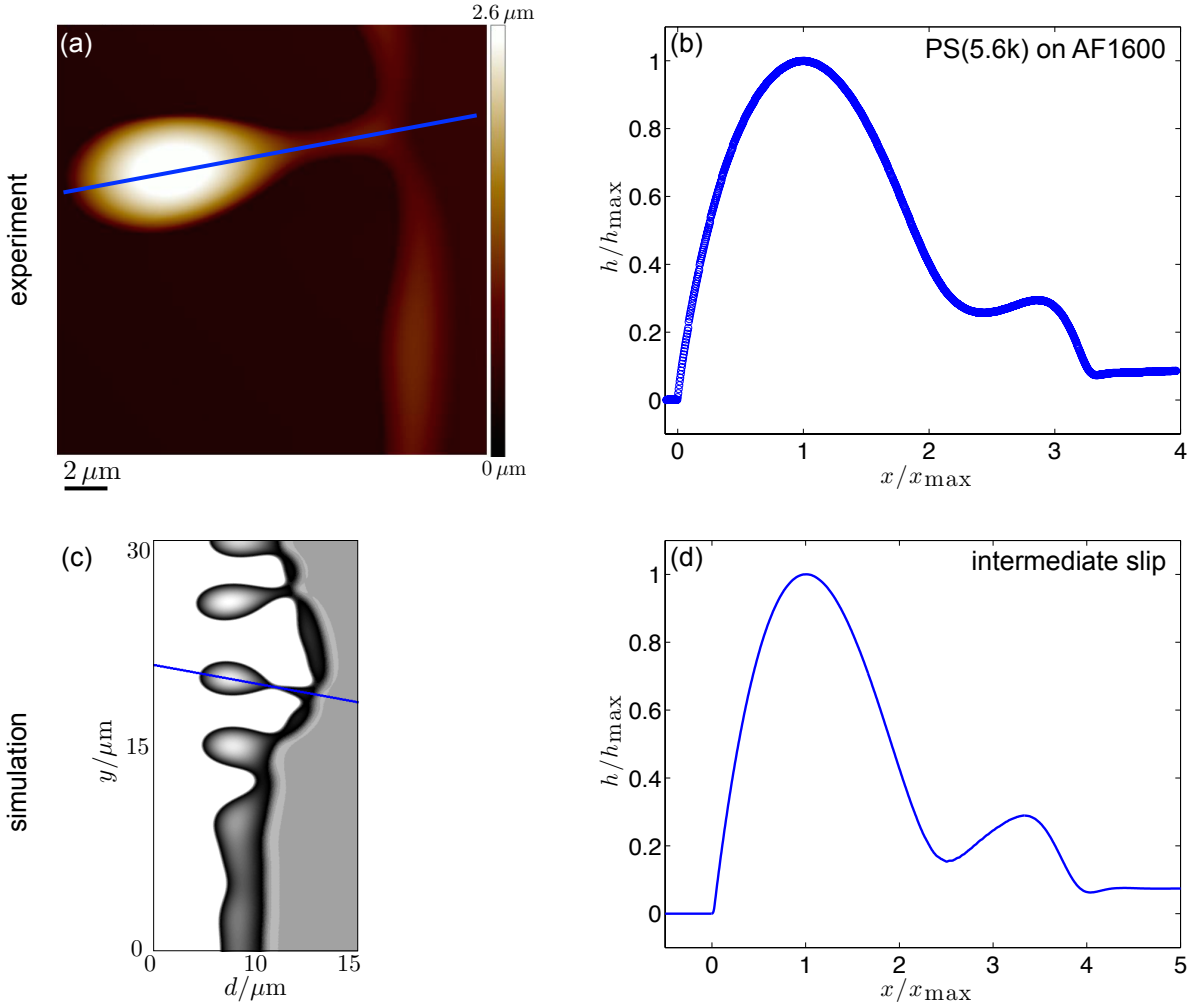


**Figure 7.5:** Comparison of experiment and simulation during the fingering regime of the RPI: (a) AFM image of a dewetting PS(5.6k) film on AF1600 taken after $t = 256\,\text{min}$, where the front already displays a finger ($T = 110\,^\circ\text{C}$, $h_0 = 125 \pm 5\,\text{nm}$ and $b = 53 \pm 34\,\text{nm}$ [35], weak slip). (b) Normalized AFM scan line taken from image (a) along the finger (blue line). (c) Numerical simulation of a dewetting straight liquid front for intermediate slip, illustrating the fingering regime of the instability. (d) Normalized height profile taken from image (c) along the finger (blue line) [141].

unstable and forms undulations with peaks and valleys. For the reason of having a good temporal ($\Delta t = 1\,\text{min}$) and spatial (1024 lines with 1024 samples/line) resolution, a scan size of 20 x 20 $\mu\text{m}^2$ has been chosen, accepting the fact of imaging one peak and two valleys only. The comparison of the course of the height profiles $h(x,t)$, normalized by the coordinates at the maximum $h_{\max}$ and $x_{\max}$, both extracted at the position of a valley (see the solid blue lines in Fig. 7.4a,c), shows excellent agreement between experiment and simulation (Fig. 7.4b,d):

the linear scaling between the rim width $w$ and the maximal rim height $h_{\max}$ as well as the oscillatory decay of the rim profile into the residual film are captured by the simulation.

The formation of fingers is the most important fingerprint of the RPI of a receding straight front in a thin film, where slippage is present. Figure 7.5 illustrates again experimental as well as theoretical results. This time, the data is obtained from the fingering regime. The experimental top view AFM image shows a snapshot of a droplet, which is still connected to the receding rim via a thinning liquid PS bridge - the finger (see Fig. 7.5a). As described in Sec. 7.2.1, the droplet and consequently the finger originate from a peak: as the velocity depends on the width of the rim, $v = v(w)$, the peaks dewet much slower than the valleys. Furthermore, by regarding the lower half of Fig. 7.5a it becomes noticeable that the receding valley does even start to undergo the RPI a second time. The illustrated droplet exhibits a height, which is much larger than the initial film height $h_0$. In addition, the droplet displays an elongated shape along the finger axis, which is caused by the retraction of the connected finger. The numerical simulation shows excellent agreement with the experiments and does also reveal the formation of fingers. Even the second RPI of the valleys is captured by the simulation. Figure 7.5b and d represent the respective experimentally and numerically obtained height profiles $h(x,t)$ along the finger (see the solid blue lines in Fig. 7.5a and c), normalized by $h_{\max}$ and $x_{\max}$. Here, again both profiles feature the same characteristic shape: the decaying height profile of the elongated droplet into the finger is followed by a small 'shoulder' in the height profile. Having a closer look at $h/h_{\max}$ associated with the finger shows that the decay of the finger has already been initiated, starting at the tip, where the finger is in direct contact to the droplet. In the further course of the dewetting process, the finger will thin out even more, which finally leads to the detachment of the droplet. Note that the results obtained from the numerical simulations offer a slightly later stage of the fingering regime compared to the experimental data (see Fig. 7.5). Accordingly, the length of the liquid bridge is longer. Furthermore, we see that in agreement with the earlier stage of $h/h_{\max}$, shown in Fig. 7.4b and d, the decay of the height profile into the residual film is still oscillatory.

**Short Summary**

- Using a finite element method to numerically solve the equation of motion for thin liquid films with $m(h) = h^2$ shows excellent qualitative agreement with the experimental findings (for weak slip) concerning the height profiles $h(x,t)$.
- The height profiles $h(x,t)$, obtained from a receding front which undergoes the fingering regime, feature the elongated droplet shape (caused by the finger formation) followed by the thinning of the liquid finger.

In summary, the data presented in this chapter show that, in comparison to the findings by Bäumchen *et al.* [85], the same morphological fingerprints of the RPI of a receding straight front can be induced on AF1600 substrates by varying the slip length $b$ via the molecular weight, with $M_{\mathrm{w}} > M_{\mathrm{c}}$. The presented numerical simulations for $m(h) = h^2$ are in excellent qualitative agreement with the experimental findings and capture all characteristic features with respect to the lateral morphology as well as the height profiles.

# 8 Summary and Outlook

The role of the hydrodynamic boundary condition at the interface between a solid and a liquid has become of enormous significance within the framework of micro- and nanofluidic devices. The goal of this thesis was to clarify the influence of the hydrodynamic boundary condition at the solid/liquid interface on the spatial and temporal evolution of the Rayleigh-Plateau instability of liquid thin films. Two different geometries were considered: thin films on cylindrical fibres and straight fronts in thin flat films. In the following, the short term 'boundary condition' will be used, which always refers to the hydrodynamic boundary condition at the solid/liquid interface.

### The Rayleigh-Plateau instability on a fibre

The RPI of a viscous liquid film with a thickness of $e_0$ on a microfibre of radius $r$ was revisited by varying the hydrodynamic boundary condition at the fibre/liquid interface from the classical case of no slip to slip. A no-slip system was generated by applying an entangled polystyrene film ($M_\mathrm{w} = 78\,\mathrm{kg/mol}$) on a bare glass fibre. Applying the same PS film on a hydrophobic AF2400-coated fibre provided a slip situation. **The wavelength $\lambda^*$ of the fastest growing mode was found to be insensitive to the boundary condition**: $\lambda^*$ grows linearly with the initial total radius $h_0$ of the system, in quantitative agreement with the classical prediction from Rayleigh and Plateau, i. e. $\lambda^* = 2\sqrt{2}\pi h_0$. At short times, the instability exhibits an exponential temporal growth. We present the respective growth rates $1/\tau^*$ of the fastest growing modes for both boundary conditions, which reveal a qualitatively similar dependence on the system geometry: $1/\tau^*$ shows a decrease for either very thick films compared to the fibre radius or for very small ratios of $e_0/r$. For the no-slip situation, the maximum of $1/\tau^*$ was found for $e_0/r \sim 4$. In case of a slip boundary condition, the maximum is shifted to a smaller value for $e_0/r$, which is due to the non-zero velocity of the liquid molecules at the interface. Finally, the analysis of the growth rates shows a significant influence of the hydrodynamic boundary condition for a given system geometry: **the growth dynamics of the instability is considerably increased by slippage**.

A fibre thin film model has been developed that is based on the Stokes equation and the lubrication approximation for thin films and that includes hydrodynamic slip. This model turned out to be in excellent agreement with the measured wavelength and growth rate data. **The comparison between the experimentally obtained and theoretically predicted growth rates does even provide the possibility to measure the capillary velocity $\gamma/\eta$ and the slip length $b$.**

Having established a robust technique to quantify hydrodynamic slip, the influence of an increase in the molecular weight ($M_\mathrm{w} = 186\,\mathrm{kg/mol}$) as well as the influence of the choice of

the substrate on the slip length is quantified. In order to vary the slip-inducing mechanism, the PS(78k) films were applied to silanized (DTS) fibres. Hence, slippage was induced by a combination of two mechanisms: by a modification of the substrate and by using entangled polymer melts. In agreement with the results obtained for PS(78k) on glass and AF2400 fibres, **the wavelength $\lambda^*$ is unaffected by an increase of the molecular weight as well as the varied origin of slip**. The experiments for PS(186k) on AF2400 fibres did, however, reveal an enhanced amount of slip, i. e. an enhancement of the mobility at the interface, which causes the RPI to evolve even faster compared to PS(78k) films on AF2400 fibres. The results obtained from experiments with a changed origin of slip corroborate these findings: the temporal evolution of the RPI is unaffected by the mechanism chosen to induce slippage. Only the amount of slippage at the interface, i. e. the absolute value of the slip length $b$, affects the growth rates $1/\tau^*$. As the slip length for PS(78k) on DTS exhibits a lowered value compared to $b$ obtained on AF2400 fibres, the growth of the instability is slowed down. **Hence, slippage can be induced and tuned by the molecular weight as well as the surface treatment. The RPI is, however, not sensitive to the slip-inducing mechanism. The temporal growth of the instability is only governed by the amount of slip**.

### Capillary droplet propulsion on a fibre

The late stage of the liquid column breakup on a hydrophobic fibre provided moving droplets. That enabled the examination of the transport process of droplets along a filament. Subsequent to the spontaneous formation of a three-phase contact line at one side of a droplet, the imbalance of contact angles caused the droplets to move. First, we report on the motion process, which is purely governed by viscous dissipation. **We find that the droplet dynamics is linear in time over the entire dewetting process, which comprises the accumulation of the thin residual film and the coalescence with static droplets.** The local dewetting velocity is alternating around a certain mean velocity $\overline{v}$: while the accumulation of the thin film features a constant velocity, the coalescence of the moving and a static droplet is accompanied by a sudden increase in the droplet speed, in combination with a decrease of the receding contact angle $\theta_{\mathrm{rec}}$. At the end of the merging process, $\theta_{\mathrm{rec}}$ recuperates and the velocity decelerates again. The analysis of the local droplet speed $v$ for various molecular weights ($M_{\mathrm{w}} = 4.2\,\mathrm{kg/mol}{-}78\,\mathrm{kg/mol}$) and temperatures, where coalescence steps have been neglected, showed that **the inverse local dewetting velocity $1/v$ scales linearly with the melt viscosity $\eta$. The comparison of the measured velocity data with a force balance model based on purely viscous friction reveals a single constant of proportionality capturing all data sets.**

In order to study the influence of slippage on the droplet propulsion dynamics, we report on experiments using long-chained PS droplets ($M_{\mathrm{w}} = 186\,\mathrm{kg/mol}$ and $390\,\mathrm{kg/mol}$). From recording the local velocity of the contact line of the droplets we observe that the dewetting dynamics is not linear over the entire process. Given the fact that the image recording of the dewetting process was started right after the onset of the droplet motion, the analysis of the dynamics does, however, yield a linear scaling between the inverse global droplet velocity $1/\overline{v}$ and (a) the viscosity $\eta$, (b) the initial width of the droplet $w(t_0)$ and (c) the inverse of the polymer chain length.

Locally the dewetting process exhibits three characteristic features: **(i) the local droplet velocity during the accumulation of the thin residual film is constant, but the velocity values vary between the separate accumulation steps. (ii) The displacement data during the merging of a moving and a static droplet is linear in time. The coalescence speed does, however, vary for the different merging events. (iii) In contrast to the results obtained for droplets which are governed by purely viscous flow, the displacement towards the receding droplet was observed for static droplets which exhibit an apparent contact angle $\beta$ that is larger than the receding contact angle.**

The analysis of the initial droplet motion regime, which is defined as the period between the onset of the droplet motion and the first coalescence event, provided the initial droplet velocity $v_0$. **The comparison between $v_0$ and a force balance model, which additively superposes viscous dissipation and slippage, enabled the estimation of the slip length**. The analysis of the local dewetting velocity $v$ subsequent to any coalescence step does, however, not conform with this trend and we rather found a first signature of a linear relation between $v$ and the speed of the preceding coalescence event. The detailed understanding of the mechanisms which govern the droplet dynamics, using high molecular weights, requires further experiments with a systematic variation of viscosity, molecular weight and initial droplet width.

### Comparison of slip lengths obtained from different studies and approaches

Both studies, the RPI of liquid films as well as the capillary-driven droplet transport on hydrophobic fibres, allowed for the determination of the slip length from the comparison of the experimentally obtained results to the respective theoretical models. **The slip lengths obtained on the AF-coated fibres are in excellent agreement with former studies and corroborate the well-established trend for $M_\mathrm{w} > M_\mathrm{c}$, i. e.** $b \sim M_\mathrm{w}^3$. Note that $M_\mathrm{c} = 35\,\mathrm{kg/mol}$ displays the critical chain length, above which polymer chains start to form entanglements [8]. While the results on the slip length determined for AF-coated substrates are independent of the temperature, the slip lengths on DTS are known to show a significant temperature dependence: the slip length decreases with increasing temperature. In previous studies, the slip length has been determined from the analysis of the rim profiles of holes in thin films on planar DTS substrates using temperatures in the range of $105\,^\circ\mathrm{C} \leq T \leq 130\,^\circ\mathrm{C}$. The results presented in this thesis were obtained from studying the RPI on DTS fibres using a temperature of $T = 180\,^\circ\mathrm{C}$. **In consideration of the temperature dependence on DTS, the slip lengths from different studies are in excellent agreement**.

### The Rayleigh-Plateau instability of a receding straight front

In order to study the influence of slip on the evolution of the RPI of a receding straight front in a thin film on a planar substrate, PS(101k) and PS(5.6k) films were applied to AF1600-coated Si wafers. The initial film thickness of the PS films varied between $100\,\mathrm{nm} \leq h_0 \leq 130\,\mathrm{nm}$.

While the PS(101k) films with a slip length to film thickness ratio of $b/h_0 \approx 5$ offered an intermediate-slip condition, PS(5.6k) with $b/h_0 = 0.4$ accounted for a weak-slip scenario.

In case of slippage being present, also the RP-type instability of a receding straight front in a thin film displays an amplified growth of the instability, which is in agreement with the classical case of a decaying freestanding liquid cylinder and the breakup of a viscous liquid film on a fibre. Not only the dynamics, but also the morphology of the RPI was found to show certain fingerprints, which are characteristic for a slip boundary condition.

In other words, if interfacial slip is present, the receding front passes through different characteristic regimes: at a certain dewetted distance, undulations form, which grow into bulges, followed by the formation of fingers, which finally result in the pinch-off of droplets. The comparison to former studies, where slippage was induced by the presence of a silane substrate, revealed the independence of the morphological characteristics from the origin of slip. In addition, we report on numerical calculations, where a finite element method was used to solve the equation of motion for thin films featuring an intermediate-slip boundary condition. This enabled a qualitative comparison between the experimentally obtained and numerically calculated results with respect to the morphological characteristics. In contrast to former studies, the numerical simulations are even able to capture the late stage of the RPI evolution: the fingering regime as well as the droplet pinch-off. **The theoretical results are shown to be in excellent qualitative agreement with the experimental findings and capture all characteristic features concerning the lateral morphology as well as the rim profiles**. The quantitative comparison between the results for PS(101k), which exhibit an intermediate-slip boundary condition, and the numerical calculations for $m(h) = h^2$ showed that the RPI evolves faster in the simulations, i. e. the characteristic morphological features set in at smaller dewetted distances. Potentially, the consistent and systematic deviation is caused by a discrepancy in the mobility term $m(h)$.

## Outlook

The findings of this work highlight the importance of the hydrodynamic boundary condition at the solid/liquid interface on the stability and the dynamics of thin film flows. Future studies concerning the influence of the interactions between a liquid and a solid on the RPI on a fibre may consider the case of a strong-slip boundary condition. From former works on the RPI of a receding straight front in a thin PS film on a planar substrate with a strong-slip boundary condition it is known that, within the experimentally accessible time and length scales, the receding front does not undergo a RP-type instability, the front maintains its straight shape [131]. Note that the experimental window size of dewetting experiments is limited by the coalescence of the receding rim with others in the late stage of the experiment. In contrast, the fibre system provides the huge advantage of an unlimited experimental window size and the absence of a three-phase contact line. A potential experimental system to study the RPI with strong-slip, where the influence of viscoelastic effects and non-Newtonian fluid behavior can safely be excluded, can be realized by the combination of a PS film with a low molecular weight and a silanized fibre.

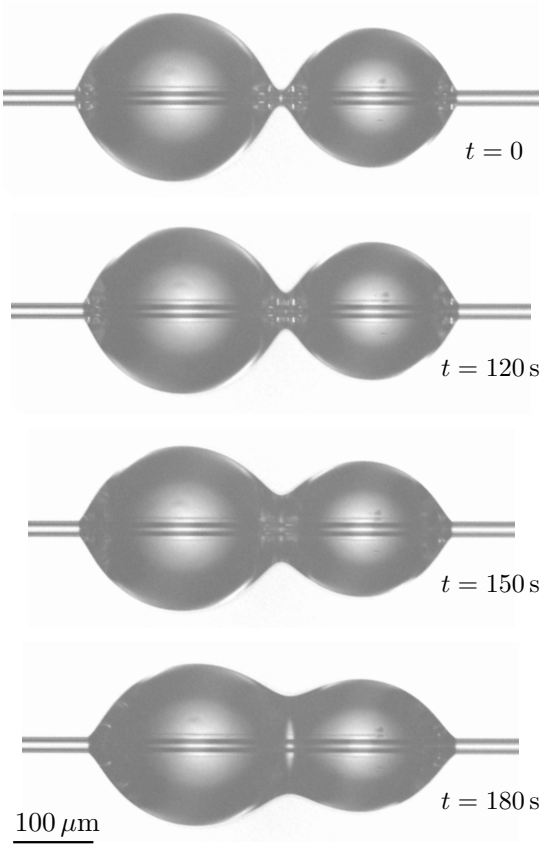


**Figure 8.1:** Time series of the coalescence process of two PS(78k) droplets on a AF2400 fibre at $T = 175\,^{\circ}\mathrm{C}$. Both droplets[3] exhibit a three-phase contact line and move towards each other. As the droplets come into contact, the difference in the Laplace pressure results in a large driving force which causes the liquid neck in between the droplets to level rapidly.

A recent work by Henann *et al.* proved a potential approach to eliminate the RPI on a fibre [77]: the study showed that a liquid film coated on an elastic cylindrical fibre remains stable if the fibre radius $r$ is smaller than $\gamma/6G$, with surface tension $\gamma$ and elastic modulus $G$. Hence, the question arises how the thickness and the modulus of an elastic coating on a solid fibre influences the dynamics and morphology of the RPI of a liquid film.

As presented in this thesis, the RPI of a liquid film on a fibre provides a robust and reliable technique to quantify hydrodynamic slip at the fibre/liquid interface. In addition, the experiments allow for higher temperatures compared to the dewetting experiments on planar substrates. Hence, the fibre setup provides an efficient tool to revisit the studies concerning

[3]Note that the microscope light undergoes optical refraction on the droplet surface and generates the optical illusion the droplets were not entirely convex and continuous. The use of contrast enhancement of the image fortifies this effect.

the origin of slip on OTS and DTS with respect to the determination of the slip length for high temperatures.

The fact that the late stage of the RPI on a fibre allows for the formation of moving droplets bares the possibility for studies on the coalescence of droplets. So far, the merging process of droplets on planar substrates as well as the influence of a variation in the droplet sizes is well-understood [145, 146]. The fibre system provides the advantage of investigating the coalescence event in 3D and allows for testing the role of the boundary condition at the solid/liquid interface. Figure 8.1 shows a time series of the merging process of two droplets on a hydrophobic fibre. Both droplets exhibit a three-phase contact line and move towards each other. Understanding the role of the boundary condition on the coalescence of droplets is of great importance. As an illustrative example, technological applications, such as chemical reactions, may be initiated through droplet coalescence, where only small amounts of liquids are required. In this regard, future studies should additionally address liquid flows in fibre networks, including a variation of the boundary condition.

The presented results on the RPI of a receding straight front with a slip boundary condition showed the evolution of characteristic fingerprints, as e. g. the formation of liquid fingers (see Fig. 8.2) and the final pinch-off of droplets. As these characteristic features represent a further way to access slippage, future studies should address the mechanisms which determine the length of the fingers and the droplet detachment process.

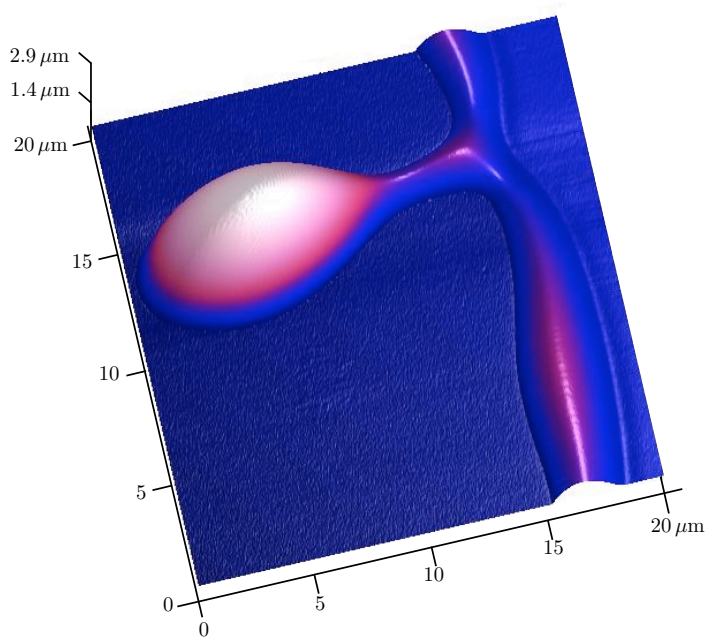


**Figure 8.2:** AFM image of a liquid finger which is connected to a receding straight front in a thin PS(5.6k) film ($h_0 = 125 \pm 5\,\mathrm{nm}$) on AF1600 at $T = 110\,^{\circ}\mathrm{C}$ recorded after $t = 256\,\mathrm{min}$.

# 9 Addenda

# Addendum I - Nanofluidics of thin polymer films: Linking the slip boundary condition at solid–liquid interfaces to macroscopic pattern formation and microscopic interfacial properties

Authors: J. D. McGraw, O. Bäumchen, M. Klos, S. Haefner, M. Lessel, S. Backes, and K. Jacobs

Department of Experimental Physics, Saarland University, 66041 Saarbrücken, Germany.

*Advances in Colloid and Interface Sciences* **210**, 13–20 (2014).
(http://www.sciencedirect.com/science/article/pii/S0001868614001353)



**Author contributions:**

J. D. McGraw, O. Bäumchen, M. Klos, S. Haefner, M. Lessel, S. Backes and K. Jacobs performed experiments and analyzed the data. Research was designed by all authors. The manuscript was written by J. D. McGraw, M. Klos and S. Haefner. All authors contributed to the research and manuscript preparation.

**Abstract -** If a thin liquid film is not stable, different rupture mechanisms can be observed causing characteristic film morphologies: spinodal dewetting and dewetting by nucleation of holes. This rupturing entails liquid flow and opens new possibilities to study microscopic phenomena. Here we use this process of dewetting to gain insight on the slip boundary condition at the solid–liquid interface. Having established hydrodynamic models that allow for the determination of the slip length in a dewetting experiment based on nucleation, we move on to the quantification and molecular description of slip effects in various systems. For the late stage of the dewetting process involving the Rayleigh–Plateau instability, several distinct droplet patterns can be observed. We describe the importance of slip in determining what pattern may be found. In order to control the slip length, we use polymeric liquids on different hydrophobic coatings of silicon wafers. We find that subtle changes in the coating can lead to large changes in the slip length. Thus, we gain insight into the question of how the structure of the substrate affects the slip length.

Advances in Colloid and Interface Science 210 (2014) 13–20

Contents lists available at ScienceDirect

Advances in Colloid and Interface Science

journal homepage: www.elsevier.com/locate/cis

# Nanofluidics of thin polymer films: Linking the slip boundary condition at solid–liquid interfaces to macroscopic pattern formation and microscopic interfacial properties

Joshua D. McGraw, Oliver Bäumchen [1], Mischa Klos, Sabrina Haefner, Matthias Lessel, Sebastian Backes, Karin Jacobs *

*Experimental Physics, Saarland University, D-66041 Saarbrücken, Germany*

ARTICLE INFO

Available online 12 April 2014

*Keywords:*
Slip
Nucleation
Polymer thin films
Thin film equations
Solid–liquid interfaces

ABSTRACT

If a thin liquid film is not stable, different rupture mechanisms can be observed causing characteristic film morphologies: spinodal dewetting and dewetting by nucleation of holes. This rupturing entails liquid flow and opens new possibilities to study microscopic phenomena. Here we use this process of dewetting to gain insight on the slip boundary condition at the solid–liquid interface. Having established hydrodynamic models that allow for the determination of the slip length in a dewetting experiment based on nucleation, we move on to the quantification and molecular description of slip effects in various systems. For the late stage of the dewetting process involving the Rayleigh–Plateau instability, several distinct droplet patterns can be observed. We describe the importance of slip in determining what pattern may be found. In order to control the slip length, we use polymeric liquids on different hydrophobic coatings of silicon wafers. We find that subtle changes in the coating can lead to large changes in the slip length. Thus, we gain insight into the question of how the structure of the substrate affects the slip length.



**Contents**



## 1. Introduction

Boundary conditions play an important role in the development and understanding of many phenomena, from quantum to classical physics. In the case of quantum physics, periodic boundary conditions are useful for the description of the crystalline materials which have been at the focus of condensed matter physics and materials science for over a century, for example. In the field of classical physics, boundary conditions play a central role in the study of fluid flows. In this paper, we consider the importance of the boundary condition prescribed at the interface between a solid and a liquid.

* Corresponding author.
*E-mail address:* k.jacobs@physik.uni-saarland.de (K. Jacobs).
[1] Present address: Max Planck Institute for Dynamics and Self Organization (MPIDS), 37077 Göttingen, Germany.

http://dx.doi.org/10.1016/j.cis.2014.03.010
0001-8686/

Throughout much of the history of fluid mechanics, the no-slip boundary condition between a fluid and a solid has been assumed [1]. This boundary condition states that there is no relative motion between molecules in the fluid and those in the solid at the interface. For macroscopic flows (*e.g.*, flow of air past a plane wing or that of water through a kitchen faucet) with length scales large in comparison to molecular sizes, this no-slip condition is a good approximation. However, when system sizes approach molecular dimensions, as in 'lab-on-a-chip' microfluidic devices [2] or in nanometric polymer films [3–8], the relative motion between molecules at the solid–liquid boundary, referred to as hydrodynamic slip, must be considered [9–14].

A common quantification for this idea of fluid molecules sliding past molecules in the solid is through the Navier slip condition [12,13,15]. According to the linear model developed by Navier [15], viscous and frictional stresses are balanced at the solid–liquid interface and we may write

$$u|_{z=0} = b\frac{\partial u}{\partial z}|_{z=0}. \quad (1)$$

Here $u$ is the horizontal component of the velocity field, $\mathbf{u} = (u,w)$ for two dimensional flows, $z$ is the vertical distance from the substrate-fluid interface, and $b$ is referred to as the slip length. Using this definition, $b$ is the vertical distance from the substrate-fluid interface over which the horizontal fluid velocity, $u$, linearly extrapolates to zero.

There are many methods that can be used to quantify the presence of slip experimentally. These include the use of a surface forces apparatus [16] colloidal probe atomic force microscopy [17–19], particle image velocimetry [20], and fluorescence recovery after photo-bleaching [21–23]. These and other techniques have been reviewed by Lauga et al. [1] and in detail by Neto et al. [24].

Recently, the use of colloids to probe the boundary condition has regained some attention [25–27]. In the case of references [25,26], Wang and co-workers observed anisotropic diffusion coefficients using a particle in an optical trap. This optical trapping method offers a simplification of the particle trajectory analysis since the hydrodynamic response of a cantilever does not need to be included, where this may be necessary with colloidal probe AFM [27]. In this study, the authors compared the measured correlations of a particle's position with model predictions dependent on the slip boundary condition. Near a solid surface, it was found that the particle mobility is decreased as compared to the bulk. Near a liquid–vapour boundary, *i.e.* a full slip (no stress) boundary, it was observed that the particle had increased mobility compared to the bulk. While these observations are expected, Schlomovitz and co-workers [28] have shown using a similar technique that the particle mobility is indeed sensitive to the molecular details of an interface. Thus, the fully submerged optically trapped particle shows promise for the analysis of slippery solid–liquid interfaces, such as the one described by Cuenca and Bodiguel [29] discussed below. However, care has to be taken when assigning differences to boundary conditions, since close to an interface van der Waals forces also influence the mobility of fluid molecules [30]. Additionally the wettability and polarizability of the particle in the respective liquid can play a role in the observed slip length [31].

In a second case of a recent colloidal probe investigation [27], a colloidal probe AFM was used in gaseous environments near a flat solid surface, and a scaling theory was used to connect a hydrodynamic regime (particle far from the wall, compared to the mean free path of the gas molecules) to a molecular kinetic regime (particle close to the wall). The authors argue that slip is not necessary to explain their observations for small scale flows, provided that the hydrodynamic picture is replaced with a molecular kinetic framework. Although real hydrodynamic slip, that is the relative motion of liquid molecules against an interface, is likely to occur in many liquid systems, the Lissandrello study [27] highlights the importance of considering apparent slip [1,20,24].

Apparent slip refers to a situation in which the no-slip condition is actually valid at small scales, though seems to be violated at larger scales. This effect may occur in an inhomogeneous medium or in a system displaying shear thinning near a boundary. A slip length could be extracted using a model employing the assumption of homogeneity or Newtonian flow where these assumptions are invalid. Using polymer solutions flowing through micro and nanoslits, Cuenca and Bodiguel [29] have recently studied an apparent slip that is reportedly due to an inhomogeneity in the form of a depletion of polymer chains near the interface of the channels. In this work, it was shown that reducing the size of flow channels suppressed the flow more than would be expected assuming a constant slip length, the apparent slip being due to a depletion layer near the solid–liquid boundary. They interpreted their results as a shrinking of the depletion layer with channel size, thus reducing the apparent slip.

In past years, much of the effort in our research group [4–7,32–34] has been complimentary to the techniques listed above. We experimentally observe the process of dewetting [3,35–39] in thin liquid films and use full hydrodynamic models [4,10,12,13,32] to understand the results quantitatively. As will be described below, the slip lengths observed in our studies range from several nanometres up to more than ten times the film thickness, $h_0 \sim 100$ nm. In the dewetting processes we consider, a thin polymer film is placed onto a substrate and is heated above the glass transition temperature, $T_g$. In all cases, the growth of a circular hole reduces the surface energy of the system. See Fig. 1 for a schematic depiction of a typical sample and dewetting experiment. We note that the dewetting process involves internal capillary forces only — no external forces are required. The observation of the evolution is solely based on optical microscopy and atomic force microscopy (AFM) and no tracer particles or dyes are involved. Thus, our dewetting system is free of any complications arising from the use of a particular marker particle, which may change the state of a liquid in its immediate vicinity [30]. The use of tracer particles has the advantage of being a direct measure of the average velocity within the measurement layer (as small as ~ 50 nm for evanescent wave techniques [23]), with the possible limitations as described above [30,31]. In contrast, by studying height profiles with *e.g.* an AFM we observe the form of a liquid–air interface and infer the slip length at the substrate–liquid interface with the use of hydrodynamic models, avoiding the introduction of foreign particles. With regard to the discussion above, the nature of our measurement makes the distinction between real and apparent slip difficult. In order to

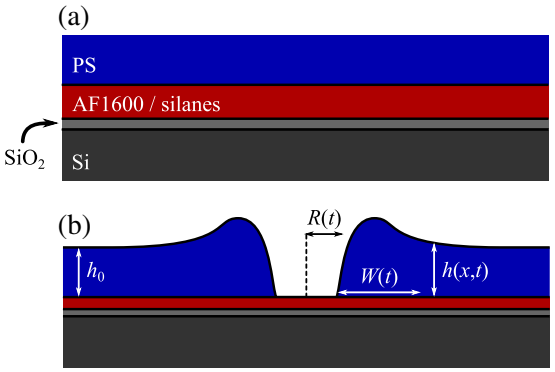


**Fig. 1.** (a) Schematic of the as-prepared samples under investigation in this study. From top to bottom: the polystyrene (PS) films are $h_0 \sim 100$ nm thick; the hydrophobic coatings have thicknesses of approximately 20 nm for AF1600 fluoropolymer coatings and 2 nm for the self-assembled silane monolayers; native oxide ($SiO_2$) layers have thicknesses of ~ 2 nm and the Si wafers are some hundreds of micrometres thick. (b) Schematic of a dewetting hole showing the contact line radius, $R(t)$, and the local height, $h(x,t)$, which decays to $h_0$ at large distances. The rim width, $W(t)$, is typically measured as the distance from the contact line to where the wet side of the rim reaches $1.1h_0$. Note that the vertical scales are not equivalent in (a) and (b).

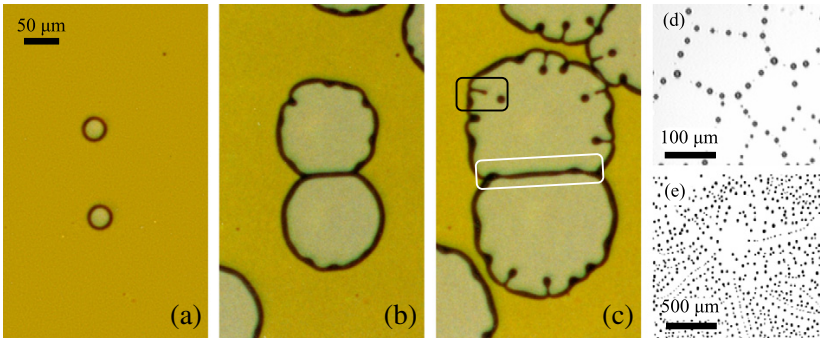


**Fig. 2.** Optical microscopy images of thin-film dewetting with slip. (a)–(c) Nucleation and growth of holes in a 272 nm thick PS(65 k) film dewetting from an OTS substrate at 135 °C. In (a) is shown the initial stages of isolated holes with azimuthally invariant rims. Eventually, the holes collide in (b) forming a ribbon; an instability in the azimuthal direction of the rim is also seen to develop. (c) In the black box is shown the breakup of a radially directed finger which follows from the rim instability; the white box encloses a ribbon formed due to the coalescence of holes, which begins to show a Raleigh–Plateau instability. (d) Final droplet pattern formed on a weak-slip substrate not displaying the rim instability before hole coalescence. (e) Final droplet pattern on a strong-slip substrate with a low density of holes.

investigate the structure of the solid–liquid interface, complementary experimental techniques such as x-ray reflectometry or neutron reflectometry are needed, as will be discussed below [40]. See refs. [7,40] for a complete discussion of the possible role of apparent slip in our studies, for entangled and unentangled polymers, respectively.

In the case of viscous film bursting (*e.g.* [41] and [42]), a uniform thickening of free-standing films can be observed as holes grow. This thickening occurs over timescales comparable to the speed of sound in the liquids, *i.e.* much faster than the hole opening time. When a similar film is placed into contact with a substrate, however, the significant friction at the solid–liquid interface prevents material from being transported so quickly. In any case, volume conservation is a requirement. "In a supported film" a rim with characteristic width, $W$ (see Fig. 1), is thus formed ahead of the three-phase contact line. Since at large distances it is also required that the supported film be undisturbed, there must be a smooth decay of the rim building near the contact line to the far field portions of the film.

It is precisely this decay, quantified using the mathematical models reviewed in Section 3, that allows us to extract information about the slip length and capillary velocity. The morphological details of this rim and its temporal evolution can provide much insight into the slip boundary condition. In particular, the slip length can be accessed in two complimentary ways. First, the dynamics for the radius of a hole, $R(t)$, can be observed with the use of optical microscopy [5,7]. Combining the energy dissipation mechanisms of viscous [43] and substrate frictional [9] losses within the rim leads to a quantification of the slip length [5]. Second, the full shape of the dewetting front can be revealed using AFM either *in situ* or after a quench to below $T_g$. Using hydrodynamic models [4,10,32], it is possible to relate the detailed shape of the rim near the undisturbed liquid film (the 'wet side' of the dewetting rim) to the slip length, $b$, and the capillary number,

$$Ca = \dot{R}\eta\gamma^{-1}, \tag{2}$$

where $\eta$ is the fluid viscosity, $\gamma$ is the liquid–vapour surface tension, and $\dot{R}$ is the velocity of the three-phase contact line.

Fig. 2 shows the results of experiments highlighting the importance of slip in pattern formation during dewetting. In these images, contrast arises from variations in optical path length, largely determined by local thickness of the film. Figs. 2(a) to (c) show the evolution of a thin film sample undergoing nucleated dewetting, with the coalescence of two holes and a fingering instability in the dewetted rim both breaking up due to separate Rayleigh–Plateau instabilities. Figs. 2(d) and (e) show the late-stage pattern of droplets left behind from completely dewetted thin liquid films. In Fig. 2(d), a cellular pattern is observed on a substrate displaying weak-slip, while in Fig. 2(e) 'rays' of droplets can be seen on a substrate displaying strong-slip[2]. These observations, while discussed in detail below, motivate part of the discussion presented in this work: Why are the morphological evolutions and the final droplet patterns seen in Fig. 2 different on different substrates, even while the liquids are the same? Here, we will discuss the importance of slip in determining the resulting pattern formation.

In a recent work [7], we noted that for identical liquids, the driving force on an AF1600 fluoropolymer coating is larger than on a silanized substrate, yet hole growth proceeds faster on the silanes. Furthermore, for nearly identical wettability (*i.e.* silanes with different chain lengths), it is possible to observe slip lengths that differ significantly. What is the origin of this trend in the slip lengths? To answer this question, we must try to understand the microscopic origin of slip. Here we will discuss recent experiments that elucidate this question.

## 2. Experiments

For all experiments presented here, polystyrene (PS, purchased from PSS Polymer Standards Service) with weight averaged molecular weights $M_w$ = 10.3, 12.5, 13.7 or 65 kg/mol and polydispersity indices, PI < 1.1 have been used. PS was dissolved in toluene with various concentrations. These solutions were spin coated onto freshly cleaved mica substrates, resulting in films with thicknesses $80<h_0<300$ nm, and floated onto the surface of an ultra-clean water bath (Milli-Q, 18.2 MΩ cm at 25 °C, total organic carbon content less than 6 ppb). These films were then picked up using hydrophobized Si wafers (Wacker Siltronic or Si-Mat Silicon Materials, 100 crystal orientation). This floating procedure is necessary because of the hydrophobicity of the substrates used. Attempting to spin coat directly onto the wafers results in an ejection of the polymer solution. It is difficult to make a film of sufficient uniformity or extent without floating.

Hydrophobization was accomplished in two ways. First, peroxymonosulphuric acid ('piranha,' composed of equal parts $H_2O_2$ and $H_2SO_4$) cleaned Si wafers with a native $SiO_2$ [44] layer present were dip coated from a solution containing the fluorinated polymer AF1600 (Poly[4,5-difluoro-2,2-bis(trifluoromethyl)-1,3-dioxide-co-tetrafluoroethylene], Sigma-Aldrich) dissolved in the perfluoro-compound FC-75 ($C_8F_{16}O$, Acros Organics). Second, hydrophobization was accomplished by silanization with octadecyl- or dodecyl-trichlorosilane (OTS from Sigma-Aldrich or DTS from Fluka). A detailed description of this silanization procedure can be found in [45]. A schematic of the typical substrates we use is seen in Fig. 1.

[2] Weak-slip indicates that $b \ll h_0$. Strong-slip indicates $b \gg h_0$.

In order to capture the dynamics of dewetting holes, samples are heated to above $T_g \approx 100$ °C and holes are nucleated heterogeneously. Optical microscopy (Leitz) and AFM (Bruker Dimension Fastscan or Multimode) are used to record the evolution, giving $R(t)$ and $h(x,t)$ respectively[3].

## 3. Determination of the slip length

As previously mentioned, it is possible to determine a slip length, $b$, from observations of $R(t)$ and from $h(x,t_0)$ for a given time, $t_0$; $R$ and $h$ are schematically defined in Fig. 1. It is important to note that this analysis is valid only for intermediate stages of dewetting; that is, late enough for the rim to be self-similar, but early enough as in Fig. 2(a), for which the Rayeigh–Plateau instability has not yet been observed, as in Fig. 2(b) and (c). The model to be summarized assumes no flow along the rim, a condition which is violated as soon as undulations of the rim set in. Furthermore, we assume everywhere that gravitational forces can be neglected; all films have thicknesses $h_0 \sim 100$ nm, which is much less than the capillary length [48] $\kappa^{-1} = \sqrt{\gamma/\rho g} \approx 1$ mm for PS, where $\rho$ is the liquid density and $g$ is the gravitational acceleration. We also assume that van der Waals forces can be neglected except directly in the vicinity of the contact line [49]. In previous works [4,5,7] the models have been described in detail. Furthermore, the assumptions and consequences of these models have been extensively tested [33]. As such, we provide here only a brief description of the methods for completeness.

### 3.1. Hole growth dynamics

The main idea for the determination of $b$ from $R(t)$ data is that the surface energy gained by dewetting is dissipated, as discussed by Brochard-Wyart and co-workers, either as viscous dissipation in a wedge of fluid near the contact line [43], or through friction with the substrate beneath the rim of dewetted material [9]. For a no-slip substrate, nearly all of the energy is dissipated in a wedge of fluid near the contact line. In this no-slip case, the viscously dissipated power is

$$P_v \propto v_v = C_v(\theta)\frac{|S|}{\eta}, \tag{3}$$

where $v_v$ is the dewetting velocity in a pure no-slip case and

$$S = \gamma_{sv} - (\gamma + \gamma_{sl}) = \gamma(cos\theta - 1), \tag{4}$$

is the spreading parameter [48], which provides the driving force for dewetting. $\gamma_{ij}$ is the surface tension between components $i$ and $j$, with $v$, $l$ and $s$ representing the vapour, liquid and solid phases. $C_v$ is a proportionality constant [43] that depends on the contact angle, $\theta$, at the three-phase contact line.

For a full-slip situation, also referred to as 'plug flow' in which the fluid velocity is uniform in the $z$-direction, the energy is predominantly dissipated through friction along the width, $W$, of the rim at the liquid–substrate interface. In this case, the power dissipated is

$$P_s \propto v_s = \frac{|S|b}{3\eta W}, \tag{5}$$

where $v_s$ is the dewetting velocity in the pure plug flow case. By volume conservation and self-similarity, the rim width is related to the hole radius through $W = C_s\sqrt{h_0 R}$, where $C_s$ is a constant that can be determined by plotting the width of the rim as a function of the hole radius [5] for a given $h_0$.

[3] For the PS molecular weights used here, which are significantly lower than the critical molecular weight for entanglements [46], long-term annealing effects related to non-equilibrium entanglement networks [47] are not expected to play a role. This independence was demonstrated in [7] and was verified here.

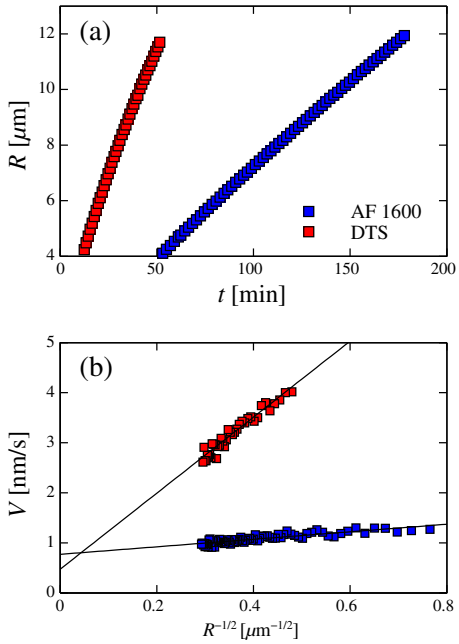


**Fig. 3.** Hole growth data for PS(10 k) films annealed at $T = 110$ °C with $h_0 = 102$ nm and $h_0 = 93$ nm for AF1600 and DTS. (a) Hole radius, $R$, as a function of time, $t$, as measured by optical microscopy. (b) Contact line velocity, $V$, as a function of $R^{-1/2}$, the inverse square root of the hole radius for the data represented in (a), and with the use of an identical colour scheme.

Viscous friction in a wedge near the contact line and friction arising from the liquid sliding against the substrate are the two dominant energy loss mechanisms in a dewetting front [9,43]. Therefore, the sum of these two contributions accounts well for the dewetting dynamics as captured by $R(t)$ [50]. If the results are consistent with our model, then combining Eqs. (3) and (5) we find that the dewetting velocity should satisfy

$$V = \dot{R} = V_0 + \frac{K}{\sqrt{R}}, \tag{6}$$

where $V_0$ and $K$ are constants for a given dewetting film. Written in this way, we see that plotting the dewetting rate as a function of the inverse square root of the contact line radius, we expect a straight line to be observed [5]. In particular, we have:

$$V_0 = C_v\frac{|S|}{\eta}, \tag{7}$$

and

$$K = \frac{1}{3}\frac{|S|}{\eta}\frac{b}{C_s\sqrt{h_0}}. \tag{8}$$

With the exception of $b$, all the quantities in Eq. (8) are measurable from the dewetting experiment or can be found independently [5]. Obtaining $K$ from a dewetting experiment is thus one method by which the slip length of a dewetting polymer film can be determined.

Fig. 3(a) shows the dynamics, $R(t)$, for PS(10 k) films dewetting at 110 °C. This data clearly shows that the temporal evolution for all samples is non-linear. This non-linearity indicates that the simple no-slip model [43] as expressed by Eq. (3) is not satisfied (constant velocity dewetting gives $R \sim t$ [43]). Alternatively, Fig. 3(b) shows $V(R^{-1/2})$ following Eq. (6). As predicted, we see that all data in Fig. 3(b) are well

described by linear functions. Clearly, the film dewetting on DTS shows the largest slope in this representation, indicating that DTS gives rise to a larger slip length than does AF1600.

Using the data in Fig. 3, an estimate for the slip length is possible through Eq. (8)[4]. Before reporting specific values for the slip lengths, however, we discuss a second method of determining $b$ from dewetting experiments. This second method is consistent with the hole growth analysis when comparing slip lengths between different systems. It is also more powerful in differentiating slip on no- or weak-slip substrates, and relies only on a single measurement: that of the height profile, $h(x, t_0)$ for a given time, $t_0$.

### 3.2. Rim profile analysis

A second method of determining the slip length in a dewetting experiment is by analysing the decay of the rim into the undisturbed film at large distances [4,7,10,32,51]. Normalized height profiles of two dewetting rims are shown in Fig. 4. Non-universality of the curves in this normalized representation indicates that there are parameters other than the film height and hole radius governing their shapes; in the following we outline steps leading to the conclusion that $b$ and $Ca$ are also required for a complete description. The starting point of this analysis is the Stokes equation for the flow field $\mathbf{u} = (u,w)$:

$$-\nabla p + \eta\nabla^2\mathbf{u} = 0, \tag{9}$$

with the no-stress condition at $z = h$. The slip length, $b$, enters through the Navier slip boundary condition, Eq. (1), applied at $z = 0$. In Eq. (9), $p$ is the pressure, which is dominated by the Laplace pressure, $p \approx -\gamma\partial_x^2 h$. The problem can be rescaled according to the lubrication approximation using the small parameter $\epsilon = H/L \ll 1$ with $H$ and $L$ the typical height and length scales. After rescaling, the problem is cast in terms of the stream function and local film height [4], $\psi$ and $h(x,t)$ where the stream function is defined through $\partial_z\psi = u$ and $-\partial_x\psi = w$; this stream function guarantees incompressibility: $\nabla \cdot \mathbf{u} = 0$. Having reformulated the scaled Stokes equation, Eq. (9), the problem is then linearized through $h = h_0 + \delta\tilde{h}$ and $\psi = \delta\tilde{\psi}$ with $\delta \ll 1$. The ansatz

$$\tilde{\psi} = \hat{\psi}(z)exp(k\xi) \quad \text{and} \quad \tilde{h} = \hat{h}exp(k\xi), \tag{10}$$

is used, with $\xi = x - R(t)$ being the horizontal coordinate in the reference frame of the moving contact line. It is through $\xi$ that the capillary number enters the solution. The inverse length scales, which may be complex, are denoted by $k$. This ansatz leads to the final result [4,51]: a characteristic equation in $k$ that depends on $b$ and $Ca$, see Eqs. (1) and (2). Expanding the characteristic equation to third order in $\epsilon$, one gets

$$\left(1+\frac{h_0}{3b}\right)(h_0k)^3 + 4Ca\left(1+\frac{h_0}{2b}\right)(h_0k)^2 - Ca\frac{h_0}{b} = 0. \tag{11}$$

This characteristic equation has two roots which satisfy the condition that the film height goes to $h_0$ as $x \to \infty$.

Rim profiles have been measured and are shown in Fig. 4. There we observe damped oscillatory decays into $h_0$, characterized by a dip near the undisturbed film[5]. We fit the profiles using a superposition of exponentials, where the $k$ can be either purely real or imaginary (while not observed in these profiles, a purely monotonic profile is also commonly observed [7,32,36,52]). Both monotonic and damped oscillatory approaches to $h_0$ are captured by the characteristic equation, Eq. (11), corresponding to purely real and negative $k$, or complex $k$ respectively. A third solution to the characteristic polynomial is unphysical since it has positive real $k$, predicting an amplification of the perturbation.

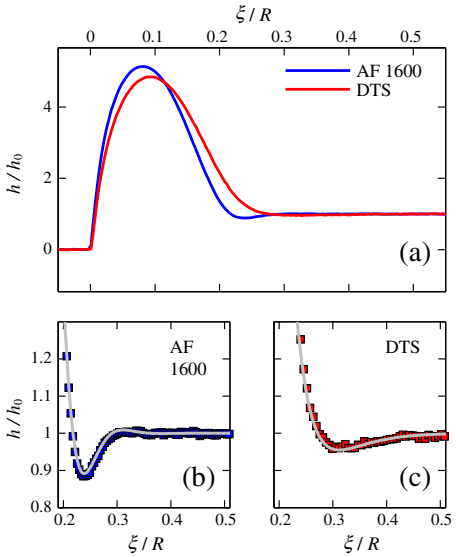


**Fig. 4.** Normalized height profiles for PS(10 k) films annealed at $T = 110$ °C. (a) Full profiles for films on: AF1600, $h_0 = 92$ nm, $R = 12.3$ μm; and DTS, $h_0 = 96$ nm, $R = 11.8$ μm. (b) and (c) show the same data as in (a), but also show best fits of Eq. (15) to the data.

For a monotonically decaying rim displaying no dip (or oscillation), the fitting function is a superposition of two damped exponentials

$$\delta h_{\text{mono}} = \delta_1 exp(k_1\xi) + \delta_2 exp(k_2\xi). \tag{12}$$

With the two inverse length scales, $k_1$ and $k_2$, determined Eq. (11) is inverted and the slip length is found according to [4,51]

$$b_{\text{mono}} = \frac{1}{4h_0}\frac{k_1^2 + k_1k_2 + k_2^2}{k_1^2k_2^2} - \frac{h_0}{2}. \tag{13}$$

Independently[6], it is possible to determine the capillary number according to

$$Ca_{\text{mono}} = -\frac{h_0}{4}\frac{k_1^2 + k_1k_2 + k_2^2}{k_1 + k_2} + \frac{h_0^3}{6}\frac{k_1^2k_2^2}{k_1 + k_2}. \tag{14}$$

For oscillatory profiles the fitting function has the form

$$\delta h_{\text{osc}} = \delta_0 exp(k_r\xi)cos(k_i\xi + \phi), \tag{15}$$

and in Eqs. (13) and (14), we instead use $k_{1,2} = k_r \pm ik_i$. In this oscillatory case, Eqs. (13) and (14) become

$$b_{\text{osc}} = \frac{1}{4h_0}\frac{3k_r^2 - k_i^2}{\left(k_r^2 + k_i^2\right)^2} - \frac{h_0}{2}, \tag{16}$$

[4] With $K$ measured, one uses a measured film height, $h_0$, the spreading parameter, $|S|$ (for the systems used here see [7]), $C_s$ values from $W(R)$ [5], and $\eta$ from viscometry [8] to isolate the slip length, $b$.

[5] Though not prominent here, oscillatory profiles often show a prominent second maximum on the wet side of the rim. See for example Fig. 6 in Section 4.2 and ref. [32].

[6] If the two inverse length scales, $k_{1,2}$, cannot be distinguished and a single exponential fit describes the data well, obtaining $Ca$ from hole growth data, $R(t)$, is required, from which $b_{\text{mono}}$ can be obtained.

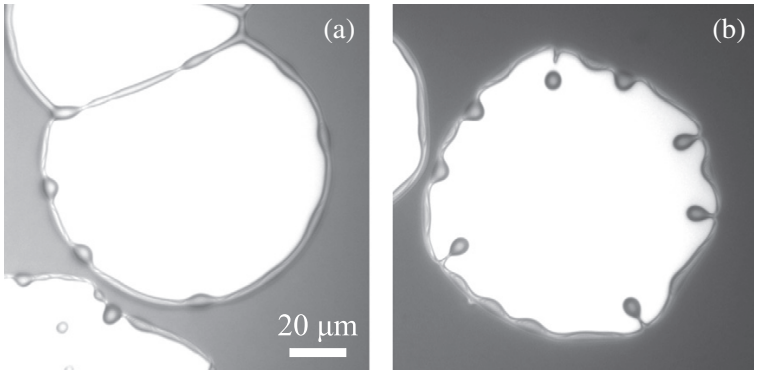


**Fig. 5.** Optical microscopy images of 80 nm PS(12 k) films annealed at 120 °C. (a) Dewetting on a weak-slip AF1600 substrate showing a less developed rim instability as compared to DTS (b) at similar hole radii. The hole on DTS shows a well developed rim instability and pinch-off. The scale bar applies to both images.

and

$$Ca_{osc} = -\frac{h_0}{8}\frac{3k_r^2 - k_i^2}{k_r} + \frac{h_0^3}{12}\frac{\left(k_r^2 + k_i^2\right)^2}{k_r}. \tag{17}$$

In Figs. 3 and 4, we show respectively data for the dynamics of hole growth and a rim shape analysis of 10 kg/mol PS on AF1600 and DTS (OTS omitted for clarity). For the rim shape analysis, profiles were measured at the same hole radius, thus the volume of the rim is nearly identical in each case. Each of the films was annealed at the same temperature and had identical thickness. Therefore, differences in the dynamics or rim shapes are entirely due to the substrate on which dewetting occurs. We have extracted slip lengths using both methods described in Section 3. From the rim shape analysis of several oscillatory profiles such as those seen in Fig. 4, we find that for PS(10 k) at 110 °C

$$\begin{aligned} b_{AF1600} &= 50 \pm 40 \text{ nm}, \\ b_{OTS} &= 160 \pm 30 \text{ nm}, \\ b_{DTS} &= 1500 \pm 200 \text{ nm}, \end{aligned} \tag{18}$$

which are consistent with our previous studies using PS(13 k) [4,7]. Since the molecular weight and temperature for the polymer films giving these slip lengths are identical, they should also have the same viscosity. Using Eq. (17) we have determined the corresponding capillary numbers and determined the viscosities for PS(10 k) through Eq. (2), $\gamma = 30.8$ mN/m [53] and $\dot{R}$ from data as shown in Fig. 3. We find that these viscosities are independent of the substrate, and the value obtained is $\eta = (1.4 \pm 1) \times 10^6$ Pa s. Through the WLF equation [46,54] for the temperature dependence of the viscosity, our reported viscosity is consistent with previous studies [7] and bulk measurements of the polymer viscosity [4].

## 4. Discussion

In the previous section we observed three different slip lengths on three different substrates. On one hand, it is perhaps not surprising that chemically different surfaces give rise to different slip lengths, as between AF1600 and the self-assembled silanes. On the other hand, systematic and disparate slip lengths are consistently [4,7,33] observed on chemically identical [7] silanes. This observation is yet to fully be explained on a molecular level.

This section is divided into three parts. We first take advantage of the different slip lengths reported above to elucidate the origins of different droplet patterns observed in Fig. 2(d) and (e). Second, we use these different slip lengths to motivate a discussion concerning a possible mechanism for the microscopic origin of the slip. In this second part we place an emphasis on the role of liquid–substrate interfacial ordering [23,55]. In the third and final part, we give an outlook on future research directions.

### 4.1. Droplet patterns

Concerning the droplet pattern in Fig. 2(d), we see for the case of dewetting from no- or weak-slip substrates, such as unentangled PS on AF1600, that a cellular droplet pattern arises [3]. To explain this droplet distribution, we note that during the drying of a film, holes nucleate heterogeneously across the surface. In the weak-slip regime realized by PS on AF1600, these holes grow with material being collected in a rim surrounding the dry spot. Eventually, holes coalesce and form a ribbon of fluid on the substrate, see Figs. 2 and 5(a). This ribbon is unstable to the Rayleigh–Plateau instability (RPI). Thus, the droplet pattern observed in the absence of slip is determined by the distribution of hole nucleation sites on the substrate. Droplets predominantly appear only where two holes collide.

When the dewetting fluid is on a substrate with significant slip, such as PS on DTS, the situation is quite different [56]. The evolution of holes in a typical dewetting experiment is shown in Fig. 2(a)–(c). The late stage of a rim instability on substrates with strong-slip can be seen in 2(e) and in Fig. 5(b). If the hole density is low enough, a RPI in the dewetting rim can be observed before the coalescence of distinct holes occurs. This instability leads to a fingering effect, the details of which are described in [56], and a radial droplet pattern is then observed due to a RPI in the fingers. Thus, the droplet pattern is sensitive to the slip length in comparison with the film thickness, and to the distribution of nuclei for dewetting.

The difference between droplet patterns observed in the strong- and weak-slip systems described in the previous two paragraphs can be explained by comparing Eqs. (3) and (5). For the no-slip case, energy dissipation mainly occurs in a small region near the contact line — the dissipation rate does not depend on the rim width.

In contrast, energy dissipation for a strong-slip dewetting scenario, as indicated in Eq. (5), depends directly on the rim width as $P_s \propto W^{-1}$. Since the energy dissipation rate is proportional to the dewetting velocity, any spatial modulation of the rim width along the rim can lead to a spatial modulation in the local dewetting velocity[7]. As seen in Fig. 2, a RPI in the rim represents such a rim width perturbation.

In the weak-slip case observed on AF1600, this width perturbation has no significant effect on the dewetting velocity as captured by Eq. (3). However, a rim width perturbation in the strong-slip case, as observed on DTS, becomes amplified [56] as a result of the dominant

[7] This argument is valid when the driving force is spatially uniform, which is the case here.

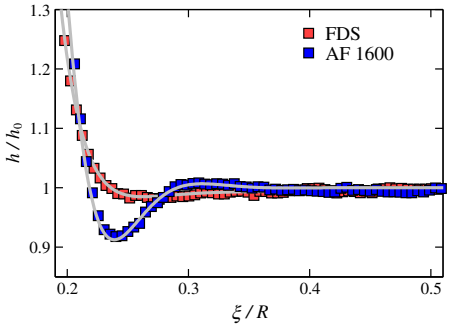


**Fig. 6.** Height profiles for PS(13 k) films annealed at $T = 110$ °C on: AF1600, $h_0 = 118$ nm, $R = 12.0\ \mu$m; and FDS, $h_0 = 119$ nm, $R = 12.0\ \mu$m.

energy dissipation mechanism. The larger rim width at bulges, see Fig. 2(b), leads to a smaller velocity as compared to the thinner rim sections of the rim between bulges (the 'valleys'). As the RPI proceeds, material from the valleys empties into the bulges due to the Laplace pressure gradient and the dewetting velocity difference is therefore further amplified. This amplification leads to the formation of liquid fingers [56] in the late stages of dewetting. These radial fingers eventually break up leaving behind the droplet pattern observed in Fig. 2(e). Thus, the observation of radial droplet distributions is a strong indication for a strong-slip dewetting scenario.

### 4.2. Molecular origin of slip

As mentioned above, the slip lengths measured for identically prepared films of PS(10 k) on AF1600, OTS and DTS range over approximately 2 orders of magnitude. This is particularly surprising in the case of slip lengths on OTS and DTS, since their composition differs only in the number of carbon atoms they contain along their backbones: for OTS, there are 18 carbon atoms while for DTS there are 12. To state this simply, OTS and DTS are chemically identical resulting in identical wetting properties [7]. However, slip lengths on these surfaces are consistently observed to be different for identical PS films [4,5,51]. This observation begs the question: why are the slip lengths different?

In the following, we summarize our recent efforts aimed at answering this question. In a combined x-ray and neutron reflectivity study [40] the structure of the self-assembled monolayers (SAMs) and the density of the adjacent PS were determined. The x-ray data of bare substrates (without PS) suggest that OTS molecules are bound upright on the Si surfaces. The same type of reflectivity data suggest that DTS molecules are tilted by up to 30° with respect to the Si surface-normal direction [40]. With the addition of a PS layer atop the SAMs, it was found that the x-ray data could be explained by assuming an ordering of phenyl rings (the PS side groups, which are distributed randomly on either side of the chain backbone, see Fig. 8) that replicates the structure of the SAM. We proposed [40] that this order may be induced by the orientation of the silanes, providing a possible mechanism for the difference in slip lengths observed on OTS and DTS.

The importance of substrate structure has also been tested using fluorinated silane molecules containing 10 carbon atoms in the backbone (2-H perfluorodecyltrichlorosilane, here called FDS). In these silanes, most of the hydrogen atoms of a 'regular' silane are replaced with fluorine atoms[8]. In this way, the surface energy of the resulting substrates is comparable to that of the AF1600 substrates used (Young's contact angle of $\theta_Y = 88°$ for PS, and advancing contact angle $\theta_a = 128°$ for ultra-pure water [7]), but the self-assembled monolayer structure of the OTS or DTS covered substrates is retained. In Fig. 6 are shown two dewetting rim profiles for which the polymer films are nearly identical, and for which the only difference is the underlying substrate. The two substrates used were AF1600 and FDS. Using the rim shape analysis described in Section 3.2 applied to several samples such as those depicted in Fig. 6, we find that for PS(13 k) at 110 °C

$$b_{\mathrm{AF1600}} = 20 \pm 40\ \mathrm{nm},\quad b_{\mathrm{FDS}} = 420 \pm 40\ \mathrm{nm}. \tag{19}$$

Thus, the slip lengths on FDS are significantly larger than those observed on amorphous AF1600 for dewetting of identical PS films. These results are consistent with the idea that the substrate structure (and not necessarily the surface energy) can be responsible for inducing specific solid–liquid interfacial structure, which in turn may give rise to enhanced slip. In Fig. 7 is shown a summary of the slip lengths, in order of increasing slip, we have measured on the various substrates discussed here for PS(13 k) at 110 °C. The results using PS(10 k) on DTS, OTS and AF1600 at the same temperature (Section 3) are qualitatively consistent with this picture. We finish this discussion by noting that the horizontal axis in Fig. 7 is not quantitative, and we hope that future investigations, for example using molecular dynamics simulations and/or the further experiments outlined below, may help to assign the appropriate x-coordinate(s).

### 4.3. Outlook

As a final note, we mention that a specific substrate order on its own may not be enough to induce strong slip. Rather, the combination of substrate and liquid (in our experiments PS melts on silanized Si wafers) is likely to be responsible for the observation of strong slip. To test this idea, dewetting studies with polymethylmethacrylates (PMMA) and polyvinylpyridines (PVP) with molecular weights comparable to those of the PS used here have been initiated. Preliminary results indicate a much weaker slip effect of PMMA as compared to the PS on the same substrates and with liquids of a similar viscosity. The slip lengths observed between PVP and silanized Si wafers are intermediate to those of PS and PMMA. This observation is enticing, since it indicates that the monomeric structure of the liquid (see Fig. 8) has an effect on the macroscopic phenomenon of slip. According to our observations, the presence of a phenyl ring in the side group of a polymer

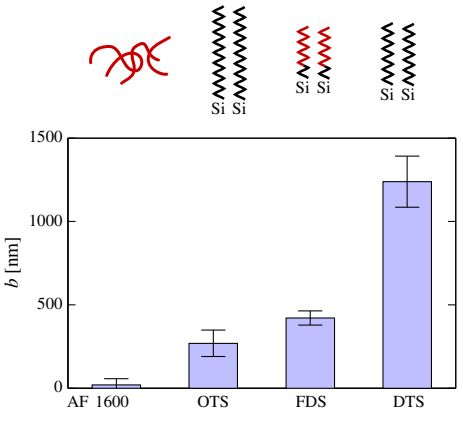


**Fig. 7.** Slip lengths measured for PS(13 k) at 110 °C on the four substrates discussed in this work. The schematics above the main plot indicate the substrate structure, with AF1600 an amorphous polymer layer while the silanes are self assembled monolayers (structural details of OTS and DTS layers can be found in [40]). Red lines indicate fluorinated carbon backbones, while black lines indicate hydrogenated carbon backbones; for the silanes, each line segment represents a carbon–carbon bond, except for the terminal Si group, which is bonded to the amorphous $SiO_2$ layer at the top of the Si substrates.

[8] For a given FDS molecule described here, the eight carbon atoms closest to the substrate–fluid interface are saturated with fluorine atoms.

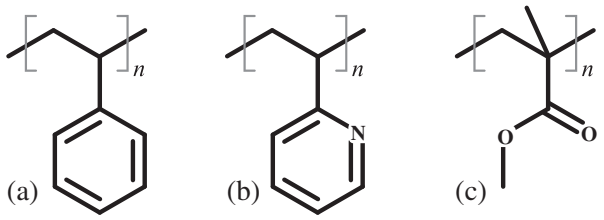


**Fig. 8.** Schematic representation of the different monomers used in preliminary dewetting experiments. (a) Shows the styrene monomer, (b) the 2-vinyl pyridine monomer and (c) the methyl methacrylate monomer. Where not indicated, junction points represent carbon atoms and these atoms are saturated with hydrogen. The grey brackets indicate the bounds of the monomer, which in a given polymer is repeated *n* times.

chain is correlated with slip on a silanized Si substrate. While our interpretation is speculative, these observations suggest that the specific interactions between polymer side groups and solid surface structure [23,55] play a large role in the determination of slip. Future research efforts will be aimed at more precisely elucidating this idea.

## 5. Conclusion

In the last decade, a microfluidic probe that takes advantage of internal capillary forces to determine, in particular, information about the solid–liquid boundary condition has been developed. With the help of hydrodynamic models, a determination of the slip length in thin polymer films can be achieved. In recent times, this framework has led to investigations of macroscopic pattern formation of dewetting films, and the dependence of these patterns on slip. In conjunction with techniques such as neutron and x-ray reflectivity, it is also possible to probe details about the slip boundary condition at the monomer level.

On the macroscopic level, we have here discussed the resulting droplet patterns that are formed from various dewetted thin films. The final droplet distribution is highly sensitive to the slip length in comparison with the film thickness: a radial droplet pattern of dewetted droplets is a strong indication of the presence of strong slip.

We have also summarized the possible importance of a substrate–fluid interfacial structure. The specific case studied here is that of silanized substrates covered by unentangled polymers. Early results indicate that different interfacial structures between phenyl rings and different silanes may be responsible for the different slip lengths observed. Future research efforts will be designed to elucidate these differences, and to test the claim that the phenyl ring orientation can play an important role in the magnitude of slip.

Finally, we wish to emphasize that the developed theoretical framework, in addition to the experimental systems described, allows for a systematic variation of the slip length. In particular, either by changing the length of the self-assembled silane molecules, or by using FDS in conjunction with AF1600, it is possible to achieve different slip lengths while keeping the substrate surface energy constant. We hope that this will be a powerful general tool that may help to elucidate the effect of slip in other nano-fluidic processes yet to be studied.

## Acknowledgement

For financial support, the authors: wish to thank the German Research Foundation (DFG) under grants JA905/3 within the priority programme 1164 (Micro- and Nanofluidics) and BA3406/2; they thank the graduate school GRK1276 at Saarland University; and JDM gratefully acknowledges NSERC of Canada. We also warmly thank R. Fetzer, A. Münch, B. Wagner, and M. Rauscher for many useful discussions and fruitful ongoing collaboration.

## References

[1] Lauga E, Brenner M, Stone H. Handbook of experimental fluid mechanics. New York: Springer; 2007.
[2] Squires T, Quake S. Rev Mod Phys 2005;77:1016.
[3] Reiter G. Phys Rev Lett 1992;68:75.
[4] Fetzer R, Münch A, Wagner B, Rauscher M, Jacobs K. Langmuir 2007;23:10559.
[5] Fetzer R, Jacobs K. Langmuir 2007;23:11617.
[6] Bäumchen O, Jacobs K. Soft Matter 2010;6:6028.
[7] Bäumchen O, Fetzer R, Klos M, Lessel M, Marquant L, Hähl H, et al. J Phys Condens Matter 2012;24:325102.
[8] McGraw J, Salez T, Bäumchen O, Raphaël E, Dalnoki-Veress K. Phys Rev Lett 2012; 109:128303.
[9] Brochard-Wyart F, de Gennes P, Hervet H, Redon C. Langmuir 1994;10:1566.
[10] Münch A, Wagner B, Witelski T. J Eng Math 2005;53:359.
[11] Bocquet L, Charlaix E. Chem Soc Rev 2009;39:1073.
[12] Oron A, Davis S, Bankoff S. Rev Mod Phys 1997;69:931.
[13] Craster M, Matar O. Rev Mod Phys 2009;81:1131.
[14] Blossey R. Thin liquid films: dewetting and polymer flow. Springer; 2012.
[15] Navier C. Mem Acad Sci Inst Fr 1823;6:389.
[16] Zhu Y, Granick S. Phys Rev Lett 2002;88:106102.
[17] Sun G, Bonaccurso E, Franz V, Butt H-J. J Chem Phys 2002;117:10311.
[18] Bonarcuso E, Butt H-J, Craig S. Phys Rev Lett 2003;90:144501.
[19] Vinogradova O, Belyaev A. J Phys Condens Matter 2011;23:184104.
[20] Tretheway D, Meinhart C. Phys Fluids 2002;14:L9.
[21] Pit R, Hervet J, Léger L. Tribol Lett 1999;7:147.
[22] Pit R, Hervet J, Léger L. Phys Rev Lett 2000;85:980.
[23] Schmatko T, Hervet H, Léger L. Phys Rev Lett 2005;94:244501.
[24] Neto C, Evans D, Bonaccurso E, Butt H-J, Craig V. Rep Prog Phys 2005;68:2859.
[25] Wang G, Prabhakar P, Sevick E. Phys Rev Lett 2009;103:248303.
[26] Wang G, Prabhakar R, Gao Y, Sevick E. J Opt 2011;13:044009.
[27] Lissandrello C, Yakhot V, Ekinci K. Phys Rev Lett 2012;108:084501.
[28] Schlomovitz R, Evans A, Boatright T, Dennin M, Levine A. Phys Rev Lett 2013;110: 137802.
[29] Cuenca A, Bodiguel H. Phys Rev Lett 2013;110:108304.
[30] Täuber D, Trenkmann I, Borczyskowski C. Langmuir 2013;29:3583.
[31] Cho J-HJ, Law B, Rietaud F. Phys Rev Lett 2004;92:166102.
[32] Fetzer R, Jacobs K, Münch A, Wagner B, Witelski T. Phys Rev Lett 2005;95:127801.
[33] Fetzer R, Rauscher M, Münch A, Wagner B, Jacobs K. Europhys Lett 2006;75:638.
[34] Bäumchen O, Fetzer R, Jacobs K. Phys Rev Lett 2009;103:247801.
[35] Brochard-Wyart F, Daillant J. Can J Phys 1990;68:1084.
[36] Seemann R, Herminghaus S, Jacobs K. Phys Rev Lett 2001;87:196101.
[37] Seemann R, Herminhaus S, Jacobs K. Phys Rev Lett 2001;86:5534.
[38] Reiter G, Akhrass SA, Hamieh M, Damman P, Gabriele S, Vilmin T, et al. Eur Phys J Spec Top 2009;166:165.
[39] Raegen A, Chowdhury M, Calers C, Schmatulla A, Steiner U, Reiter G. Phys Rev Lett 2010;105:227801.
[40] Gutfreund P, Bäumchen O, Fetzer R, van der Grinten D, Maccarini M, Jacobs K, et al. Phys Rev E 2013;87:012396.
[41] Debrégas G, Martin P, Brochard-Wyart F. Phys Rev Lett 1995;75:3886.
[42] Dalnoki-Veress K, Nickel B, Roth C, Dutcher J. Phys Rev E 1999;59:2153.
[43] Redon C, Brochard-Wyart F, Rondelez F. Phys Rev Lett 1991;66:715.
[44] Loskill P, Hähl H, Faidt T, Grandthyll S, Müller F, Jacobs K. Adv Colloid Interf Sci 2012; 107:179182.
[45] Lessel M, Bäumchen O, Klos M, Hähl H, Fetzer R, Seemann R, et al. arXiv: 1212.0998 [cond-mat.mtrl-sci]; 2013.
[46] Rubinstein M, Colby R. Polymer physics. Oxford University Press; 2003.
[47] Barbero D, Steiner U. Phys Rev Lett 2009;102:248303.
[48] de Gennes P, Brochard-Wyart F, Quéré D. Capillarity and wetting phenomena: drops, bubbles, pearls, waves. New York: Springer; 2003.
[49] Seemann R, Herminghaus S, Neto C, Schlagowski S, Podzimek D, Konrad R, et al. J Phys Condens Matter 2005;17:S267.
[50] Jacobs K, Seemann R, Schatz G, Herminghaus S. Langmuir 1998;14:4961.
[51] Bäumchen O, Fetzer R, Münch A, Wagner B, Jacobs K. IUTAM symposium on advances in micro- and nanofluidic. Springer; 2009. p. 51.
[52] Reiter G, Hamieh M, Damman P, Sclavons S, Gabriele S, Vilmin T, et al. Nat Mater 2005;4:754.
[53] Brandrup J, Immergut E, Grulke E. Polymer handbook, vol. 4. New York: Wiley; 1999.
[54] Williams M, Landel R, Ferry J. J Am Chem Soc 1955;77:3701.
[55] Gutfreund P, Wolff M, Maccarini M, Gerth S, Ankner J, Browning J, et al. J Chem Phys 2011;134:064711.
[56] Bäumchen O, Marquant L, Blossey R, Münch A, Wagner B, Jacobs K. Influence of slip on the Rayleigh–Plateau rim instability in dewetting viscous films; 2014 [under review].

# Addendum II - Influence of slip on the Plateau-Rayleigh instability on a fibre

Authors: S. Haefner[1,2], M. Benzaquen[3], O. Bäumchen[2,4], T. Salez[3], R. Peters[2], J. D. McGraw[1], K. Jacobs[1], E. Raphaël[3], and K. Dalnoki-Veress[2,3]

[1] Department of Experimental Physics, Saarland University, 66041 Saarbrücken, Germany.
[2] Department of Physics and Astronomy, McMaster University, 1280 Main Street West, Hamilton, Ontario, Canada, L8S 4M1.
[3] PCT Lab, UMR CNRS 7083 Gulliver, ESPCI ParisTech, PSL Research University, 75005 Paris, France.
[4] Max Planck Institute for Dynamics and Self-Organization (MPIDS), 37077 Göttingen, Germany.

*Nature Communications* **6**, 7409 (2015).
(`http://dx.doi.org/10.1038/ncomms8409`)



**Author contributions:**

S. Haefner developed the technique to apply homogeneous polymer films to fibres. S. Haefner performed all experiments and analyzed all data sets. Research was designed by O. Bäumchen, K. Dalnoki-Veress and S. Haefner. The custom-made software to analyze the data was written by R. Peters. The theoretical background was developed by M. Benzaquen, T. Salez and E. Raphaël. The manuscript was written by S. Haefner. All authors contributed to the research and manuscript preparation.

**Abstract -** The Plateau–Rayleigh instability of a liquid column underlies a variety of fascinating phenomena that can be observed in everyday life. In contrast to the case of a free liquid cylinder, describing the evolution of a liquid layer on a solid fibre requires consideration of the solid–liquid interface. Here we revisit the Plateau–Rayleigh instability of a liquid coating a fibre by varying the hydrodynamic boundary condition at the fibre–liquid interface, from no slip to slip. Although the wavelength is not sensitive to the solid–liquid interface, we find that the growth rate of the undulations strongly depends on the hydrodynamic boundary condition. The experiments are in excellent agreement with a new thin-film theory incorporating slip, thus providing an original, quantitative and robust tool to measure slip lengths.

nature COMMUNICATIONS

ARTICLE

Received 16 Jan 2015 | Accepted 5 May 2015 | Published 12 Jun 2015

DOI: 10.1038/ncomms8409 OPEN

# Influence of slip on the Plateau–Rayleigh instability on a fibre

Sabrina Haefner[1,2], Michael Benzaquen[3], Oliver Bäumchen[2,4], Thomas Salez[3], Robert Peters[2], Joshua D. McGraw[1], Karin Jacobs[1], Elie Raphaël[3] & Kari Dalnoki-Veress[2,3]

The Plateau–Rayleigh instability of a liquid column underlies a variety of fascinating phenomena that can be observed in everyday life. In contrast to the case of a free liquid cylinder, describing the evolution of a liquid layer on a solid fibre requires consideration of the solid–liquid interface. Here we revisit the Plateau–Rayleigh instability of a liquid coating a fibre by varying the hydrodynamic boundary condition at the fibre–liquid interface, from no slip to slip. Although the wavelength is not sensitive to the solid–liquid interface, we find that the growth rate of the undulations strongly depends on the hydrodynamic boundary condition. The experiments are in excellent agreement with a new thin-film theory incorporating slip, thus providing an original, quantitative and robust tool to measure slip lengths.

[1] Department of Experimental Physics, Saarland University, D-66041 Saarbrücken, Germany. [2] Department of Physics and Astronomy, McMaster University, 1280 Main Street West, Hamilton, Ontario, Canada, L8S 4M1. [3] PCT Lab, UMR CNRS 7083 Gulliver, ESPCI ParisTech, PSL Research University, 75005 Paris, France. [4] Max Planck Institute for Dynamics and Self-Organization (MPIDS), 37077 Göttingen, Germany. Correspondence and requests for materials should be addressed to K.D.-V. (email: dalnoki@mcmaster.ca).

Glistening pearls of water on a spider's web[1] or the breakup of a cylindrical jet of water into droplets are familiar manifestations of the Plateau–Rayleigh instability (PRI)[2,3]. By evolving into droplets, the surface area of the liquid and consequently the surface energy are reduced. This instability also acts for a liquid film coating a solid fibre[4–12], a situation where the flow boundary condition at the solid–liquid interface provides additional complexity to the system. Although the breakup of a homogeneous film into droplets on a fibre may be a nuisance in coating technologies of, for example, wires and optical fibres, this fundamental instability turns out to be very useful: take for example water collection through fog harvesting[13,14], a biomimetic approach that is perfected in nature by the spider's web[1]. Hence, taking advantage of the PRI on a fibre enables gaining physical insight into the solid–liquid boundary condition. Indeed, understanding the breakdown of the no-slip boundary condition[15] is of major interest to the scientific and industrial communities, as it has practical implications in areas that involve small-scale fluid systems, such as lab-on-a-chip devices, flows in porous media, as well as biological flows, to name a few.

The classical case of the breakup of a laminar free-flowing liquid stream is dependent on material properties and geometry[16]. Although there are some studies of this instability in geometries other than free cylindrical liquid flows[17–23], the role of the boundary condition at the solid–liquid interface on the evolution of the PRI is less well understood[24,25]. It has been shown that the appearance of a dewetting liquid rim undergoing a Plateau–Rayleigh-type instability is influenced by the hydrodynamic boundary condition at the solid–liquid interface[26]; however, a general quantitative match between the growth dynamics of the PRI in experiments and analytical theory involving hydrodynamic slip has thus far not been achieved.

Characterization of slip boundary conditions at interfaces and their controlling parameters has been actively investigated in the literature[27–31]. The classical boundary condition assumes no slip at the solid–liquid interface. That is, for simple shear flow in the $x$ direction along a solid interface placed at $z=0$, the tangential flow velocity, $v_x(z)$, vanishes at the solid–liquid interface: $v_x(0)=0$. However, as already noted by Navier[32], there is no fundamental principle requiring $v_x(0)=0$ and one can also have hydrodynamic slippage at this interface, as defined by the slip length: $b=[v_x/\partial_z v_x]|_{z=0}$, where $b=0$ corresponds to the classical no-slip case.

Here we explicitly address the effect of a varying boundary condition, from no-slip to slip at the solid–liquid interface, on the PRI of a viscous liquid layer on a solid fibre. We find that the growth rate of the instability is strongly affected by the solid–liquid interface, with a faster breakup into droplets for a slip boundary condition compared with an equivalent sample with no slip. In contrast, the wavelength $\lambda^*$ of the fastest growing mode is not sensitive to the solid–liquid interface. The linear stability analysis of a newly developed thin-film equation incorporating slip is in excellent agreement with our data. The theory is valid for all Newtonian liquids and enables the precise determination of the capillary velocity $\gamma/\eta$ and most importantly of the slip length $b$.

## Results

**The experimental approach**. An entangled polystyrene (PS, 78 kg mol$^{-1}$) film with homogeneous thickness $e_0$ (5–93 μm) is coated onto a fibre with radius $a$ (10–25 μm), resulting in a PS-coated fibre with radius $h_0=a+e_0$, as schematically shown in Fig. 1a. Glass fibres provide a simple no-slip boundary condition[33]. In contrast, a slip interface results from coating the entangled PS film onto a glass fibre pre-coated with a nanometric thin amorphous fluoropolymer (AF2400, 14 ± 1 nm)[34]. The fluoropolymer coating on glass was used, because it is well established that PS, above a critical molecular weight ($M_c\sim 35$ kg mol$^{-1}$), exhibits significant hydrodynamic slip at this solid–liquid interface[34]. Henceforth, we will refer to these as the 'no-slip' and 'slip' fibres.

All samples were prepared and stored at room temperature, well below the PS glass transition temperature ($T_g\sim 100$ °C), thereby ensuring that there is no flow in the PS film before the start of the experiment. Before each experiment, the PS-coated fibre was measured with optical microscopy as shown in the $t=0$ image of Fig. 1b. To initiate the experiments, samples were annealed in ambient atmosphere at 180 °C—well above $T_g$—which causes the PRI to develop. The evolution of the surface profile was recorded with optical microscopy. Figure 1b shows a typical evolution for a PS film on a no-slip fibre.

Above $T_g$, the liquid PS film becomes unstable, which causes variations in the local axisymmetric surface profile, $h(x,\ t)=h_0+\zeta(x,\ t)$, over the axial coordinate $x$ and time $t$. The amplitude $\zeta(x,\ t)$ of the undulations grows with time and finally results in a droplet pattern displaying a uniform wavelength. By measuring the spatial variation of $\zeta(x,\ t)$ in the initial development and locating the maxima, the PRI wavelength $\lambda^*$ of each sample was determined (see Fig. 1a). Typically, four or five wavelengths were averaged per sample. In addition, by measuring the temporal change in radius of an individual bulge, we gained information about the growth rate of the instability and consequently the influence of the hydrodynamic boundary condition.

**The theoretical approach**. The experimental findings can be understood within the lubrication approximation, from a thin-film model based on the Laplace pressure-driven Stokes equation. We assume incompressible flow of a viscous Newtonian liquid film of thickness varying from 5 to 93 μm, which is well above the film thickness where disjoining pressure plays a role (a few tens of nanometres)[35]. Gravitational effects can be neglected, as all length scales involved in the problem are well below the capillary length $l_c\simeq 1.73$ mm. Finally, the velocities of the liquid films are small (for example, the fastest observed rate of change in the amplitude is $\sim 25$ nm s$^{-1}$). Thus, the Reynolds and Weissenberg numbers are orders of magnitude smaller than 1, and inertial and viscoelastic effects can be ignored.

We non-dimensionalize the problem (see Fig. 1 for variable definitions) through

$$H_0=\frac{h_0}{a},H=\frac{h}{a},X=\frac{x}{a},\Lambda^*=\frac{\lambda^*}{a},B=\frac{b}{a},T=\frac{\gamma}{\eta}\frac{t}{a}, \qquad (1)$$

where the capillary velocity $\gamma/\eta$ is the ratio of the liquid–air surface tension to the viscosity of PS. By assuming volume conservation, no stress at the liquid–air interface and the Navier slip condition at the solid–liquid boundary, one obtains (see Supplementary Methods) the governing equation for the dimensionless profile $H(X,\ T)$

$$\partial_T H+\frac{1}{H}\left[\frac{H'+H^2H'''}{16}\mathcal{M}(H,B)\right]'=0\,, \qquad (2)$$

where

$$\mathcal{M}(H,B)=4H^2\log H+(4B-3)H^2+4-8B+\frac{4B-1}{H^2}\,, \qquad (3)$$

and where the prime denotes the partial derivative with respect to $X$. It is noteworthy that equation (2) is a composite equation in the sense that we have kept a second-order lubrication term in the pressure contribution: the axial curvature. It is the lowest order

NATURE COMMUNICATIONS | DOI: 10.1038/ncomms8409 ARTICLE

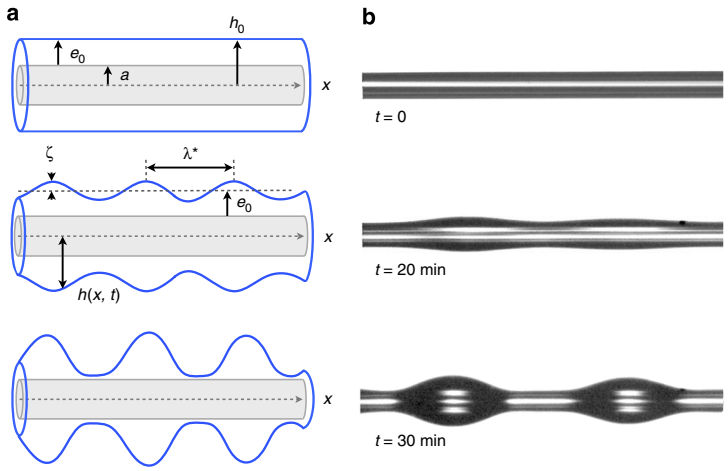


**Figure 1 | Plateau–Rayleigh instability on a fibre.** (**a**) Schematic and (**b**) optical micrographs illustrating the PRI for a liquid PS film on a glass fibre. At $t = 0$, the PS film on the no-slip fibre has a thickness $e_0 = 13.2 \pm 1\,\mu$m and the glass fibre radius is $a = 9.6 \pm 1\,\mu$m. The width of the optical images is 560 μm.

term counterbalancing the driving radial curvature and it is thus crucial to obtain the actual threshold of the instability. The dynamical aspect of the flow is however well described at the lowest lubrication order. An interesting discussion on this matter can be found in ref. 9.

Performing linear stability analysis, namely letting $H(X, T) = H_0 + \varepsilon(T)e^{iQX}$, where $\varepsilon(T) \ll 1$, yields an exponential growth of the perturbation of the form $\varepsilon(T) \propto e^{T/\tau(Q)}$, where the rate function is given by

$$\frac{1}{\tau(Q)} = Q^2\left(1 - H_0^2Q^2\right)\frac{\mathcal{M}(H_0, B)}{16H_0} \,. \qquad (4)$$

We define the fastest growing mode $Q^*$ corresponding to the smallest time constant $\tau^* = \tau(Q^*)$ and obtain $Q^* = 1/(H_0\sqrt{2})$. Writing $Q^*$ in terms of the dimensionless wavelength leads to

$$\Lambda^* = 2\pi\sqrt{2}H_0 \,, \qquad (5)$$

which is similar to the classical PRI dominant wavelength for inviscid jets with no solid core. We note that the correspondence between Rayleigh's result and ours is dependent on both the assumption of Stokes flow and on the presence of a solid core in our system.

The dimensionless growth rate of the fastest growing mode is given by

$$\frac{1}{\tau^*} = \alpha B + \beta \,, \qquad (6)$$

where $B$ is the dimensionless slip length, defined in equation (1), and where $\alpha$ and $\beta$ are parameters that depend on geometry only

$$\alpha = \frac{1}{16H_0^3}\left(H_0 - \frac{1}{H_0}\right)^2 \qquad (7a)$$

$$\beta = \frac{1}{64H_0^3}\left(4H_0^2\log H_0 - 3H_0^2 - \frac{1}{H_0^2} + 4\right). \qquad (7b)$$

As one sees, the wavelength of the fastest growing mode depends exclusively on the initial total radius, whereas the corresponding growth rate is a linear function of the slip length. It is worth noting that in the case of shear-thickening liquids, the PRI should be significantly slowed down as a result of the increasing viscosity associated with an increasing strain rate.

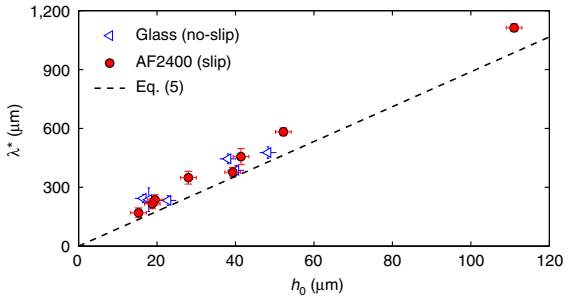


**Figure 2 | Influence of the geometry on the wavelength of the instability.** Wavelength of the fastest growing mode as a function of the total initial radius (see Fig. 1a). The black dashed line represents equation (5). The error bars are calculated from the error in the geometry and the inaccuracy given by the wavelength measurement.

Conversely, a shear-thinning liquid is expected to accelerate the rise of the instability. In the case of a viscoelastic material, Maxwell-like rheological models[36] can be implemented and may reveal interesting physics beyond the scope of the present study.

**The spatial evolution of the instability**. Figure 2 displays the wavelength $\lambda^*$ of the fastest growing modes, measured on no-slip and slip fibres, as a function of the initial total radius $h_0$. As expected from equation (5), the wavelength $\lambda^*$ grows linearly with increasing radius of the fibre–polymer system and is identical on slip and no-slip fibres. This is consistent with experiments and a theoretical framework for retracting liquid ridges on planar substrates[26]. The spatial morphology of the instability at short times is thus unaffected by the solid–liquid boundary condition. Although it is clear from Fig. 2 that the wavelength is the same on slip and no-slip fibres, there is a small systematic deviation from the theory. This slight deviation could perhaps be related to the lowest lubrication order of the present model[9], but could also be attributed to the experimental contribution of several modes and the asymmetry of the rate function (see equation (4)) in the vicinity of the fastest growing mode.

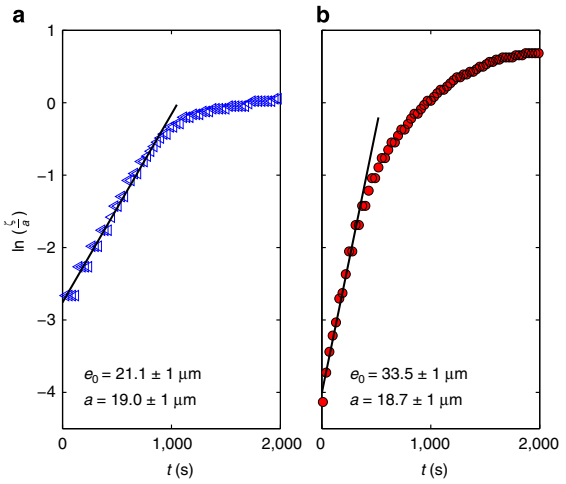


**Figure 3 | Temporal growth of the perturbation.** Semi-logarithmic plot of the evolution of the perturbation on (**a**) a no-slip fibre (glass) and (**b**) a slip fibre (glass coated with AF2400). The radius of the fibre $a$ and initial thickness of the polymer film $e_0$ (see Fig. 1a) are indicated. The solid line is the best linear fit in the initial regime.

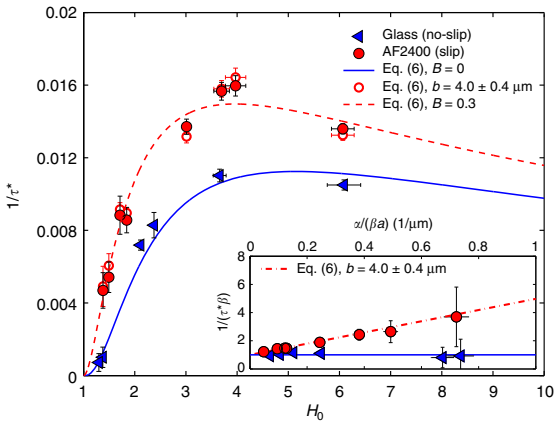


**Figure 4 | Influence of slip on the growth rate.** The inset shows the dimensionless growth rate $1/\tau^*$ normalized by the no-slip case $\beta$, as a function of $\alpha/(\beta a)$, see equation (6) and equations (7a,b). The slip length $b$ is obtained from a best linear fit (dash-dotted) to the slip data. The error bars are calculated from the error in the geometry and the inaccuracy given by the growth rate measurement. The main curve shows the dimensionless growth rate of the fastest growing mode on no-slip (glass) and slip (AF2400) fibres, as a function of the dimensionless initial total radius $H_0 = 1 + e_0/a$ (see Fig. 1a). Open symbols represent growth rates calculated from equation (6) using $b = 4.0 \pm 0.4\,\mu$m and the respective experimental geometries. Also shown is the theoretical curve for no slip (equation (6), with $B = 0$). Furthermore, the theoretical curve for slip (equation (6), with $B = 0.3$) is plotted as a guide to the eye.

**The temporal evolution of the instability**. We now turn from the spatial morphology of the instability to the temporal evolution. From the experimental images (see Fig. 1b), we extract the maximal radius of an individual bulge as it develops, to obtain the amplitude $\zeta$ as a function of time. The linear stability analysis presented predicts a perturbation that grows exponentially with a dimensionless growth rate $1/\tau^*$ for the fastest growing mode (see equation (6)). Figure 3 displays typical data for the logarithm of the perturbation amplitude normalized by the radius of the fibre, $\zeta/a$, as a function of $t$, for both no-slip and slip fibres. The data for both boundary conditions are consistent with the expected exponential growth in the early regime. Thus, the initial slopes of these curves provide reliable measurements of the growth rates.

The dimensionless growth rates $1/\tau^*$ are shown in Fig. 4 for both slip and no-slip fibres as a function of the dimensionless initial total radius $H_0$. We see that for both the slip and no-slip boundary conditions, the growth rates show a similar geometry dependence. The maxima for the slip and no-slip data can be easily understood: a decreasing growth rate as $H_0$ converges to 1 is due to the diminishing thickness of the liquid film, and thus to the reduced mobility, whereas the decreasing growth rate for large $H_0$ is due to smaller curvatures and thus a smaller driving force of the instability.

According to equation (6) with $B = 0$ (no slip), a maximum in the growth rate is expected for $H_0 = 1 + e_0/a = 5.15$. This prediction is entirely consistent with the data. Thus, a coated fibre of a given diameter is maximally unstable when the ratio of the film thickness to the fibre radius is about $e_0/a \sim 4$, consistent with an earlier theoretical study[5]. The capillary velocity is the only adjustable parameter in the no-slip case. We obtained $\gamma/\eta = 294 \pm 43\,\mu$m min$^{-1}$, which is in agreement with previous data[33] adjusted to the temperature used here, through the Wiliams–Landel–Ferry equation[37,38]. For the slip case, there are now two free parameters: the capillary velocity $\gamma/\eta$ and the dimensionless slip length $B$. If we take the value of the capillary velocity to be that of the no-slip case, we are left with only one true fitting parameter.

To quantify the slip length in our system, the growth rates normalized by $\beta$ are plotted as a function of $\alpha/(\beta a)$ (see inset of Fig. 4, equation (6) and equations (7a,b)). As expected, the no-slip data is consistent with the theoretical prediction of $1/\tau^* = \beta$ for all geometries. In contrast, the ratio $1/(\tau^*\beta)$ reveals that the amplification due to slip on the rise of the instability is more pronounced as $\alpha/(\beta a)$ increases. For the fibre radii used here, large $\alpha/(\beta a)$ corresponds to small $H_0$ (see equations (7a,b)). The stronger influence of slip observed for smaller values of $H_0$ is due to a non-zero velocity of polymer molecules at the solid–liquid interface[31,34]. For the smallest value of $H_0$, corresponding to $e_0/a \sim 0.4$, the slip-induced amplification factor of the growth rate is as large as $\sim 4$. On the contrary, in thick polymer films, the impact of slip is diminished. From a best linear fit to the slip data shown in the inset of Fig. 4, the slip length is found to be $b = 4.0 \pm 0.4\,\mu$m. Obtaining a slip length in the range of micrometres is in accordance with former studies on the dewetting of entangled polymer films from substrates with a fluoropolymer coating[34].

Having determined the value of $b$ and knowing the fibre radii, we obtain $B$ for each of the experimental geometries. Based on the theoretical model (equation (6)) corresponding growth rates can be calculated and are shown to be in excellent agreement with the experimental data (see Fig. 4). The dimensionless slip length $B = b/a$ ranges from 0.25 to 0.37 in our experiments. To guide the eye, a typical curve calculated with $B = 0.3$ is shown in Fig. 4. We see that for the fibres with the slip boundary condition, the growth rate is larger than in the no-slip case for a given geometry and the maximum of the growth rate $1/\tau^*$ corresponds to a smaller value of $H_0$. As expected, a slippery surface facilitates a higher mobility and hence a faster growth of the instability. This enhanced mass transport also explains the horizontal shift of the maximum of the growth rate: for a given geometry—and thus curvature—the mobility of the slip case is increased in

comparison with no-slip case. Therefore, the maximum of the growth rate is shifted to lower values of $H_0$.

## Discussion

We report on the PRI of a viscous liquid PS layer on a solid fibre of radius $a$, when the boundary condition at the solid–liquid interface is varied between the classical case of no-slip and the relevant situation of slippage. The wavelength of the fastest growing mode on a slip fibre shows a linear dependence on the initial total polymer-fibre radius, $h_0 = a + e_0$, and is not affected by the boundary condition, consistent with the lubrication theory developed. For both slip and no-slip fibres, we observe an exponential temporal growth of the instability at short times and the respective growth rates show a qualitatively similar geometry dependence. In the case of a slip fibre, the geometry corresponding to the maximum of the growth rate $1/\tau^*$ is shifted to a smaller value of $h_0/a$ and the rise of the instability is faster due to the added mobility at the solid–liquid interface. The slip-induced amplification of the growth rate is significant in a parameter range that is of paramount technological relevance. The linear stability analysis of the thin-film equation developed here is in excellent agreement with the data, valid for all Newtonian liquids, and provides a robust measure of two fundamental quantities: the capillary velocity $\gamma/\eta$ and the slip length $b$.

## Methods

**Preparation of fibres.** Glass fibres were prepared by pulling heated glass capillary tubes to final radius in the range $10 < a < 25$ μm using a pipette puller (Narishige, PN30). To prepare the slip boundary condition, the glass fibres were hydrophobized by dip coating in a 0.5 wt% solution of AF2400 (Poly[4,5-difluoro-2,2-bis (trifluoromethyl)-1,3-dioxole-co-tetrafluoroethylene]) (Aldrich) in a perfluoro-compound solvent (FC72™, Fisher Scientific), to form an amorphous fluoropolymer layer ($T_g \sim 240$ °C). A dip-coating speed of 1 mm s$^{-1}$ resulted in an AF2400 layer with a thickness of $14 \pm 1$ nm. The hydrophobized fibres were annealed in a vacuum chamber at 80 °C for 90 min to remove excess solvent.

**Preparation of homogeneous PS films.** To prepare homogeneous PS films, a concentrated solution (35 wt%) of atactic PS (Polymer Source Inc.) with a molecular weight of 78 kg mol$^{-1}$ and low polydispersity ($M_w/M_n = 1.05$) was dissolved in chloroform (Fisher Scientific). A droplet of the highly viscous polymer solution was placed between two glass slides, forming a meniscus at the edge of the glass slides. We note that the chloroform does not dissolve the underlying AF2400 coating on the slip fibres. A slip or no-slip fibre could then be placed in the middle of the gap between the slides and pulled out of the droplet with a constant speed using a motorized linear translation stage. By varying the pulling speed $v_0$ in the range $80 < v_0 < 150$ mm s$^{-1}$, we obtained film thicknesses that ranged from $e_0 = 5$ to 93 μm after the solvent had evaporated.

**Experimental setup.** The as-prepared samples were placed into a heated sample cell to initiate the PRI. With two ~0.5-mm-thick spacers, the coated fibres were suspended above a reflective Si wafer (to improve contrast) and placed on a microscope hot stage (Linkam). A metal ring in direct contact with the hot stage supported a glass cover over the sample and Si wafer (see Supplementary Fig. 1 and Supplementary Methods), thereby ensuring good thermal contact and temperature control to within 1 °C. The surface profiles were analysed from the optical micrographs taken at various times using a custom-made edge detection software written in MATLAB.

## References


1. Zheng, Y. *et al.* Directional water collection on wetted spider silk. *Nature* **463,** 640–643 (2010).
2. Plateau, J. *Experimental and Theoretical Steady State of Liquids Subjected to Nothing but Molecular Forces* (Gauthiers-Villars, Paris, 1873).
3. Rayleigh, F. On the instability of jets. *Proc. Lond. Math. Soc.* **s1-10,** 4 (1878).
4. Goren, S. L. The shape of a thread of liquid undergoing break-up. *J. Colloid Interface Sci.* **19,** 81–86 (1964).
5. Roe, R.-J. Wetting of fine wires and fibres by a liquid film. *J. Colloid Interface Sci.* **50,** 70–79 (1975).
6. Donnelly, R. J. & Glaberson, W. Experiments on the capillary instability of a liquid jet. *R. Soc. Lond. Proc. Ser. A Math. Phys. Eng. Sci.* **290,** 547–556 (1966).
7. Eggers, J. Nonlinear dynamics and breakup of free-surface flows. *Rev. Mod. Phys.* **69,** 865–929 (1997).
8. Kliakhandler, I. L., Davis, S. H. & Bankoff, S. G. Viscous beads on vertical fibre. *J. Fluid. Mech.* **429,** 381–390 (2001).
9. Craster, R. V. & Matar, O. K. On viscous beads flowing down a vertical fibre. *J. Fluid. Mech.* **553,** 85–105 (2006).
10. Craster, R. V. & Matar, O. K. Dynamics and stability of thin liquid films. *Rev. Mod. Phys.* **81,** 1131–1198 (2009).
11. Duprat, C., Ruyer-Quil, C. & Giorgiutti-Dauphiné, F. Spatial evolution of a film flowing down a fiber. *Phys. Fluids* **21,** 042109 (2009).
12. González, A. G., Diez, J. A., Gratton, R., Campana, D. M. & Saita, F. A. Instability of a viscous liquid coating a cylindrical fibre. *J. Fluid Mech.* **651,** 117–143 (2010).
13. Bai, H. *et al.* Controlled fabrication and water collection ability of bioinspired artificial spider silks. *Adv. Mater.* **23,** 3708–3711 (2011).
14. Ju, J. *et al.* A multi-structural and multi-functional integrated fog collection system in cactus. *Nat. Commun.* **3,** 1247 (2012).
15. Lauga, E. *et al.* In: *Springer Handbook of Experimental Fluid Mechanics.* (eds. Tropea, C., Yarin, A. & Foss, J. F.) Ch. 19 1219–1240 (Springer, New York, 2007).
16. Eggers, J. & Villermaux, E. Physics of liquid jets. *Rep. Prog. Phys.* **71,** 036601 (2008).
17. Brochard-Wyart, F. & Redon, C. Dynamics of liquid rim instabilities. *Langmuir* **8,** 2324–2329 (1992).
18. Sharma, A. & Reiter, G. Instability of thin polymer films on coated substrates: rupture, dewetting, and drop formation. *J. Colloid Interface Sci.* **178,** 383–399 (1996).
19. Khare, K. *et al.* Dewetting of liquid filaments in wedge-shaped grooves. *Langmuir* **23,** 12138–12141 (2007).
20. Pairam, E. & Fernández-Nieves, A. Generation and stability of toroidal droplets in a viscous liquid. *Phys. Rev. Lett.* **102,** 234501 (2009).
21. Villermaux, E. & Bossa, B. Single-drop fragmentation determines size distribution of raindrops. *Nat. Phys.* **5,** 697–702 (2009).
22. McGraw, J. D., Li, J., Tran, D. L., Shi, A.-C. & Dalnoki-Veress, K. Plateau-Rayleigh instability in a torus: formation and breakup of a polymer ring. *Soft Matter* **6,** 1258–1262 (2010).
23. Shabahang, S., Kaufman, J. J., Deng, D. S. & Abouraddy, A. F. Observation of the Plateau-Rayleigh capillary instability in multi-material optical fibers. *Appl. Phys. Lett.* **99,** 161909 (2011).
24. Choi, S.-H. & Newby, B. M. Z. Dynamic contact angle in rim instability of dewetting holes. *J. Chem. Phys.* **124,** 054702 (2006).
25. Münch, A. & Wagner, B. Impact of slippage on the morphology and stability of a dewetting rim. *J. Phys. Condens. Matter* **23,** 184101 (2011).
26. Bäumchen, O. *et al.* Influence of slip on the Rayleigh-Plateau rim instability in dewetting viscous films. *Phys. Rev. Lett.* **113,** 014501 (2014).
27. Brochard, F. & de Gennes, P. G. Shear-dependent slippage at a polymer/solid interface. *Langmuir* **8,** 3033–3037 (1992).
28. Neto, C., Evans, D. R., Bonaccurso, E., Butt, H.-J. & Craig, V. S. J. Boundary slip in Newtonian liquids: a review of experimental studies. *Rep. Prog. Phys.* **68,** 2859–2897 (2005).
29. Schmatko, T., Hervet, H. & Leger, L. Friction and slip at simple fluid-solid interfaces: the roles of the molecular shape and the solid-liquid interaction. *Phys. Rev. Lett.* **94,** 244501 (2005).
30. Bocquet, L. & Barrat, J.-L. Flow boundary conditions from nano- to micro-scales. *Soft Matter* **3,** 685–693 (2007).
31. Fetzer, R. & Jacobs, K. Slippage of newtonian liquids: influence on the dynamics of dewetting thin films. *Langmuir* **23,** 11617–11622 (2007).
32. Navier, C. L. M. H. Mémoire sur les lois du mouvement des fluides. *Mem. Acad. Sci. Inst. Fr.* **6,** 389 (1823).
33. McGraw, J. D., Salez, T., Bäumchen, O., Raphaël, E. & Dalnoki-Veress, K. Capillary leveling of stepped films with inhomogeneous molecular mobility. *Soft Matter* **9,** 8297–8305 (2013).
34. Bäumchen, O., Fetzer, R. & Jacobs, K. Reduced interfacial entanglement density affects the boundary conditions of polymer flow. *Phys. Rev. Lett.* **103,** 247801 (2009).
35. Seemann, R., Herminghaus, S. & Jacobs, K. Dewetting patterns and molecular forces: a reconciliation. *Phys. Rev. Lett.* **86,** 5534–5537 (2001).
36. Benzaquen, M., Salez, T. & Raphaël, E. Viscoelastic effects and anomalous transient levelling exponents in thin films. *Europhys. Lett.* **106,** 36003 (2014).
37. Williams, M. L., Landel, R. F. & Ferry, J. D. The temperature dependence of relaxation mechanisms in amorphous polymers and other glass-forming liquids. *J. Am. Chem. Soc.* **77,** 3701–3707 (1955).
38. Rubinstein, M. & Colby, R. H. *Polymer Physics* (Oxford Univ. Press. Inc., 2003).


## Acknowledgements

We thank Martin Brinkmann for insightful discussions. We also thank the graduate school GRK 1276, NSERC of Canada, the German Research Foundation (DFG) under grant numbers BA3406/2 and SFB 1027 for financial support.

## Author contributions

S.H. led the experimental work and wrote the first draft of the manuscript. M.B. led the theoretical work. All authors contributed to the research and manuscript preparation.

## Additional information

**Supplementary Information** accompanies this paper at http://www.nature.com/naturecommunications

**Competing financial interests:** The authors declare no competing financial interest.

**Reprints and permission** information is available online at http://npg.nature.com/reprintsandpermissions/

**How to cite this article:** Haefner, S. *et al.* Influence of slip on the Plateau–Rayleigh instability on a fibre. *Nat. Commun.* 6:7409 doi: 10.1038/ncomms8409 (2015).

1

**Supplementary Figures**

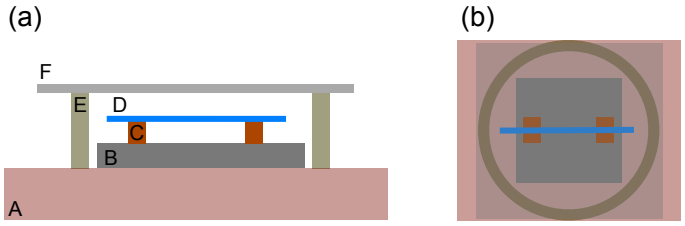


Supplementary Figure 1: **Schematic of the sample chamber.** Representation of (a) the side view and (b) the top view of the experimental setup. On top of a hot stage (A), a Si wafer (B) with two teflon spacers (C) is placed. Freely suspended filaments are realized by depositing the fibre (D) across the spacers. The fibre is surrounded by a metal ring (E) with a glass cover (F).

**Supplementary Method**

**Fibre thin film equation with slip:**

Here, we provide the main steps of the derivation of the fibre thin film equation (see Eqs. (2) and (3) in the article). Let us consider a viscous liquid film coating a cylindrical fibre of constant radius $a$ (see Fig. 1 in the article). The axis of the fibre, along the $x$ direction, is chosen as a reference for the radial coordinate $r$. We assume cylindrical invariance of the free-surface profile described by $r = h(x,t)$, at position $x$ and time $t$. Furthermore, we assume an incompressible flow of the viscous Newtonian fluid, where gravity, disjoining pressure and inertia are negligible. Defining the local excess pressure $p(r,x,t)$ and the velocity field $\boldsymbol{v}(r,x,t)$, and assuming the lubrication approximation to first order, namely that the slopes of the profiles remain small and the velocity is mainly oriented along the fibre axis, $\boldsymbol{v} = v\boldsymbol{e}_x$, leads to the two projections of the Stokes equation:

$$\partial_x p = \eta\left(\partial_{rr} v + \frac{\partial_r v}{r}\right) \tag{1a}$$

$$\partial_r p = 0 \,, \tag{1b}$$

where $\eta$ is the dynamical shear viscosity that we assume to be homogeneous and constant. The lubrication approximation is valid since the profile slopes remain small in comparison to 1 at early times – the regime in which the linear analysis is performed – and since the typical horizontal length scale of the flow is expected to be larger than the minimal wavelength of the Plateau-Rayleigh instability, that is given by $\lambda_{\min} = 2\pi h_0 \gg e_0$. This is indeed always the case as even in the worst case geometry, $e_0 \approx 5a$, one has $e_0/\lambda_{\min} \approx 0.13 \ll 1$. According to Supplementary Eq. (1b), the excess pressure is invariant in the radial direction, to first order in the lubrication approximation. Thus, the excess pressure is set by the Laplace boundary condition at the free surface which, within the small slope approximation, reads:

$$p = \gamma\left(\frac{1}{h} - h''\right) \,, \tag{2}$$

where $\gamma$ denotes the air-liquid surface tension, taken to be homogeneous and constant, and where the prime denotes the derivative with respect to $x$. The two terms on the right hand side of Supplementary Eq. (2) correspond to the radial and axial curvatures of the free surface. Note that, as already mentioned in the body of the article, we have kept a second order lubrication term in the pressure contribution: the axial curvature $-h''$. This is because it is the lowest order term counterbalancing the driving radial curvature $1/h$, and it is thus crucial to obtain the actual threshold of the instability [9]. Regarding the boundary conditions, we assume no shear at the free surface and the Navier slip condition at the solid-liquid interface, namely:

$$\partial_r v|_{r=h} = 0 \tag{3a}$$

$$\partial_r v|_{r=a} = \frac{v|_{r=a}}{b} \,, \tag{3b}$$

where $b$ denotes the slip length. Integrating Supplementary Eq. (1), together with Supplementary Eqs. (2) and (3), yields:

$$v = \frac{\gamma\left(h' + h^2 h'''\right)}{4\eta h^2}\left[2h^2 \log\left(\frac{r}{a}\right) - r^2 + \frac{2b}{a}h^2 + a^2 - 2ab\right] \,, \tag{4}$$

for all $r \in [a,h]$. Volume conservation requires that:

$$\partial_t h + \frac{Q'}{h} = 0 \,, \tag{5}$$

where we introduced the volume flux per radian:

$$Q = \int_a^h \mathrm{d}r\, rv \,. \tag{6}$$

3

Combining Supplementary Eq. (5) together with Supplementary Eqs. (4) and (6) yields the fibre thin film equation:

$$\partial_t h + \frac{\gamma}{16\eta h}\left[\left(h' + h^2 h'''\right)\left(4h^2 \log\left(\frac{h}{a}\right) + \left(\frac{4b}{a} - 3\right)h^2 + 4a^2 - 8ab + \left(4ab - a^2\right)\frac{a^2}{h^2}\right)\right]' = 0\,. \tag{7}$$

Finally, introducing the dimensionless variables (see Eq. (1) in the article) into Supplementary Eq. (7) yields the dimensionless fibre thin film equation (see Eqs. (2) and (3) in the article).

**Experimental setup and details:**

The as-prepared samples were annealed in ambient atmosphere at 180 °C - well above $T_g$ - which causes the polystyrene films to melt and the PRI to develop. The evolution of the PRI was recorded with an inverted optical microscope (Olympus BX51). At various times, images were taken using a 5x magnification objective and a camera with a resolution of 1392 x 1040 pixels (QImaging, QIClick), resulting in a pixel size of 1.28 $\mu$m. To ensure free standing filaments, the coated fibres (D) were placed along two $\sim$ 0.5 mm thick teflon spacers (C) located on a Si wafer (B) (see Supplementary Figure 1). The Si wafer was used to improve the optical contrast. A metal ring (E) in direct contact with the hot stage supported a glass cover (F) over the sample and Si wafer. The temperature within the sample cell is uniform (within 1°C) and convection does not affect the measurements. By using spacers (C) made of teflon, we ensured that there is no drainage of the liquid PS film towards the edges (PS does not wet teflon). The surface profiles were analysed from the optical micrographs taken at various times, using a custom-made edge detection software written in MATLAB.

# Addendum III - Capillary droplet propulsion on a fibre

Authors: S. Haefner[1], O. Bäumchen[2], and K. Jacobs[1]

[1] Department of Experimental Physics, Saarland University, 66041 Saarbrücken, Germany.
[2] Max Planck Institute for Dynamics and Self-Organization (MPIDS), 37077 Göttingen, Germany.

*Soft Matter* **11**, 6921-6926 (2015).
(`http://pubs.rsc.org/en/content/articlehtml/2015/sm/c5sm01228g`)



**Author contributions:**

S. Haefner performed all experiments and analyzed all data sets. The custom-made software to analyze the data was written by S. Haefner. Research was designed by S. Haefner. The theoretical background was developed by O. Bäumchen and S. Haefner. The manuscript was written by S. Haefner. Writing was supervised by O. Bäumchen and K. Jacobs. All authors contributed to the research.

**Abstract -** A viscous liquid film coating a fibre becomes unstable and decays into droplets due to the Rayleigh–Plateau instability (RPI). Here, we report on the generation of uniform droplets on a hydrophobized fibre by taking advantage of this effect. In the late stages of liquid column breakup, a three-phase contact line can be formed at one side of the droplet by spontaneous rupture of the thinning film. The resulting capillary imbalance leads to droplet propulsion along the fibre. We study the dynamics and the dewetting speed of the droplet as a function of molecular weight as well as temperature and compare to a force balance model based on purely viscous dissipation.

Volume 11 | Number 35 | 21 September 2015 | Pages 6907–7068

# Soft Matter

www.softmatter.org

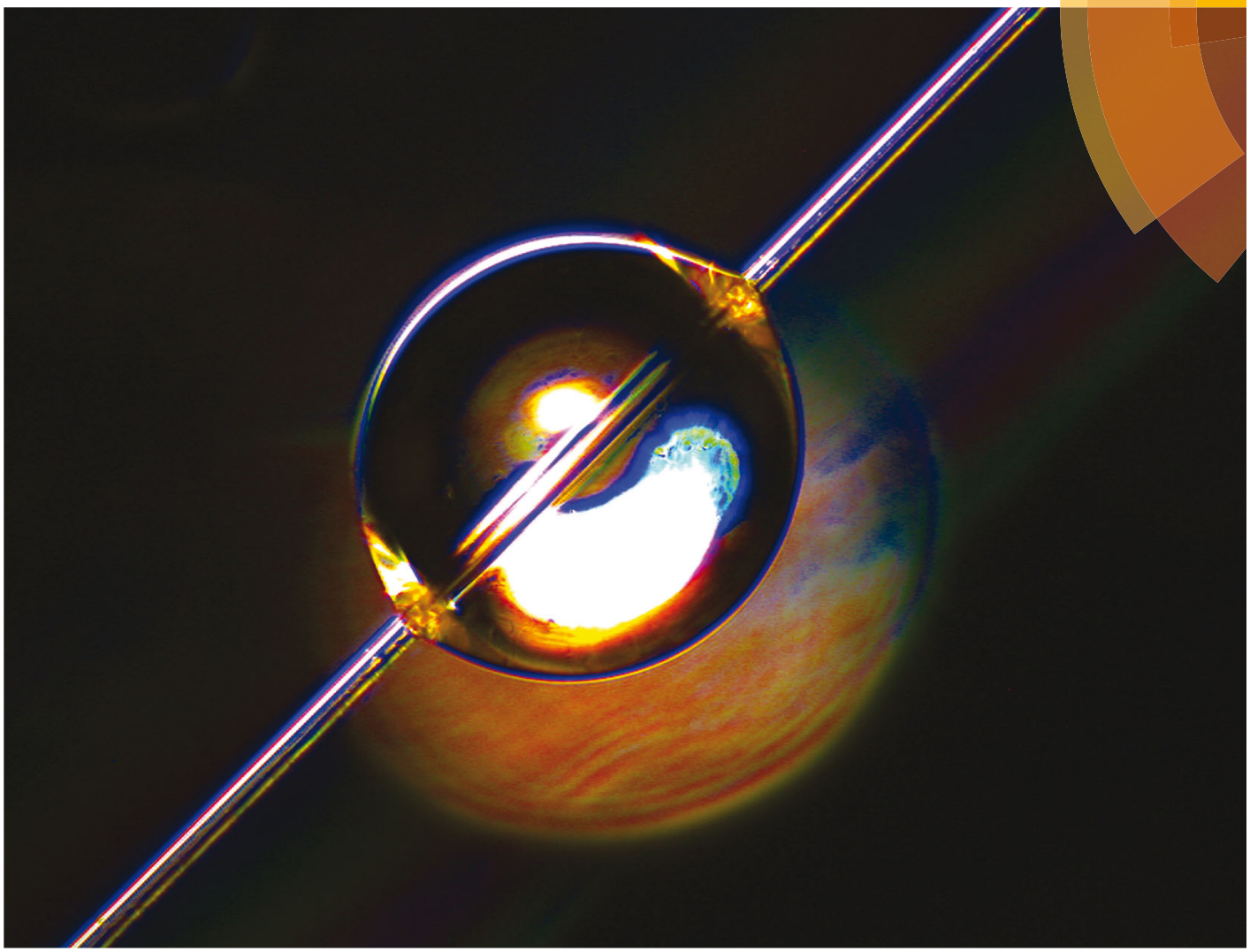

ISSN 1744-683X

ROYAL SOCIETY OF CHEMISTRY

PAPER
Karin Jacobs *et al.*
Capillary droplet propulsion on a fibre

Soft Matter

PAPER

# Capillary droplet propulsion on a fibre†

Sabrina Haefner,[a] Oliver Bäumchen[b] and Karin Jacobs*[a]

Cite this: *Soft Matter*, 2015, **11**, 6921

Received 20th May 2015,
Accepted 23rd June 2015

DOI: 10.1039/c5sm01228g

www.rsc.org/softmatter

A viscous liquid film coating a fibre becomes unstable and decays into droplets due to the Rayleigh–Plateau instability (RPI). Here, we report on the generation of uniform droplets on a hydrophobized fibre by taking advantage of this effect. In the late stages of liquid column breakup, a three-phase contact line can be formed at one side of the droplet by spontaneous rupture of the thinning film. The resulting capillary imbalance leads to droplet propulsion along the fibre. We study the dynamics and the dewetting speed of the droplet as a function of molecular weight as well as temperature and compare to a force balance model based on purely viscous dissipation.

## 1 Introduction

Regular droplet patterns on a fibre are a well-known phenomenon, which can be found in everyday life, *e.g.* dew drops on a spider's web.[1] Thereby, small drops are pinned on the web filament, whereas big droplets are affected by gravitational flow and eventually coalesce with others. The destabilization and the subsequent breakup into uniform droplets of a liquid film on a fibre is caused – like in a free liquid jet – by the Rayleigh–Plateau instability[2,3] (RPI). Although, this is an obstructive effect in coating techniques, the capability to form regular droplets with an adjustable size and the control of their motion are very advantageous and important for technical applications *e.g.* water collection processes,[4–6] patterning,[7] chemical reactions[8] and printing.[9] The instability of liquid threads and its characteristics have been studied intensively over the last two centuries and is still of great interest.[3,10–13] Furthermore, many studies investigated the motion of beads flowing down a vertical fibre, sliding or rolling on a fibre or the mechanisms of droplet movement in filament networks.[14–20] However, only a few studies identify the motion of droplets in the absence of gravitational forces, where droplets are propelled along a fibre or on a planar substrate by taking advantage of different effects. For example, Yarin *et al.* studied the movement of drops along a cylindrical filament due to a temperature gradient,[21] yet also a difference in pressure can lead to a propelling force.[22] Remarkably, liquid droplets can even detect and move along stiffness gradients of an underlying substrate (durotaxis).[23] Another well-established and commonly used way of producing and transporting equally sized droplets on the micro scale is realized by using microfluidic devices, where droplets are generated and transported inside a channel.[24]

Here, we report on viscous liquid droplets moving along the outer surface of a hydrophobized solid fibre, purely driven by capillary forces. For that purpose, droplets are generated by taking advantage of the RPI: in the course of the destabilization of a thin homogeneous film, liquid droplets separated by valleys are emerging. By spontaneous rupture of the thinning liquid film in between the equally distributed droplets, an axisymmetric three-phase contact line can be formed at one side of the droplet at the late stages of liquid column breakup. This leads to a capillary imbalance between the two ends of the droplet, which causes the drop to dewet on the fibre. Fig. 1b shows a typical example of a receding polystyrene (PS) droplet on a hydrophobized glass fibre (see ESI,† Video V1). The motion process is studied as a function of molecular weight and temperature and is compared to the classical case of a dewetting ridge on a substrate.

## 2 Experimental

Glass fibres were prepared by pulling heated glass capillary tubes (World Precision Inst.) to final diameters of 20 to 30 μm using a pipette puller (Narishige, PN30). By dip-coating the glass fibres in a 0.5 wt% solution of AF2400 (poly[4,5-difluoro-2,2-bis(trifluoromethyl)-1,3-dioxole-*co*-tertrafluoroethylene]) (Aldrich) in a perfluoro-compound solvent (FC72™, Fisher Scientific), a hydrophobic amorphous fluoropolymer layer ($T_g \sim 240$ °C) is deposited on the fibres. In order to remove excess solvent, fibres were annealed to 80 °C for 90 minutes in ambient atmosphere.

To create droplets on a fibre, we apply a homogeneous polystyrene (PS) film with thickness $e_0$ (5 to 90 μm) onto the

[a] *Saarland University, Department of Experimental Physics, 66041 Saarbrücken, Germany. E-mail: k.jacobs@physik.uni-saarland.de*
[b] *Max Planck Institute for Dynamics and Self-Organization (MPIDS), 37077 Göttingen, Germany*

† Electronic supplementary information (ESI) available. See DOI: 10.1039/c5sm01228g

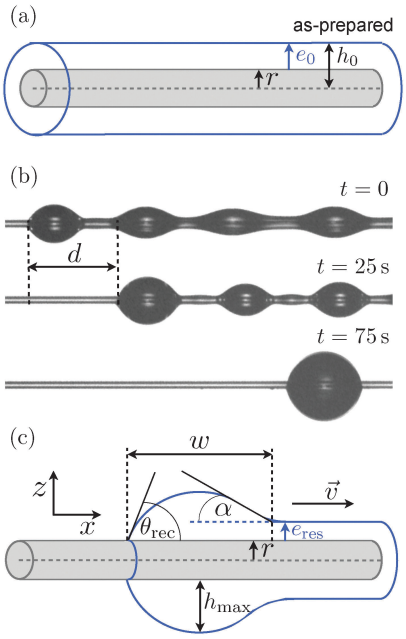


Fig. 1 (a) Schematic representation of the as-prepared samples: a homogeneous PS film with thickness $e_0$ is applied to a hydrophobized fibre with radius $r$. (b) Optical micrographs illustrating the time evolution of a polystyrene ($M_w$ = 8.1 kg mol$^{-1}$) droplet receding on a hydrophobized fibre at a temperature of $T$ = 150 °C. The regular droplet pattern at $t$ = 0 is achieved by utilizing the breakup of a homogeneous film on a cylindrical fibre into droplets, which are separated by a thin film. The spontaneous formation of a three-phase contact line at the left side of the far left droplet leads to a capillary imbalance, which causes the droplet to move to the right along the fibre. After a certain time $t$, the droplet has covered a particular distance $d$, while accumulating the residual thin film and static droplets. The width of the optical images is 1120 μm. (c) Schematic representation of a droplet on a fibre during the motion process. All system geometries and parameters are indicated.

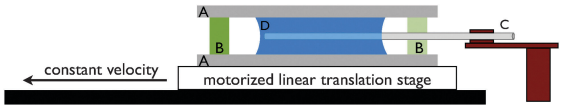


Fig. 2 Schematic representation of the PS film application setup (not to scale): a droplet of a highly viscous PS solution (D) is placed on a hydrophobized fibre (C), which is positioned close above a glass slide (A). Covering the system with a second glass slide on top of two Si-spacers (B) leads to the formation of a meniscus at the edges. The fibre (C) is located in the center of the PS droplet (D). By using a motorized linear translation stage, the PS solution is pulled along the fibre with a constant velocity, which results in the formation of a homogenous PS film with thickness $e_0$ surrounding the axisymmetric fibre.

hydrophobized fibre (see Fig. 1a): atactic polystyrene (Polymer Source Inc.) with molecular weights varying between 4.1 and 78 kg mol$^{-1}$ and low polydispersities ($M_w/M_n$ = 1.05) was dissolved in chloroform (Fisher Scientific). A droplet of a highly viscous (35 wt%) polymer solution was placed onto a hydrophobized fibre, which was positioned close above a glass slide (see Fig. 2). Covering the system with a second glass slide on top of two Si-spacers leads to the formation of a meniscus at the edges. By using a motorized linear translation stage (Newport), the PS solution is pulled along the fibre with a constant velocity, which results in the formation of a homogeneous PS film with thickness $e_0$ surrounding the axisymmetric fibre. By varying the speed between 80 and 120 mm s$^{-1}$ films with thicknesses $e_0$ of 5 to 90 μm could be generated after solvent evaporation. All samples were prepared at room temperature, which is well below the glass transition temperature $T_g$ of all used molecular weights.[25,26]

In order to initiate the formation of droplets on a fibre, the as-prepared samples (see Fig. 1a) were annealed above $T_g$ in ambient conditions. By placing the fibres across two 0.5 mm thick spacers, which are located on top of a reflective Si wafer, we achieve free standing filaments. This setup was positioned on a microscope hot stage (Linkam), while surrounded by a metal ring in direct contact with the hot stage. Finally, the metal ring is covered by a glass slide. Thereby, good thermal contact and temperature control within 1 K was ensured. As a result of annealing above the glass transition temperature, the liquid films became unstable and were subjected to the Rayleigh–Plateau instability.[13] Axisymmetric barrel shape[27,28] droplets with a certain spacing were formed. As the droplet size is related to the film thickness $e_0$ and the fibre radius $r$, the typical droplet height $h_{\mathrm{max}}(t)$ (see Fig. 1c) is in the range of 40 to 200 μm. The width $w(t)$ of the droplets (see Fig. 1c) varies between 100 and 320 μm. The fact that films below $e_0$ = 5 μm start to dewet prior to the formation of droplets on a hydrophobized fibre implies that by using this technique of droplet generation, the lowest limit of possible droplet sizes has already been reached.

The thin liquid film in between the droplets represents a metastable situation, as can be concluded from the shape of the effective interface potential which comprises short-range and long-range interactions.[29,30] Any chemical or topographical heterogeneity can act as a nucleus leading to the formation of a hole in the film. This random process causes the axisymmetric rupture of the film and thus the formation of a three-phase contact line at one side of a droplet. Consequently, at this side of the droplet the contact angle is adapted to the receding contact angle $\theta_{\mathrm{rec}}$ (see Fig. 1c). On the opposite side, however, where the droplet merges into the residual PS film, the apparent angle $\alpha$ remains constant. This causes the Laplace pressure to be different on both sides of the droplet and the capillary imbalance leads to droplet propulsion along the fibre. During droplet motion the residual material (thin film and static droplets) is accumulated. Thereby, the total volume of the system is conserved and the droplet grows in size. Typically, the height of the droplet $h_{\mathrm{max}}(t)$ increases by a factor of 1.5 to 2 and the width $w(t)$ grows by a factor of 1.2 to 1.7 over the entire dewetting process. As long as one side of the moving droplet is connected to the residual material, the capillary force on the 'wet' side is negative and the three-phase contact line recedes. Thus, the droplet accumulates all the remaining material until the dewetting process finally results in the formation of isolated droplets sitting on the fibre (see Fig. 1b, $t$ = 75 s). In this final configuration, the droplet has two 'dry' sides and the

 

motion of the droplet stops as soon as both contact angles adapt to the equilibrium contact angle $\theta_e$. The receding and the equilibrium contact angle, $\theta_{rec}$ and $\theta_e$, of PS on an AF2400 fibre were determined from optical micrographs by using an image analysis software (Image Pro Plus, Media Cybernetics). Note that $\theta_{rec}$ has been evaluated during the accumulation of residual thin film $e_{res}$ only (see Fig. 1c). Here, we measured $\theta_{rec} = 60 \pm 5^\circ$ and $\theta_e = 83 \pm 5^\circ$. The ratio between these two angles is in good agreement with studies on polymer films dewetting on planar hydrophobized surfaces,[31–33] which showed a fixed relation of $\theta_e/\theta_{rec} \approx \sqrt{2}$. To determine the PS film thickness $e_0$, the initial total radius of the coated fibre $h_0$ was measured by optical microscopy with an accuracy of $\pm 1$ μm (see Fig. 1a). The fibre radius $r$ was measured (with an accuracy of $\pm 1$ μm) after the PS film dewetted (see Fig. 1b, $t = 75$ s). From their difference $e_0 = h_0 - r$, we achieve $e_0$. The motion of the droplet was recorded with optical microscopy. Fig. 1b shows a typical time evolution of a droplet receding on a hydrophobized fibre (also see ESI,† Video V1). A custom made edge detection software in MATLAB is applied in order to record the travelled distance $d$ (see Fig. 1b), *i.e.* the distance moved by the three-phase contact line of the droplet in a certain time $t$.

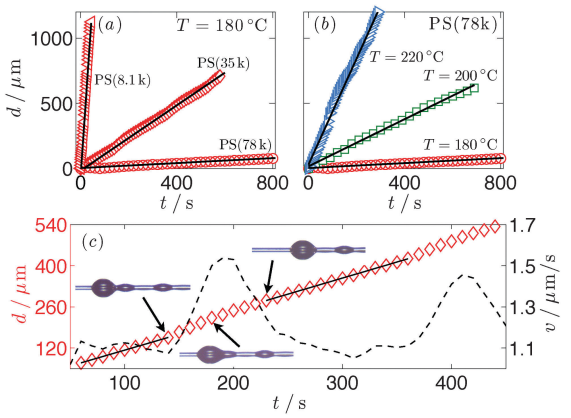


Fig. 3 Position $d$ of the three-phase contact line on the fibre axis $x$ as a function of time $t$ for (a) different PS molecular weights at $T = 180$ °C and (b) PS(78k) at different temperatures $T$. The black lines indicate the best linear fit for each data set. (c) Symbols indicate the travelled distance $d$ as a function of time for a PS(35k) droplet at $T = 180$ °C during the different steps of the dewetting process. The black dashed line displays the respective local speed $v$ obtained by using the Savitzky–Golay[36] algorithm (here: $n = 7$, $p = 2$). The black straight lines indicate the best linear fit excluding coalescence steps.

## 3 Results and discussion

This section incorporates the results of the experiments described above, followed by a comparison to a model based on a balance of capillary driving force and dissipation through viscous friction. In Section 3.1, we focus on the global dewetting process of a droplet on a fibre for various molecular weights and temperatures. Thereby, we identify the global dewetting velocity $\bar{v}$ including both processes, the accumulation of the residual thin PS film as well as the coalescence with remaining static droplets. Section 3.2 comprises a more local analysis of the dewetting behavior. We investigate the two different dewetting processes in more detail and determine the local velocity $v$ as a function of molecular weight and temperature neglecting coalescence steps. A description of the model and a comparison with experimental data is given in Section 3.3.

### 3.1 Global droplet dynamics

From the experimental images (see Fig. 1b) we measure the distance $d$, which gives the distance the three-phase contact line of the droplet has moved along the fibre axis $x$ during a certain time interval. Fig. 3a displays typical data for different molecular weights using a constant temperature of $T = 180$ °C. In analogy, Fig. 3b shows a variation in temperature for a constant molecular weight of $M_w = 78$ kg mol$^{-1}$. We find that for all data sets the motion of the dewetting droplet is linear in time (linear fits in Fig. 3a and b) over the entire process. Thus, the slope of these curves provides a reliable measurement of the global mean droplet velocity $\bar{v}$. Fig. 3a shows that for a constant annealing temperature $T$, the global mean velocity of a moving droplet is increasing when decreasing the molecular weight $M_w$, which is accompanied by a decrease in the viscosity $\eta$.[34,35] This observation is entirely consistent with Fig. 3b, where for a constant molecular weight we observe an increase in the global mean speed with increasing the temperature, again equivalent to a decrease in $\eta$. Furthermore, the linearity in the mean velocity during the entire motion (see Fig. 3a and b) indicates that there is no influence of the increase in the height $h_{max}(t)$ and width $w(t)$ of the droplet (due to material accumulation) on the dewetting dynamics.

### 3.2 Local analysis of the droplet velocity

Having characterized the global droplet dynamics, we now turn to a more local analysis of the droplet velocity. Based on the algorithm by Savitzky and Golay,[36] the local velocity $v$ is calculated from the three-phase contact line displacement-time data. We chose a frame size of $n = 3$ and a second order polynomial ($p = 2$) for the interpolation of the experimental data. Fig. 3c shows typical data of the travelled distance $d$ as a function of time (symbols, see Fig. 3a). We found that the local velocity $v$ of the droplet (dashed line) is alternating around the global mean velocity $\bar{v} = 1.2$ μm s$^{-1}$: as the droplet dewets and accumulates the residual thin PS film, both, the receding contact angle $\theta_{rec}$ and the velocity $v$ remain constant. As soon as the moving droplet gets in contact with one of the static droplets on the fibre, a sudden increase of the driving force due to the pressure gradient between the droplets is observed. The neck in between the two droplets levels rapidly, which causes the dewetting velocity $v$ to increase (see Fig. 3c) and consequently the contact angle $\theta_{rec}$ to decrease. At the end of the coalescence process, the droplet shape recuperates, which goes in line with a deceleration of the speed and the adjustment of the receding contact angle. Thus, for simplicity, we consider in the following only the local velocity of a droplet during the consumption of the residual thin film, referred to as $v$. Accordingly, the coalescence steps with immobile droplets

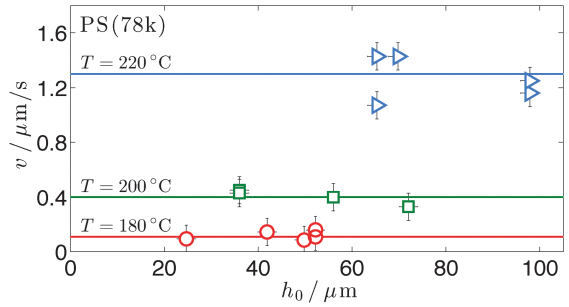


Fig. 4 Local velocity $v$ of dewetting droplets on a fibre with a molecular weight of 78 kg mol$^{-1}$ at different temperatures as a function of the initial system radius $h_0$. The straight lines indicate the local mean dewetting velocity for the different temperatures averaged over the respective experiments. The error bars are calculated from the error in the geometry and the error given by the dewetting velocity measurement.

are neglected for the purpose of determining the droplet velocity $v$. The solid black lines in Fig. 3c show the linear best fit to the respective sections of the data. The local velocity turns out to be consistent for different sections of the data. Thus, there is no evidence for the local velocity $v$ to be systematically affected by the change of the droplet size. Fig. 4 represents typical data for the local velocity as a function of the initial system radius $h_0$ for three different viscosities ($M_w$ = 78 kg mol$^{-1}$, $T$ = 180 °C, 200 °C, 220 °C). The solid lines display the local mean dewetting speed averaged over the respective experiments. We see that varying the initial system radius $h_0$ (by varying the PS film thickness $e_0$ and the fibre radius $r$), which is directly linked with the size of the droplets, does not cause a significant change in the velocity.

### 3.3 Model

The mathematical description of a dewetting wedge-shaped liquid front has been addressed in previous studies.[37,38] The effective driving force per unit length $F_{drive}$ of a dewetting liquid wedge (see Fig. 1c) is equal to the spreading parameter $|S|$. It denotes the energy difference per unit area between a dry substrate and a liquid covered surface and is given by $|S| = |\gamma_{lv}(\cos\theta_e - 1)|$, where $\gamma_{lv}$ = 30.8 mN m$^{-1}$ is the surface tension between the liquid (l) and the vapor (v) phase for polystyrene in air.‡[39] Based on the work of Huh and Scriven,[40] de Gennes developed a simplified model for the energy dissipation in a liquid wedge exhibiting a Poiseuille-type velocity profile $u(z)$, where the viscous dissipation power per unit length is described by:

$$D_{visc} = \int_0^\infty \int_0^\zeta \eta \left(\frac{du}{dz}\right)^2 dx dz = \int_0^\infty \frac{3\eta v^2}{\zeta} dx = \int_0^\infty \frac{3\eta v^2}{x \tan\theta_{rec}} dx, \quad (1)$$

with $\zeta = x\tan\theta_{rec}$ representing the local film height, $\eta$ being the fluid viscosity and $v$ standing for the velocity of the receding wedge.

‡ Note, that the surface tension of a polymer melt depends on temperature and molecular weight. Here, the variation in $\gamma_{lv}$ is very small (<10%) and the mean value of $\gamma_{lv}$ = 30.8 mN m$^{-1}$ is used. The error caused by using the averaged surface tension value is negligible compared to the uncertainty of the viscosity (as mentioned later in the text).

The divergence of the integral at both ends can be avoided by cutting the integral at the lateral position $x = w$ (which is an appropriate upper limit length scale like the width of the drop) and at the molecular size $x = a$ representing a lower limit, which leads to:

$$D_{visc} = \frac{3\eta l}{\tan\theta_{rec}} v^2, \quad (2)$$

where $l \equiv \ln(w/a)$ denotes a dimensionless coefficient. With the power balance $F_{drive}\, v = D_{visc}$, the velocity $v$ of a dewetting wedge on a planar substrate is given by:

$$\frac{1}{v} = \frac{3l}{|S|\tan\theta_{rec}}\eta = A\eta. \quad (3)$$

This implies that in case of a purely viscous flow at the solid/liquid interface the velocity of a moving wedge is inversely proportional to the melt viscosity $\eta$, with $A = 3l/(|S|\tan\theta_{rec})$ representing the constant of proportionality.

Fig. 5 shows a semi-logarithmic plot of the inverse local droplet velocity $1/v$ for various molecular weights ranging from 4.2 to 78 kg mol$^{-1}$ as a function of temperature $T$ (symbols). Typically, four to eight separate velocity measurements were averaged per data point. In addition, the respective viscosity data versus temperature is shown as dashed lines. The viscosities were determined from independent viscosimeter and ellipsometric measurements[33] by projecting the data according to the Williams–Landel–Ferry (WLF) equation:[34,35]

$$\eta = \eta_0 \exp\left(\frac{B}{f_0}\frac{T_g - T}{T - T_\infty}\right), \quad (4)$$

where $\eta_0 = 6.3 \times 10^8$ Pa s represents the viscosity at the glass transition temperature $T_g = T_g(\infty) - C/M_w$ for the respective $M_w$, with $T_g(\infty)$ = 372 K and $C$ = 70 K kg mol$^{-1}$ for PS. The Vogel

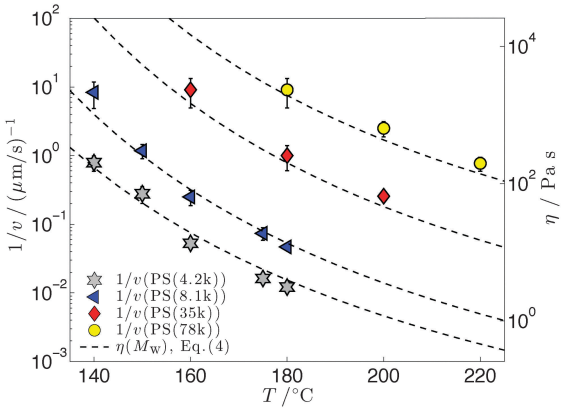


Fig. 5 Semilogarithmic representation of the inverse droplet velocity $1/v$ (symbols) and viscosity $\eta$ according to eqn (4) and independent viscosimeter measurements (dashed lines) for different molecular weights as a function of temperature $T$. The error bars represent the standard deviation of different dewetting velocity measurements. The inverse of the dewetting speed scales linearly with viscosity, exhibiting a universal constant of proportionality $A$ = 3900 ± 300 m N$^{-1}$.

 

temperature is given by $T_\infty = T_g - 48$ K and the ratio $B/f_0 = 30.3$ is taken from literature.[35]

In order to match the velocity data $1/v$ (symbols, left $y$-axis), the viscosities (dashed lines, right $y$-axis) are rescaled by a single constant prefactor $A$, which was found to be $3900 \pm 300$ m N$^{-1}$. This finding is consistent with experimental studies on dewetting holes in thin liquid polystyrene films with low molecular weights on hydrophobized flat surfaces.[33] Fig. 6 displays the inverse of the measured local mean velocity $1/v$ as a function of viscosity $\eta$. The black line represents the linear scaling between $1/v$ and $\eta$ with the universal proportionality constant $A$, as predicted by the force balance model based on purely viscous dissipation (eqn (3)). Imposing the universal prefactor $A$ as given above, this model turns out to be in good agreement with the experimental velocity data. Knowing the spreading parameter $|S|$ and $\theta_{rec}$ from the experimental data, the dimensionless coefficient $l$ is the only free parameter. We obtain $l = 61 \pm 10$, which is in the same order of magnitude as in previous numerical studies,[38] where $l$ was found to range from 15 to 20. Experimental studies,[31] *e.g.* on dewetting of PDMS on non-wettable surfaces by Redon *et al.* have reported a dimensionless coefficient of $l = 20$, whereas for more viscous alkanes $l = 6$ was obtained. A potential source of the deviation in $l$ compared to other studies might originate from the fact that the polymer viscosity is very sensitive to variations in temperature and already a difference in $T$ of 1 K can lead to a considerable systematic change in the dewetting dynamics. A second hypothesis is as follows: dissipative particle dynamics simulations by Meriaba *et al.* did provide evidence that the viscous dissipation of a dewetting liquid front is predominantly located at the three-phase contact line.[41] Nevertheless, it is shown that viscous friction at the position, where the front merges into the residual thin film, represents a weak additional contribution to the dissipated energy. Assuming energy dissipation localized at both sides of the moving liquid front does not alter the scalings, eqn (3), but justifies a decrease in the free parameter $l$.[37,38] In summary, we find that the model based on purely viscous dissipation captures the capillary-driven propulsion of axisymmetric droplets on hydrophobized fibres.

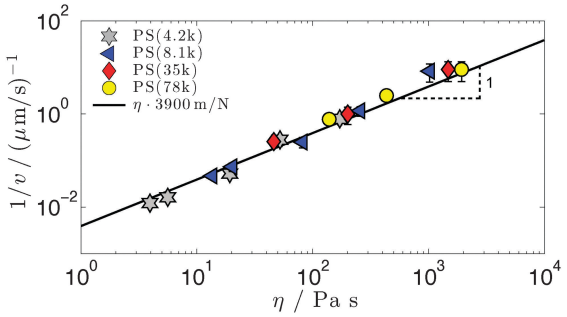


Fig. 6 Inverse droplet velocity $1/v$ as a function of viscosity $\eta$ according to eqn (4) and independent viscosimeter measurements. The error bars represent the standard deviation of different dewetting velocity measurements and do not include the uncertainty of the viscosity data taken from the WLF equation (see eqn (4)). The black line represents the linear scaling between $1/v$ and $\eta$ with the universal proportionality constant $A = 3900 \pm 300$ m N$^{-1}$.

In the following paragraph, we will discuss friction at the solid/liquid interface, which has been identified as a potentially significant source of energy dissipation in thin film flows:[32,33,42] from an earlier study on the growth rates of amplitudes during the RPI it is known that PS(78k) on a hydrophobized fibre can exhibit significant hydrodynamic slip at the fibre/liquid interface.[13] The slip length $b$,[43] which provides a quantitative measure for the amount of slip at the solid/liquid interface, was found to be $b = 4.0 \pm 0.4$ μm for the exact same system. As the slip length scales with molecular weight,[44,45] lower molecular weights are expected to exhibit a smaller slip length.

Despite providing a slip boundary condition, which leads to a non-zero velocity of the polymer molecules at the solid/liquid interface,[32,46] we find that the dynamics of a dewetting droplet is linear in time.[32,33] In addition, the local velocity $v$ does not depend on the initial radius of the system $h_0$ (see Fig. 4) or rather the droplet size (height $h_{max}(t)$ and width $w(t)$), within the range of droplets sizes tested in our experiments. For smaller droplets one would expect to see an increase in the dewetting velocity as the PS film becomes sensitive to the enhanced mobility at the interface. By measuring the maximum droplet height $h_{max}(t)$ (see Fig. 1c) we see that for all times $t$, the ratio between slip length $b$ and maximal droplet height is equal to $b/h_{max}(t) < 0.1$. This implies that the size of the droplets compared to $b$ is too large to identify a considerable influence of the enhanced mobility at the solid/liquid interface on the dewetting speed. For large droplets, with $b/h_{max}(t) < 0.1$, viscous friction at the contact line dominates over slippage. Thus, in our study, the dewetting dynamics is exclusively controlled by local dissipation at the contact line and the experimentally determined proportionality constant $A$, describing the linear scaling between $1/v$ and $\eta$, is universally valid (see Fig. 6).

## 4 Conclusions

Here, we have reported on the generation of uniform polystyrene droplets on a hydrophobized fibre by taking advantage of the Rayleigh–Plateau instability. Nucleation causes the spontaneous formation of a three-phase contact line at one side of a droplet. This leads to a capillary imbalance, which in turn causes the droplet to dewet on the fibre. Thereby, we found that the dynamics of a droplet is linear for all times and is as well geometry invariant. Considering the entire motion process including the accumulation of the residual thin film and the coalescence steps with static droplets shows that the dewetting velocity of the droplet is alternating around a certain mean velocity $\bar{v}$: the consumption of the thin polymer film features a constant droplet speed, but the coalescence process between moving and static droplets causes a local increase in velocity combined with a decrease in the receding contact angle. However, at the end of the merging procedure, $\theta_{rec}$ recovers and the speed is again decelerated. By neglecting the coalescence steps, the evaluation of the local droplet dynamics for varying molecular weights and temperatures exhibits a linear scaling between the inverse local dewetting velocity $1/v$ and viscosity $\eta$, consistent with the classical force balance model of a

dewetting liquid wedge on a substrate based on purely viscous friction (see eqn (3)). We found a single proportionality constant describing all data sets, which is in good agreement with former experimental studies on dewetting holes in thin films on hydrophobized surfaces.[33] Hence, we see that viscous dissipation dominates over slip-induced dissipation at the solid/liquid interface, for droplets which exhibit a height of at least ten times the corresponding slip length.

We expect these findings to be valid for all Newtonian liquids that are driven by capillarity and mediated by viscous forces. The precise control of droplet propulsion on microfibres might play an important role for practical applications and motivate novel designs of open microfluidic devices for chemical reactions and biological analysis. One might also envision new approaches and improvements in liquid deposition and patterning techniques. Finally, it provides a reliable and rapid method to determine the viscosity of a liquid.

## Acknowledgements

The authors thank the graduate school GRK 1276, the German Research Foundation (DFG) under grant number BA3406/2 and NSERC of Canada. The authors also thank Kari Dalnoki-Veress, Thomas Salez, Michael Benzaquen, Elie Raphaël, Robert Peters and Joshua McGraw for fruitful discussions.

## References

1 Y. Zheng, H. Bai, Z. Huang, X. Tian, F.-Q. Nie, Y. Zhao, J. Zhai and L. Jiang, *Nature*, 2010, **463**, 640–643.
2 J. Plateau, *Experimental and theoretical steady state of liquids subjected to nothing but molecular forces*, Gauthier-Villars, Paris, 1873.
3 F. Rayleigh, *Proc. London Math. Soc.*, 1878, **s1–10**, 4.
4 H. Bai, J. Ju, R. Sun, Y. Chen, Y. Zheng and L. Jiang, *Adv. Mater.*, 2011, **23**, 3708–3711.
5 J. Ju, H. Bai, Y. Zheng, T. Zhao, R. Fang and L. Jlang, *Nat. Commun.*, 2012, **3**, 1247, DOI: 10.1038/ncomms2253.
6 K.-C. Park, S. S. Chhatre, S. Srinivasan, R. E. Cohen and G. H. McKinley, *Langmuir*, 2013, **29**, 13269–13277.
7 P. Ferraro, S. Coppola, S. Grilli, M. Paturzo and V. Vespini, *Nat. Nanotechnol.*, 2010, **5**, 429–435.
8 P. Azenbacher and M. A. Palacios, *Nat. Chem.*, 2009, **11**, 80–86.
9 J.-U. Park, M. Hardy, S. J. Kang, K. Barton, K. Adair, D. K. Mukhopadhyay, C. Y. Lee, M. S. Strano, A. G. Alleyne, J. G. Georgiadis, P. M. Ferreira and J. A. Rogers, *Nat. Mater.*, 2007, **6**, 782–789.
10 S. L. Goren, *J. Colloid Interface Sci.*, 1964, **19**, 81–86.
11 R.-J. Roe, *J. Colloid Interface Sci.*, 1975, **50**, 70–79.
12 J. Eggers, *Phys. Fluids*, 2014, **26**, 033106.
13 S. Haefner, M. Benzaquen, O. Bäumchen, T. Salez, R. Peters, J. McGraw, K. Jacobs, E. Raphaël and K. Dalnoki-Veress, *Nat. Commun.*, 2015, **6**, 7409, DOI: 10.1038/ncomms8409.
14 D. Quéré, *Europhys. Lett.*, 1990, **13**, 721–726.
15 B. J. Mullins, I. E. Agranovski, R. D. Braddock and C. M. Ho, *J. Colloid Interface Sci.*, 2004, **269**, 449–458.
16 R. V. Craster and O. K. Matar, *J. Fluid Mech.*, 2006, **553**, 85–105.
17 T. Gilet, D. Terwagne and N. Vandewalle, *Appl. Phys. Lett.*, 2009, **95**, 014106.
18 T. Gilet, D. Terwagne and N. Vandewalle, *Eur. Phys. J. E: Soft Matter Biol. Phys.*, 2010, **31**, 253–262.
19 R. Mead-Hunter, T. Bergen, T. Becker, R. A. O'Leary, G. Kasper and B. J. Mullins, *Langmuir*, 2012, **28**, 3483–3488.
20 F. Boulogne, L. Pauchard and F. Giorgiutti-Dauphiné, *J. Fluid Mech.*, 2012, **704**, 232–250.
21 A. L. Yarin, W. Liu and D. H. Reneker, *J. Appl. Phys.*, 2002, **91**, 4751–4760.
22 E. Lorenceau and D. Quéré, *J. Fluid Mech.*, 2004, **510**, 29–45.
23 R. W. Style, Y. Che, S. J. Park, B. M. Weon, J. H. Je, C. Hyland, G. K. German, M. P. Power, L. A. Wilen, J. S. Wettlaufer and E. R. Dufresne, *Proc. Natl. Acad. Sci. U. S. A.*, 2013, **110**, 12541–12544.
24 R. Seemann, M. Brinkmann, T. Pfohl and S. Herminghaus, *Rep. Prog. Phys.*, 2012, **75**, 016601.
25 J. K. Keddie, R. A. Jones and R. A. Cory, *Europhys. Lett.*, 1994, **27**, 59–64.
26 S. Herminghaus, K. Jacobs and R. Seemann, *Eur. Phys. J. E: Soft Matter Biol. Phys.*, 2001, **5**, 531–538.
27 G. McHale and M. I. Newton, *Colloids Surf., A*, 2002, **206**, 79–86.
28 H. B. Eral, J. de Ruiter, R. de Ruiter, J. M. Oh, C. Semprebon, M. Brinkmann and F. Mugele, *Soft Matter*, 2011, **7**, 5138.
29 R. Seemann, S. Herminghaus and K. Jacobs, *Phys. Rev. Lett.*, 2001, **86**, 5534–5537.
30 R. Seemann, S. Herminghaus and K. Jacobs, *Phys. Rev. Lett.*, 2001, **87**, 196101.
31 C. Redon, F. Brochard-Wyart and F. Rondelez, *Phys. Rev. Lett.*, 1991, **66**, 715–718.
32 R. Fetzer and K. Jacobs, *Langmuir*, 2007, **23**, 11617–11622.
33 O. Bäumchen, R. Fetzer, M. Klos, M. Lessel, L. Marquant, H. Hähl and K. Jacobs, *J. Phys.: Condens. Matter*, 2012, **24**, 325102.
34 M. L. Williams, R. F. Landel and J. D. Ferry, *J. Am. Chem. Soc.*, 1955, **77**, 3701–3707.
35 M. Rubinstein and R. H. Colby, *Polymer Physics*, Oxford Univ. Press. Inc., New York, 2003.
36 A. Savitzky and M. J. E. Golay, *Anal. Chem.*, 1964, **36**, 1627–1639.
37 P. G. de Gennes, *Rev. Mod. Phys.*, 1985, **57**, 827–863.
38 P. G. de Gennes, F. Brochard-Wyart and D. Quéré, *Capillarity and wetting phenomena: drops, bubbles, pearls, waves*, Springer-Verlag New York Inc., 2004.
39 J. Brandrup, E. H. Immergut and E. A. Grulke, *Polymer Handbook*, John Wiley & Sons Inc., New York, 1999.
40 C. Huh and L. E. Scriven, *J. Colloid Interface Sci.*, 1971, **35**, 85–101.
41 S. Merabia and J. B. Avalos, *Phys. Rev. Lett.*, 2008, **101**, 208304.
42 O. Bäumchen and K. Jacobs, *J. Phys.: Condens. Matter*, 2010, **22**, 033102.
43 C. L. M. H. Navier, *Mem. Acad. Sci. Inst. Fr.*, 1823, **6**, 389.
44 P. G. de Gennes, *C. R. Seances Acad. Sci., Ser. B*, 1979, 324.
45 O. Bäumchen, R. Fetzer and K. Jacobs, *Phys. Rev. Lett.*, 2009, **103**, 247801.
46 L. Bocquet and J.-L. Barrat, *Soft Matter*, 2007, **3**, 685–693.

 

# Bibliography


[1] H. Staudinger, *Berichte der Deutschen Chemischen Gesellschaft*, **53**, 1073 (1920).

[2] K. Ziegler, K. Nagel and W. Pfohl, *Ann.Chem.*, **629**, 1-3 (1960).

[3] G. Natta, I. Pasquon and A. Zambelli, *J. Am. Chem. Soc.*, **84**, 1488-1490 (1962).

[4] P. L. Flory, *Principles of polymer chemistry*, Cornell Univ. Press, New York, 1953.

[5] P.-G. de Gennes, *Scaling concepts in polymer physics*, Cornell Univ. Press, New York, 1979.

[6] J. D. Ferry, *Viscoelastic properties of polymers*, John Wiley & Sons Inc., 1980.

[7] G. R. Strobl, *The physics of polymers*, Springer, Berlin Heidelberg, 2007.

[8] M. Rubinstein and R. H. Colby, *Polymer Physics*, Oxford University Press, New York, 2003.

[9] J. L. Keddie, R. A. L. Jones and R. A. Cory, *Europhys. Lett.*, **27**, 59-64 (1994).

[10] K. Dalnoki-Veress, J. A. Forrest, P.-G. de Gennes and J. R. Dutcher, *J. Phys. IV France*, **10**, 7221-7226 (2000).

[11] S. Herminghaus, K. Jacobs and R. Seemann, *Eur. Phys. J. E*, **5**, 531-538 (2001).

[12] S. Herminghaus, K. Jacobs and R. Seemann, *Eur. Phys. J. E*, **12**, 101-110 (2003).

[13] J. S. Sharp and J. A. Forrest, *Phys. Rev. Lett.*, **91**, 235701 (2003).

[14] O. Bäumchen, J. D. McGraw, J. A. Forrest and K. Dalnoki-Veress, *Phys. Rev. Lett.*, **105**, 055701 (2012).

[15] M. L. Williams, R. F. Landel and J. D. Ferry, *J. Am. Chem. Soc.*, **77**, 3701-3707 (1955).

[16] P.-G. de Gennes, *J. Chem. Phys.*, **55**, 572 (1971).

[17] O. Bäumchen, R. Fetzer, M. Klos, M. Lessel, L. Marquant, H. Hähl and K. Jacobs, *J. Phys.: Condens. Matter*, **24**, 325102 (2012).

[18] J. D. McGraw, T. Salez, O. Bäumchen, E. Raphaël and K. Dalnoki-Veress, *Soft Matter*, **9**, 8297-8305 (2013).

[19] R. Fetzer, *Einfluss von Grenzflächen auf die Fluidik dünner Polymerfilme*, Dissertation (Saarland University) and Logos Verlag, Berlin, ISBN 3-8325-1354-X, 2006.

[20] A. Münch, B. Wagner and T. P. Witelski, *J. Eng. Math.*, **53**, 359-383 (2005).

[21] L. D. Landau and E. M. Lifshitz, *Fluid Mechanics: Course of Theoretical Physics*, Elsevier, 2013.

[22] A. Oron, S. H. Davis and S. G. Bankoff, *Rev. Mod. Phys.*, **69**, 931-980 (1997).

[23] J. Brandrup, E. H. Immergut and E. A. Grulke, *Polymer Handbook*, John Wiley & Sons Inc.: New York, 1999.

[24] S. Wu, *J. Phys. Chem.*, **74**, 632 (1970).

[25] J. C. Moreira and N. R. Demarquette, *J. Appl. Polym. Sci.*, **82**, 1907-1920 (2001).

[26] C. L. M. H. Navier, *Mem. Acad. Sci. Inst. Fr.*, **6**, 389 and 432 (1823).

[27] V. S. J. Craig, C. Neto and D. R. M. Williams, *Phys. Rev. Lett.*, **87**, 054504 (2001).

[28] O. I. Vinogradova, H.-J. Butt, G. E. Yakubov and F. Feuillebois, *Rev. Sci. Instrum.*, **72**, 2330 (2001).

[29] D. C. Tretheway and C. D. Meinhart, *Phys. Fluids*, **14**, L9-L11 (2002).

[30] D. C. Tretheway and C. D. Meinhart, *Phys. Fluids*, **16**, 1509 (2004).

[31] O. I. Vinogradova, *Langmuir*, **11**, 2213-2220 (1995).

[32] R. Fetzer, A. Münch, B. Wagner, M. Rauscher and K. Jacobs, *Langmuir*, **23**, 10559-10566 (2007).

[33] R. Fetzer, K. Jacobs, A. Münch, B. Wagner and T. P. Witelski, *Phys. Rev. Lett.*, **95**, 127801 (2005).

[34] R. Fetzer and K. Jacobs, *Langmuir*, **23**, 11617-11622 (2007).

[35] O. Bäumchen, R. Fetzer and K. Jacobs, *Phys. Rev. Lett.*, **103**, 247801 (2009).

[36] J.-L. Barrat and L. Bocquet, *Phys. Rev. Lett.*, 82, 4671-4674 (1999).

[37] R. Pit, H. Hervet and L. Léger, *Phys. Rev. Lett.*, **85**, 980-983 (2000).

[38] C. Cottin-Bizonne, S. Jurine, J. Baudry, J. Crassous, F. Restagno and E. Charlaix, *Eur. Phys. J. E*, **9**, 47-53 (2002).

[39] L. Léger, *J. Phys.: Condens. Matter*, **15**, S19-S29 (2003).

[40] C. Cottin-Bizonne, J.-L. Barrat, L. Bocquet and E. Charlaix, *Nat. Mater.*, **2**, 238-240 (2003).

[41] J. W. G. Tyrell and P. Attard, *Phys. Rev. Lett.*, **87**, 176104 (2001).

[42] P.-G. de Gennes, *Langmuir*, **18**, 3413-3414 (2002).

[43] R. Steitz, T. Gutberlet, T. Hauss, B. Klösgen, R. Krastev, S. Schemmel, A. C. Simonsen and G. H. Findenegg, *Langmuir*, **19**, 2409-2418 (2003).

[44] N. V. Priezjev, A. A. Darhuber and S. M. Troian, *Phys. Rev. E*, **71**, 041608 (2005).

[45] T. Schmatko, H. Hervet and L. Léger, *Phys. Rev. Lett.*, **94**, 244501 (2005).

[46] S. Heidenreich, P. Ilg and S. Hess, *Phys. Rev. E*, **75**, 066302 (2007).

[47] K. B. Migler, H. Hervet and L. Leger, *Phys. Rev. Lett.*, **70**, 287-290 (1993).

[48] F. Brochard-Wyart and C. Redon, *Langmuir*, **8**, 2324-2329 (1992).

[49] A. Ajdari, F. Brochard-Wyart, P.-G. de Gennes, L. Leibler, J.-L. Viovy and M. Rubinstein, *Physica A*, **204**, 17-39 (1994).

[50] G. Gay, *Eur. Phys. J. B*, **7**, 251-262 (1999).

[51] M. A. Tchesnokov, J. Molenaar, J. J. M. Slot and R. Stepanyan, *J. Chem. Phys.*, **122**, 214711 (2005).

[52] P.-G. de Gennes, *C. R. Acad. Sci. Paris Ser. B*, **288**, 219 (1979).

[53] C. Redon, J. B. Brzoska and F. Brochard-Wyart, *Macromolecules*, **27**, 468-471 (1994).

[54] H. D. Rowland, W. P. King, J. B. Pethica and G. L. W. Cross, *Science*, **322**, 720 (2008).

[55] D. R. Barbero and U. Steiner, *Phys. Rev. Lett.*, **102**, 248303 (2009).

[56] H. R. Brown and T. P. Russell, *Macromolecules*, **26**, 798-800 (1996).

[57] K. Kargupta, A. Sharma and R. Khanna, *Lamgmuir*, **20**, 244-253 (2004).

[58] R. Seemann, S. Herminghaus and K. Jacobs, *Phys. Rev. Lett.*, **86**, 5534-5537 (2001).

[59] S. Dietrich, *Phase Transition and Critical Phenomena*, ed. C. Domb and J. L. Lebowitz, Vol. 12, Academic Press, London, 1988.

[60] K. Jacobs, R. Seemann and S. Herminghaus, *Thin liquid films*, ed. O. Tsui and T. Russel, World Scientific, 2008.

[61] J. N. Israelachvili, *Intermolecular and surface forces*, Academic Press, San Diego, 1991.

[62] A. Vrij, *Farad. Discuss.*, **42**, 23 (1966).

[63] F. Rayleigh, *Proc. London Math. Soc.*, **s1-10**, 4 (1878).

[64] R. Seemann, S. Herminghaus, C. Neto, S. Schlagowski, D. Podzimek, R. Konrad, H. Mantz and K. Jacobs, *J. Phys.: Condens. Matter*, **17**, 267-290 (2005).

[65] G. Reiter, *Phys. Rev. Lett.*, **68**, 75–78 (1992).

[66] K. Jacobs, R. Seemann, G. Schatz and S. Herminghaus, *Langmuir*, **14**, 4961–4963 (1998).

[67] F. Brochard-Wyart, P.-G. de Gennes, H. Hervet and C. Redon, *Langmuir*, **10**, 1566-1572 (1994).

[68] P.-G. de Gennes, *Rev. Mod. Phys.*, **57**, 827-863 (1985).

[69] P.-G. de Gennes, F. Brochard-Wyart and D. Quéré, *Capillarity and wetting phenomena: drops, bubbles, pearls, waves*, Springer, 2004.

[70] C. Huh and L. E. Scriven, *J. Colloid Interface Sci.*, **35**, 85-101 (1971).

[71] S. Merabia and J. B. Avalos, *Phys. Rev. Lett.*, **101**, 208304 (2008).

[72] F. Savart, *Annales de chimie*, 1833.

[73] J. Plateau, *Experimental and theoretical steady state of liquids subjected to nothing but molecular forces*, Gauthiers-Villars, Paris, 1873.

[74] Saarland University, *Physiker gewinnen neue Einsicht über dynamische Eigenschaften dünner Polymerfilme*, Pressemitteilung, 04.08.2014.

[75] J. Eggers and E. Villermaux, *Rep. Prog. Phys.*, **71**, 036601 (2008).

[76] S. Mora, T. Phou and J.-M. Fromental, *Phys. Rev. Lett.*, **105**, 214301 (2010).

[77] D. Henann and K. Bertoldi, *Soft Matter*, **10**, 709-717 (2014).

[78] M.Tjahjadi, H. A. Stone and J. M. Ottino, *J. Fluid Mech.*, **243**, 297-317 (1992).

[79] C. Wagner, Y. Amarouchene, D. Bonn and J. Eggers, *Phys. Rev. Lett.*, **95**, 164504 (2005).

[80] R. Sattler, C. Wagner and J. Eggers, *Phys. Rev. Lett.*, **100**, 164502 (2008).

[81] R. Sattler, S. Gier, J. Eggers and C. Wagner, *Phys. Fluids*, **24**, 023101 (2012).

[82] G. Reiter and A. Sharma, *Phys. Rev. Lett.*, **87**, 166103 (2001).

[83] G. Reiter, *J. Adhesion*, **81**, 381-395 (2005).

[84] A. Münch and B. Wagner, *J. Phys.: Condens. Matter*, **23**, 184101 (2011).

[85] O. Bäumchen, L. Marquant, R. Blossey, A. Münch, B. Wagner and K. Jacobs, *Phys. Rev. Lett.*, **113**, 014501 (2014).

[86] K. Khare, M. Brinkmann, B. M. Law, E. L.Gurevich, S. Herminghaus and R. Seemann, *Langmuir*, **23**, 12138-12141 (2007).

[87] E. Pairam and A. Fernandez-Nieves, *Phys. Rev. Lett.*, **102**, 234501 (2009).

[88] J. D. McGraw, J. Li, D. L. Tran, A.-C. Shi and K. Dalnoki-Veress, *Soft Matter*, **6**, 1258-1262 (2010).

[89] V. Duclax, C. Clanet and D. Quéré, *J. Fluid Mech.*, **556**, 217-226 (2006).

[90] L. V. Zhang, P. Brunet, J. Eggers and R. D. Deegan, *Phys. Fluids*, **22**, 122105 (2010).

[91] S. L. Goren, *J. Colloid Interface Sci.*, **19**, 81-86 (1964).

[92] I. L. Kliakhandler, S. H. Davis and S. G. Bankoff, *J. Fluid Mech.*, **429,** 381-390 (2001).

[93] R. V. Craster and O. K. Matar, *J. Fluid Mech.*, **553**, 85-105 (2006).

[94] R. V. Craster and O. K. Matar, *Rev. Mod. Phys.*, **81**, 1131-1198 (2009).

[95] C. Duprat, C. Ruyer-Quil and F. Giorgiutti-Dauphine, *Phys. Fluids*, **21**, 042109 (2009).

[96] S. L. Goren, *J. Fluid Mech.*, **12**, 309-319 (1962).

[97] R.-J. Roe, *J. Colloid Interface Sci.*, **50**, 70-79 (1975).

[98] L. Bocquet and J.-L. Barrat, *Soft Matter*, **3**, 685-693 (20007).

[99] R. E. Rosensweig, *Ferrohydrodynamics*, Cambridge University Press, 1985.

[100] A. L. Yarin, A. Oron and P. Rosenau, *Phys. Fluids A*, **5**, 91-98 (1993).

[101] Y. Zheng, H. Bai, Z. Huang, X. Tian, F.-Q. Nie, Y. Zhao, J. Zhai and L. Jiang, *Nature*, **463**, 640-643 (2010).

[102] A. de Ryck and D. Quéré, *Lamgmuir*, **14**, 1911-1914 (1998).

[103] D. Quéré, *Annu. Rev. Fluid Mech.*, **31**, 347-384 (1999).

[104] D. Quéré, *Europhys. Lett.*, **13**, 721-726 (1990).

[105] H. Bai, J. Ju, R. Sun, Y. Chen, Y. Zheng and L. Jiang, *Adv. Mater.*, **23**, 3708-3711 (2011).

[106] J. Ju, H. Bai, Y. Zheng, T. Zhao, R. Fang and L. Jiang, *Nat. Commun.*, **3**, 1247 (2012).

[107] K.-C. Park, S. S. Chhatre, S. Srinivasan, R. E. Cohen and G. H. McKinley, *Langmuir*, **29**, 13269-13277 (2013).

[108] P. Ferraro, S. Coppola, S. Grilli, M. Paturzo and V. Vespini, *Nat. Nanotechnol.*, **5**, 429-435 (2010).

[109] J.-U. Park, M. Hardy, S. J. Kang, K. Barton, K. Adair, D. K. Mukhopadhyay, C. Y. Lee, M. S. Strano, A. G. Alleyne, J. G. Georgiadis, P. M. Ferreira and J. A. Rogers, *Nat. Mater.*, **6**, 782-789 (2007).

[110] P. Anzenbacher and M. A. Palacios, *Nat. Chem.*, **11**, 80-86 (2009).

[111] F. Weyer, M. Lismont, L. Dreesen and N. Vandewalle, *Soft Matter*, **11**, 7086-7091 (2015).

[112] R. Seemann, M. Brinkmann, T. Pfohl and S. Herminghaus, *Rep. Prog. Phys.*, **75**, 016601 (2012).

[113] B. J. Mullins, I. E. Agranovski, R. D. Braddock and C. M. Ho, *J. Colloid Interface Sci.*, **269**, 449-458 (2004).

[114] T. Gilet, D. Terwagne and N. Vandewalle, *Appl. Phys. Lett.*, **95**, 014106 (2009).

[115] T. Gilet, D. Terwagne and N. Vandewalle, *Eur. Phys. J. E*, **31**, 253-262 (2010).

[116] R. Mead-Hunter, T. Bergen, T. Becker, R. A. O'Leary, G. Kasper and B. J. Mullins, *Langmuir*, **28**, 3483-3488 (2012).

[117] F. Boulogne, L. Pauchard and F. Giorgiutti-Dauphiné, *J. Fluid. Mech.*, **704**, 232-250 (2012).

[118] A. L. Yarin, W. Liu and D. H. Reneker, *J. Appl. Phys.*, **91,** 4751-4760 (2002).

[119] E. Lorenceau and D. Quéré, *J. Fluid Mech.*, **510**, 29-45 (2004).

[120] E. Q. Li and S. T. Thoroddsen, *Phys. Fluids*, **25**, 052105 (2013).

[121] R. W. Style, Y. Che, S. J. Park, B. M. Weon, J. H. Je, C. Hyland, G. K. German, M. P. Power, L. A. Wilen, J. S. Wettlaufer and E. R. Dufresne, *Proc. Natl. Acad. Sci. U.S.A.*, **110,** 12541-12444 (2013).

[122] B. J. Carroll, *J. Colloid Interface Sci.*, **57**, 488-495 (1976).

[123] B. J. Carroll, *Lamgmuir*, **2**, 248-250 (1986).

[124] C. Bauer and S. Dietrich, *Phys. Rev. E*, **62**, 2428-2438 (2000).

[125] G. McHale and M. I. Newton, *Colloids Surf. A*, **106**, 79-86 (2002).

[126] H. B. Eral, J. de Ruiter, R. de Ruiter, J. M. Oh, C. Semprebon, M. Brinkmann and F. Mugele, *Soft Matter*, **7**, 5138 (2011).

[127] R. de Ruiter, J. de Ruiter, H. B. Eral, C. Semprebon, M. Brinkmann and F. Mugele, *Langmuir*, **28**, 13300-13306 (2012).

[128] S. Haefner, M. Benzaquen, O. Bäumchen, T. Salez, R. Peters, J. D. McGraw, K. Jacobs, E. Raphaël and K. Dalnoki-Veress, *Nat. Commun.*, **6**, 7409 (2015).

[129] O. Bäumchen, Personal communication, 2013.

[130] M. Lessel, O. Bäumchen, M. Klos, H. Hähl, R. Fetzer, M. Paulus, R. Seemann and K. Jacobs, *Surf. Interface Anal.*, **47**, 557-564 (2015).

[131] S. Haefner, *Fließverhalten komplexer Flüssigkeiten - Einfluss des Rutschens auf die Entnetzungsmorphologie gerader Polymerfronten*, Diplomarbeit (Saarland University), 2012.

[132] S. Haefner, O. Bäumchen and K. Jacobs, *Soft Matter*, **11**, 6921-6926 (2015).

[133] P.-G. de Gennes, *Eur. Phys. J. E*, **6**, 421-424 (2001).

[134] Product description and specifications, Fisher scientific.

[135] G. Binnig, C. F. Quate and C. Gerber, *Phys. Rev. Lett.*, **56**, 930 (1986).

[136] B. Bhushan (ed.), *Springer Handbook of Nanotechnology*, Springer, Berlin, Heidelberg, New York, 2004.

[137] H. G. Tompkins and W. A. McGahan, *Spectroscopic ellipsometry and reflectometry: a user's guide*, John Wiley & Sons, New York, 1999.

[138] C. Redon, F. Brochard-Wyart and F. Rondelez, *Phys. Rev. Lett.*, **66**, 715-718 (1991).

[139] A. Bach, K. Almdal, H. Koblitz and O. Hassager, *Macromolecules*, **36**, 5174-5179 (2003).

[140] O. Bäumchen, *Fluidics of thin polymer films - boundary condition and interfacial phenomena*, Dissertation (Saarland University), 2010.

[141] D. Peschka, Personal communication, 2015.

[142] A. L. Bertozzi, *Notices Am. Math. Soc.*, **45**, 689 (1998).

[143] D. Peschka, *J. Comput. Phys.*, **295**, 770-778 (2015).

[144] L. Marquant, *Rim instability in dewetting of thin polymer films*, Dissertation (Saarland University), 2013.

[145] J. F. Hernandez, L. A. Lubbers, A. Eddi and J. H. Snoeijer, *Phys. Rev. Lett.*, **109**, 184502 (2012).

[146] A. Eddi, K. G. Winkels and J. H. Snoeijer, *Phys. Rev. Lett.*, **111**, 144502 (2013).

# Publications and Conference Contributions

## Publications

- J. D. McGraw, O. Bäumchen, M. Klos, S. Haefner, M. Lessel, S. Backes and K. Jacobs, Nanofluidics and thin polymer films: Linking the slip boundary condition at solid-liquid interfaces to macroscopic pattern formation and microscopic interfacial properties, *J. Colloid Interface Sci.*, **210**, 13 (2014).
- S. Haefner, M. Benzaquen, O. Bäumchen, T. Salez, R. Peters, J. D. McGraw, K. Jacobs, E. Raphaël and K. Dalnoki-Veress, *Nat. Commun.*, **6**, 7409 (2015).
- S. Haefner, O. Bäumchen and K. Jacobs, *Soft Matter*, **11**, 6921-6926 (2015).

## Selected scientific talks

- "Influence of the Polystyrene Chain Length on the Instability of a Dewetting Liquid Front", *DPG Spring Meeting*, Berlin (GER) (03/2012).
- "Influence of Slip on the Rayleigh-Plateau Rim Instability in Dewetting Polymer Films", *DPG Spring Meeting*, Regensburg (GER) (03/2013).
- "The Rayleigh-Plateau Instability on a Fibre Revisited - Influence of the Hydrodynamic Boundary Condition", *Soft Matter Retreat*, Buckhorn (ON, CA) (06/2013).
- "The Rayleigh-Plateau Instability on a Fibre - Influence of the Hydrodynamic Boundary Condition", *APS March Meeting*, Denver (CO, USA) (03/2014).
- "The Rayleigh-Plateau Instability on a Fibre - Influence of the Hydrodynamic Boundary Condition", *DPG Spring Meeting*, Dresden (GER) (03/2014).
- "Rayleigh-Plateau Instability and Capillary Droplet Propulsion on a Fibre", *APS March Meeting*, San Antonio (TX, USA) (03/2015).

## Selected poster presentations

- "Influence of Slip on the Rayleigh-Plateau Rim Instability in Dewetting Polymer Films", *APS March Meeting*, Baltimore (MD, USA) (03/2013).
- "The Rayleigh-Plateau Instability - Influence of the Hydrodynamic Boundary Condition", *International Soft Matter Conference*, Rom (I) (09/2013).

# Danke!

Ich möchte mich an dieser Stelle bei all denjenigen bedanken, die mich während meiner Promotion begleitet und unterstützt haben.

In allererster Linie gilt mein Dank Prof. Dr. Karin Jacobs, die es mir ermöglicht hat sowohl meine Diplomarbeit also auch meine Doktorarbeit in Ihrer Gruppe anzufertigen. Danke für all die Unterstützung und die Freiräume, die ich während dieser Zeit erleben und genießen durfte. Der Besuch vieler nationaler und internationaler Konferenzen war eine besondere Erfahrung. Vor allem möchte ich mich bei Ihr dafür bedanken, dass Sie mir die Möglichkeit geboten hat, im Rahmen der Promotion, einige Zeit in Kanada in der Gruppe von Prof. Dr. Kari Dalnoki-Veress zu verbringen.

Ein besonderer Dank für die großzügige finanzielle Unterstützung gilt dem Graduiertenkolleg 1276 "Strukturbildung und Transport in komplexen Systemen". Ich bedanke mich sehr herzlich bei den beiden Sprechern, Prof. Dr. Manfred Lücke und Prof. Dr. Ludger Santen.

Ich möchte mich ebenfalls bei allen Mitgliedern der AG Jacobs dafür bedanken, dass vor allem der Spaß bei der Arbeit nie zu kurz kam. Danke an meine Mitstreiter Mischa Klos, Nicolas Thewes, Samuel Grandthyll, Christian Spengler, Thomas Faidt und Jonas Heppe, sowie Dr. Frank Müller, Dr. Hendrik Hähl, Dr. Matthias Lessel, Dr. Christian Zeitz und besonders Dr. Joshua D. McGraw sowie Dr. Peter Loskill für den freundschaftlichen Umgang und die gegenseitige Unterstützung. Ein Dankeschön für die schöne und lustige Zeit geht ebenfalls an die Mitglieder der AG Seemann, besonders an Dr. Stefan Bommer, Dr. Hagen Scholl, Dr. Michael Hein sowie Prof. Dr. Ralf Seemann.

Liebe Judith, Liebe Monika, Danke! Danke dafür, dass Ihr mir immer den Rücken frei gehalten habt: Ihr habt Euch mit allen organisatorischen und bürokratischen Hürden herumgeschlagen und hattet immer eine Lösung (meist sogar) auf dem kurzen Dienstweg parat. Danke aber vor allem dafür, dass Ihr jederzeit ein offenes Ohr für mich hattet!

Ich möchte mich auch sehr herzlich für die gute Zusammenarbeit mit Dr. Dirk Peschka, Prof. Dr. Barbara Wagner und Prof. Dr. Andreas Münch aus Berlin und Oxford bedanken. Danke vor allem für die besondere Unterstützung in den letzten Wochen.

A very big thanks goes out to Prof. Dr. Kari Dalnoki-Veress and his soft matter research group. Thanks for having me and being a part of your research team. Working and 'sharpening the axe' with Rafael Schulman, Paul Fowler, Sean Ridout, Sara Cormier, Dr. Jessica Carvalho, Dr. Marc Ilton, Dr. Matilda Backholm, Dr. Robert Peters, Dr. Oliver Bäumchen and Prof. Dr. Laura Parker was great fun. Thanks for the KDV experience!

Moreover, I would like to thank 'team Paris', who are Dr. Thomas Salez, Dr. Michael Benzaquen and Prof. Dr. Elie Raphaël. Merci beaucoup pour cette bonne collaboration! I really enjoyed working with you. Thanks for all your help and the vivid discussions - via Skype, e-Mail or in person - at any time at day and at night!

Ein besonderer Dank gilt meinen Freunden und meiner Familie, vor allem dafür, dass sie mich von der Arbeit abgelenkt und auf andere Gedanken gebracht haben. Ein riesiges Dankeschön geht an meine beste Freundin, die weltbeste Sophie. Danke fürs Zuhören, Dasein und Erden!

Lieber Oliver, ich danke Dir von ganzem Herzen dafür, dass Du mich motiviert, unterstützt und mir mit Rat und Tat zur Seite gestanden hast. Du hast ganz selbstverständlich Freud und Leid mit mir geteilt und mir immer wieder neuen Mut gemacht.

Mein größter Dank gebührt meinen Eltern, Anita und Horst Haefner. Ihr seid es, die mir diesen Weg überhaupt ermöglicht haben. Danke dafür, dass ich mich zu jeder Zeit bedingungslos unterstützt!

*Sabrina*

# Eidesstattliche Erklärung

Hiermit versichere ich an Eides statt, dass ich die vorliegende Arbeit selbständig und ohne Benutzung anderer als der angegebenen Hilfsmittel angefertigt habe. Die aus anderen Quellen oder indirekt übernommenen Daten und Konzepte sind unter Angabe der Quelle gekennzeichnet.

Die Arbeit wurde bisher weder im In- noch im Ausland in gleicher oder ähnlicher Form in einem Verfahren zur Erlangung eines akademischen Grades vorgelegt.

Saarbrücken, den

(Sabrina Haefner)